Characterization of the Sarcolemma in Limb-Girdle Muscular Dystrophy

Dissertation

In fulfillment of the requirements for the degree

"Doctor rerum naturalium (Dr. rer. nat.)"

integrated in the International Graduate School for Myology MyoGrad

in the Department for Biology, Chemistry and Pharmacy at the Freie Universität Berlin

in Cotutelle Agreement with the Ecole Doctorale 515 "Complexité du Vivant" at the

Université Pierre et Marie Curie Paris

Submitted by Séverine Kunz

born in Ludwigshafen am Rhein

Berlin 2014

This work was prepared from April 2010 to September 2014 under the supervision of Prof. Dr. Simone Spuler (Experimental and Clinical Research Center (ECRC) of the Charité and the Max-Delbrück-Center for Molecular Medicine (Berlin, Germany)) and Prof. Dr. Thomas Voit from the Institute of Myology (Paris, France). I conducted the main part of my thesis in the laboratory of Prof. Dr. Simone Spuler in the Muscle Research Unit at the ECRC in Berlin. During my PhD, I worked for 14 months in the laboratory of Dr. Jean Cartaud in the Cell Biology Program at the Institute Jacques Monod in Paris.

Reviewers / Members of Doctorate Committee

PhD supervisor from the Freie Universität Berlin: Prof. Dr. Simone Spuler

Freie Universität Berlin

PhD supervisor from the Université Pierre et Marie Curie: Prof. Dr. Thomas Voit

Université Pierre et Marie Curie
Paris

1st external scientific expert: Prof. Dr. Joachim Weis

Universitätsklinikum Aachen

2nd external scientific expert: Dr. Claire Legay

Université Paris Descartes

Date of thesis submission: 09.09.2014

Date of thesis defense: 22.10.2014

Affidavit

I hereby declare that I wrote my doctoral thesis entitled "Characterization of the Sarcolemma in Limb-Girdle Muscular Dystrophy" independently and with no other sources and aids than quoted.

Berlin, September 2014

_____

(Signature)

Table of contents

Table of contents

Table of contents

List of figures

List of figures

List of tables

List of tables

List of abbreviations

AChR	Acetylcholine receptor
AFM	Atomic force microscopy
ANO5	Anoctamin 5 (gene)
Ano-5	Anoctamin 5 (protein)
ATPase	Adenosine triphosphatase
BCS	Bicinchononic acid assay
Bin-1	Myc box-dependent-interacting protein 1
BSA	Bovine serum albumin
CAV3	Caveolin-3 (gene)
Cav-3	Caveolin-3 (protein)
CaCC	Calcium-activated chloride channel
CCP	Clathrin-coated pit
CD	Cluster of differentiation
CLEM	Correlative light and electron microscopy
CTB	Cholera toxin B
Ctrl	Control (cell line)
DACM	Distal anterior compartment myopathy
dH$_2$O	Distilled water
DHPR	Dihydropyridine receptor
DNA	Deoxyribonucleic acid
DRM	Detergent-resistant membranes
DYSF	Dysferlin (gene)
Dysf	Dysferlin (protein)
ECL	Enhanced chemiluminescence
EGFP	Enhanced green fluorescent protein
EH	EPS15 homology
EHD2	EH-domain containing protein 2
EM	Electron microscopy
FA	Formaldehyde
FACS	Fluorescence-activated cell sorting
F-actin	Filamentous actin
g	G (gravitational)-force acceleration
GAPDH	Glyceraldehyde 3-phosphate dehydrogenase
GO	Gene ontology
GPI	Glycophosphatidylinositol
GTPase	Guanosine triphosphatase
GUV	Giant unilammelar vesicle
HPF	High pressure freezing
HRP	Horseradish peroxidase
IgG	Immunoglobulin G
IP	Immunopurification
IPA	Ingenuity pathway analysis
IR	Infrared
KEGG	Kyoto Encyclopedia of Genes and Genomes
LC-MS	Liquid chromatography–mass spectrometry
LGMD	Limb-girdle muscular dystrophy
LGMD 1C	LGMD type 1C

List of abbreviations

LGMD 2B	LGMD type 2B
LGMD 2L	LGMD type 2L
LM	Light microscopy
LR	Lipid raft
LTQ	Linear trap quadrupole
mβCD	Methyl-β-cyclodextrin
MT	Myotube
MB	Myoblast
MD	Muscular dystrophy
MG53	Mitsugumin 53
MHC	Myosin heavy chain
MM	Miyoshi myopathy
MR	Membrane rafts
MS	Mass spectrometry
MT	Myotube
MuSK	Muscle-specific tyrosine-protein kinase receptor
N	Nucleus
NADH	Nicotinamide adenine dinucleotide
NCAM	Neural cell adhesion molecule
NGS	Next generation sequencing
NMJ	Neuromuscular junction
PM	Plasma membrane
PTRF	Polymerase I and transcript release factor
rAb	Rabbit antibody
RNA	Ribonucleic acid
SDS/PAGE	Sodium docedyl sulphate- polyacrylamide gel electrophoresis
SEM	Standard error of the mean
S-EM	Scanning electron microscopy
Si-PVA	Tungstosilicic acid -polyvinyl alcohol
STED	Stimulated emission depletion microscopy
STORM	Stochastic optical reconstruction microscopy
SV 40	Simian virus 40
TAT	Trans-activator of transcription
TCA	Tricloroacetic acid
TEM	Transmission electron microscopy
TFRC1	Transferrin receptor protein 1
TIRF	Total internal reflection fluorescence
TMEM 16E	Transmembrane protein 16E
UA-MC	Uranylacetate-methylcellulose
VHH	Variable heavy chain antibody fragment
WB	Western blot

SI units and prefixes were used according to the International System of Units.

X

Summary

Limb-girdle muscular dystrophies (LGMD) are a heterogeneous group of slowly progressive muscular dystrophies (MD) with common features such as hyperCKemia and skeletal muscle weakness. Mutations in the dysferlin gene cause a spectrum of adult-onset muscular dystrophies including LGMD 2B, Miyoshi myopathy (MM) and distal anterior compartment myopathy (DACM) commonly referred to as dysferlinopathies. Human skeletal muscle from LGMD 2B patients displays known dystrophic features such as variations in fiber size and centralized nuclei, but also a rather unusual accumulation of subsarcolemmal vesicles. Dysferlin is a transmembrane protein and its subcellular localization is predominantly allocated to the plasma membrane, but also to developing T-tubules and intracellular vesicles. At the sarcolemma, dysferlin was shown to be crucial for efficient membrane repair, although it has been proposed to have a role in many other cellular functions such as vesicle fusion and intracellular trafficking, cell adhesion, immune response, and metabolism. LGMD 1C, another type of LGMD, is caused by mutations in the caveolin-3 (cav-3) gene. Cav-3 is the muscle-specific isoform of the caveolin protein family which represent, together with the cavin protein family, the major structural and functional components of caveolae. Caveolae are plasma membrane invaginations of 40-80 nm size and belong to a specialized type of membrane microdomains referred to as lipid rafts. Lipid rafts are highly dynamic membrane domains, distinct in their protein and lipid composition, with multiple roles in cellular signaling, endocytosis, lipid and cholesterol metabolism, and mechanosensing. Cav-3 is known to regulate dysferlin localization and rate of endocytosis at the plasma membrane. However, it remains to be elucidated how both proteins are functionally linked to each other. Recently, recessive mutations in the anoctamin gene could also be related to LGMDs. As seen for dysferlinopathies, *ANO5* mutations can lead to a LGMD or MM clinical phenotype. Anoctamin-5 is a member of the anoctamin protein family, which is characterized by distinct structural features. Anoctamins are thought to contain eight transmembrane domains and to function as calcium-activated chloride channels. Interestingly, the clinical picture of anoctaminopathies display various similarities compared to dysferlinopathies.

In order to reveal the molecular mechanisms underlying LGMD and to investigate the putative interactions of dysferlin, cav-3, and ano5, experiments on primary skeletal muscle cell lines with disease-related mutations in *DYSF*, *CAV3*, and *ANO5* have been analyzed in this study. Cell lines were characterized by immunofluorescence labelling and western blot analysis. To investigate the impact of mutations in genes causing LGMD on the morphology of the sarcolemma, transmission electron microscopy (TEM) analysis of differentiated myotubes was done. Endocytic structures at the plasma membrane such as

Summary

caveolae, subsarcolemmal vesicles, and clathrin-coated pits were quantified. To explore the functional association of dysferlin and cav-3, investigations on membrane rafts from normal and LGMD 2B myotubes were done biochemically by purification of detergent-resistant membranes (DRMs). In order to reveal new dysferlin functions an immunopurification assay was established. Intracellular dysferlin-containing vesicles were isolated by subcellular fractionation followed by immunopurification (IP). Characterization of these vesicles was done on ultrastructural level by TEM analysis and on protein level by liquid chromatography–mass spectrometry (LC-MS) analysis.

Immunolabeling studies revealed that dysferlin and cav-3 are partially colocalized in vesicular structures at the plasma membrane of human primary myotubes. Biochemical purification of DRMs from differentiated myotubes showed that dysferlin is associated with lipid rafts linked to the actin-cytoskeleton. TEM analysis of myotubes derived from skeletal muscle of LGMD patients revealed alterations of caveolae abundance at the plasma membrane correlating with the disease-causing mutations. Interestingly, myotubes from patients with *CAV3* mutations displayed morphological intact caveolae at the sarcolemma. Ultrastructural studies on the subcellular localization of dysferlin showed plasma membrane, but also intracellular localization in cytosolic vesicles. IP of intracellular dysferlin-containing vesicles revealed the presence of cav-3 and other known dysferlin interacting partners such as annexin A1 and A2, ahnak, and polymerase I and transcript release factor (PTRF). These vesicles contained a subset of approximately 500 proteins detected by LC-MS, which might represent vesicular structural proteins, vesicle cargo, and putative new dysferlin interaction partners.

Results from this study lead to the conclusion that caveolae play a crucial role in the context of LGMD. Especially for LGMD 2B, caveolae abundance at the plasma membrane in human primary myotubes can be correlated with LGMD-causing mutations. Dysferlin and cav-3 seem to be closely linked on structural as well as on functional level. In this study, we propose that dysferlin function during membrane repair is mediated by actin-linked lipid raft formation, although the underlying molecular mechanisms remain to be elucidated. Our results confirm that dysferlin is localized in cytosolic vesicles, which are involved in multiple cellular processes such as vesicle transport, endo- and exocytosis, cell-adherence, and lipid raft dynamics. Taken together, the close association of dysferlin and cav-3 on cellular functions, especially on caveolae, could be demonstrated in this study.

Zusammenfassung

Als Gliedergürtelmuskeldystrophien (LGMD) bezeichnet man eine heterogene Gruppe von Muskeldystrophien, die sich durch einen langsam progressiven Krankheitsverlauf mit Schwächung der Skelettmuskulatur und erhöhten Kreatinkinasewerten auszeichnet. Mutationen im Dysferlin-Gen führen klinisch in den meisten Fällen zu zwei unterschiedlichen Ausprägungen; der Gliedergürtelmuskeldystrophie Typ 2B mit primärem Befall der proximalen Skelettmuskulatur der Extremitäten und der Miyoshi Myopathie mit Beeinträchtigung der distalen Muskulatur. Beide Myopathien werden autosomal-rezessiv vererbt und als Dysferlinopathien zusammengefasst. Skelettmuskel von Patienten mit LGMD Typ 2B zeigt dystrophe Veränderungen ähnlich zu anderen Muskeldystrophien, aber auch histologische Besonderheiten wie die Akkumulierung von subsarkolemmaren Vesikeln. Dysferlin ist ein Transmembranprotein, welches primär am Sarkolemm von Skelettmuskel aber auch in entwickelnden T-Tubuli und innerhalb der Muskelfaser lokalisiert ist. Es konnte gezeigt werden, dass Dysferlin eine zentrale Rolle in der Membranreparatur von Muskelzellen nach Verletzung spielt. Intrazelluläre Lokalisation des Proteins in primären Muskelzellen zeigt neben der Lokalisierung an der Zellmembran ebenfalls eine Assoziation zu zytosolischen Vesikeln, deren Funktion noch unklar ist. Eine weitere Form der Gliedergürtelmuskeldystrophie, die autosomal-dominant vererbbare LGMD Typ 1C, wird durch Mutationen im Caveolin-3-Gen hervorgerufen. Caveolin-3 ist eine muskelspezifische Isoform der Caveolinproteinfamilie, welche eine wichtige strukturelle- sowie funktionelle Komponente von Caveolae darstellt. Caveolae sind Plasmamembraneinstülpungen von 40 bis 80 nm Durchmesser, die eine wichtige Rolle in vielen zellulären Prozessen wie zum Beispiel der Signaltransduktion, der Endozytose und dem Lipid- und Cholesterolstoffwechsel spielen. Sie unterscheiden sich essenziell in ihrer Protein- und Lipidzusammensetzung von ihrer Membranumgebung und stellen dadurch dynamische funktionelle Einheiten dar, die auch als „Lipid rafts" bezeichnet werden. Untersuchungen haben gezeigt, dass Caveolin-3 die Lokalisierung und Endozytoserate von Dysferlin an der Plasmamembrane reguliert, wobei die genaue molekulare Interaktion beider Proteine unklar bleibt. Die Gliedergürtelmuskeldystrophie LGMD Typ 2L zeigt im klinischen Bild eine große Ähnlichkeit zur LGMD Typ 2B. Sie wird autosomal-rezessiv vererbt und durch Mutationen im Anoctamin-5-Gen hervorgerufen. Anoctamin-5 gehört zu der Anoctaminproteinfamilie, die durch bestimmte Proteinstruktureigenschaften charakterisiert ist. Proteine der Anoctaminfamilie bestehen aus acht Transmembrandomänen und wirken als Kalzium-aktivierte Chloridkanäle. Ziel der Studie war demnach zu untersuchen, ob es einen funktionellen Zusammenhang zwischen Dysferlin, Caveolin-3 und Anoctamin-5 innerhalb der Muskelzelle gibt.

Zusammenfassung

Um die molekularen Prozesse, die zu LGMD führen, zu entschlüsseln, wurden Untersuchungen an primären Zelllinien, isoliert aus Skelettmuskelbiopsien von LGMD-Patienten mit Mutationen in Dysferlin, Caveolin-3 und Anoctamin-5, durchgeführt. Die humanen Muskelzellen wurden zu vielkernigen Myotuben differenziert und mit Hilfe von immunhistologischen und proteinbiochemischen Methoden charakterisiert. Die Ultrastruktur der Plasmamembran wurde mittels Elektronenmikroskopie näher untersucht. Endozytotische membranäre Strukturen wie Caveolae, Plasmamembranvesikel und „Clathrin-coated pits" konnten quantifiziert werden. Um die Interaktion von Dysferlin und Caveolin-3 in funktionellen Zusammenhang mit „Lipid Rafts" zu bringen, wurden diese aus LGMD Typ 2B-Myotuben biochemisch aufgereinigt. Eine Methode zur Aufreinigung von morphologisch intakten, intrazellulären Dysferlinvesikeln wurde etabliert und durch mikroskopische und biochemische Methoden weiter untersucht. Eine detaillierte Charakterisierung des Proteingehalts dieser Vesikel wurde mittels Flüssigchromatographie gekoppelt mit Massenspektrometrie durchgeführt.

Durch immunozytologische Studien an humanen Skelettmuskelzellen konnten nachwiesen werden, dass Dysferlin und Caveolin-3 in intrazellulären, vesikulären Strukturen zu finden sind und ebenfalls partiell an der Zellmembran kolokalisieren. Biochemische Untersuchungen an „Lipid rafts" konnten zeigen, dass Dysferlin an diese assoziiert ist und in Zusammenhang mit dem Aktin-Zytoskelett wirkt. Ein weiterer Nachweis für eine funktionelle Interaktion von Dysferlin mit „Lipid rafts" konnte, durch elektronenmikroskopische Analysen der Zellmembran von Muskelzellen von LGMD Typ 2B-Patienten, erbracht werden. Die Anzahl der Caveolae, ein Subtyp von „Lipid rafts", an der Plasmamembran zeigt eine Korrelation mit der Ausprägung verschiedener Dysferlinmutationen. Myotuben von LGMD Typ 1C-Patienten hingegen sind bezüglich ihrer Caveolaemorphologie sowie –anzahl nicht beeinträchtigt. Die Charakterisierung von intrazellulären Dysferlinvesikeln bestätigte die Spezifität der Aufreinigungsmethode, da Dysferlin selektiv angereichert werden konnte und bereits beschriebene Dysferlininteraktionspartner wie Annexin A1 und A2, Ahnak und PTRF (polymerase I and transcript release factor) bestätigt werden konnten. Es wurden circa 500 Dysferlin-spezifische Proteine detektiert, die diversen zellulären Mechanismen wie zum Beispiel dem Vesikeltransport, der Endo- und Exozytose aber auch möglicherweise neuen Dysferlinfunktionen zugeordnet werden können.

Ergebnisse dieser Studie bestätigen, dass Dysferlin und Caveolin-3 in engem funktionellen Zusammenhang stehen und dass Caveolae eine entscheidende Rolle im Kontext von LGMD spielen. Wir konnten zeigen, dass Dysferlin neben der Zellmembran wesentlich auch in intrazellulären zytosolischen Vesikeln lokalisiert ist. Diese

dysferlinhaltigen Vesikel scheinen eine wesentliche Rolle in multiplen zellulären Prozessen wie dem vesikulärem Transport, der Endo- und Exozytose, der Zelladhäsion, der Aktin-regulierten Signaltransduktion sowie „Lipid raft"-Dynamiken zu spielen. Diese im Laufe meiner Doktorarbeit gewonnenen Erkenntnisse können dazu beitragen die vielfältigen Funktionen von Dysferlin im Skelellmuskel zu dechiffrieren und legen dadurch einen wesentlichen Grundstein für die Entwicklung neuer Therapien.

Résumé

Les dystrophies musculaires des ceintures (LGMD) sont un groupe hétérogène de dystrophies musculaires à progression lente (DM), dont les caractéristiques communes sont : une augmentation de la créatine kinase, ainsi qu'une faiblesse du muscle squelettique. Des mutations du gène de la dysferline causent un spectre de DM ; la LGMD de type 2B, la myopathie de Miyoshi (MM) et la myopathie du compartiment distal antérieur (MCAD) communément appelés dysferlinopathies. Le muscle squelettique des patients atteints de LGMD de type 2B montre un phénotype dystrophique, tels que des variations de la taille des fibres, ainsi que des noyaux centralisés, mais aussi une accumulation inhabituelle de vésicules sous le sarcolemme. La dysferline est une protéine transmembranaire dont la localisation sous-cellulaire est principalement attribuée à la membrane plasmique, mais aussi au développement des tubules-T et aux vésicules intracellulaires. Au niveau du sarcolemme, il a été démontré que la protéine dysferline est essentielle pour une réparation efficace de la membrane, elle jouerait également un rôle dans plusieurs autres fonctions cellulaires telles que la fusion des vésicules, le trafic intracellulaire, l'adhésion cellulaire, la réponse immunitaire ainsi que dans le métabolisme. La LGMD de type 1C, un autre type de LGMD, est due à des mutations dans le gène de la cavéoline-3 (cav-3). La cav-3 est l'isoforme spécifique au muscle de la famille des protéines des cavéolines, qui avec la famille des protéines cavines représentent les composants structurels et fonctionnels majeurs des cavéoles. Les cavéoles sont des invaginations de la membrane plasmique de 40 à 80 nm de diamètre appartenant à un type spécialisé de microdomaines membranaires appelés « lipid rafts » (LR). Les LR sont des domaines membranaires très dynamiques, qui se distinguent par leur composition en protéines et en lipides, avec des rôles multiples dans la signalisation cellulaire, l'endocytose, le métabolisme des lipides et du cholestérol et dans le « mechanosensing ». La protéine cav-3 est connue pour réguler la localisation de la dysferline, ainsi que le taux de l'endocytose à la membrane plasmique. Les deux protéines sont considérées comme étant fonctionnellement liées l'une à l'autre. Récemment, des mutations récessives dans le gène anoctamine-5 (ano-5) ont été démontrées comme pouvant être liées aux LGMD. Il a déjà été observé dans les dysferlinopathies que des mutations dans le gène *ANO5* peuvent conduire à un phénotype clinique de type LGMD ou MM. La protéine ano-5 est un membre de la famille des protéines anoctamines. On pense que les anoctamines contiennent huit domaines transmembranaires et qu'ils fonctionnent comme des canaux de chlorure activés par le calcium. Il est à noter que le phénotype clinique des anoctaminopathies montre plusieurs ressemblances avec les dysferlinopathies.

Dans le but d'analyser les mécanismes moléculaires des LGMD et d'étudier les potentielles interactions de la dysferline, de la cav-3 et de la ano5, des expériences sur des cellules musculaires primaires portant des mutations associées aux gènes *DYSF*, *CAV3*, et *ANO5* ont été analysées. Les lignées cellulaires ont été caractérisées par des méthodes conventionnelles telles que le marquage en immunofluorescence et l'analyse par Western blot. Afin d'étudier l'effet des mutations des gènes causant les LGMD sur la morphologie du sarcolemme, des analyses de microscopie électroniques à transmission (MET) sur des myotubes différenciés ont été réalisées. Des structures d'endocytose telles que : les cavéoles, les vésicules sous-sarcolemmales ont été quantifiées. Afin d'explorer l'association fonctionnelle de la dysferline et de la cav-3, une isolation biochimique des LR de myotubes contrôles et de myotubes LGMD de type 2B a été effectué et ceci par purification de membranes résistants aux détergents (DRMs). Une analyse de l'immunopurification de vésicules contenant de la dysferline a été établie afin de révéler de nouvelles fonctions de la dysferline. Ces vésicules ont été isolées par fractionnement cellulaire suivi d'une immunopurification (IP). La caractérisation de ces vésicules a été faite au niveau de l'ultrastructure cellulaire par MET et au niveau protéique par chromatographie en phase liquide couplée à la spectrométrie de masse (LC-MS).

Les études d'immunomarquage ont montré que la protéine dysferline et la cav-3 sont partiellement colocalisées dans des structures vésiculaires de la membrane plasmique des myotubes primaires humains. La purification biochimique des DRMs issus des myotubes différenciés a montré que la dysferline est associée aux LR liées aux cytosquelettes d'actine. L'analyse de la MET sur les myotubes issus des muscles des patients atteints de LGMD a montré des altérations dans l'abondance des cavéoles à la membrane plasmique qui est en corrélation avec les mutations causant la maladie. Il est intéressant de noter que les myotubes issus de patients avec des mutations dans le gène *CAV3* montrent des cavéoles intactes. L'analyse de l'ultrastructure cellulaire a montré que la dysferline est localisée à la membrane plasmique mais également dans des vésicules cytosoliques. L'immunopurification de ces vésicules contenant de la dysferline a révélé la présence de la cav-3 ainsi que et d'autres partenaires de la dysferline tels que l'annexine A1 et A2, AHNAK, et PTRF (synonyme à cavine-1). Ces vésicules contiennent environ 500 protéines détectées par LC-MS, ce qui pourrait représenter des protéines structurales vésiculaires, ainsi que des nouveaux partenaires potentiels d'interaction de la dysferline.

Les résultats de cette étude permettent de conclure que les cavéoles jouent un rôle essentiel dans le contexte des LGMD. Surtout pour les LGMD de type 2B, l'abondance des cavéoles à la membrane plasmatique dans les myotubes primaires humains peut être corrélée avec les mutations qui causent la maladie. La dysferline et la cav-3 paraissent

Résumé

être liées au niveau structurel et fonctionnel. Dans cette étude, nous proposons que la fonction de la dysferline dans la réparation membranaire soit médiée par la formation des LR liée à l'actine, même si les mécanismes moléculaires sous-jacents restent à être élucides. Nos résultats confirment que la dysferline est localisée dans des vésicules cytoplasmiques, qui sont impliqués dans des multiples mécanismes cellulaires tels que le transport vésiculaire, l'endo- et exocytose, l'adhésion cellulaire et dans la dynamique des LR. Dans l'ensemble, l'association de la dysferline et de la cav-3 dans les fonctions cellulaires, en particulier sur les cavéoles, peut être démontrée dans cette étude.

1 Introduction

1.1 Skeletal muscle

In mammals, muscle tissue varies corresponding with its location and function within the body. There are three types of muscles; skeletal or striated muscle, smooth or non-striated muscle, and cardiac muscle. Skeletal muscle is the most abundant tissue in the mammalian body. Around 40 % of the total body weight is captured by muscle tissue. Main functions are locomotion and sustaining posture of the body. The musculoskeletal system in vertebrates is a great evolutionary achievement responsible for movement by combining the properties of the skeletal with the muscular system. In vertebrates, skeletal muscles are always associated with the skeleton attached to bones through tendons. Smooth muscles are located in the wall of internal organs such as blood vessels, stomach, and intestine, and are important for essential bodily functions like control of blood pressure and digestion. Cardiac muscle is solely located in the heart and has unique features allowing synchronized contraction of the myocardium. Smooth and cardiac muscle contract involuntarily whereas skeletal muscle contracts upon consciously control by the central nervous system. Reflexes are exceptions of non-conscious contraction of skeletal muscle but remain induced by the central nervous system.

Muscle fibers or cells are highly organized structures defined by packed tubular myofibrils which contain repeating sections of sarcomeres. Figure 1.1 illustrates the distinctive organization of myofibrils within a muscle fiber. They have a cylindrical structure and are surrounded by the plasma membrane of muscle cells, also called the sarcolemma. Together with the overlying basal lamina the sarcolemma groups the muscle fibers into bundles (fascicles) which form a muscle. The sarcolemma thereby acts as a physiological barrier to the extracellular space but is also crucial for signaling processes between the muscle cell and surrounding tissue. The cytoplasm of skeletal muscle is called sarcoplasm and contains organelles such as mitochondria, Golgi apparatus, glycogen granules, myoglobin, and the muscle-specialized endoplasmic reticulum, the sarcoplasmic reticulum (SR). As myofibers are tightly packed in a highly organized way, the mentioned organelles but also nuclei are arranged mostly at the periphery of the muscle fibers. The T-tubule system, consisting of invaginations of the sarcolemma, is organized in an interfibrillar manner and makes it possible to transmit action potentials from the sarcolemma to the SR. This direct connection is crucial for the excitation of muscle because the action signal thereby transverses the muscle fiber and induces a calcium-release from the SR. The close connection of SR to the muscle units is achieved by forming a network around the fibers (Gilbert, 2000).

Introduction

The basic functional unit of striated muscle is defined as the sarcomere (see Figure 1.1 A). In transmission electron microscopy (TEM) the "striations" eponymous for skeletal and cardiac muscle are visible as a highly organized system of repetitively arranged light and dark structures on longitudinal sections (see Figure 1.1 B). The two most important proteins defining muscle structure and function are myosin, which forms the thick filament and actin, which forms the thin filament, respectively. Basically, muscle contraction and relaxation is done by sliding of these two long fibrous filaments past each other (sliding filament theory). The thin filaments form the I-band which is seen as light band, whereas the A-band is made of thick filaments which expose a dark contrast. Longitudinal sections expose other visible structures of the sarcomere like the M-line (or middle disc) which dissects the A-band and the Z-disc marks the boundary of the sarcomere. During contraction the Z-lines move closer and as a result the whole muscle contracts. In peripheral myofibrils the Z-lines are directly linked to the sarcolemma by costameres, specialized subsarcolemmal protein assemblies important for transmitting contraction-induced forces between the muscle fibers and the extracellular space.

A
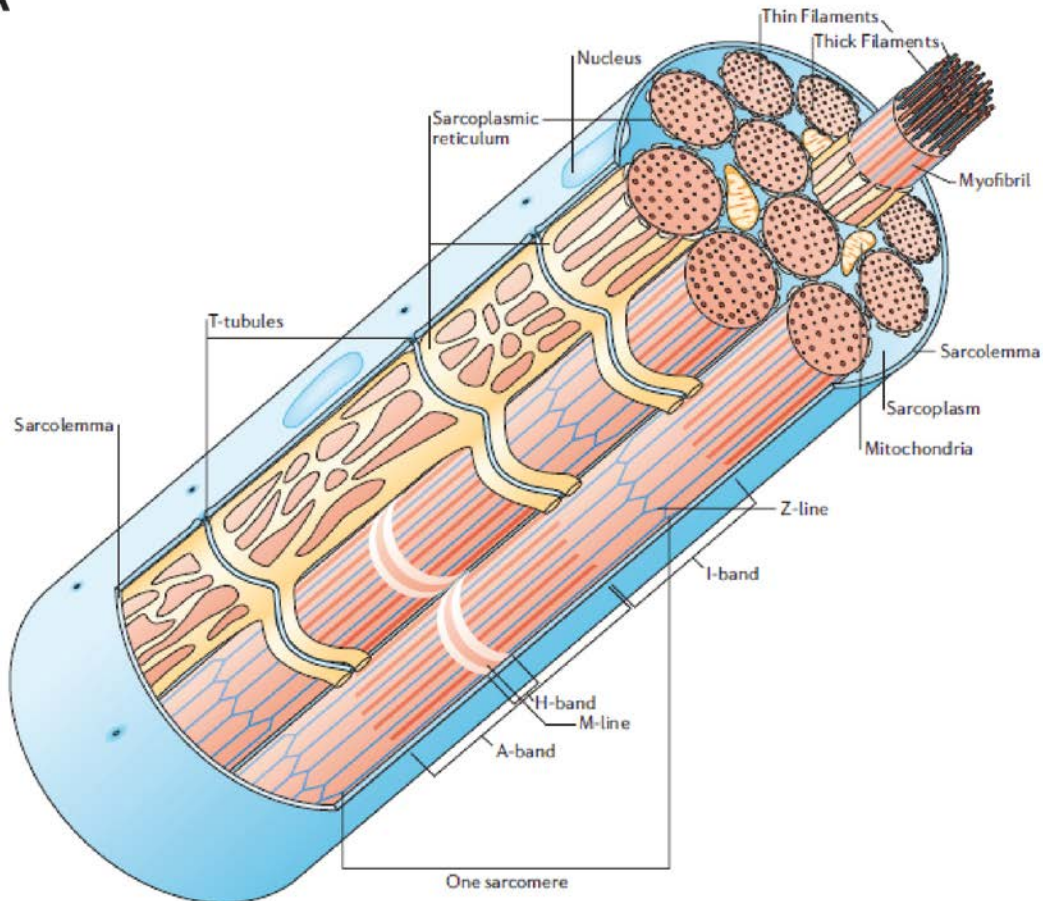
B
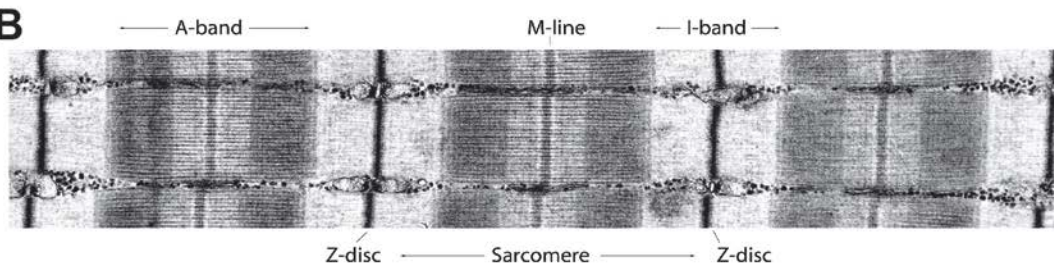
Figure 1.1 Structure of human skeletal muscle

Human skeletal muscle fibers are organized in bundles of myofibrils within the sarcoplasm surrounded by the sarcolemma (A). The functional unit of muscle is the sarcomere which contains thick myosin and thin actin filaments. The organization of these filaments appears as dark A-band and light I-band in electron microcopy (B). Picture A is modified from Davies and Nowak (2006) and picture B is courtesy of R. Craig (University of Massachusetts, USA).

During embryonic development, muscle cells which are also referred to as muscle fibers, are formed by a process called myogenesis (Gilbert 2000). Differentiation from mesodermal progenitor cells to committed myoblasts depends on the expression and equilibrium between different myogenic transcription factors such as PAX3, PAX7, MyoD, Myf5, myogenin and Myf6 (see Figure 1.2). During early embryonic development myoblasts proliferate in the presence of myogenic growth factors (Buckingham, 2007). The fusion process begins when myoblasts leave the cell cycle due to depletion of growth

factor signals. Fibronectin is secreted into the extracellular matrix and bound by integrins (Menko & Boettiger, 1987). The next step during differentiation is the alignment of programmed myoblasts into lanes induced by cadherins and CAMs (Knudsen, 1990). Finally, aligned myoblasts fuse to multinucleated myotubes in a calcium-dependent process. Multiple fusion events occur until multinucleated cylindrical myofibers are formed.
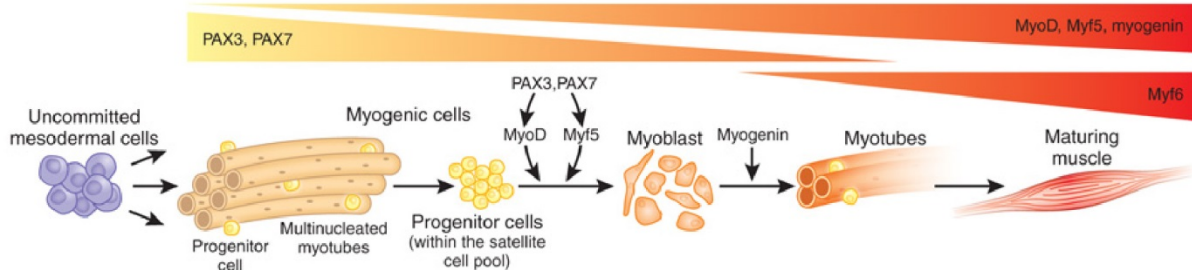
Figure 1.2 Scheme for skeletal myogenesis

Differentiation from the mesoderm to the mature muscle fibers is a stepwise process coordinated by multiple growth and transcription factors such as PAX3, PAX7, MyoD, Myf5, Myf6 and myogenin. Figure is modified from Hettmer and Wagers (2010).

Skeletal muscle has a remarkably high regeneration capacity and thereby is able to rapidly repair muscle damage induced by exercise or disease. Satellite cells play a crucial role in this regeneration processes. Satellite cells were first described by Alexander Mauro in 1961 and named after their position within a mature muscle fiber. These cells are located in a so called satellite cell niche at the periphery of muscle fibers outside the sarcolemma but inside the basal lamina where they stay in a quiescent state (Mauro, 1961). Muscle injury triggers activation of the quiescent satellite cell pool, induces proliferation, and thus a switch to the myoblast state. Proliferation stops, fusion of myoblasts with each other or existing muscle fibers occurs, and thereby repairs injured muscle (Charge & Rudnicki, 2004). Another intriguing feature of muscle is its capacity of repetitive regeneration due to the fact that satellite cells manage to obtain their satellite cell pool even after activation through injury. A minor fraction of the satellite cells are able to self-renew or generate themselves and might even return to a quiescent state (C. A. Collins et al., 2005).

1.1 Muscular dystrophies

1.1.1 Muscular dystrophies of the sarcolemma

Muscular dystrophies (MD) are a group of highly heterogeneous genetic diseases characterized by progressive weakness and degeneration of skeletal muscle. Severity of muscle weakness may vary from mild clinical presentation with loss of ambulation in late stages of disease course, over impairment of muscles involved in breathing and eating, to severe cases of premature death. Historically, the classification of MDs was done on the basis that mutations in different genes typically target specific muscle groups. In limb-girdle muscular dystrophies (LGMDs) proximal limb muscles such as shoulders and hips are affected. In distal myopathies like Miyoshi myopathy (MM) mutations lead to involvement of distal muscles (see also Figure 1.4). Subclassification was done due to the mode of inheritance and the genetic defect underlying the disease. MDs type 1 are inherited in a dominant mode and MDs type 2 in a recessive mode respectively. A, B, C labeling is according to when the disease-causing genes were identified (K. M. Bushby, 1999).

Classification of MDs as well as the allocation to a distinct disease-causing gene becomes more and more difficult. On the one hand, mutations of the very same protein, in some cases even the identical mutations, can lead to different myopathies (phenotypic divergence). Homozygous mutation in the protein titin for example can cause LGMD 2J, whereas heterozygous mutations lead to tibial MD (TMD) (Hackman et al., 2002). On the other hand, mutations in several genes can lead to the same disease. This phenotypic convergence was demonstrated for Emery-Dreifuss MD (EDMD) which is caused by mutations in the emerin or *LMNA* gene which encode for the nuclear proteins lamin A and lamin C. Additionally, proteins involved in MDs can also be affected in other diseases which do not primary affect skeletal muscle. This has been reported for mutations in the *LMNA* gene. They can cause MDs such as EDMD or an aging disease called Hutchinson-Gilford progeria syndrome (Bonne et al., 1999; Eriksson et al., 2003). A review list on the MD-classification is annually published by the journal *Neuromuscular Disorders* (Kaplan & Hamroun, 2013); at present, 713 neuromuscular diseases caused by 361 different genes have been mapped.

The first identified gene causing an MD encodes for dystrophin, a major component of the dystrophin-sarcoglycan complex at the sarcolemma (Hoffman, Brown, & Kunkel, 1987). Mutations in the dystrophin gene resulting in absence or loss of function of the proteins are causing the most common MD, Duchenne muscular dystrophy (DMD). Protein truncation and reduced protein levels lead to a milder form called Becker muscular

dystrophy (BMD) presents (Darras, Koenig, Kunkel, & Francke, 1988). Since then, a great variety of genes causing multiple muscle- and neuromuscular disorders have been identified. Proteins of the <u>d</u>ystrophin-<u>a</u>ssociated <u>p</u>rotein <u>c</u>omplex (DAPC) associated with MDs play important roles in sarcolemma structure and stability. The DAPC includes dystrophin and dystrophin-associated proteins and is the major cellular component linking the extracellular matrix with the intracellular cytoskeleton (Ehmsen, Poon, & Davies, 2002). Decreased levels of dystrophin, and therefore destabilization of the DAPC, leads to severe forms of MDs and results in secondary reduction of other proteins of the DAPC. This highlights the close interaction of many proteins involved in different MDs and may explain the variable and complex mechanisms underlying the disease.

The great variety of MDs, however, is not only caused by loss of structural proteins of the sarcolemma but also by impairment of mechanisms involved in plasma membrane repair, cell signaling, and metabolism. Protein functions altered in MDs can be as variable as the localization of the affected protein within the muscle fiber. Proteins from the nucleus, nuclear membrane, Golgi apparatus, the sarcoplasmic reticulum, and the sarcomere can be affected. Sarcolemmal proteins still represent the biggest group of proteins involved in MD especially proteins from the DAPC, as well as sarcolemmal proteins like dysferlin or caveolin-3 (cav-3) (see Figure 1.3).
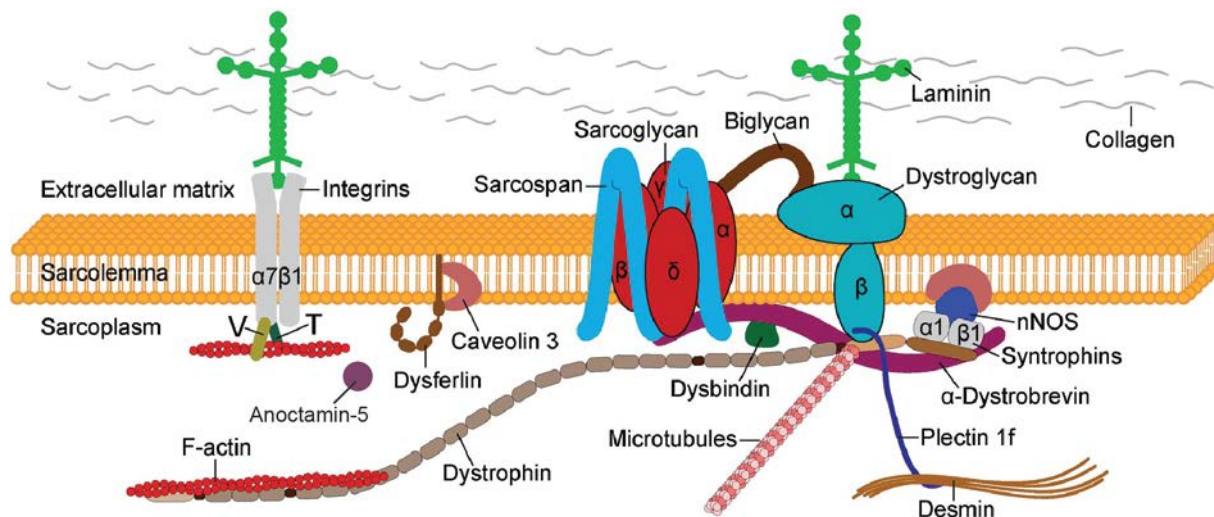
Figure 1.3 Sarcolemmal proteins involved in muscular dystrophies

Most sarcolemmal proteins are part of the DAPC which links the intracellular cytoskeleton to the extracellular matrix. The N-terminus of dystrophin binds to the cytoskeleton and the C-terminus to the DAPC which associates with the extracellular matrix via dystroglycans and laminin. Other sarcolemmal proteins such as dysferlin and cav-3 were shown to interact with the DAPC but represent no closely associated members of the complex. Anoctamin-5 is thought to have eight transmembrane domains but subcellular localization is still a matter of debate. Image is modified from Rahimov and Kunkel (2013).

1.1.2 Limb-girdle muscular dystrophies

LGMDs are a group of disorders with wide genetic and clinical heterogeneity, originally named by the distinct involvement of the shoulder and pelvic girdle musculature. Often, patients display involvement of other muscle groups or mixed MD phenotypes (see Figure 1.4). Additionally, cardiac and respiratory impairment might be present. As for MDs in general, LGMDs classification and clinical diagnosis therefore became more and more complex. The clinical presentation may vary from severe forms with early age of onset to milder forms with slow progression and presentation of symptoms in late adulthood. Ten years ago, the list of LGMDs included 19 gene loci, whereas today mutations in over thirty different genes may cause LGMDs (Nigro & Savarese, 2014). Depending on their mode of inheritance, eight autosomal and 23 autosomal-recessive LGMDs can be named (see Table 1-1). Autosomal dominant LGMDs contribute to less than 10% of all LGMDs and therefore are relatively rare. They present with an adult-onset and milder progression. More common are LGMDs with a recessive mode of inheritance with a cumulative prevalence of 1:15,000 (Nigro, 2003). Prevalence varies between different populations depending on carrier distribution and rate of consanguinity (Urtizberea et al., 2008). The most common LGMD is calpainopathy (LGMD 2A). The overall prevalence of dysferlinopathies is still hard to estimate in larger and less consanguineous areas. For the United States, a percentage of 15 % of LGMD 2B from all LGMDs was estimated (Moore et al., 2006).

Affected proteins in LGMD are important players for muscle membrane integrity and stability such as sarcoglycans (LGMD 2C-F), for sarcomeric structure and function such as titin (LGMD 2J), or for distinct processes important for muscle cell maintenance such as membrane repair (dysferlin, LGMD 2B). As mentioned above, mutations in a certain gene might lead to an allelic myopathy. For dysferlinopathies as well as caveolinopathies and anoctaminopathies, mutations in the respective gene (*DYSF, CAV3* and *ANO5*) can lead to LGMD as well as to distal MM.

Table 1-1 Classification of limb-girdle muscular dystrophies

Disease	OMIM number	Gene symbol	Chromosome localization	Protein name	Allelic disease(s)
Autosomal dominant mode of inheritance					
LGMD1A	159000	MYOT	5q31	Myotilin	Myotilinopathy, MFM, sheroid body myopathy
LGMD1B	159001	LMNA	1q22	Lamin A/C	EDMD2, EDMD3, CMD1A, CMD2B1 (several other phenotypes)
LGMD1C	607801	CAV3	3q25	Caveolin-3	DM, hyper Ckemia, RMD2,

					CMH, LQT9
LGMD1D	603511	DNAJB6	7q36.2	DnaJ (Hsp40) homolog, subfamily B, member 6	-
LGMD1E	602067	DES	2q35	Desmin	Myofibrillar myopathy, CMD1I, ARVD7
LGMD1F	608423	TNPO3	7q31.1-q32	Transportin 3?	-
LGMD1G	609115	?	4q21	?	-
LGMD1H	-	?	3q25.1-p23	?	-

Autosomal recessive mode of inheritance					
LGMD2A	253600	CAPN3	15q15.1	Calpain 3	-
LGMD2B	253601	DYSF	2q13	Dysferlin	MM,DACM
LGMD2C	253700	SGCG	13q12	Gamma-Sarcoglycan	-
LGMD2D	608099	SGCA	17q12-q21.33	Alpha-Sarcoglycan	-
LGMD2E	604286	SGCB	4q12	Beta-Sarcoglycan	-
LGMD2F	601287	SGCD	5q33	Delta-Sarcoglycan	CMD1L
LGMD2G	601954	TCAP	17q12	Titin-cap	Congenital MD with telethonin defect, CMD1N
LGMD2H	254110	TRIM32	9q31.2	Tripartite motif containing 32	Sarcotubular myopathy
LGMD2I	607155	FKRP	19q13.3	Fukutin related protein	MDC1C, WWS, MEB
LGMD2J	608807	TTN	2q31	Titin	Congenital myopathy with fatal cardiomyopathy, TMD, HMERF, CMH9, CMD1G
LGMD2K	609308	POMT1	9q34	Protein 0-mannosyltransferase 1	WWS
LGMD2L	611307	ANO5	11p14.3	Anoctamin 5	Early onset calf DM
LGMD2M	611588	FKTN	9q31-q33	Fukutin	FCMD , WWS, dilated cardiomyopathy
LGMD2N	613158	POMT2	14q24	Protein O-mannosyl	WWS, MEB
LGMD2O	613157	POMGNT1	1p34	Protein O-linked	WWS, MEB
LGMD2Q	613723	PLEC1	8q24	Plectin	MDEBS, Myastenic syndrome with plectin defect
LGMD2R	615325	DES	2q35	Desmin	Other desminopathies
LGMD2S	615356	TRAPPC11	4q35.1	Trafficking protein	-
LGMD2T	615352	GMPPB	3p21.31	GDP-mannose pyrophosphorylase B	MDDGA14, MDDGB14

LGMD with primary alpha-dystroglycan defect	613818	DAG1	3p21	Alpha-dystroglycan, dystroglycan 1	-
MD with glycosylation defect	612937	DPM 3	1q22	Dolichyl-phosphate mannosyltransferase polypeptide 3	-
LGMD related to ISPD	-	ISPD	7p21.2	Isoprenoid synthase domain containing	WWS, MDDGA7

Abbreviations are MD (Muscular Dystrophy), DM (Distal Myopathy), MFM (Myofibrillar Myopathy), MCD (Congenital MD), EDMD (Emeri-Dreifuss MD), CMD (Dilated Cardiomyopathy), RMD (Rippling Muscle Disease), CMH (Familial Hypertrophic Cardiomyopathy), MM (Miyoshi Myopathy), DACM (Distal Anterior Compartment Myopathy), WWS (Walker-Warburg syndrome), MEB (Muscle-eye-brain Disease), TMD (Tibial MD), HMERF (Hereditary Myopathy with early respiratory failure), FCMD (CMD related to fukutin), MDDGA (Fukuyama Congenital MD), ARVD (Arrhythmogenic Right Ventricular Dysplasia), LQT (Long QT Syndrome). Table is modified from Kaplan and Hamroun (2014).

To establish a proper diagnosis, several parameters should be taken into account; progressive course of disease, primary involvement of skeletal muscle, whereas in some cases cardiac muscle might be affected, elevated serum creatine kinase (CK) levels (hyperCKemia) and degenerative /regenerative changes in muscle tissue from patient biopsies. Besides the critical clinical investigations on patient and family history, the histopathological characterization of muscle biopsies presents a powerful tool for diagnosis. LGMD muscle features dystrophic alterations like centralized nuclei, variances in fiber diameter, increase of interfibrillar connective tissue, necrosis, and fibrosis (Urtizberea et al., 2008) (see Figure 1.5). For several disease-causing candidates immunostaining of muscle biopsies can be done to determine if specific proteins are present, reduced, or totally absent. For other candidates with no suitable antibodies available or to confirm histopathological findings, molecular genetic testing can be used to identify the specific disease-causing mutations. Extensive genetic investigations on patient family history and on animal models so far, have been fruitful to get a better insight in molecular mechanism underlying the disease. Nevertheless, given the speed of discovery of new disease-causing genes, targeted next generation sequencing (NGS) of a panel of genes which already have been associated with LGMD should be considered for diagnosis (Nigro & Piluso, 2012).
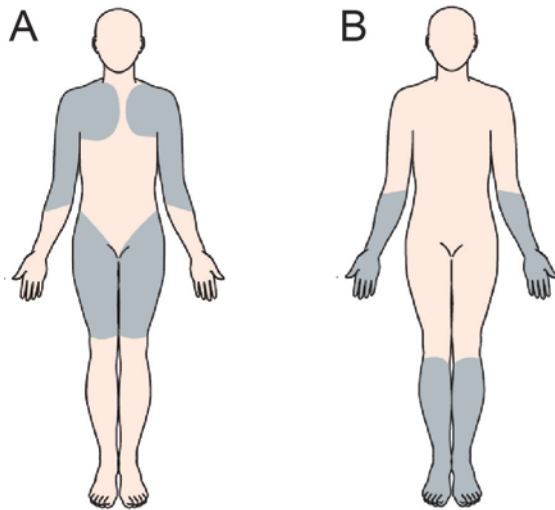
Figure 1.4 Muscle groups affected by dysferlinopathy

Dysferlinopathies predominantly present as limb-girdle muscular dystrophy (LGMD) 2B or Miyoshi Myopathy 1 (MM). In LGMD, skeletal muscles of the limb-girdle such as shoulder and pelvic muscles are affected, proximal greater than distal (A). In MM affected muscles are distal limb muscles, like lower arms, hands, calves and feet (B). Scheme modified from Mercuri and Muntoni (2013).

1.2   Limb-girdle muscular dystrophy type 2B

1.2.1 Clinical presentation and histopathology

LGMD 2B is caused by mutations in the dysferlin gene (Bashir et al., 1998; Liu et al., 1998) and is the second most frequent recessive LGMD form in most countries (Nigro & Savarese, 2014). As LGMD 2B has a recessive mode of inheritance, high prevalence occur mostly in populations with higher incidence of consanguinity (Nalini & Gayathri, 2008; Urtizberea et al., 2008) in contrast to most European countries (van der Kooi et al., 2007). As mentioned above, *DYSF* mutations also cause other muscular dystrophies like distal Miyoshi myopathy (MM) and distal anterior compartment myopathy (DACM), which can be summarized as dysferlinopathies (Liu et al., 1998). Classification is determined by which muscle groups are involved, however in later stages of disease progression mixed phenotypes might be present. CK levels are generally remarkably elevated ranging from 20-150 times above normal levels (Mahjneh, Bushby, Pizzi, Bashir, & Marconi, 1996). The clinical presentation might display variations in age of onset, speed of progression and affected muscles. In contrast to other MDs, affected patients show normal or even above average sports performance before onset of the disease (K. Bushby, 2009).

Skeletal muscle biopsies from dysferlinopathy patients display dystrophic alterations such as variable fiber diameters, centralized nuclei, and increase of endomysial and perimysial connective tissue (Fanin & Angelini, 2002) (see Figure 1.5). So far no correlation of

clinical severity, CK levels, or histopathological changes has been reported (Fanin & Angelini, 2002; Mahjneh et al., 1996). *DYSF* mutations were shown to form amyloid deposits within muscle fibers. Our group could demonstrate that amyloid deposits in LGMD 2B muscle contain fragments of dysferlin protein (Carl, Rocken, & Spuler, 2009; Spuler et al., 2008). Another finding from our group showed that in skeletal muscle of dysferlin-deficient mice and patients the decay-accelerating factor (DAF)/CD55 was down-regulated on mRNA and protein level (Wenzel et al., 2005). CD55 is a complement inhibitor known to be responsible for the deposition of the membrane attack complex (MAC) on the surface of non-necrotic muscle fibers in LGMD 2B (Spuler, Engel 1998). Down regulation of CD55 was shown to lead to an increased susceptibility of myotubes to complement attack *in vitro*. In LGMD 2B patient muscle fatty infiltrations have been observed, most notably at an advanced state of disease and in strongly affected muscle (unpublished data). In cooperation with Miranda Grounds, our group could show an increase of lipid droplets in human skeletal muscle from dysferlinopathy patients. This was exclusive for LGMD 2B patient muscle and has not been observed in other muscular dystrophies (Grounds et al., 2014).
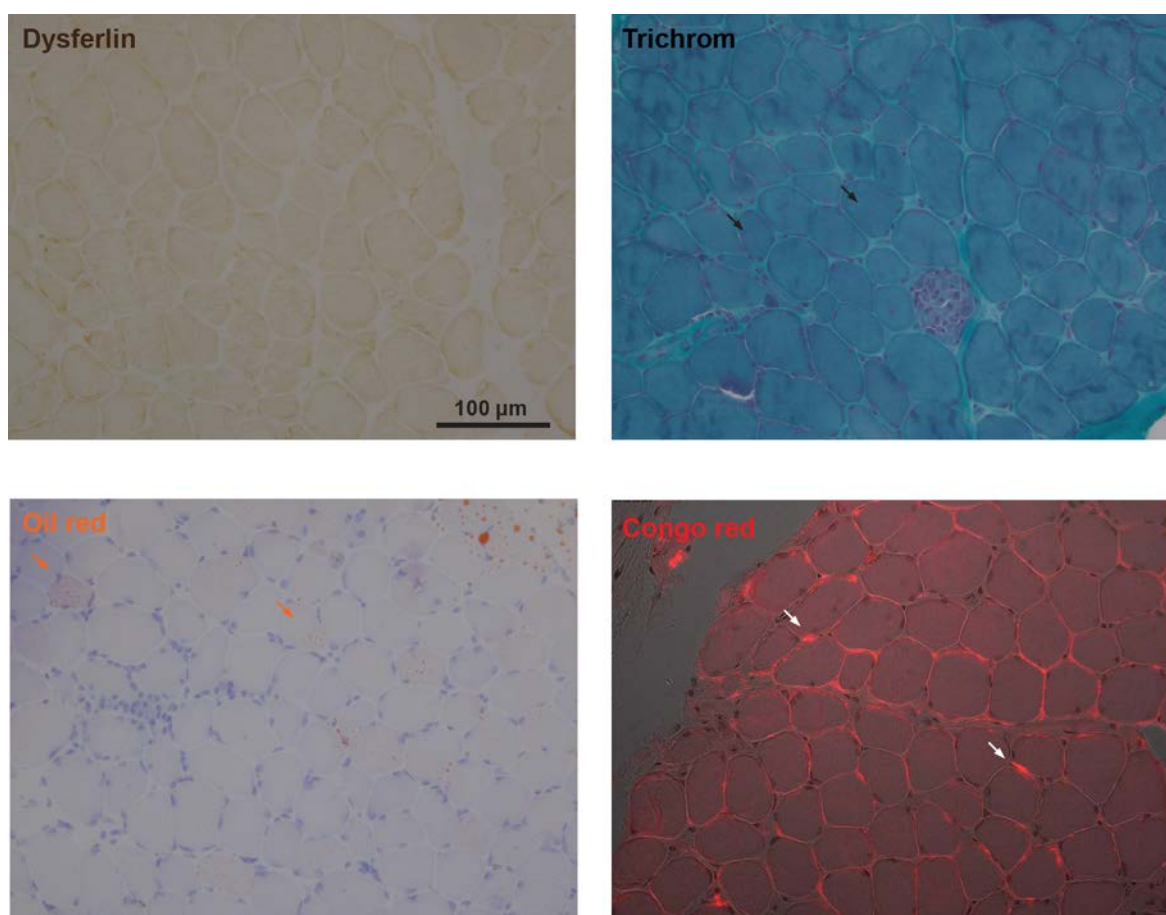
Figure 1.5 Histopathology of human LGMD 2B skeletal muscle

Cross sections from *vastus lateralis muscle* biopsy from a LGMD 2B patient show reduced levels in dysferlin and dystrophic alterations such as centralized nuclei (black arrows), variances in fiber size and increase in

connective tissue. The patient harbors two compound heterozygous mutations; one in exon 9 and one in intron 8, which was found to lead to mRNA decay Wenzel et al. (2006). Oil red staining reveals fatty infiltrations of the interfibrillar space but also within muscle fibers (orange arrows). Mutations in dysferlin can lead to amyloid deposits around muscle fibers as displayed by Congo red stain visualized under rhodamine optics (white arrows).

Dysferlin is localized at the sarcolemma of normal human skeletal muscle, but interestingly also localizes inside muscle fibers of the oxidative type 2 (see Figure 1.6). Analysis on the metabolome of dysferlinopathy primary myotubes, as well as in a mouse model, revealed strongly disturbed glucose metabolism. Results indicate a decrease in metabolites belonging to the upper glycolytic pathway and also revealed compensatory upregulation of intermediates of fatty acid oxidation and TCA-cycle associated anaplerotic reactions (Schoewel, Keller et al., 2014; submitted manuscript).
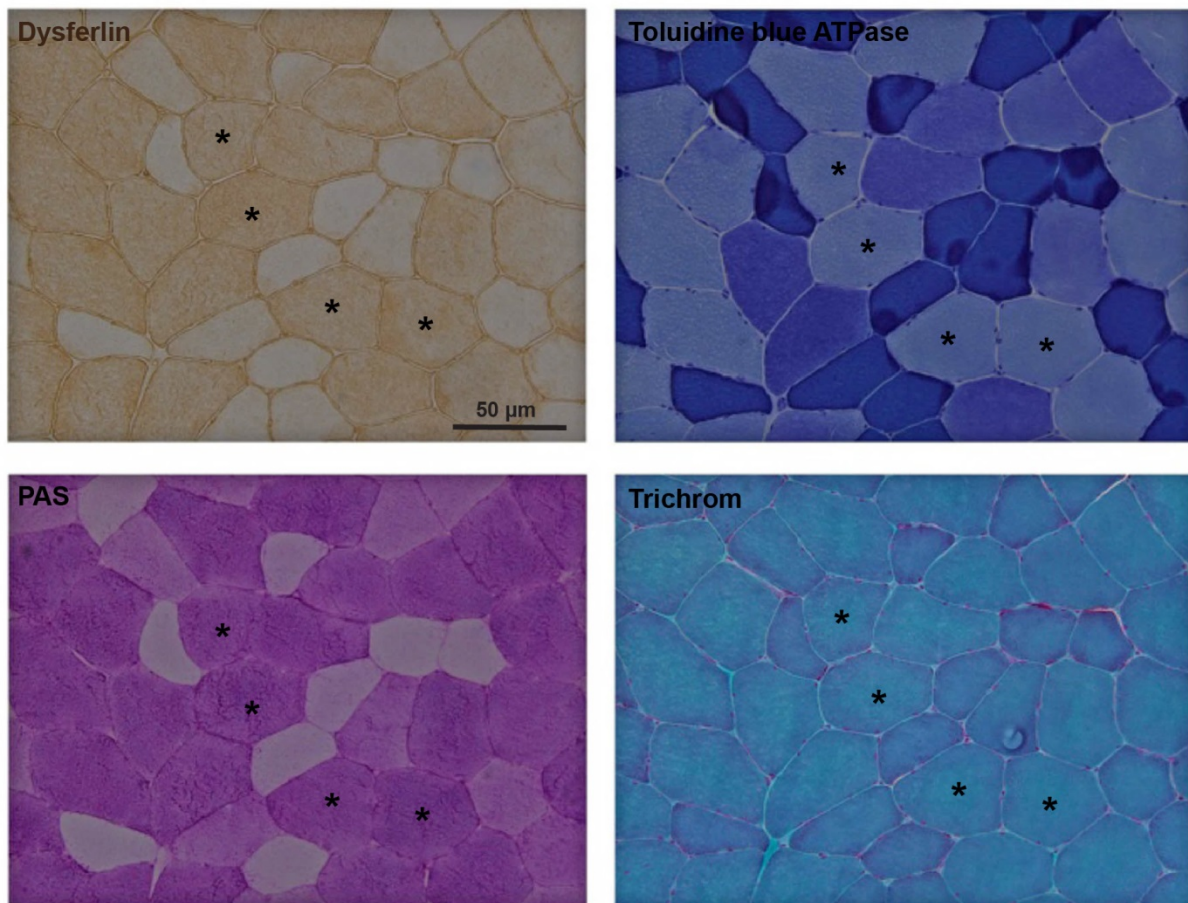
Figure 1.6 Dysferlin localization in normal human skeletal muscle

Dysferlin localization in human skeletal muscle cross sections is predominantly found at the sarcolemma. After antigen-retrieval it can also be found inside muscle fibers (asterisks). Toluidine blue ATPase and periodic acid stain (PAS) reveal interfibrillar labeling for dysferlin to glycolytic type 2 fibers. Picture was taken from our group (Prof. Simone Spuler, Muscle Research Unit, Berlin).

1.2.2 Dysferlin gene

DYSF is located on chromosome 2p.13.3 and spans over a genomic sequence of 237 kb (NM_003494) (Aoki et al., 2001). The *DYSF* gene encodes for 2080 amino acids resulting in a protein with a size of approximately 230 kDa. The most common transcript (isoform 8) harbors 55 exons, whereas 15 isoforms are result from alternative splicing. Dysferlin is well conserved within mammals with a 90 % sequence identity between mouse and human (Vafiadaki et al., 2001). It shows high expression in skeletal and cardiac muscle, but is also present in other tissues and cells including macrophages and endothelium (Anderson et al., 1999). The dysferlin protein is predominantly localized at the sarcolemma, developing T-tubules, the sarcoplasmic reticulum, but also inside fibers (Klinge, Harris, et al., 2010; Klinge et al., 2007). Dysferlin protein harbors a transmembrane domain at the C-terminus responsible for its localization to membranous structures (see Figure 1.7).
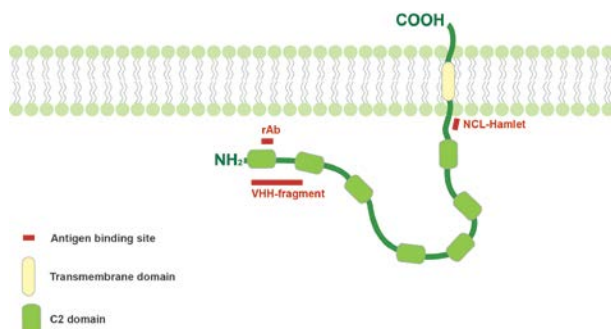
Figure 1.7 Protein structure of dysferlin and antibody binding sites

Dysferlin protein harbors six C2-domains spanning over the whole protein and a transmembrane domain close to the C-terminus. Antibodies used in this study targeted the protein part which is thought to be facing the cytosol.

The different sites of localization nicely correlate with the multiple functions such as membrane fusion, cell-cell fusion, T-tubule biogenesis and maintenance, and cell adhesion. Most notably, dysferlin accumulates at the site of membrane rupture after injury in muscle cells, highlighting its important role as membrane fusion protein during membrane repair (Bansal et al., 2003). The localization of dysferlin to the plasma membrane in muscle cells is crucial for its function during membrane resealing. Muscle cell lines derived from LGMD patients with dysferlin mutations often show mislocated intracellular accumulated protein. We showed that cell-penetrating TAT-peptides, which were designed to target dysferlin, could reallocate mutant dysferlin to the plasma membrane. Redirected to its site of function, membrane resealing capacity of dysferlin could be restored (Schoewel et al., 2012). Additional studies on the localization and function of hexokinase-2 in dysferlinopathy revealed dysferlin-dependent localization of hexokinase-2 in an intracellular "lake-like" compartment. This gives strong evidence on a

close interplay of hexokinase-2 and dysferlin and highlights possible new functions of dysferlin as vesicles trafficking protein in metabolic processes (Schoewel, Keller et al. 2014, submitted manuscript).

Mutations leading to dysferlinopathy are scattered over the whole gene with no hotspots (Carl et al., 2009; Spuler et al., 2008). Most mutations are point mutations but insertions or deletions of various sizes also exist. Results from our group could show that many mutations lead to nonsense-mediated mRNA decay (Wenzel et al., 2006). Other mutations might lead to truncated or misfolded protein, which mislocalizes within the cell or is degraded by autophagy by the endoplasmic reticulum associated degradation system (Fujita et al., 2007). The high variability of dysferlin mutations reveals no genotype-phenotype correlation (Carl et al., 2009; Klinge, Aboumousa, et al., 2010; Klinge et al., 2008). According to the Leiden Muscular Dystrophy data base, up to 508 unique DNA variants have been reported until March 2013 (http://www.dmd.nl).

1.2.3 Dysferlin and the ferlin protein family

Dysferlin belongs to the ferlin protein family. Ferlin is a homologue from *caenorhabditis elegans* (Fer1) and mediates vesicle fusion to the plasma membrane during spermatogenesis (Achanzar & Ward, 1997). Six mammalian ferlin genes (Fer1L1-L6) encode for transmembrane proteins characteristically containing several C2 domains and a C-terminal transmembrane domain. Human orthologues with known functions are otoferlin, myoferlin and Fer1L5. The two ferlins implemented in human disease are dysferlin and otoferlin. Otoferlin is mainly expressed in hair cells in the inner ear playing an essential role in exocytosis of synaptic vesicles as well as calcium-dependent fusion of vesicles to the plasma membrane (Roux et al., 2006). Mutations in otoferlin result in an autosomal recessive form of deafness (Yasunaga et al., 1999). Myoferlin shows the highest sequence similarity with dysferlin and high expression levels in myoblasts. It is known to interact with dysferlin and plays an important role in myoblast-myoblast as well as myoblast-myotube fusion (Doherty et al., 2005). For myoferlin and for dysferlin, the C2A domain was demonstrated to be important for calcium-dependent phospholipid binding, whereas the other C2 domains showed no affinity for phospholipids. Throughout myoblast differentiation, myoferlin is highly expressed in proliferating myoblasts and nascent in myotubes, while dysferlin is highly expressed in mature myotubes (Davis, Delmonte, Ly, & McNally, 2000; Doherty et al., 2005).

1.2.4 Dysferlin and membrane repair

Skeletal muscle is a tissue permanently exposed to mechanical forces during contraction, thus sarcolemma integrity and stability as well as injury repair are substantial for functional muscle. Especially the plasma membrane in muscle cells is subjected to physical, chemical, and biological stress factors making it inevitable necessary to have efficient membrane repair to reconstitute cell homeostasis. Membrane repair is thought to be a process involving several steps; (a) sensing of the injury site by calcium-influx, (b) recruiting of intracellular membrane vesicle, (c) formation of a membrane patch, and (d) resealing of the membrane rupture (see Figure 1.8). The first response to injury was shown to occur in a scale of seconds, but membrane remodeling and rearrangements might take minutes (Marg et al., 2012). It has to be kept in mind that various processes besides the resealing of the membrane rupture are part of this complex mechanism. Accumulated proteins needed for resealing have to be removed and transported to their original compartment. Recruited proteins have to be redirected to intracellular compartments and transmembrane proteins like dysferlin might be dislodged by endocytosis. Another process involves the restoration of the cytoskeleton near the site of membrane damage.
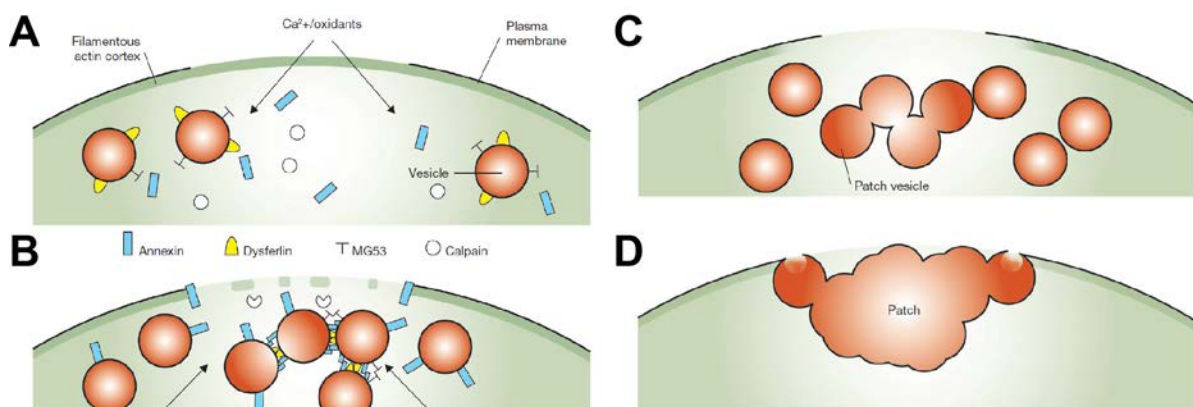
Figure 1.8 Scheme of dysferlin-dependent membrane repair

The membrane repair process can be separated in four steps: Following membrane disruption extracellular components (A) trigger recruitment of several proteins such as MG53, calpain and annexins as well as dysferlin-containing vesicles to site of injury (B). Dysferlin and other proteins of the repair machinery mediate fusion of subsarcolemmal vesicles to a membrane patch (C) used to reseal the injury (D). Scheme is taken from McNeil (2009).

Dysferlin was the first protein found to be crucial for membrane repair in muscles cells (Bansal et al., 2003), whereas the dysferlin C2A domain was shown to be able to bind phospholipids in a calcium-dependent way (Davis, Doherty, Delmonte, & McNally, 2002). Additionally, it was shown by Han et al. (2012) that dysferlin mediates lysosomal fusion to the site of injury upon FasL-stimulation in endothelial cells. The other dysferlin C2 domains (C2B-C2E) do not seem to be crucial for localization and function at the plasma

membrane (Azakir et al., 2012; Davis et al., 2002). It was shown that these domains are involved in dimerization of dysferlin, however, the role and function of dysferlin dimers remains unclear (Xu et al., 2011). Recent investigations in a zebrafish dysferlinopathy model revealed the complexity of the formation of the membrane resealing patch (Roostalu & Strahle, 2012). They could show that accumulation of dysferlin on the surface of vesicles at the myofiber lesion was prominent. More interestingly, the origin of membrane used for the sarcolemmal resealing patch seems to be from dysferlin-enriched plasma membrane. Thus, no membrane markers such as cav-3 were found. This indicates that a specialized membrane compartment containing dysferlin is crucial for membrane resealing. This is consistent with results from our group resolving a distinct repair dome structure at the site of membrane wounding where dysferlin but not cav-3 could be detected (Marg et al., 2012).

1.2.5 Dysferlin interacting partners

The first interaction partner of dysferlin described was cav-3 (Matsuda et al., 2001). Its expression is largely restricted to striated muscle where cav-3 is a crucial structural component of caveolae (Parton, Way, Zorzi, & Stang, 1997). In human skeletal muscle, cav-3 is localized at the sarcolemma and at the intersection between invaginating T-tubules, and mutations lead to muscular dystrophy (see chapter 1.3.). Patients often show secondary reduced dysferlin levels at the sarcolemma. Cav-3 copurifies with dysferlin and more interestingly was found to regulate plasma membrane localization of dysferlin (Hernandez-Deviez et al., 2006). Furthermore cav-3 is crucial for endocytosis of dysferlin through a clathrin-independent pathway (Hernandez-Deviez et al., 2008).

Shortly after resolving the importance of dysferlin in membrane resealing, it was described that dysferlin binds annexin A1 and A2 (Lennon et al., 2003). Annexins represent a large protein family capable of binding phospholipids in a calcium-dependent manner involved in exo- and endocytosis and stabilizing various membrane compartments (Menke, Gerke, & Steinem, 2005). Another interesting aspect of annexins is that they are able to associate to multimeric complexes. It was proposed that annexin A5, which can form trimers and subsequently crystal-like matrices, is involved in preventing further loss of membrane integrity at the site of injury (Bouter et al., 2011). As mentioned earlier, a zebrafish model for dysferlinopathy was developed which was used to extensively study the involvement of annexin in the patch formation by *in vivo* imaging (Roostalu & Strahle, 2012). They showed that the initial response to membrane injury involves recruitment of dysferlin-enriched membranes to the site of damage in parallel but independently from annexin A6.

These two proteins seem to build up a first membrane scaffold crucial for the recruitment of annexin A2 followed by annexin A1 to the site of injury.

Annexin A1 and A2 interact with calpain-3, which also plays an important role in membrane repair (Lennon et al., 2003). Calpain-3 is the skeletal muscle specific member of the calpain superfamily of calcium-dependent cysteine proteases and mutations in calpain-3 lead to LGMD 2A, the most common form of LGMDs in Northern and Central Europe. Calpain functions as protease whose substrates are mainly components of the cytoskeleton (Barnes & Gomes, 2002). Hence, the role of calpain is thought to be on cytoskeleton structure and its interaction with the plasma membrane. It is also known to be involved with the ryanodine receptor at the sarcoplasmic reticulum (SR). Additionally, interaction of dysferlin with the dihydropyridine receptor (DHPR) could be shown by immunoprecipitation and is emphasized by partial colocalization in skeletal muscle fibers (Ampong, Imamura, Matsumiya, Yoshida, & Takeda, 2005). DHPR forms an L-type calcium-channel, acts as voltage sensor, and plays a role in the initiation cascade for excitation-contraction coupling. Patients with calpainopathy seem to have decrease levels of calcium release from the SR (Kramerova et al., 2008). Recently, Sandra Cooper' team proposed dysferlin as substrate for calpain resulting in a mini-dysferlin consisting only of the C-terminus with two remaining C2 domains. Functional vesicles enriched with the mini-dysferlin are thought to be rapidly recruited to the site of injury sensed by MG53 (Lek et al., 2013).

MG53 is a cardiac and skeletal muscle-specific protein belonging to the tri-partite motif protein family and therefore also known as tripartite motif 72 (TRIM72). It was first identified by a proteome approach from skeletal muscle (Weisleder, Takeshima, & Ma, 2008). Cai et al. (2009) presented a MG53-deficient mice displaying late-onset myopathy with typical dystrophic features in skeletal. They demonstrated an increase in susceptibility of mouse skeletal muscle to membrane injury after extensive downhill running, indicating a defect in membrane repair. MG53 is proposed to act upstream of dysferlin. It could be shown that MG53-deficiency leads to failure of accumulation of vesicles at the damage site (Cai, Masumiya, et al., 2009; Wang et al., 2010). In contrast to dysferlin, the translocation of MG53 to the plasma membrane is not dependent on calcium, but seems to be regulated by cholesterol instead. It was speculated that MG53-mediated vesicle recruitment to the site of injury and calcium-dependent vesicle fusion are two distinct processes during membrane repair (R. Han, 2011). A linkage between these two processes could be mediated by cavin-1 which was found to interact with dysferlin, and proposed to link MG53 to cholesterol during membrane repair (Zhu et al., 2011). Cavin-1 was first described as transcription regulatory factor PTRF (polymerase and

transcript release factor) (Jansa, Mason, Hoffmann-Rohrer, & Grummt, 1998). In humans, pathogenic *MG53* mutations have not been identified so far, although an up-regulation in some muscular dystrophy patients were reported (Waddell et al., 2011). Recently, an alternative function for MG53 as an E3 ubiquitin-ligase targeting the insulin receptor and insulin receptor substrate 1 for degradation was presented, indicating a central role of MG53 in skeletal muscle insulin signaling (Levy, Campbell, & Glass, 2013; Song et al., 2013).

Results from our group emphasize a role of EHD2 in membrane repair. EHD2 belongs to the EPS15 homology (EH) domain containing protein family of dynamin-related ATPases which are involved in membrane remodeling in the endosomal system. EHD2 dimers oligomerize into rings around highly curved membranes and interact with pacsin2 and PTRF. It was shown to be associated with caveolae at the plasma membrane, thus representing another structural component of caveolae besides caveolins and cavins (Moren et al., 2012). We showed a colocalization of EDH2 together with the cytoskeleton protein F-actin and annexin A1 at the site of membrane injury in a defined structure named "repair dome". As expected, EHD2 colocalized with the muscle-specific caveolae protein cav-3 at the plasma membrane in human myotubes. Surprisingly, cav-3 was not found in the repair dome during the resealing process, indicating a more indirect impact on membrane repair (Marg et al., 2012).

Another interacting partner of dysferlin is ahnak, a ubiquitously expressed giant plasma membrane protein with high expression levels in cardiac and skeletal muscle (Gentil, Delphin, Benaud, & Baudier, 2003). Dysferlin and ahnak were shown to colocalize at the sarcolemma and in T-tubules. Interaction of both proteins was first discovered by immunoprecipitation by Huang *et al.* in 2007. Binding sites for dysferlin and ahnak are the C2A domain and the N-terminus, respectively. Calpain-3, which is mutated in LGMD 2A (see above), is known to cleave ahnak indicating a direct link of dysferlin, ahnak, and calpain-3. In human skeletal muscle, ahnak levels are reduced at the sarcolemma in LGMD 2B but not in LGMD 2A patients. In both LGMD phenotypes it localizes predominantly within the connective tissue surrounding the muscle fibers. In muscle cells ahnak is known to be localized to enlargeosomes, which can undergo quick exocytosis at the plasma membrane (Huang et al., 2007). This could be confirmed by results from our group showing that ahnak was present in vesicles exocytosed upon increase of intracellular calcium by human primary myotubes in culture (Zacharias et al., 2011). The function of ahnak in skeletal muscle remains unclear. It could be speculated that ahnak plays a role in dysferlin-mediated membrane repair and that dysferlin participates on ahnak localization at the sarcolemma.

Affixin, an integrin-linked kinase focal adhesion protein, was shown to interact with dysferlin (Matsuda et al., 2005). It is thought to be involved in reorganizing the subsarcolemmal cytoskeleton by activating actin by Rac1 through α and β PAK-interactive exchange factors (PIXs). Other focal adhesion molecules have been described in context with dysferlin. Proteomic analysis identified other focal adhesion proteins like vinculin, actinin and talin (de Morree et al., 2010). Rearrangements of the cytoskeleton during membrane repair might not only be due to actin interactions but also due to direct interactions of dysferlin with α-tubulin and histone deacetylase 6 (Azakir, Di Fulvio, Therrien, & Sinnreich, 2010). A recent approach on resolving the LGMD interactome by applying a large-scale screen with yeast-two-hybrid systems and a human skeletal-muscle cDNA library was done by the group of Isabelle Richard. They built up a proteome-scale map of protein-protein interactions centered on proteins involved in LGMD. Among others, they proposed further dysferlin interacting partners. These candidates were grouped by their involvement in different cellular processes such as endocytosis, microtubule-associated intracellular transport, and regulation of gene expression. Especially, direct interactions among dysferlin with titin and sarcoglycan have been highlighted (Blandin et al., 2013). These results might help to discover causative mutated genes in orphan LGMDs, although putative new interacting partners of dysferlin remain to be validated experimentally.

1.2.6 Dysferlin mouse models and therapy

Dysferlin mouse models help to get a better insight into the molecular mechanism of different dysferlin functions and make it possible to test potential therapeutic strategies. Many initial studies were performed on naturally occurring animal models for dysferlinopathy, the SJL/J (Swiss) mice with 15 % residual dysferlin and later on the dysferlin-deficient A/J (A/J$^{dys-/-}$) mice (Kobayashi, Izawa, Kuwamura, & Yamate, 2010, 2012). Studies comparing the dystrophy in muscles of both models confirmed an earlier onset in SJL/J mice compared with A/J and a more rapid rate of progression (Kobayashi2010). More recently, the BLAJ mouse model (B6.A-Dysf$^{[prmd]}$/GeneJ), where the A/J$^{dys-/-}$ mutation was introduced into the well-known C57B1/6J background (Hornsey, Laval, Barresi, Lochmuller, & Bushby, 2013), got more interest. Most dysferlinopathy mouse models show a slow progressive muscle wasting and a late onset of dystropathology.

So far no curative therapy for dysferlinopathy has been established. Different approaches have been used, including interference with the immune response reaction and excitation-contraction coupling. To diminish the effect of increased immune reactions observed in

dysferlinopathy patients, a Rho-kinase inhibitor has been tested. Unfortunately, decrease of immune response did not lead to increase in muscle strength or reduction of dystrophic changes (Rayavarapu et al., 2010). Another approach addressing the inhibition of B cells by rituximab was shown to lead to slight increase in muscle strength (Lerario et al., 2010). Interfering with the ryanodine receptor, and thereby inhibiting the calcium-release from SR, led to an increase of the disease course in some dysferlinopathy patients (Hattori et al., 2007). An alternative option to overcome the whole spectrum of dysferlinopathy-related symptoms would be gene therapy. As dysferlin is a large gene and the encapsulation in adeno-associated viral vehicles is normally limited to 4 kb, this technique is not suitable. A dysferlinopathy patient with late onset and mild progression of the disease having a mini-dysferlin was described by Krahn et al. (2010). Treatment of dysferlin-deficient mice with the mini-dysferlin showed correct localization at the sarcolemma and increase properties in membrane repair, but did not improve dystrophic alteration within the muscle. This indicates that dysferlin-mediated membrane repair is not the only process disrupted in dysferlinopathy. Therefore, targeted gene therapy approaches delivering a full-length protein should be considered. A compromise would be an exon skipping approach, where single or multiple exons shown to be dispensable for protein function are removed. Exon skipping as successful application of this technique has been already shown for dystrophin (Aartsma-Rus et al., 2010; Wein et al., 2010). In our group a trans-splicing approach has been developed. Mutated areas of the coding regions are replaced by a normal copy restoring a full length dysferlin protein (Philippi et al. 2014; unpublished data).

1.3   Limb-girdle muscular dystrophy type 1C

Mutations in *CAV3* lead to various human MDs such as LGMD 1C, distal myopathy (DM), hyperCKemia (H-CK), rippling muscle disease (RMD), and in rare cases familial hypertrophic cardiomyopathy (HCM) (Williams & Lisanti, 2004; Woodman, Sotgia, Galbiati, Minetti, & Lisanti, 2004). These different diseases can be summarized as caveolinopathies and might even occur within one family. In some cases overlapping clinical features were observed like for LGMD and RMD (Fee, So, Barraza, Figueroa, & Pulst, 2004). RMD is a mechanically and activity-induced silent muscle contraction characterized by a lateral wave-like movement across the muscle. Most *CAV3* mutations are inherited in an autosomal dominant way but few cases with recessive mode of inheritance have been observed (Muller et al., 2006). Minetti et al. (1998) first described Italian families with mutations in the *CAV3* gene. Mutations can span over the whole gene affecting different protein domains; however no genotype-phenotype correlation could be reported so far (reviewed in Gazzerro et al., 2010).

In LGMD 1C the age of disease onset varies from early childhood to late adulthood. Predominately skeletal muscle is affected but cardiac involvement is common (Hayashi et al., 2004). Patients usually present with elevated CK values and weakness in limb-girdle muscles, proximal greater than distal. Progression of the disease is slow to moderate and adults often remain ambulant. However, variances even within the same affected family do occur. Histological alterations in LGMD 1C patient muscle display variability of fiber size, increase in centralized nuclei, degeneration and regeneration of muscle fibers, a rather mild increase in connective tissue and expression of cav-3 protein is often reduced (Woodman et al., 2004).

1.3.1 The Caveolins

About 40 years after the first description of caveolae, the discovery of the caveolin proteins family gave new insights into caveolae regulation and formation. There are three caveolins in vertebrates. Caveolin-1 (cav-1) was identified in 1992 by Kurzchalia as vesicular integral membrane protein 21 (VIP-21) involved in trans-Golgi-network-derived transport. In the same year, Rothberg renamed the protein to cav-1 and defined it as a structural key component of caveolae. Caveolin-2 (cav-2) was first described by Scherer et al. (1996) and represents together with cav-1 the minimal structural units necessary for caveolae assembly in most cells. Both proteins are usually found to be expressed in the same tissues with high abundance in adipocytes, fibroblasts and endothelial cells. Cav-3 represents the isoform specific for all muscle cells (Way & Parton, 1996). In skeletal and cardiac muscle, cav-3 was found to predominantly localize in caveolae at the sarcolemma. An association of non-caveolar cav-3 with an internal membrane system was also observed during differentiation of primary cultured muscle cells and the development of mouse skeletal muscle *in vivo* (Parton, 1997). Cav-3 was also found at T-tubules from adult myofibers, localized in accumulated areas at the neck of the tubules in the subsarcolemmal space (Minetti et al., 2002). The *CAV3* gene is found on chromosome 3 (p25) (Minetti et al., 1998).*CAV3* gene spans 12 kb of genomic DNA and contains two exons. The cav-3 protein consists of 151 amino acids arranged in five different domains; the N-terminus, a membrane-scaffolding, a transmembrane, a palmytolated, and the C-terminal domain (Parton, 1996) (see Figure 1.9). Cav-3 is known to be synthesized in the endoplasmic reticulum and transported to the Golgi complex as homo-oligomers. After leaving the Golgi complex, the caveolin oligomers are thought to associate with glycospingolipids and cholesterol, then are transported to the plasma membrane where they fuse to form final caveolae (Galbiati et al. 2001; Gazzerro et al. 2010). The transmembrane domain is crucial for the integration in the plasmamembrane, it forms a

hairpin loop in the cytosolic plasma membrane sheet with the N-and C-terminus facing the cytosol (see Figure 1.9).

The role of caveolins was emphasized by studies showing that caveolin expression is needed to form caveolae (Fra, Williamson, Simons, & Parton, 1995). Generation of cav-1 and cav-3 knockout mice revealed complete lack of caveolae in the respective tissues. Knockout animals also showed various phenotypes in muscle, lung tissues as well as lipid disorders (Le Lay & Kurzchalia, 2005). Cav-1 and cav-2 are usually co-expressed in many tissues, whereas in muscle cells the main structural component of caveolae is cav-3. Cav-3 knockout mice show signs of muscular dystrophy, alterations in T-tubules, and remarkably have a lack of caveolae in muscle tissue (Galbiati et al., 2001). Mice overexpressing cav-3 also display a phenotype mimicking DMD and an increase of CK levels (Galbiati et al., 2000). Mouse models for caveolinopathy present defects in metabolic processes such as development of insulin resistance and increase of adiposity (Capozza et al., 2005). This reflects the various functions of cav-3 as component of caveolae, which are involved in multiple cellular processes (see chapter 1.3.3). As mentioned above, mutations in the *CAV3* gene induce alterations in striated muscle and lead to muscular dystrophy (see 1.3). *CAV1* mutations lead to lipodystrophy due to premature protein termination with impact on smooth-muscle and non-muscle cells (Cao, Alston, Ruschman, & Hegele, 2008; Kim et al., 2008). In the Leiden Muscular Dystrophy database 70 unique DNA variants and 436 individuals with variants have been reported and reviewed last updated in March 2013 (www.dmd.nl).
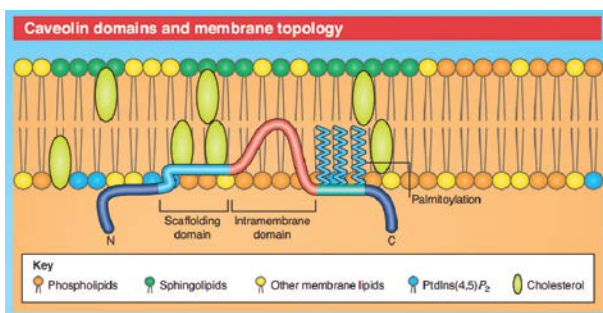
Figure 1.9 Caveolin protein domains and membrane topology

Caveolin are inserted into the plasma membrane by their intramembrane domain, whereas the N- and C-terminus remain intracellular. It is still a matter of debate, if the scaffolding domain is also integrated within the membrane system or if it is accessible for interaction. Membrane environment in caveolae is enriched in cholesterol, sphingolipids, and phosphatidylinositol (4,5)-bisphosphate (PtdIn(4,5)-P2). Scheme taken from Bastiani and Parton (2010).

1.3.2 Caveolae, a subtype of lipid rafts

Caveolae were first described by electron microscopy about 60 years ago in blood capillaries by Palade (1953). Two years later, Yamada reported similar structures in

mouse bladder epithelium and described them as "caveolae intracellulares" (1955). Hence, caveolae have been defined by their distinct morphology as small flask-shaped plasma membrane invaginations of 40-80 nm diameter found abundantly in many cell types (reviewed in Bastiani and Parton (2010)). More recently, the characteristical caveolae structure was corrected from flask-shaped to a rather cup-shape with an open neck. The morphology of caveolae in TEM preparations seems to be sensitive to glutaraldehyde fixation (Schlormann et al., 2010). The distinct morphology of caveolae at the plasma membrane did propose a role in endocytosis similar to clathrin-coated pits. Clathrin-coated pits expose in contrast to caveolae an electron dense cytoplasmic coat in conventional resin-embedded TEM specimens (see Figure 1.10). However, it was shown that caveolae indeed harbor a coat complex assembling around the caveolar bulb (Rothberg et al. 1992; Ludwig et al. (2013).
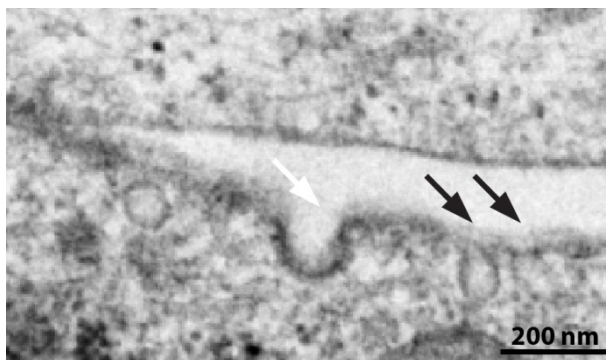
Figure 1.10 Caveolae morphology in transmission electron microscopy

Preparation for conventional electron microscopy results in a appearance of caveolae as flask-shaped invaginations at the plasma membrane of 40-80 nm size (black arrows). Clathrin-coated pits can be distinguished from caveolae by their electron dense protein coat and larger size (white arrow).

Major structural components of caveolae are the caveolins; cav-1 and cav-2 in caveolae of non-muscle cells and cav-3 in caveolae of striated muscle as well as in some smooth-muscle cells (Fra et al., 1995; Way and Parton, 1996). Lack of these proteins leads to loss of caveolae in the respective cell types, whereas cav-2 was found to be dispensable for caveolae formation *in vivo* (Razani et al., 2002). Caveolae formation is achieved by oligomerization of caveolins and association with cholesterol-dense lipid raft (LR) domains at the plasma membrane. Caveolin are thought to bind 1-2 cholesterol molecules and cholesterol depletion was shown to result in disruption of caveolae structure. It is estimated that 144 molecules of caveolin assemble to a single caveola (Pelkmans and Zerial, 2005). Caveolae have been found to be enriched, besides cholesterol, in sphingolipids especially in sphingomyelin and glycoshpingolipids ganglioside GD3, GM1, and GM3, and phosphatidylinositol (4,5)-bisphosphate. They remain in close association with the actin skeleton and microtubules (Richter et al., 2008).

Introduction

Other main structural components besides the caveolins are cavins 1-4, Pacsin 2, and the ATPase EHD2. The cavins have been described as second important structural components for caveolae formation and integrity. A cavin complex is assembled by direct interactions of the four cavins, whereby the different cavins regulate distinct aspects of caveolae formation and function. Cavin-1 was first described as transcription regulatory factor PTRF (Jansa et al., 1998). Later, it could be correlated to cav-1 expression and abundance of caveolae (Vinten et al., 2001). Mutations leading to a lack of PTRF in humans lead to the drastic phenotype of generalized lipodystrophy, muscular dystrophy and other diseases (Rajab et al., 2010). Cavin-2 and cavin-3 both are protein kinase C (PKC) substrates, and are expressed in muscle and non-muscle cells, and their expression profile correlates with cav-1. The fourth member of the cavin family, cavin-4 was first reported as muscle-restricted, coiled-coil protein (MURC) and was linked to cav-3 function. The cavin complex associates selectively only with the caveolin pool at the plasma membrane, and thereby is directly associated with caveolae function (Bastiani et al., 2009).

Pacsin 2, also called syndapin2, colocalizes with a subset of caveolae, contains a membrane curvature binding BAR domain, and plays a role during caveolae formation (Hansen, Howard, & Nichols, 2011). As Pacsin was found to colocalize only with a subset of caveolae, it is speculated that its interaction is temporally regulated. Another important protein involved in caveolae formation and morphology is the EHD2. Its localization in caveolae seems to be restricted to the neck, in comparison to caveolin which is dispersed over the whole bulb (Shvets, Ludwig, & Nichols, 2014). It was shown to interact with other caveolar proteins such as PTRF and pascin-2. EHD2 was shown to regulate caveolar dynamics and also plays a role during caveolae-mediated membrane repair (see also 1.3.3.1) (Corrotte et al., 2013; Moren et al., 2012). EHD2 might also interact with dynamin which was also found at the neck of caveolae (Henley, Krueger, Oswald, & McNiven, 1998). Dynamin is involved in many endocytic pathways and is thought to regulate caveolar dynamics especially membrane fission during caveolae budding.

1.3.3 Caveolar functions

1.3.3.1 Caveolae and membrane integrity

Caveolae have been implicated in various cellular processes like endocytosis, cell signaling, lipid metabolism, and as sensors of membrane tension. Plasma membrane localized cav-3 is thought to interact with the DAPC, the major regulator of sarcolemmal stability and integrity. Cav-3 and dystrophin thereby act competitively to the same binding

site of β-dystroglycan (Sotgia et al., 2000). Overexpression of cav-3 *in vivo* results in a dystrophic phenotype with decreased amounts of dystrophin and other DAPC proteins at the sarcolemma (Galbiati et al., 2001). In muscular dystrophy associated with *CAV3* mutations however, cav-3 protein levels are often reduced or absent, whereas dystrophin and the DAPC seem to be unaffected (Minetti et al. 1998). The coexistence within one protein complex was proposed after immunoprecipitation experiments, however the association of the DAPC with cav-3 is not as strong as with other members of the DAPC (Crosbie, Yamada, Venzke, Lisanti, & Campbell, 1998). It seems like only a part of the cav-3 at the plasma membrane associates with DAPC.

A crucial role for caveolae in mechanosensing was presented by Sinha *et al.* in 2011. They showed that cells use caveolae as compensatory mechanism for cell membrane stress. Cells were subjected to osmotic or mechanical stress, and caveolae were shown to flatten out as response to plasma membrane tension. It was proposed that this mechanism is accompanied by disassembly of the caveolar coat formed by cavins (Pietuch, Bruckner, & Janshoff, 2013; Sinha et al., 2011). In this model caveolae function as membrane reservoir to buffer lateral membrane forces resulting in disassembly of caveolae. Interestingly, recruitment of caveolae to sites of membrane injury induced by lateral forces was also proposed to be essential for membrane repair.

This interesting function of caveolae related to membrane integrity was described by Corotte *et al.* (2013). He proposed an alternative model for the repair mechanism in which specialized intracellular vesicles are recruited to the site of injury. They form a patch to reseal the membrane disruption (see chapter 1.2.4). Experiments on cells treated with streptolysin O, a toxin causing membrane pores that cannot be resealed using patches, showed the formation of caveolae-like vesicles. These vesicles were found to contain caveolar proteins and more interestingly, internalized the toxin by endocytosis resulting in repaired plasma membrane. Membrane injury may lead to calcium influx followed by recruitment of lysosomal vesicles releasing chemicals which trigger the formation of caveolae. These caveolae remove toxins and injured plasma membrane by endocytosis, and are thereby able to restore plasma membrane integrity.

1.3.3.2 Caveolae in cellular signaling pathways

Caveolae have been proposed to be involved in many cellular signaling processes by regulating signaling molecules such as the platelet-derived growth factors (PDGF) or GTPases (Patel, Murray, & Insel, 2008). Well characterized is the interaction of caveolae with the endothelial nitric oxide synthase (eNOS). Caveolin is thought to interact with eNOS through its scaffolding domain (see Figure 1.9) and thereby inhibiting eNOS

function (Bucci et al., 2000; Garcia-Cardena et al., 1997). This region has also been proposed to play a role in signaling through Src tyrosine kinases and H-Ras (Li, Couet, & Lisanti, 1996). This is intriguing, as the scaffolding domain is proposed to insert into the plasma membrane, and thereby is masked in caveolae (Epand, Sayer, & Epand, 2005). A possible explanation is that interaction and regulation of cellular signaling is mediated by the non-caveolar caveolins at the plasma membrane or within the secretory pathway. This could explain the multiple interacting partners found for caveolins which cannot be addressed to caveolae at the cell surface. In agreement with this hypothesis, it could be shown that overexpression of cav-1 *in vivo* leads to an inhibition of eNOS function but no increase of caveolae formation (Bauer et al., 2005). Recent bioinformatics analysis on caveolin-binding motifs in many signaling proteins revealed that they might not be involved in binding of the caveolae scaffolding domain at all (B. M. Collins, Davis, Hancock, & Parton, 2012). Most of these binding motifs are buried within the tertiary structure of the protein and are found in many organism that lack caveolins. It is thereby highly unlikely that they are crucial for recruitment to caveolae. This leads to the fact that many reports on interactions of signaling molecules with caveolae, described by peptides based of the sequence of the caveolin scaffolding domain, need to be revised.

1.3.3.3 Caveolae and endocytosis

There are various known endocytic pathways which can be grouped according to their recruitment of clathrin and the GTPase dynamin. Clathrin-independent endocytic events include phago- and pino-cytosis, flotillin, and caveolin-mediated pathways. Endocytic pathways dependent on the integral membrane raft protein flotillin are also dynamin independent, whereas caveolae are dependent on dynamin. Endocytic pathways involving the membrane scaffolding protein caveolin are dependent on the vesicles fission protein dynamin and EHD2. Other dynamin-dependent processes are described to be either clathrin-dependent or –independent. The most prevalent and well described endocytic pathway is the clathrin-and dynamin-mediated pathway, which is involved in many cellular signaling processes. The idea that caveolae are involved in endocytosis is quite old. Although, caveolae have been shown to be relatively immobile structures at the plasma membrane (Kirkham et al. 2005). Several ligands of caveolae such as integrins and glycosphingolipids have been proposed (reviewed in Cheng, Singh, Marks, and Pagano (2006)). Independent from the internalized cargo, caveolar endocytosis involves subsequent reorganization of the underlying actin-cytoskeleton, dynamin, Src kinases, and protein kinase C (Mayor & Pagano, 2007).The Simian virus 40 (SV 40) was proposed to have a direct role on caveolar budding during virus entry (Pelkmans, Kartenbeck, & Helenius, 2001). However further studies could not confirm that SV 40 is specifically taken

up by caveolae (Damm et al., 2005). Internalization of β1-integrin, an integral membrane protein, stimulated by glycosphingolipids highlights the role of caveolar endocytosis in cell adhesion (D. K. Sharma et al., 2005). Diverse roles for caveolae-mediated endocytosis have been described for diverse cargos such as some G-protein coupled receptors, epidermal and transforming growth factor receptors, the insulin receptor and many more (Patel et al., 2008). However the molecular details on the budding mechanism and endocytic intracellular processes remains to be elucidated.

1.3.3.4 <u>Caveolae in metabolism</u>

Caveolae are very abundant in endothelial cells and adipocytes, and can build up interconnected clusters resulting in an increase of the cellular surface up to 70 % (Richter et al., 2008). Several alterations in lipid metabolism in human disease and mouse models associated with caveolin mutations have been reported. *Cav-1* knockout mice show a drastic metabolic phenotype as they are resistant to diet-induced obesity and show decreased adiposity (Razani et al., 2002). Caveolae seem to play an important role in uptake of fatty acids and storage within the cells. Expression of cav-1 in cells which have no endogenous caveolin, leads to an increase in fatty acid uptake as well as in free cholesterol and of cholesterol export (Fielding & Fielding, 2001). *Cav1*-null mice show a strong reduction of lipid droplets during liver regeneration *in vivo* and a decrease in survival after partial hepatectomy (Fernandez et al., 2006). Cav-1 was shown to associate with lipid droplets after stimulation with cholesterol, and caveolae budding mediated by Src and PKC activation was increased. It was proposed that caveolae itself act as site of fatty acid uptake and mediate their storage in lipid droplets (Le Lay et al., 2006). Lipodystrophy, a human disease associated with caveolin mutations, might be due to increased sensitivity of adipose tissue to fatty acids and underlines the complex role of caveolins and caveolae in metabolism.

Caveolae were shown to regulate metabolism via control of Akt activity. However, recent studies showed that increase in cav-1 expression presented with an increase in aerobic glycolysis rather than decrease in caveolae numbers (Tahir et al., 2013). They proposed an interaction of cav-1 with LRP6, a regulator of the Wnt/beta-catenin signaling pathway and with the insulin receptor (Yamamoto, Sakane, Michiue, & Kikuchi, 2008). *In vivo* studies remain to elucidate the role of caveolae in Wnt/beta-catenin signaling. Additionally, caveolae are proposed to be involved in metabolic processes in the liver, although it has to be kept in mind that many changes in metabolism can be due to secondary compensatory effects of adipocyte dysfunction (Fernandez-Rojo et al., 2013).

1.4 Limb-girdle muscular dystrophy type 2L

LGMD 2L is caused by autosomal recessive mutations in the anoctamin-5 gene (*ANO5*). Recessive mutations in *ANO5* lead to various muscle diseases with symptoms ranging from asymptomatic hyperCKemia, over exercise-induced myalgia, to proximal and/or distal muscle weakness. *ANO5*-muscular dystrophy is considered as one of the most frequent forms of muscular dystrophies in Northern and Central Europe (Hicks et al., 2011; Witting et al., 2013). LGMD 2L shows a male prevalence and milder disease manifestations for females (Penttila et al., 2012). Distal MM3, is less common and is characterized by age of onset in early adulthood and involvement of distal muscles, mostly calve muscles (Hicks et al., 2011; Penttila et al., 2012).The onset of first symptoms in LGMD 2L ranges from early to late adulthood. Calf weakness or hyperCKemia might occur in early adulthood around an age of 20 years. Initial symptoms include difficulties in walking and climbing of stairs, reduced sports performance, and in some cases exercise-induced myalgia (Bolduc et al., 2010; Hicks et al., 2011). Very often, patients have been athletes during early adulthood preliminary to the appearance of first symptoms (unpublished data). For LGMD 2L the manifestation of muscle weakness and atrophy is predominantly seen for proximal muscles of the lower limbs. Many affected individuals might show an involvement of proximal muscles of the upper limbs from the beginning or during a later disease state. As known for LGMD 2B, patients with *ANO5* mutations often show asymmetric muscle involvement of limb-girdle muscles (see Figure 1.11). Not all patients with *ANO5*-muscular dystrophy manifested with muscle weakness (Liewluck et al., 2013). Dilated cardiomyopathy and dilatation of the left ventricle have been reported for some individuals whereas only few patients with anoctaminopathy have been subjected to systematic cardiac investigations (Liewluck et al., 2013; Wahbi et al., 2013). Progression of disease is slow for the proximal LGMD as well as the distal MM form and ambulation is preserved until the very late state of the disease.

Figure 1.11 Clinical presentation in LGMD 2L

Picture of 59 years old patient from our outpatient clinic (Prof. Simone Spuler, Muscle Research Unit, Berlin, Germany) is shown. Asymmetric muscle atrophy of limb-girdle muscles were observed for the right side with prevalence in upper arm and thigh muscles (arrows). The patient reported problems with climbing of stairs with 50 years. Progression is slowly and patient remains ambulant. Note that the patient has been very active during early adulthood. Genetic testing revealed the founder mutation c.191dupA in a homozygous state.

Anoctaminopathies show several similarities to dysferlinopathies, therefore raising the question whether anoctamin-5 (ano-5) and dysferlin have similar functions in skeletal muscle. Recessive mutations in both genes lead to muscular dystrophies with proximal and distal involvement resulting in LGMD or MM clinical presentation, respectively. Asymmetric muscle atrophy and weakness might be present. In some cases amyloid deposits around blood vessels in the interstitial space between muscle fibers have been reported, which has been already described for dysferlinopathies (Liewluck et al., 2013; Milone, Liewluck, Winder, & Pianosi, 2012).

The mutations c.191 dupA in exon 5 and c.2272C>T in exon 20 are the most common disease causing mutations in Northern and Central Europe (Hicks et al., 2011; Penttila et al., 2012). Mutation c.191 dupA has been attributed as founder mutation. The duplication of adenine introduces a shift in the reading frame and has been shown to induce nonsense-mediated mRNA decay (Bolduc et al., 2010). It results in the amino acid change p.Asn64LysfsX15, located at the N-terminus of the anoctamin protein (see Figure 1.12). The founder mutation can occur in a compound heterozygous as well as a homozygous state. High prevalence for the founder mutation in Europe might not be the case for other populations. The mutations described to this date are evenly distributed along the gene without any mutational hotspot as known for mutations in *DYSF* or *DMD*. Most mutations seem to be missense mutations, some affect putative splicing sites, and others lead to frame shift insertions and deletions. So far no correlation between mutation location and clinical severity has been described (Penttilä et al., 2012).

1.4.1 Anoctamin-5 gene

ANO5 is located on chromosome 11 at the locus 11p14.3, spans over 90,701bp and contains 23 exons (*Homo sapiens*, gene ID: 203859). Alternative gene names are transmembrane protein 16E (*TMEM16E*) or *GDD1*. Tsutsumi et al. (2004) reported the identification and characterization of the *GDD1* gene, which is mutated in patients with gnathodiaphyseal dysplasia, an unusual skeletal syndrome with autosomal dominant mode of inheritance. They claimed that human *GDD1* is a novel gene without any human homologs. Shortly afterwards, Katoh and Katoh (2004) emphasized that *GDD1* was identical to *TMEM16E,* a member of the *TMEM16* gene family. In the Leiden Muscular Dystrophy database, 70 unique DNA variants and 185 individuals with variants have been reported and reviewed until June 2014 (www.dmd.nl).

1.4.2 The anoctamin protein family

Anoctamins are evolutionary conserved and can be found in various organism from eukaryotes to higher vertebrates. Whereas most organisms have three to four anoctamin paralogs, the protein family in vertebrate has ten members. Throughout the different organisms, there is a high level of sequence identity within the different subfamilies indicating similar functions (Milenkovic, Brockmann, Stohr, Weber, & Strauss, 2010). Anoctamins are thought to contain eight transmembrane domains with the N- and C-terminus facing the cytosolic compartment (Duran, Qu, Osunkoya, Cui, & Hartzell, 2012; Kunzelmann et al., 2011) (see Figure 1.12 A). In humans, two alternatively spliced isoforms have been reported so far. The major transcript variant expressed in muscle is isoform a (913 aa), whereas the other transcript isoform b is slightly shorter (912 aa). Preliminary experiments on the tertiary structure of anoctamins were done by targeted amino acid mutagenesis by Yang, Cho et al. (2008). Besides the eight transmembrane domains, another structural feature seems to be crucial for the function of anoctamins: a pore formed by a reentering-loop inserted in the plasma membrane between the 5th and 6th transmembrane helices (Figure 1.12 A). As anoctamins are expressed in various tissues, it has been proposed that more than one anoctamin molecule might be involved in the pore formation (Fallah et al., 2011; Kunzelmann et al., 2011). Anoctamins show structural homologies within the protein family proposing similar cellular functions of all family members (see Figure 1.12 B). Anoctamin-1 (ano-1) and anoctamin-2 (ano-2) show a 60 % amino acid identity, which correlates with the fact that both proteins can recapitulate calcium-activated chloride currents similar to endogenous calcium-activated chloride channels (CaCCs) *in vitro.* Evolutionary analysis supports the hypothesis from electrophysiological studies that anoctamins have evolved distinctive functional properties developed after gene duplications (Milenkovic et al., 2010).
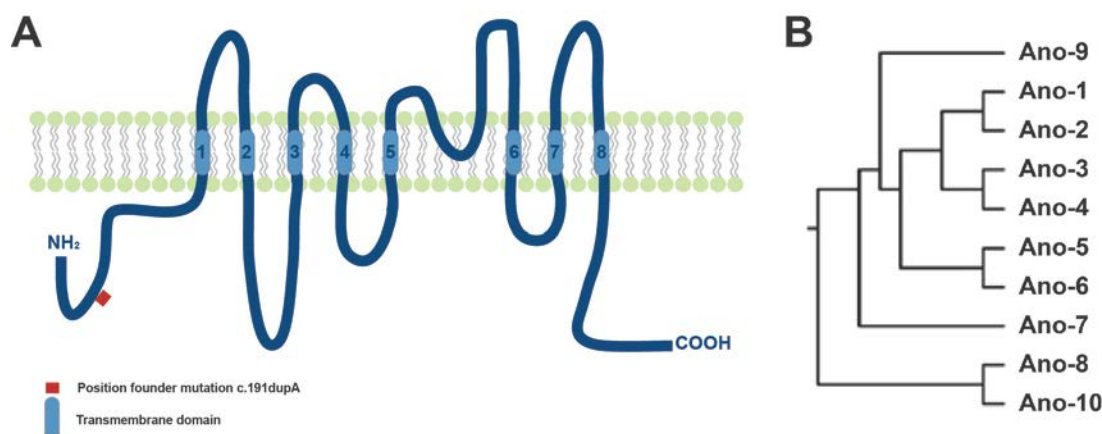
Figure 1.12 Scheme of anoctamin-5 protein structure and phylogenetic three of anoctamin protein family

Anoctamins are thought to have eight transmembrane domains, whereas the N- as well as the C-terminus remains intracellular (A). A re-entrant loop between the 5th and the 6th transmembrane domain is proposed as important structural component. The position of the founder mutation c.191dupA is located near the N-terminus of the protein. Members of the anoctamin protein family show strong homologies represented by hierarchical clustering. Phylogenetic three is modified from Schroeder, Cheng, Jan, and Jan (2008).

1.4.3 Anoctamin functions

The anoctamin protein family consists of 10 members with highly conserved structural features defining their membrane association (see Figure 1.12). So far only *ANO5, ANO6,* and *ANO7* have been associated with human disease.

The function of ano-5 is still unknown. For ano-1 and ano-2 however, which share significant sequence homology with ano-5, there is multiple evidence that they function as CaCCs ((Almaca et al., 2009); Schroeder et al. (2008); (Stephan et al., 2009; Stohr et al., 2009; Yang et al., 2008). CaCCs play important roles in physiological processes including sensory transduction, epithelial secretion, and neural excitability (Eggermont, 2004). Three groups independently identified and characterized the ano-1 gene (*ANO1* or *TMEM16A*). *ANO1* encodes for ano-1, a transmembrane protein, which mediates chloride currents activated through intracellular calcium similar to endogenous CaCCs ((Almaca et al., 2009); Schroeder et al. (2008); (Stephan et al., 2009; Stohr et al., 2009; Yang et al., 2008). Ano-1 is highly expressed in epithelial tissues and plays an important role in calcium-dependent chloride secretion (Dutta et al., 2011). Ano-2 also functions as CaCCs in olfactory sensory neurons and photoreceptor synapses (Rasche et al., 2010; Stohr et al., 2009). For anoctamin-6 (ano-6), which shares strong homology with ano-5, functions at the plasma membrane have been reported. It was proposed to have a role as Fas-ligand-activated chloride channel and can induce scramblase activity in platelets (Martins et al., 2011; Suzuki et al., 2013). Interestingly, loss-of-function mutations in ano-6 have

Introduction

been reported for patients suffering from the Scott syndrome which is associated with deficiencies in blood coagulation.

Investigation of molecular functions of ano-5 have been done before involvement in muscular dystrophies have been described. As already mentioned *ANO5* was initially described as *GDD1 or TMEM16E*. Tsutsumi et al. (2004) transfected COS-7 cells with a human *ANO5* vector construct and showed a colocalization of ano-5 with calreticulin, a marker for the endoplasmic reticulum. They proposed a function as intracellular calcium-release channel involved in the regulation of calcium-dependent signaling pathway. Additionally, they showed higher levels of *ANO5* transcripts in cardiac and skeletal muscle and an upregulation during differentiation of murine C2C12 cells. *In situ* experiments in mice revealed *ANO5* expression exclusively in the myotomal component of somites and developing skeletal muscle cells during embryogenesis. Subcellular fractionation revealed association with high and low density microsome membrane fractions indicating localization in intracellular vesicles and function as membrane integral glycoprotein (Mizuta et al. (2007)). These results contradicted with the previous reported localization to the ER, which might be due to artefacts by overexpression of non-endogenous protein. Ano-5 could be detected in murine cardiac and skeletal muscle tissue by western blot and seemed to have increased levels in dystrophic skeletal muscle of MDX mice, a mouse model for duchenne muscular dystrophy.

Schreiber et al. showed in 2010 that when ano-1-2, - 5-7, and -9 are overexpressed in HEK293 cells, they localized at the plasma membrane. Functional analysis by ATP-induced iodide quenching of YFP fluorescence, revealed that ano-1 and ano-2, but also anoc-6 and ano-7 induced chloride conductance. Contrarily, (Duran et al., 2012) showed that expression of anoctamins 3-7 in HEK293 cells did not induce generation of chloride currents measured by whole cell patch clamp electrophysiology. Anoctamins 3-7 seem to have an intracellular localization with putative association with the endoplasmic reticulum. The results from Schreiber et al. (2010) were confirmed by the group again for HEK293 cells. They again showed strong plasma membrane localization for ano-1, and ano-4-7 (Tian, Schreiber, & Kunzelmann, 2012). Additionally, they found evidence for chloride currents in all anoctamins when induced by increased intracellular calcium levels. In contrast to expression studies, for endogenous anoctamin very low levels at the plasma membrane have been reported indicating an intracellular rather than plasma membrane associated function for some of the anoctamins. As anoctamins are expressed in various tissues it has been proposed that more than one anoctamin molecule might be involved in the formation of CaCCs with ano-1 as major structural and functional component (Duran et al., 2012; Schreiber et al., 2010; Yang et al., 2008). Up to this date, it remains unclear if

the intracellular anoctamins function as CaCCs or have other roles in ion transport within the cell.

Introduction

2 Aim of the study

Limb-girdle muscular dystrophies (LGMDs) are a heterogeneous group of muscular dystrophies with common features such as hyperCKemia, skeletal muscle weakness, and a slowly progressive course of the disease. Remarkably, most proteins affected in LGMD function at the sarcolemma, the plasma membrane of muscle cells, and are crucial for membrane stability and integrity.

The aim of my work was to characterize the sarcolemma in LGMD and dissect the cellular mechanisms underlying the disease. We hypothesized that dysferlin, caveolin-3 (cav-3), and anoctamin-5 (ano-5) might be connected through their cellular functions. Understanding how they might interact on molecular level could help to understand the variability in LGMDs and thus, help to gain knowledge about possible therapeutic targets.

My project could be subdivided into three parts. The first objective of this work was the characterization of skeletal muscle tissue and muscle cell lines of human patients and controls. This included

- Characterization of muscle tissue by immunohistochemistry
- Characterization of human skeletal muscle cell lines *in vitro*
    - Investigations on protein level by western blotting
    - Investigations on subcellular localization of dysferlin and cav-3 by immunofluorescence microscopy and transmission electron microscopy (TEM)
    - Characterization of the plasma membrane morphology on ultrastructural level by conventional TEM

Morphological studies and quantification of endocytic structures at the plasma membrane indicated a connection of dysferlin to caveolae, which represent specialized lipid raft (LR) domains. Thus, the second objective of my thesis was to investigate the association of dysferlin with LRs. This was done by biochemical purification of detergent-resistant membranes from control and LGMD 2B myotubes. Results further supported a link between dysferlin and cav-3 in context with caveolae. One of the main functions described for dysferlin is membrane repair, which is thought to be mediated by fusion of vesicles recruited to the injury site. The content and origin of these vesicles, however, remain a matter of debate. In the third part of my thesis, we aimed to characterize dysferlin-containing vesicles to understand more about dysferlin function in membrane repair as well as in other processes such as vesicular traffic, cell signaling, and metabolism. Therefore an immunopurification assay for morphological intact dysferlin-containing

vesicles was established. In order to reveal possible new dysferlin interaction partners, as well as protein cargo of these vesicles, we conducted detailed proteome analysis of immunopurified vesicles by liquid chromatography-mass spectrometry (LC-MS).

My major goal was to explore the protein function of dysferlin, cav-3, and ano-5 at the sarcolemma as well as within intracellular compartments. The multiple actions of these proteins on cellular mechanism might explain the variability in LGMD phenotype and help to understand the molecular basis of the disease.

3 Material & Methods

3.1 Material

3.1.1 Biopsies

Skeletal muscle biopsies were obtained from *vastus lateralis, triceps brachii* or *deltoid muscle.* All patients contributed to this study which was approved by the Charité Internal Review Board, and therefore signed a written informed consent. A full list with all patient details is shown in Table 3-1.

Under local anesthesia of the skin and surrounding non-muscular tissue, the neurosurgeon dissected skeletal muscle tissue of approximately $5\,mm^3$ size and transferred it directly into solution A for storage (see Table 3-3). Within 24-48 hours skeletal muscle cells were isolated from biopsies.

Table 3-1   Details on LGMD patients included in the study

Patient ID	LGMD	Skeletal muscle biopsy	Age at biopsy	Gender
DYSF_1	2B	*Triceps*	36	F
DYSF_2	2B	*Vastus lateralis*	37	M
DYSF_3	2B	*Deltoid*	57	M
DYSF_4*	2B	*Quadrizeps*	29	F
CAV-3_1*	1C	*N. A.*	N.A. (born 1969)	F
CAV-3_2	1C	*Vastus lateralis*	20	F
CAV-3_3	1C	*Triceps*	44	M
ANO-5_1	2L	*Vastus lateralis*	N.A. (born 1964)	M
ANO-5_2	2L	*Vastus lateralis*	43	M
CTRL_1	-	*Quadrizeps*	74	F
CTRL_2	-	*Vastus lateralis*	N.A.	N.A.
CTRL_3	-	*Vastus lateralis*	44	M
CTRL_4*	-	*Gracilis*	25	M
CTRL_5*	-	*Pectoralis major*	41	M
CTRL_6*	-	*Quadrizeps*	79	F

Biopsies have been taken at the Helios clinic (Berlin, Germany) by Dr. Andreas Spuler in cooperation with Prof. Simone Spuler. Patients marked with asterics (*) have been recruited by local physicians and isolation of myoblasts was done by the following institutions: DYSF_4: provided by Nicolas Levy, Medical Faculty, Marseille, France; CAV-3_1 and CTRL_1, CTRL_4-6: provided by Dr. Vincent Mouly, Human Cell Culture Platform, Myology Institute, Paris, France.

3.1.2 Primary and immortalized human skeletal muscle cells

Table 3-2   Details on human skeletal muscle cell lines

Cell line	Patient	Cells	Affected gene	State	Exon	Mutation (cDNA)	Mutation (protein)
Dysf-1	DYSF_1	i	*Dysferlin*	Heterozygous	16	c.1448C>A	p.S483X
				Heterozygous	55	c.*107T>A	3'UTR
Dysf-2	DYSF_2	i	*Dysferlin*	Heterozygous	8in	c.855+1delG	mRNA decay
				Heterozygous	9	c.895G>A	p.G299R
Dysf-3	DYSF_3	i	*Dysferlin*	Homozygous	38	c.4022T>C	p.L1341P
Dysf-4*	DYSF_4	i	*Dysferlin*	Heterozygous	4in	c.342-1G>A	
				Heterozygous	32	c.3516-3517delTT	p.S1173X
Cav3-1*	CAV3_1	i	*Caveolin-3*	Heterozygous	1	c.83C>T	p.P28L
Cav3-2	CAV3_2	i	*Caveolin-3*	heterozygous	1	c.80G>A	p.R27E
Cav3-3	CAV3_3	i	*Caveolin-3*	heterozygous	1	c.80G>A	p.R27E
Ano5-1	ANO5_1	p	*Anoctamin-5*	Homozygous	5	c.191dupA	p.N64K fsX15
Ano5-2	ANO5_2	p	*Anoctamin-5*	Heterozygous	5	c.191dupA	p.N64K fsX15
				Heterozygous	21in	c.2521-1delG	Putative splice site
PTRF-/-*	-	P	*Polymerase I and transcript release factor*	Homozygous	-	c.160delG	p.V54CfsX2
Ctrl-1	CTRL_1	p	-	-	-	-	-
Ctrl-2	CTRL_2	p	-	-	-	-	-
Ctrl-3	CTRL_3	p	-	-	-	-	-
Ctrl-4*	CTRL_4	i	-	-	-	-	-
Ctrl-5*	CTRL_5	i	-	-	-	-	-
Ctrl-6*	CTRL_6	i	-	-	-	-	-

Primary cell lines have been isolated and purified in the laboratory of Prof. Simone Spuler. Immortalization was done by Dr. Vincent Mouly at the Institute of Myology (Paris, France). Cell lines marked with asterisks (*) have been provided as a gift from other laboratories (Dysf-4: provided by Nicolas Levy, Medical Faculty, Marseille, France; Cav3-1, Ctrl-4-6: provided by Dr. Vincent Mouly; PTRF-deficient fibroblasts: provided from Prof. Dr. Markus Schülke-Gerstenfeld, NeuroCure Clinical Research Center, Charité, Berlin, Germany). As nomenclature for intronic, cDNA and protein sequences the abbreviations in, c, and p were used. (i: immortalized, p: primary)

3.1.3 Chemicals and devices

3.1.3.1 Cell culture

Table 3-3   Cell culture solutions and devices

Name	Components	Company
Proliferation medium	Skeletal Muscle Cell Growth Medium (Basal Medium) supplemented with 10 % FBS, 1.5 % GlutaMax and 40 µg/ml gentamycin	Provitro
FBS	Fetal Bovine Serum	Biochrom
GlutaMax	GlutaMAX™-I (100x)	Gibco
Gentamycin	Gentamycin (50 mg/ml)	Gibco
Differentiation medium	Opti-MEM® I (1x), 40 µg/ml gentamycin	Gibco
PBS	DPBS (1x), [-CaCl$_2$], [-Mg Cl$_2$]	Gibco
DMSO	Dimethyl sulfoxide	Sigma-Aldrich
Trypsin	0.25 % trypsin-EDTA (1x)	Gibco
Centrifuge	3-18 K	Sigma
Counting chamber	Neubauer counting chamber	Marienfeld-Superior
Solution A	30 mM HEPES, 130 mM NaCl, 3 mM KCl, 10 mM glucose, 0.1 % phenol red, pH 7.6	-
Digest solution	4 ml collagenase type II (254 U/ml), 0.2 ml dispase II (100 U/ml in 50 mM HEPES pH 7.4, 150 mM NaCl), 0.5 ml trypsine-EDTA (1x), sterile filtered	-
Sterile filter	Rotilabo® syringe filter, PES	Roth
Sorting buffer	PBS pH 7.2, 2 mM EDTA, 0.5 % BSA, sterile filtered	-

3.1.3.2 Biochemical techniques

Table 3-4   Information on all antibodies used in western blot experiments

Antigen	Antibody name	Company	Dilution
Primary antibody			
Dysferlin	Novocastra™ lyophilized mouse monoclonal antibody dysferlin [NCL-Hamlet]	Novocastra	1:500
	Anti-Dysferlin [JAI-1-49-3]	Abcam	1:500
Calnexin	Anti-Calnexin - ER membrane marker antibody	Abcam	1:1000
Caveolin-3	Anti-Caveolin-3 antibody	Abcam	1:1000
	Caveolin-3 (A-3)	Santa Cruz Biotechnology	1:300
Golgi 58k	Anti-58K Golgi protein antibody [58K-9] - Golgi Marker	Abcam	1:400
LAMP1	Anti-LAMP1 antibody	Abcam	1:500
Myosin heavy chain (MHC)	MF 20	Developmental Studies Hybridoma Bank	1:5000
GAPDH	Anti-GAPDH antibody - Loading Control	Abcam	1:5000
Na$^+$/K$^+$-ATPase	Anti-alpha 1 Sodium Potassium ATPase [464.6] antibody - Plasma Membrane Marker	Abcam	1:1000
α-Tubulin	Anti-alpha Tubulin antibody	Sigma	1:4000
Secondary antibody			
IRDye700-anti-rabbit	Anti-Rabbit IgG (H&L)[Donkey], IRDye700 conjugated	Rockland	1:5000
IRDye700-anti-	Anti-Mouse IgG (H&L)[Goat],	Rockland	1:5000

mouse	IRDye700 conjugated		
IRDye800-anti-rabbit	Anti-Rabbit IgG (H&L)[Donkey], IRDye800 conjugated	Rockland	1:5000
IRDye800-anti-mouse	Anti-Rabbit IgG (H&L)[Donkey], IRDye800 conjugated	Rockland	1:5000
HRP-linked anti-rabbit	ECL^{TM} Anti-rabbit IgG (donkey)	GE Healthcare	1:2000
HRP-linked anti-mouse	Polyclonal Goat Anti-Mouse Immunoglobulins/HRP	Dako	1:2000

Table 3-5   Solutions used for biochemical applications

Solution	Components	Company
Lysis buffer	50 mM Tris pH 7.4, 150 mM NaCl, 0.5 % Triton X-100, 0.5 % Na-deoxycholate, 50 mM NaF, 1 mM Na-vanadat, 1 mM EDTA	-
PMSF	1 mM PMSF in 100 % 2-propanol	-
Complete protease inhibitor cocktail stock (100x)	Dissolve 1 tablet cOmplete protease inhibitor cocktail in 500 µl dH_2O	Roche
CSK buffer	0.1 M Tris, 20 mM EGTA, pH 7.4	-
Stacking gel buffer	1.5 M Tris HCl, 0.4% SDS, pH 8.8	-
Stripping buffer	-	Gene Bio-Application
SDS loading buffer (6x)	3 g SDS, 2.79 g DTT, 11.34 g glycerine, 21 ml stacking gel buffer (4x), 0.1 g bromophenol blue	-
PageRuler Plus Prestained Protein Ladder	-	Thermo Scientific
Running buffer stock (10x)	2 M glycine, 25 mM Tris, 1 % SDS	-
Transfer buffer stock (10x)	0.5 M Tris, 0.4 M glycine, 0.01 M SDS, pH 7.4	-
Transfer buffer (1x)	0.05 M Tris, 0.04 M glycine, 0.001 M SDS, 20 % MeOH	-
Coomassie stain	50 % MeOH, 10 % acetic acid, 0.25 % Brilliant Blue G250	Merck, Bio-Rad
Ponceau S stain	-	Sigma-Aldrich
TBS stock (10x)	100 mM Tris, 1.4 M NaCl	-
Washing buffer (TBS-T)	0.05 % Tween 20 in TBS (1x)	-
Blocking buffer	2 % BSA, 4 % milk powder in TBS-T (1x)	-
Antibody stripping buffer	Immunodetection removing buffer	Gene Bio-Application
ECL substrate solution	SuperSignal® West Dura Extended Duration Substrate	Thermo Scientific
Protease inhibitor cocktail	1 µg/ml leupeptine, 1 µg/ml pepstatine, 1 mM benzamidine, 2,5 µM phenyl-methyl-sulfonuyl-fluoride (PMSF), 3 µg/ml aprotinine	Invitrogen
MBS	25 mM MES, 150 mM NaCl, 2 mM EDTA, pH 7.4	-
CSK	0.1 M Tris, 20 mM EGTA, pH 7.4	-
KI	0.6 M KI in dH_2O	-
Triton X-100	20 % Triton X-100 in dH_2O	-
Protein A-beads	Dynabeads Protein A	Novex by Life Technologies

Table 3-6   Devices used for biochemical applications

Device	Name	Company
Cell scraper	Cell scraper M, 300 mm	TPP
Centrifuge	Centrifuge 5415R	Eppendorf
Chemiluminescence detection system	Emi-smart 5000	Peqlab (VWR)
Filter 0.22 µm	Rotilabo® syringe filter, PES	Roth
Fluorescence detection and	Odyssey Infrared Imaging System	Licor

scanning system

Electrophoresis chamber	XCell SureLock™ Mini-Cell	Invitrogen
Glass homogenizer	KONTES® Dounce Tissue Grinder	Kimble chase
Gradient protein gel	NuPAGE®Novex® Bis-Tris Mini Gels 8-16 %	Invitrogen
Thermomixer	Thermomixer ® compact	Eppendorf
Transfer system	Trans-Blot ® SD semi-dry transfer cell	BIO-RAD
Heating chamber	Heraeus	Thermo Scientific
Microplate absorbance reader	Sunrise™	PROTAN
Magnet	DynaMag™-Spin	Life technologies
Nitrocellulose membrane	Whatman, Protan BA85	GE Healthcare Life Sciences
Prestained protein ladder	PageRuler™ Plus	Thermo Scientific
Power supply	PowerPac™ HC	BIO-RAD
Rotating device	Intelli-mixer RM-2S	ELMI
Spectrophotometer	Sunrise	TECAN
Table centrifuge	Flexifuge® Mini Centrifuge	Biotool
18 G needle	ø1.2 x 40 mm, 18 G x 1½	Braun
23 G needle	ø 0.6 x 30 mm, 23 G x 1¼	Braun

3.1.3.3 Visualization techniques

Table 3-7   Antibodies used for immunofluorescence labeling experiments

Antigen	Antibody name	Company	Dilution
Primary antibody			
α-actinin	Monoclonal Anti-α-Actinin antibody	Sigma-Aldrich	1:1000
Bin-1	Myc box-dependent-interacting protein 1	Millipore	1:50
Caveolin-3	Anti-Caveolin-3 antibody	Abcam	1:1000
Caveolin-3	Caveolin-3 (A-3)	Santa Cruz Biotechnology	1:20
CD 4	Anti-CD4 antibody [EPR6855]	Abcam	1:100
CD 8	Anti-CD8 antibody [EP1150Y]	Epidomics	1:200
Desmin	Monoclonal Mouse Anti-Human Desmin, clone D33	Dako	1:500
Dysferlin	Novocastra™ lyophilized mouse monoclonal antibody dysferlin [NCL-Hamlet]	Novocastra	1:20
Dysferlin	Anti-Dysferlin [JAI-1-49-3]	Abcam	1:100
LAMP1	Anti-LAMP1 antibody	Abcam	1:500
Myosin heavy chain (MHC)	MF 20	Developmental Studies Hybridoma Bank	1:20
Secondary antibody			
Anti-mouse IgGs	Goat Anti-mouse IgG Antibody Alexa Fluor® 488	Life Technologies	1:500
Anti-mouse IgGs	Goat Anti-mouse IgG Antibody Alexa Fluor® 568	Life Technologies	1:500
Anti-rabbit IgG	Goat Anti-rabbit IgG Antibody Alexa Fluor® 488	Life Technologies	1:500
Anti-rabbit IgG	Donkey Anti-rabbit IgG Antibody Alexa Fluor® 568	Life Technologies	1:500
Anti-mouse IgG-Biotinylated	Anti-Mouse IgG biotinylated Antibody	Vectastain	1:100

Table 3-8   Antibodies used for immunolabeling experiments after Tokuyasu

Antibody	Dilution	Company
Primary antibody		
Anti-Dysferlin [NCL-Hamlet]	1:20	Novocastra
Anti-PTRF	1:20	BD
Rabbit anti-mouse IgG	1:100	Life Technologies
Secondary antibody		
Protein-A gold ø5, 10 and 15 nm	1:60	Utrecht Medical University
Goat anti-mouse ø12 nm	1:30	Jackson Immuno Research Laboratories

Material & Methods

Table 3-9   Solutions and devices used for immunofluorescence and electron microscopy experiments

Solution	Components	Company
Solutions for immunofluorescence		
Blocking buffer	1 % BSA in PBS	-
DAB	FAST ™ 3,3'-Diaminobenzidine	Sigma
Embedding solution	Vectashield® Mounting Medium	Vector Laboratories
Fixative	3.7 % Formaldehyde in PBS	-
Nucleic acid stain	Bisbenzimid H 33258	Sigma-Aldrich
PBS	-	Invitrogen
Permeabilization buffer	0.2 % Triton X-100 in PBS	-
Strepavidin-Peroxidase	-	KLP
Washing buffer	0.1 % BSA in PBS	-
Solutions for epon embedding and sectioning		
BEE	Butyl-2,3-epoxypropyl ether	Merck
Cacodylate buffer	0.2 M cacodylate buffer	-
Epon	Poly/Bed®812 (24 ml)	Polysciences
	Dodecenylsuccinic anhydride (DDSA) (15.5 ml)	
	Nadic methyl anhydride (NMA) (10.5 ml)	
	DMP-30 (1 ml)	
Ethanol, 30%, 50%, 70%, 90%	Ethanol 100 % diluted in dH_2O	Merck
Fixative for epon embedding	2.5 % glutaraldehyde in 0.1 M cacodylate buffer	-
Osmium tetroxide (OsO_4)	1 % osmium-VIII-oxide in 0.1 M cacodylate buffer	-
Propylene oxide	Propylene oxide (PO)	Polysciences
Tannic acid	1 % tannic acid in 0.1 M cacodylate buffer	Mallinckrodt
Ultrostain I	3 % lead citrate	Leica Microsystems
Ultrostain II	0.5 % uranyl acetate	Leica Microsystems
Solutions for labeling after Tokuyasu		
Blocking solution	1 % BSA in PBS	-
Contrast solution I	0.3 % uranyl acetate (UA)	-
	1.8 % methyl cellulose (MC)	
Contrast solution II	3 % tungstosilicic acid hydrate (Si)	-
	2.8 % polyvinyl alcohol (PVA)	
Fixative for Tokuyasu	4 % formaldehyde in PB 0.1 M	-
Gelatin 1% (2%, 12%)	1 g (2 g, 12 g) gelatin in 100 ml PB 0.1 M	-
Phosphate buffer (PB) 0.1M	Mix 0.2 M Na_2HPO_4 & 0.2 M NaH_2PO_4 81:19, dilute to 0.1 M with dH_2O, adjust to pH 7.4	-
Pic-up solutions	2 % methyl cellulose and 2.3 M sucrose in PB 0.1 M mixed in a 1:1 ratio	-
Quenching solution	0.1 % glycine in PBS	-
Washing solution	0.1 % BSA in PBS	-
Devices		
Centrifuge	3-18 K	Sigma
CDD camera	Quemesa	Olympus Soft Imaging Solutions
Contrasting automat	Leica EM AC20	Leica Microsystems
Cryo-ultramicrotome	Reichert FCS	Reichert
Ultramicrotome	Reichert Ultracut S	Reichert
TEM imaging software	iTEM, version 5.2	Olympus Soft Imaging Solutions
Transmission electron microscope	Zeiss EM 910	Zeiss

Table 3-10   Solutions and devices used for membrane wounding experiments

Solution / device	Components	Company
CaCl^2	2.5 mM CaCl^2	-
Chambered coverslips	µ-Slide 8 well	Ibidi
Fluorescent dye	FM 1-43	Molecular Probes, Invitrogen
Tyrode solution	140 mM NaCl, 5 mM KCl, 2 mM MgCl^2, 10 mM HEPES, pH 7.2	-

3.1.3.4 List of chemicals and solutions

Name	Abbreviation	Company
Bovine serum albumin	BSA	Roth
Butyl-epoxypropyl ether	BEE	Merck
Calcium chloride	CaCl$_2$	Roth
Dimethyl sulfoxide	DMSO	Sigma-Aldrich
Disodium hydrogen phosphate	Na$_2$HPO$_4$	Roth
Dithiothreitol	DTT	Roth
Ethylenediaminetetraacetic acid	EDTA	Roth
Ethylene glycol tetraacetic acid	EGTA	Roth
Ethanol	EtOH	Roth
Formaldehyde	FA	Sigma-Aldrich
Formaldehyde 3.7 %	FA 3.7 %	Roth
Formvar	-	Merck
Gelatine	-	Roth
Glutaraldehyde	GA	Fluka
Glycerine	-	Roth
Glycine	-	Merck
Hydrogen chloride	HCl	Roth
4-(2-hydroxyethyl)-1-piperazineethanesulfonic acid	HEPES	Roth
Isopropanol	2-propanol	Roth
Magnesium chloride	Mg Cl$_2$	Roth
Methanol	MeOH	Roth
Methyl cellulose	MC	Fluka
Methyl-β-cyclodextrin	mβCD	Sigma-Aldrich
Milk powder	-	Roth
Monosodium phosphate	NaH$_2$PO$_4$	Roth
2-(N-morpholino)ethanesulfonic acid	MES	Fluka
Osmium-VIII-oxide	OsO$_4$	Electron Microscopy
Phenylmethanesulfonylfluoride	PMSF	Roche
Polyvinyl alcohol	PVA	Fluka
Potassium chloride	KCl	Roth
Potassium iodide	KI	Roth
Propylenoxide	PO	Sigma-Aldrich
Sodium cacodylate trihydrate	Caco	Electron Microscopy
Sodium chloride	NaCl	Roth
Sodium deoxycholate	Na-deoxycholate	Sigma-Aldrich
Sodium dodecyl sulfate	SDS	Roth
Sodium fluoride	NaF	AppliChem
Sodium orthovanadate	Na-vanadate	AppliChem
D-Sucrose (BP 220-1)	-	Fischer Scientific

Tannic acid	-	Mallinckrodt
Tungstosilicic acid hydrate	Si	Fluka
Trichloroacetic acid	TCA	Sigma-Aldrich
Tris(hydroxymethyl)aminomethane	Tris	Roth
Triton X-100	-	Sigma-Aldrich
Tween 20	-	Serva
Uranyl acetate	UA	Serva
Vanadate	-	Sigma-Aldrich

3.2 Cell culture methods

3.2.1 Isolation and purification of primary human skeletal muscle cells

All steps during myoblast isolation were carried out under sterile conditions. Skeletal muscle biopsies stored in solution A (see Table 3-3) were washed thoroughly with PBS and minced with a scissor. Minced muscle tissue was further washed two times with PBS and pelleted by centrifugation for 5 minutes at 192 g. The pellet was resuspended in digest solution containing collagenase type II, dispase II, and trypsin (see Table 3-3), and incubated for 45 minutes at 37 °C under mild agitation. To completely homogenize the tissue, the digested muscle was resuspended eight times with a glass Pasteur pipettes. The sample was centrifuged for 5 minutes at 192 g, the pellet was resuspended in SMCGM, and transferred to a cell culture dish. The tissue lysate was cultured under normal cell culture conditions (37 °C, 5 % CO_2 and 96 % relative humidity) and medium was changed regularly every three days. After 3-6 days, myoblast outgrow of the minced and digested skeletal muscle fibers was observed and cells could be expanded further. Purity of the myoblast population was confirmed by immunolabeling with an antibody against the skeletal muscle marker desmin (see 3.3.1). If the population showed a purity of less than 90 % desmin-positive cells, magnetic cell sorting (MACS) was performed using the muscle cell surface marker CD56. For MACS, adherent myoblasts were detached with 0.25 % trypsin-EDTA and the cell number was determined (for protocol see 3.2.3). Cells in suspension were centrifuged for 10 minutes at 192 g at 4 °C and washed with cold sorting buffer. The pellet was resuspended in sorting buffer to a concentration of 10^7/80µl cells and 20 µl of microbeads conjugated to monoclonal anti-human CD56 antibodies (human CD56 Micro Beads, Miltenyi Biotech) were added. Incubation with magnetic beads was done for 15 minutes at 4 °C with mild mixing every 5 minutes. LS columns (Miltenyi Biotech) were equilibrated with cold buffer and cell-bead-suspension was added in a volume of 2 ml to the columns mounted on a magnet (MidiMACS separator, Miltenyi). The non-bound flow-through was kept for analysis of fibroblast content. After three washes with sorting buffer the column was separated from the magnet and cells were carefully eluated in sorting buffer. Myoblasts were transferred to SMCGM

and cultivated under normal conditions. Myogenicity of the flow-though and eluate was determined by immunolabeling with anti-desmin antibody (Dako). Only cell populations showing myogenicity over 90 % where used for experiments.

3.2.2 Immortalized human skeletal muscle cells

Availability of primary human myoblasts from biopsies of LGMD patients with disease-causing mutations is limited. These muscle biopsies often show drastic structural changes due to fibrosis and necrosis, which is characterized by an increase in connective and adipose tissue. This is the reason why during isolation of myoblasts from muscle biopsies, cells like fibroblasts and adipocytes have a negative impact on the purity of the myogenic population. Additionally, cultivation of primary human myoblasts has limitations due to their limited proliferative capacity. Proliferation *in vitro* for more than 10 passages can result in phenotypical variations that are linked to replicative senescence (Bigot et al., 2008). Therefore an alternative *in vitro* cell culture model was generated by immortalization of selected primary human myoblast cell lines from LGMD patients (see Table 3-2) by retroviral transduction with telomerase (*human telomerase reverse transcriptase; hTERT*) and c̲yclin-d̲ependent k̲inase 4 *(CDK*-4). It was shown that the progressive erosion of telomeres during cell division will induce p53 activation and cell-cycle exit when reached a critical length. Expression of *hTERT* in myoblasts increases the proliferation and differentiation capacity *in vitro* (Mamachaoui et al., 2011). The second major mechanism causing cellular senescence during replication in primary human myoblasts is the p16^{INK4a}-dependent stress pathway, which can be blocked by expression of *CDK*-4. Primary human myoblasts were isolated, purified, cultivated, and prepared for storage as described in 3.2.1 and 3.2.3. Selected cell lines were send to the Human Cell Culture Platform (Dr. Vincent Mouly, Myology Institute, Paris, France) for immortalization. It could be shown that the immortalization resulted in a robust *in vitro* model for LGMD and other muscular dystrophies, which also could be implanted *in vivo* (Philippi et al., 2012; Mamachaoui et al., 2011).

3.2.3 Cell cultivation protocols

Cultivation conditions

All cells were cultivated in a CO_2-incubator (BBD 6220, Thermo Scientific) at 37 °C with 5 % CO_2 and 96 % relative humidity. As proliferation medium, Skeletal Muscle Cell Growth Medium (SMCGM) complemented with 10 % fetal bovine serum (FBS), 1.5 % GlutaMax and 40 µg/ml gentamycin was used for both, primary and immortalized human myoblast. Myoblasts where grown up to 60 % confluence for a maximum of 10 passages for primary skeletal muscle cells and 20 passages for immortalized human skeletal muscle cells.

Propagation

At 60 % confluence myoblasts were washed two times with PBS, 0.25 % trypsin was added and cell were detached for 3-5min at 37 °C. SMCGM was added in a ratio of 9:1 to stop trypsinization. The desired amount of cells was transferred to a new cell culture dish and cells could adapt for at least 24 hours. If a higher concentration of cell suspension was needed, a centrifugation step at 192 g for 5 minutes at 4 °C and subsequent resuspension in the desired volume was included.

Quantification

The amount of cells in suspension was determined using a counting chamber (Neubauer, Marienfeld-Superrior). 25 µl of cell suspension was applied to the chamber and cells in 9 squares (area of 9 mm^2) were quantified. The following formula was used to determine the total number of cells in suspension:

$$Cells\ per\ \text{µl}\ suspension = \frac{Number\ of\ cells}{Area\ [mm2] * Chamber\ depth\ [mm] * Dilution}$$

Preservation

For storage, adherent cells were detached by trypsinization and the cell number was determined as described before (see above). Cells were pelleted by centrifugation at 192 g for 5 minutes at 4 °C and resuspended in storage medium (SMGM supplemented with 20 % FBS and 10 % DMSO) to a concentration of 1x10^6 cells/ml. Aliquots were frozen on dry ice and stored for 1-3 days at -80 °C before transferring to liquid nitrogen storage.

Differentiation

Mononucleated myoblasts were grown to 80-90 % confluence and subsequently switched to differentiation medium (see Table 3-3). For primary human skeletal muscle cells, fusion from myoblasts to multinucleated myotubes typically occurred after 2-4 days. For immortalized human skeletal muscle cells a longer differentiating time of 4-8 days was needed. Cells were used for downstream applications when >60 % of the total myoblast population fused to myotubes.

3.3   Visualization methods

3.3.1 Immunofluorescence microscopy

To investigate the localization of proteins within a cell, specific antigens can be targeted with antibodies. The interaction of an antibody with the antigen of interest can be visualized by a secondary fluorophore-labeled antibody.

Cells were grown to 80-90 % confluence before fixation. All labeling steps were performed at room temperature and completed by three subsequent washes in PBS. First, differentiated myotubes were fixed in 3.7 % formaldehyde solution (FA) for 20 minutes. Samples could be stored in 1 % FA for several weeks at 4 °C if not used directly for immunolabeling. If labeling of intracellular antigens was desired, a permeabilization step with 0.2 % Triton X-100 was included. After blocking with 1 % bovine serum albumin (BSA), cells were incubated with a primary antibody in blocking solution under mild agitation (30 rpm) over night at 4 °C. For antigen-antibody detection, a secondary antibody directed against the species of the primary antibody was added for 30 minutes. To stain nuclei, incubation with Hoechst stain was done for 3 minutes. Labeled cells were washes with dH$_2$O and covered with an embedding solution. Samples could be stored at 4 °C for 1-2 weeks. Images were captured by a confocal fluorescent microscope (Zeiss LSM 700 confocal microscope) with a LCI Plan-NEOFLUAR 63x/1.3 glycerol immersion objective (Zeiss, Germany) using the Zeiss LSM ZEN 2011 software (black edition, 64 bit, version 7.0).

3.3.2 Transmission electron microscopy

All experiments were done either at the Electron Microscopy Core Facility of the Institute Jacques Monod (Paris, France) under supervision of Dr. Mabel San-Roman or at the Electron Microscopy Core Facility of the Max-Delbrück-Center for Molecular Medicine (Berlin, Germany) under guidance of Dr. Bettina Purfürst.

3.3.2.1 Characterization of morphology

Preparation of biological samples for electron microscopy allows investigation of the ultrastructure on nanoscale level. Therefore, samples were fixed with glutaraldehyde, contrasted with osmium tetroxide, gradually dehydrated with ethanol, and finally embedded within a resin. After polymerization of the embedded sample, ultrathin sections can be obtained and viewed with a TEM.

Depending on the samples size and composition, either a short or longer embedding protocol was used (see Table 3-11). The short protocol was applied to smaller samples

like vesicle preparations (see page 53), because of the good accessibility to fixatives and other embedding solutions. Bigger or more compact specimen like cell pellets were treated with longer incubation times (Table 3-11; long protocol). Briefly, biological specimens were washed two times with PBS and fixed with 2.5 % glutaraldehyde for 2 hours at room temperature. Samples could be stored for several weeks in the fixative at 4 °C. To enhance contrast of membranes, an incubation step of 1 hour with 1 % tannic acid was introduced. After three washes with cacodylate buffer, cells were postfixed with 1 % osmium tetroxide for 1 hour at room temperature. This postfixation step is needed to contrast membranes and further stabilize proteins. The specimen was washed two times with cacodylate buffer followed by a gradually dehydration of the sample. In successive incubation steps an increasing ethanol concentration from 30 % to ≥98 % was introduced to the specimen. If working with cell monolayers, an incubation step with another dehydrating agent, butyl-epoxypropyl ether (BEE), for 2 minutes was added. This compound enables to separate the cell monolayer attached to a thin plastic film from the cell culturing dish. Adherent cells therefore kept their position and orientation within the sample. The cell monolayer was pelleted by a mild centrifugation for 3 minutes at 192 *g*. The cell pellet was washed two times with propylenoxide (PO) as a transition solvent. To slowly infiltrate the sample with the epoxy resin (epon), a successive incubation with two times PO/epon 1:1 and two times PO/epon 1:2 was done. This was followed by incubation in epon overnight and three more changes of epon the following day. Samples were polymerized for 2-3 days at 60 °C. When the sample is hardened, it could be sectioned with using an ultra-microtome. Sections of 50-70 nm thickness were contrasted in a contrasting automat and then viewed under 80 keV with a TEM (Zeiss, EM 910). Pictures were taken with a CDD camera integrated with the iTEM software.

Table 3-11   Embedding protocol for adherent cultured cells

Experimental steps	Embedding protocol	
	Short	Long
Fixation	1 h at RT	2 h at RT
Wash step 1	3 x 5 min	2 x 30 min
Contrasting with tannic acid	1 h at RT	1 h at RT
Wash step 2	2 x 10 min	2 x 30 min
Postfixation with OsO_4	1 h at RT	2 h at RT
Wash step 3	2 x 10 min	2 x 30 min
Dehydration with EtOH	1 x 10 min EtOH 30 %,	1 x 30 min EtOH 30 %,
	1 x 10 min EtOH 50 %,	2 x 30 min EtOH 50 %,
	1 x 10 min EtOH 70 %,	2 x 30 min EtOH 70 %,
	1 x 10 min EtOH 90 %,	2 x 30 min EtOH 90 %,
	2 x 10 min EtOH abs	2 x 30 min EtOH abs
Treatment with BEE	-	3-5 min at RT
Washes with PO	1 x 10 min	2 x 30 min
Infiltration with PO/epon	2x 10 min PO/epon 1:1,	2x 30 min PO/epon 1:1,
	2 x 10 min PO/epon 1:2	2 x 30 min PO/epon 1:2
Infiltration with epon	1 x overnight,	1 x overnight,
	3 x 1 h	3 x 1 h

3.3.2.2   Quantification of endocytic structures at the plasma membrane

Differentiated myotubes derived from skeletal muscle of different LGMD patients were prepared for TEM as described above. Adherent myotubes were pelleted during the embedding procedure resulting in a random distribution of cells during sectioning. Ultrathin sections of 50-70 nm every 10 µm were obtained and subjected to TEM visualization. For every cell line, 10-13 myotubes of one embedding preparation were analyzed. Pictures at a magnification of 5,000 were acquired and analyzed with the iTEM software. The length of the plasma membrane and the amount of distinct structures were quantified. Plasma membrane structures were differentiated in caveolae in open state, clathrin-coated pits and membrane vesicles which were found in < 200 nm proximity to the plasma membrane.

Statistical analyses were done using R software version 3.1.0 (R Core Team (2014); http://www.R-project.org/) by Dr. Andreas Busjahn (Health TwiSt, Berlin, Germany). Raw data were described by median and the 25th/75th percentile. Data were illustrated as box plots of the median with an interquartile rage (IQR) of 1.5. As data were not normally distributed, they were log-transformed before analysis and a logarithmical data presentation was chosen. A one-way analysis of variance (ANOVA) was performed, treating all myotubes as independent replications. To compare the effect of different mutations on plasma membrane structures, post-hoc unpaired t-tests were performed. A significance level of 5 % was set, nominal *P*-values were reported.

3.3.2.3   Negative contrast

A quick way to investigate the ultrastructure of cellular organelles or other structures in suspension in TEM is the so called negative contrasting technique. Briefly, suspensions can directly be transferred to electron microscopy grids, contrasted by heavy metal salts as uranium or tungsten, and viewed with a TEM.

All incubations were done at room temperature, if not indicated differently. For washing steps grids were floated on drops of 200 µl and transferred with help of tweezers (Electron Microscopy Sciences). First, grids were incubated on drops of samples in suspension for 20 minutes. For negative contrast on cryosections, first three washes for 10 minutes with PBS were included to dilute the sucrose-methylcellulose-solution (pic-up solution). Grids were passed over drops with dH$_2$O 10 times for 2 minutes. Two different contrast methods were used; (a) uranyl acetate / methyl cellulose (UA-MC) or (b) tungstosilicic acid / polyvinyl alcohol (Si-PVA). For the UA-MC contrast method, grids were passed quickly over two drops of UA-MC solution and incubated on a third drop for 10 minutes on ice. For the Si-W-PVA contrast, grids were quickly transferred over two drops of Si-W-PVA and

incubated on a third drop for 10 minutes at room temperature. To adsorb the solution, the grids were tilted to an angle of 45-60° and steadily rolled over a filter paper (Whatman® filter paper, grade 50, GE Healthcare) until a thin film of contrast solution was left. Grids were dried for 10-20 minutes samples were examined with a TEM integrated within the iTEM software (Olympus).

3.3.2.4   Immunolabeling after Tokuyasu

The Tokuyasu technique allows labeling of specific antigens on ultrathin cryosections. The samples therefore had to be fixed, embedded in gelatin, cryoprotected with sucrose and sectioned with an ultra-cryomicrotome. Accessible antigens on ultrathin cryosections then were labeled with a primary antibody and visualized by a secondary gold-conjugated antibody or protein-A gold.

First, a double-strength fixative was added in a 1:1 ratio to the cell culture medium for 10 minutes. Solution was changed to single-strength fixative and incubated for 2 hours at room temperature. As fixative either 4% formaldehyde or 2% formaldehyde / 0.2% glutaraldehyde was used. The samples were rinsed three times for 5 minutes with PBS. To scrape adherent cells, 1% gelatin was added and a rubber cell scraper was used to carefully detach the cells. The material was transferred to an Eppendorf tube and centrifuged for 5 minutes at 5,000 g. The pellet was resuspended at 37°C with 12% gelatin for 5 minutes. The cells were pelleted by centrifugation and placed on ice for 30 minutes to solidify the gelatin. The embedded cell pellet was sectioned with a razor blade into small cubes of 1 mm^3 size and infiltrated with 2.3 M sucrose in PBS at 4°C on a rotating device overnight. Sucrose protected samples were positioned on a specimen holder for electron microscopy and frozen in liquid nitrogen. In a cryo-ultramicrotome ultrathin sections of 50-70 nm were produced with a cryo diamond knife (Diatome). A drop of sucrose/methyl cellulose mixture (pic-up solution) in a wire loop was used to pick-up the cryosections. The drop was placed on an electron microscopy grid coated with formvar and sections could be stored at 4°C for several weeks. Preservation of the sample and quality of sections could quickly be checked under the TEM after by applying a negative contrast (see 3.3.2.3).

Grids with cryo-sections were placed on plates with 2% gelatin under a heating lamp until the gelatin became fluid. In a humid chamber, the grids were further incubated at 37°C on gelatin to remove the pic-up solution. All incubation steps were done at room temperature if not indicated differently. For washing steps, grids were floated on drops of 200 µl and for antibody incubation step, on drops of 5 µl, respectively. After incubation on gelatin, free aldehyde groups were quenched with 0.1% glycine five times for 2 minutes. Blocking was achieved by incubation with 1% BSA for 5 minutes. Grids were placed on drops of

blocking solution containing the first antibody for 30-60 minutes in a humid chamber. For antibodies and dilutions see Table 3-8. Changes of washing buffer five times for 2 minutes were followed by incubation on Protein-A gold or a secondary gold-labeled antibody in blocking solution for 20 minutes. Grids were floated two times for 2 minutes on washing buffer and five times for 2 minutes on PBS. Samples were fixed with 1 % glutaraldehyde in PBS for 5 minutes and washed two times for 5 minutes with PBS. Before contrasting with UA-MC or Si-W-PVA grids were floated on dH_2O six times for 2 minutes. Contrast procedure was carried out like explained in 3.3.2.3.

3.3.2.5 Pre-embedding labeling

Immunopurified vesicles linked to magnetic beads were embedded in epon and processed for ultrathin sectioning as mention in 3.3.2.1. To detect antigens on the surface of attached vesicles, a pre-embedding immunolabeling was be performed. For solutions and antibody concentrations see Table 3-8. After vesicle immunopurification (see 3.4.4) the samples were washed in PBS and fixed in 0.1 M phosphate buffer with 3 % paraformaldehyde for 1 hour at room temperature. After two washes with PBS, blocking with 4 % BSA in PBS was done for 30 minutes followed by three washes with washing buffer. The sample was incubated with the secondary gold-conjugated antibody for 20 minutes. After three final washes with PBS, samples were fixed with 2.5 % glutaraldehyde in 0.1 M cacodylate buffer for 1 hour. Samples could be stored at 4 °C in the fixative or directly processed further for epon embedding.

3.3.3 Histological staining procedures

For histological analysis of skeletal muscle tissue, biopsies were embedded in gum tragacanth and mounted on cork plates. Biopsies were first frozen in cooled isopentane and then quickly transferred to liquid nitrogen, where samples could be stored for several years. Skeletal muscle tissue was sectioned to 6 or 10 µm thickness with a cryo microtome (Cryostat CM3050S, Leica). Sectioning and histological stainings were done by Kornelia Gräning in the diagnostic facility of our laboratory. Images were captured by a Zeiss microscope (Zeiss LSM 700 confocal microscope) and processed by ImageJ software.

3.3.3.1 Gomori-Trichrome

Gomori's one-step trichrome staining includes a staining for plasma with chromotrope 2R and for connective tissue with fast green FCF in phosphotungstic acid solution with glacial acetic acid (Engel & Cunningham, 1963). Muscle fibers appear greenish blue and collagen in light green. Nuclei are stained in red and intermyofibrillar network in dark red. Sections were stained in Gill's Hematoxylin solution (Merck, modified according to GILL II) for 5 minutes and rinsed under running dH$_2$O. Staining with Gomori's trichrome (LG

solution, Sigma) was done for 10 minutes and differentiated in 0.2 % acetic acid until clear. The sections were dehydrated in 95 % and 100 % ethanol, cleared in xylene, and mounted with Vitro-Clud (Langenbrinck, Germany).

3.3.3.2   Congo red

The alkaline method of congo red staining was used to detect amyloid deposits. Sections were stained for 30 seconds with filtered Modified Mayers's Hematoxylin solution (Merck) and rinsed with dH_2O until clear. Incubation in 0.01 % sodium hydroxide in saturated sodium chloride solution was done for 10 minutes at 37 °C. Sections were dehydrated with three changes of ethanol and cleared in xylene. Staining with Congo Red Solution (AppliChem) with 0.01 % sodium hydroxide was done for 20 minutes at room temperature. Sections were dehydrate with three changes of ethanol and cleared in xylene before mounting in Vitro-Clud.

3.3.3.3   Immunohistochemistry

Immunohistochemical staining was performed on acetone-fixed frozen sections of skeletal muscle. Before immunostaining for dysferlin, an antigen retrieval step was applied by incubating in 0.01 M citrate solution at pH 6 for 5 minutes at 37 °C. Dysferlin was detected using the NCL-Hamlet antibody (Novocastra) and developed with peroxidase donkey anti–mouse antibody plus diaminobenzidine (Sigma). CD4 and CD8 were detected using secondary fluorophore-linked antibodies (Alexa 488 / Alexa 568, Invitrogen). Briefly, sections were fixed in 100 % acetone for 5 minutes at -20 °C and blocked with 1 % BSA. Incubation with primary antibody was done for 2 hours at room temperature. Sections were washed three times with PBS and incubated with secondary antibody for 1 hour at room temperature. Sections were mounted in Vitro-Clud.

3.4   Biochemical methods

3.4.1 Whole cell lysis

Samples were kept at 4 °C or on ice for the whole procedure. Myoblasts or myotubes were washed two times with cold PBS. Lysis buffer complemented with protease inhibitors (1x Roche Complete, 1 mM PMSF) was added, cells were collected with a cell scraper and incubated for 30 minutes. After centrifugation at 16,100 *g* for 15 minutes, the supernatant was transferred to a new Eppendorf tube. Total protein concentration of the cell lysate was quantified using the Pierce™ BCA Protein Assay Kit (Thermo Scientific).

3.4.2 Determination of protein concentration

The bicinchononic acid assay (BCA) is a biochemical assay, which translates protein concentration in a given solution by a biuret reaction into a colorimetric signal. A series of dilutions of BSA protein concentration was measured in parallel to samples of unknown protein concentration. The sample concentration was determined based on the BSA standard curve. For samples within the protein range of 20-2,000 µg/ml, the microplate procedure was used as described by the manufacturer's manual. 25 µl sample of unknown protein concentration and the standard samples were mixed with 200 µl of BCA working solution and incubated for 30 minutes at 37 °C in a heating chamber. For protein concentrations within the range of 5-250 µg/ml, the more sensitive procedure with incubation for 30 minutes under agitation at 60 °C was chosen. The standard curve was calculated by plotting the average blank-corrected 562 nm measurement for each BSA standard sample against its concentration in µg/ml.

3.4.3 Subcellular fractionation

3.4.3.1 Preparation of detergent-resistant membranes

The preparation of cholesterol-rich <u>detergent-resistant</u> <u>m</u>embranes (DRMs) can be used to investigate the biochemical distribution of proteins within the lipid raft (LR) compartment. This membrane compartment is characterized by its specific protein and lipid composition, which makes it more resistant to treatment with a detergent like Triton X-100. Subsequently, these DRMs can be isolated by flotation on a sucrose step gradient after equilibrium centrifugation. A subgroup of DRMs linked to the cytoskeleton was isolated from the actin-cytoskeleton by adding a low speed centrifugation step and treatment of the cytoskeleton-containing pellet with potassium iodide (KI) (see Figure 3.1).

Primary or immortalized human myoblasts were differentiated to multinucleated myotubes for 3-6 days. First, adherent cells were washed two times with PBS at 37 °C and then transferred to ice. All steps were performed on ice, and an anti-proteases cocktail was added to all solutions if not indicated differently. Cells were lysed by scraping in ice cold MBS buffer. The detergent Triton X-100 was added to a final concentration of 0.5 %, 1 % or 2 % in a protein/detergent ratio of approximately 5/1 (wt/wt). The lysate was homogenized by 20 strokes with a glass homogenizer and incubated for 15 minutes on ice. The lysate was adjusted to 40 % sucrose with 80 % sucrose-MBS stock solution. Lysate in 40 % sucrose solution was transferred to Beckmann centrifuge tubes and successively overlaid with 30 % and with 5 % sucrose. DRMs were isolated by flotation in a sucrose gradient during ultracentrifugation at 200.000 g in a SW41 Ti rotor (Beckmann) for 18 hours at 4 °C without brake. After ultracentrifugation, 1 ml fractions were collected

from the gradient from top to bottom designated to fractions 1 to 12. DRM distribution within the sucrose gradient and protein content of the sucrose fraction was determined by western blot analysis.

3.4.3.2 Preparation of detergent-resistant membranes linked to the actin-skeleton

A raft subtype of cytoskeleton-linked DRMs was isolated from the actin-cytoskeleton (protocol adapted from (Bodin et al., 2005; Cartaud et al., 2011). This was done by treatment of the detergent-insoluble cytoskeleton pellet with potassium iodide (KI) to depolymerize f-actin before equilibrium centrifugation (Figure 3.1). Cells were washed two times with 0.1 M Tris buffer (pH 7.4) and then lysed by adding ice-cold CSK buffer. Cells were collected, supplemented with 0.1 % Triton X-100 (protein/detergent ratio of 5/1 (wt/wt)) and homogenized by 20 strokes with a glass homogenizer. After an incubation of 10 minutes, the lysate was centrifuged at 16,100 g for 15 minutes to collect the detergent-insoluble cytoskeleton-containing pellet. The pellet was resuspended in CSK buffer without detergent, homogenized by three strokes with a glass homogenizer and pelleted at 16,100 g for 15 minutes at 4 °C. To disassemble the cytoskeleton component f-actin, the pellet was resuspended in 0.6 M KI buffer and incubated for 30 minutes on a rotating device. DNA was destroyed by five passages through 18 G and 21 G needles successively. After a short centrifugation at 1000 g, the supernatant was adjusted to 40 % sucrose. The sucrose step gradient was prepared and DRMs were isolated as described before (see above). A depletion of cholesterol was performed by adding 10 mM methyl-β-cyclodextrin (mβCD) to the culture medium for 30 min at 37 °C before harvesting the cells by scraping.
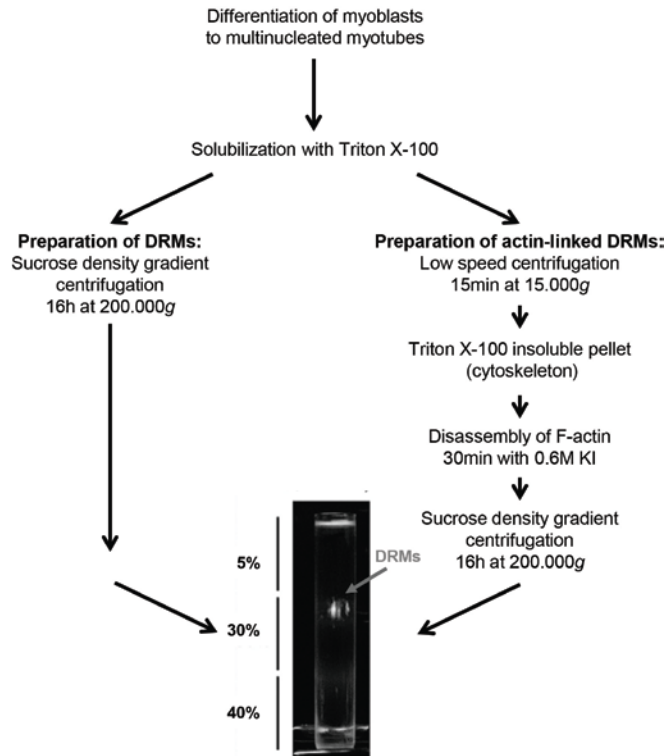
Figure 3.1 Overview on protocols for preparation of detergent-resistant membranes (DRM)

Myoblasts were cultured, differentiated and either total DRMs or a subclass of DRMs linked to the actin-cytoskeleton were purified. Briefly, myotubes were harvested by scraping in lysis buffer containing 0.1-2 % of the detergent Triton X-100 and DRMs were isolated by equilibrium centrifugation on a sucrose gradient. DRMs typically float at the 5 %/30 % sucrose interface and were detected by their turbid appearance. For isolation of DRMs linked to the actin-cytoskeleton, the detergent-insoluble cytoskeleton pellet was subjected to treatment with potassium iodide (KI) to disassemble F-actin before equilibrium sucrose density centrifugation. (Scheme has been modified from Cartaud et al. (2011))

3.4.3.3 Preparation of vesicular fraction by equilibrium centrifugation

Subcellular fractionation from total cell homogenate was performed to obtain a suitable input for the vesicle purification described on page 58. Purification of vesicular or microsomal fractions was achieved either through equilibrium centrifugation on a 0.2-1.6 M sucrose step gradient or through differential ultracentrifugation. Cell lysis was done by freezing cells at -80 °C before harvesting through scraping, followed by homogenization using a glass homogenizer. To keep intracellular membranes intact, MBS without detergent was used as lysis buffer.

Immortalized human myoblasts were cultured and differentiated as described before. Myotubes were washed with PBS at 37 °C, transferred to ice and washed with ice-cold MBS buffer. The medium was fully discarded and cells were frozen at -80 °C. All following steps were performed on ice and solutions were cooled to 4 °C. Before lysis, cells were slowly thawed on ice, MBS supplemented with protease inhibitors (1x Roche Complete, 1 mM PMSF) was added and cells were harvested by scrapping. Cells were destroyed by

20 strokes with a glass homogenizer and the lysate was centrifuged at 1,000 g for 5 minutes to discard cell debris and nuclei. The supernatant was adjusted to 1.6 M sucrose. The sample was transferred to an ultracentrifugation tube and overlaid with a step sucrose gradient of seven fractions ranging from 1.4 M to 0.2 M sucrose. An ultracentrifugation until equilibrium was done for 18 hours at 270,000 g. Subsequent fractions of 1 ml were taken from top to bottom. Gradient fractions were either directly used for immunopurification of vesicles or further processed for western blot analysis. Therefore proteins were precipitated with TCA (see page 56). Samples were resuspended in 1x SDS loading buffer and subjected to SDS-PAGE (see 3.4.5).

3.4.3.4   Preparation of microsomal fraction by differential ultracentrifugation

Cell lysate was prepared as described above (see 3.4.3.3). The microsomal fraction was purified by consecutive differential centrifugation at 1000 g, 10,000 g and 30,000 g.

After mechanical lysis with a glass homogenizer, the samples were adjusted with lysis buffer to a volume of 10 ml and centrifuged at 1,000 g for 5 minutes to discard cell debris and nuclei. For separation of bigger membranous structures like mitochondria and the golgi apparatus, the supernatant was subjected to a centrifugation at 10,000 g for 30 minutes. Filtration of the supernatant through a 0.22 µm polyethersulfone (PES) membrane filter was done to exclude other bigger cellular components according to their size. A final centrifugation step at 30,000 g for 90 minutes was applied to enrich the vesicular structures. To further reduce contaminations, the pellet was washed with isosmotic sample buffer. The microsomal fraction was carefully resuspended in PBS with anti-proteases and further processed for vesicle purification or TEM analysis.

3.4.4 Precipitation of proteins

To reduce sample volume, and thereby concentrating the protein amount within a solution, proteins could be precipitated with the use of trichloroacetic acid (TCA). The sample was adjusted to 10 % TCA and incubated for 1 hour at room temperature. After a centrifugation at 16.100 g at 4 °C, the supernatant was discarded and the protein pellet was washed with ice-cold 80 % acetone. The washing solution was discarded and the pellet was dried at room temperature for 1 hour. The pellet was resuspended directly in 1x SDS loading buffer and processed further for SDS-Page. The pH was adjusted by adding 1 M Tris if necessary.

3.4.5 Western blot

Western blotting is a technique to analyse the protein composition of a given sample. First, proteins are separated in a denatured state during sodium docedyl sulphate-

polyacrylamide g̲el e̲lectrophoresis (SDS-PAGE) proportional to their size and then transferred to a membrane. With antibodies targeting a specific antigen, proteins on the membrane can be detected.

3.4.5.1 SDS-PAGE

For each sample, 20 µg protein in SDS-loading buffer (1x) in a total volume of 20 µl was used. To completely denature proteins, samples were heated to 95 °C for 5 minutes with mixing at 300 rpm in presence of the reducing agent dithiothreitol (DTT). SDS-PAGE was run under denaturing conditions in running buffer by use of ready-to-use gradient polyacrylamide gel as described by the manufacturer's manual (Invitrogen by Life Technologies). 20 µl sample and 4 µl of a molecular weight size marker per lane were loaded on the gel. Proteins were separated by applying 100 V for 10 minutes, followed by 190 V for 50 minutes. Proteins were transferred to a nitrocellulose membrane under semi-dry conditions using a Trans-Blot system for 50 minutes at 18 V.

3.4.5.2 Detection of proteins

Transfer efficiency was monitored by coomassie staining of the protein gel and ponceau S staining of the membrane. The staining and subsequent immunolabeling procedures were done at room temperature and under agitation at 30 rpm. Coomassie is an anionic stain, which dyes proteins in an unspecific way. The staining was done by incubation of the gel in coomassie staining solution for 30 minutes. After washing in dH$_2$O for 24 hours, visualization of the staining was done by scanning with the Odyssey device. The reversible ponceau S staining was done by incubation in ponceau S solution for 3 minutes followed by washing with dH$_2$O for 5 minutes. Documentation was done with a conventional scanner (Aficcio, RICOH). If using secondary antibodies from the Licor detection system (IR dyes, Rockland), ponceau S staining was omitted due to strong background signal.

To prevent non-specific binding, nitrocellulose membranes were incubated in blocking solution containing 2 % BSA and 4 % milk powder for 60 minutes at room temperature. The first antibody diluted in blocking solution was applied overnight at 4 °C (for dilutions see Table 3-4). After three washes with TBS-T for 5 minutes, the membrane was incubated with the secondary antibody diluted in TBS-T for 30 minutes at room temperature. Depending on the antibody sensitivity, either secondary antibodies labelled with fluorescent infrared dyes (IR-dyes) or horseradish peroxidase (HRP)-linked antibodies were used. For proteins labelled with IR-dyes, membranes were washed two times in washing buffer and one time in dH$_2$O before scanning with the Odyssey device. Depending on the dye, the fluorescent signal was detected at 700 or 800 nm. For proteins

labelled with HRP-linked antibodies, the enhanced chemiluminescence (ECL) reaction was applied and the signal was detected with a CDD camera integrated in a Chemiluminescence Detection System (Peqlab). Therefore, the membrane was incubated in substrate solution for 5 minutes and the HRP-reaction signal was visualized within a time range of 5 seconds to 5 minutes.

After chemiluminescence antigen detection, antibodies could be stripped from membranes with help of a stripping buffer. Stripping was done for 15 minutes at room temperature under strong agitation. Washing with dH$_2$O was done for four times for 5 minutes in a volume of 100 ml per membrane. Full detachment of first and secondary antibodies was verified before applying subsequent antibody probes. Stripping can decrease binding of rather unstable antigens to the membrane. Membranes were only stripped when highly abundant proteins like tubulin or glyceraldehyde 3-phosphate dehydrogenase (GAPDH) were detected.

3.4.6 Immunopurification of dysferlin-containing vesicles

The immunopurification (IP) of dysferlin-containing vesicles was done by incubation of a vesicular fraction with an anti-dysferlin antibody linked to magnetic Protein A-coated beads. To target dysferlin, a rabbit monoclonal immunoglobulin 1 (IgG1) antibody (rAb) (JAI-1-49-3, Abcam) and an anti-dysferlin llama-derived heavy-chain antibody fragment (VHH) (Dysf-F4), kindly provided by Prof. Dr. Silvère van der Maarel (Leiden University Medical Center, The Netherlands), were used for IP. Both antibodies were linked to magnetic beads because of their strong affinity to Protein A. The VHH "Dysf F4" against a synthetic human peptide spanning over exon 1-7 (position 2-245 aa) has already been used in IP experiments of the dysferlin interacting complex from myoblasts, myotubes and skeletal muscle tissue (Morrée et al., 2010). The anti-dysferlin rAb also targets exon 5 (position 123-142 aa) at the N-terminus of the dysferlin protein. The putative transmembrane region of dysferlin is thought to be localized at the C-terminus. It was very probable that the N-terminus of the protein is accessible during IP of intact vesicles and therefore could be targeted by both antibodies.

Dynabeads Protein A were treated as recommended by the manufacturer (Invitrogen, Life Technologies). For washing steps, magnetic beads were handled by applying a magnetic field (DynaMag^{TM}-Spin, Life Technologies). To prevent precipitates, all antibodies were centrifuged for 10 minutes at 16,000 g before use. Beads were washed with PBS supplemented with 0.1 % Tween 20 for 2 minutes. The supernatant was removed and beads were incubated with antibodies in PBS-0.1 % Tween 20 under rotation at 30 rpm for 30 minutes at room temperature. Optimal binding was achieved using 5 µg antibody and

1.5 mg Protein A beads in a volume of 200 μl. The excess of antibody was removed and beads were washed with PBS-0.1 % Tween 20 for 5 minutes. Samples were transferred to tubes with rounded bottom to assure evenly distribution of the antibody-beads and the microsomal fraction during incubation. 20 μg of input was added to 1.5 mg Protein A-beads and incubated with rotation for 2 hours at 4 °C. The non-bound fraction was collected, proteins were precipitated, and processed for western blotting as control. The bound immunopurified fraction was washed with PBS three times for 2 minutes and transferred to a new tube to prevent processing of unspecific bound material to the tube wall. The washing buffer was discarded and the bead-vesicle complex was either fixed for TEM or resuspended in 1x SDS loading buffer for western blot and proteome analysis.

3.5 Functional assays

3.5.1 Membrane wounding assay

To investigate the plasma membrane repair process at the sarcolemma of differentiated human myotubes a laser-based injury assay was used. As readout, the time-dependent influx of a membrane integrating fluorescent dye into the cell was monitored.

Myoblast were seeded on chambered coverslips and differentiated to myotubes as described before (see 3.2.3). Before starting with the laser wounding experiment, cells were washed with tyrode solution. Then, the tyrode solution was complemented with 2.5 μM FM 1-43 green fluorescent dye and 2.5 mM CaCl^2. The plasma membrane was injured by irradiating of an area of 2.5x2.5 μm at 100 % maximum power (10 mW diode laser, 488nm laser line). Laser wounding was done for 38 seconds and consecutively 16 images in an interval of 20 seconds were taken. Experiments were done using a Zeiss LSM 700 confocal microscope with a LCI Plan-NEOFLUAR 63x/ 1.3 glycerol immersion objective (Zeiss, Germany). Pictures documenting a time course of 300 seconds were processed with Zeiss LSM Image Browser software (Zeiss ZEN 2011 software, black edition, 64 bit, version 7.0). Fluorescence intensity changes at the site of injury were measured using ImageJ.

3.6 Proteomic analysis

3.6.1 Samples

IP samples from control myotubes derived from normal human skeletal muscle were compared to IP samples from dysferlin-deficient myotubes derived from LGMD 2B patient skeletal muscle. As negative control Dynabeads Protein A were incubated with the

microsomal fraction of both cell lines. Immortalized human myotubes were lysed and subcellular fractionation was done as described in 3.4.3.4. The microsomal fraction was used as input for vesicle IP with magnetic Dynabeads Protein A (see page 58). The bound IP fraction was eluted in 1x SDS loading buffer, proteins were denatured for 5 minutes at 95 °C and stored at -20°C until use. Further processing of samples and liquid chromatography–mass spectrometry (LC-MS) measurements were done at the Integrative Proteomic and Metabolomics Platform by Tobias Opialla in cooperation with Dr. Stefan Kempa at the Max-Delbrück-Center for Molecular Medicine (Berlin, Germany).

3.6.2 SDS-PAGE & protein digestion

Samples were separated by SDS-PAGE for 10 minutes at 100 V under denaturing conditions. Gel slices containing the proteins of interest were dissected, washed in 50 mM ammonium bicarbonate (ABC) and acetonitrile (ACN) solution mixed in a ratio of 1:1, and dehydrated in ACN for 10 minutes. The gel pieces were rehydrated and proteins were reduced by addition of dithiothreitol (DTT) for 60 minutes at 56 °C. After a second dehydration round with ACN, free sulphydryl groups were blocked with 55 mM iodacetamide for 30 minutes in the dark. Gel slices were dehydrated for a third time and digested in 12.5 ng/µL trypsine in ABC solution over night at 37 °C under agitation. Acidification with trifluoroacetic acid (TFA) stopped further digestion. Supernatant containing digested proteins were dried in a SpeedVac until 10-20 % of the original volume was reached.

Immunoglobulin G (IgG) and VHH used for IP were not covalently bound to magnetic beads, and therefore eluted with purified proteins during sample preparation for SDS-PAGE. To prevent disturbances by high amounts of IgG peptides during LC-MS analysis, each gel lane was dissected in three equally sized slices and digested separately. IgGs separated during SDS-PAGE under denaturating conditions to 25 and 50 kDa monomers and VHH to 15 kDa, respectively. For LS-MC, the two digested fractions without IgG / VHH were pooled, whereas the IgG/VHH containing fraction was measured separately. For analysis, two technical replicates were measured. Data of technical replicates per sample and condition were pooled for further data processing and analysis.

3.6.3 Nano liquid chromatography-mass spectrometry analysis

5 µl of eluted peptides were injected in duplicate on a nanoflow ultra performance liquid chromatography (UPLC) system (Eksigent), using a 240 minutes gradient ranging from 5 % to 45 % of solvent B in solvent A (80 % acetonitrile, 0.1 % formic acid; solvent A= 5 % acetonitrile, 0.1 % formic acid) with a flow rate of 200 nL/min. For the chromatographic separation, 30 cm long capillary (75 µm inner diameter, 1.8 µm particle diameter) was

packed with 3 μm C_{18} beads (ReproSil-Pur C_{18}-AQ, Dr. Maisch). On one end of the capillary a nanospray tip was generated using a laser puller, allowing fretless packing. The nanospray source was operated with a spray voltage of 1.9 kV and an ion transfer tube temperature of 260 °C.

Data were acquired in data dependent mode, with one survey MS scan in the linear trap quadrupole (LTQ) Orbitrap mass analyzer (60000 resolution at 400 m\z) followed by up to 20 MS\MS scans in the ion trap on the most intense ions. Once selected for fragmentation, ions were excluded from further selection for 30 seconds, in order to increase new sequencing events.

3.6.4 Data analysis

Raw mass spectrometric data were analyzed using the MaxQuant proteomics pipeline version 1.4.1.3 and the built in Andromeda search engine (Cox J; Mann M, 2008; Cox J et al., 2011), using all reviewed protein sequences of Homo sapiens included in the Uniprot-database from 04.05.2014. Carbamidomethylation of cysteines was chosen as fixed modification, whereas oxidation of methionine and acetylation of N-terminus were chosen as variable modifications. Two missed cleavage sites were allowed and peptide tolerance was set to 7 ppm (part per million). The search engine peptide assignments were filtered at 1% false discovery rate (FDR) at both the peptide and protein level. The 'match between runs' feature was not enabled, 'second peptide' feature was enabled, while other parameters were left as default.

Max Quant output was analyzed using Perseus, a software for MaxQuant downstream bioinformatical analysis (version 1.4.1.3). Sequences from rabbit-derived IgGs and VHHs were excluded for further analysis, because of their high relative abundance. Reverse and contaminants according to MaxQuant were removed from the raw output from MaxQuant except for the following proteins: actin, collagen α-1 (III) chain, dermokine, gelsolin, profiling-1, serum albumin, thrombospondin-1, tropomyosin β-chain, and tubulin α-1B / α-1C chain. Proteins identified in only one sample were rejected from analysis. Data were displayed as raw intensities. Data plots and clustering was done using the Perseus visualization tools. Gene ontology (GO) analysis was performed with GOrilla (Eden, Navon, Steinfeld, Lipson, & Yakhini, 2009). Ingenuity pathway analysis (IPA, content version 18841524, Qiagen) allowed predictions on cellular compartments, protein function and pathways of MS data.

4 Results

4.1 Investigations on myotubes derived from patients with mutations in *ANO5*

Anoctamin-5 (ano-5) is a putative transmembrane protein whose association to the plasma membrane and cellular function is not known so far. However, it is suggested by protein domain similarity to localize at membranes and act as calcium-activated chloride channel (CaCC). Since some publications suggest a role of caveolae in calcium homeostasis, and dysferlinopathy as well as caveolinopathy patients share some clinical findings with patients with mutations in *ANO5*, we hypothesize that these three proteins might somehow be linked.

4.1.1 Clinical presentation and histological findings

Two patients with limb-girdle muscular dystrophy (LGMD) 2L, recruited from our outpatient clinic, could be included in this study. Patient ANO5-1 presented with progressive muscle weakness in calve muscles in adulthood. Biopsy of the *vastus lateralis* muscle revealed dystrophic alterations such as variation in fiber size with a diameter ranging from 10 to 80 µm, centralized nuclei, and increased amounts of connective tissue (see Figure 4.1 A). NADH-dehydrogenase reaction revealed presence of atrophic fibers (data not shown). In rare events, also necrotic, regenerating, and split-fibers could be detected. Sequencing of the *ANO5* gene revealed the founder mutation c.191dupA in a homozygous state, resulting in the protein mutation p.Asn64Lys fsX15 introducing a premature stop codon in exon 5. Patient ANO5-2 presented with asymmetric muscle weakness and atrophy in thighs and shoulders. Cross-sections of skeletal muscle displayed variances in fiber diameter ranging from 5 to 100 µm (see Figure 4.1 B). Additional dystrophic features like necrotic and split, as well as whirled and atrophic fibers could be observed. Connective tissue was significantly increased. Congo red stain visualized under rhodamine optics revealed amyloid deposits around blood vessels and less frequent under the sarcolemma. CD8-positive and less common CD4-positive T-lymphocytes showed an endo- and perimysial pattern. The ATPase fiber types stain revealed normal fiber type distribution within the muscle of both patients. Glycogen and lipid content was also normal (data not shown). Sequencing of the *ANO5* gene for patient ANO5-2 revealed two mutations in a compound heterozygous state: the founder mutation c.191dupA and the mutation c.2521-1delG in intron 21 introducing a putative splice site.

Results
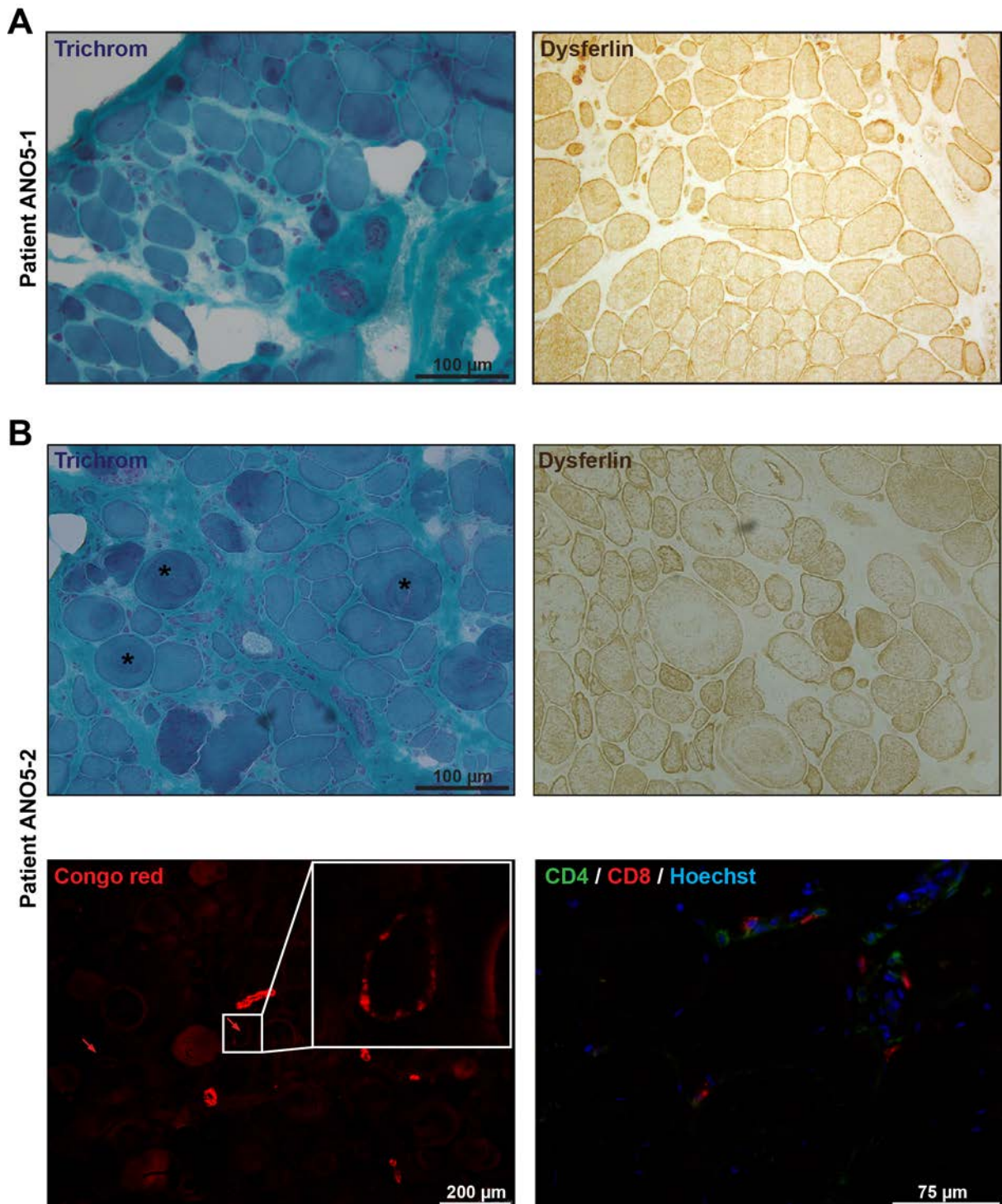
Figure 4.1 Histological characterization of LGMD 2L skeletal muscle

Biopsies from human *vastus lateralis muscle* of LGMD 2L patients ANO5-1 (c.191dupA homozygous) (A) and ANO5-2 (c.191dupA compound heterozygous / c.2521-1delG compound heterozygous) (B) have been stained for trichrome revealing dystrophic alterations as centralized nuclei, atrophy, variances in fiber diameters, and increase of connective tissue. Note that patient ANO5-2 harbors whirled fibers (asterisks). Dysferlin staining showed no abnormal distribution. Congo red stain visualized under rhodamine optics displayed amyloid deposits around blood vessels and muscle fibers (arrows). Additionally, CD4 and CD8-positive cells could be detected in patient ANO5-2. If not indicated differently, scale bars were identical in all pictures.

4.1.2 Investigations on LGMD 2L skeletal muscle cells *in vitro*

As only few facts about ano-5 function at the plasma membrane and its role in muscular dystrophies are known, primary skeletal muscle cells from patient ANO5-1 were investigated in more detail (see Figure 4.2). For Patient ANO5-2, we experienced difficulties in culturing isolated muscle cells. The myoblast population showed high numbers of contaminating fibroblasts, and therefore was excluded from immunolabeling experiments. Labeling of the myogenic differentiation markers myosin heavy chain (MHC), desmin and Bin-1 showed no alterations in differentiation properties (Figure 4.2 A). After 5 days of differentiation, LGMD 2L myotubes displayed multiple nuclei and revealed a typical presarcomeric MHC-positive pattern. Labeling of cell-cell adhesion proteins, CD56 (synonym for neural cell adhesion molecule, NCAM) and fibronectin, in non-permeabilized cells was normal. In summary, no impairment of myoblast fusion could be observed.

Localization of dysferlin and caveolin-3 (cav-3) was also not altered in LGMD 2L myotubes (see Figure 4.2 B). Labeling of these proteins showed an increase with differentiation progress as observed in control myotubes derived from unaffected skeletal muscle.
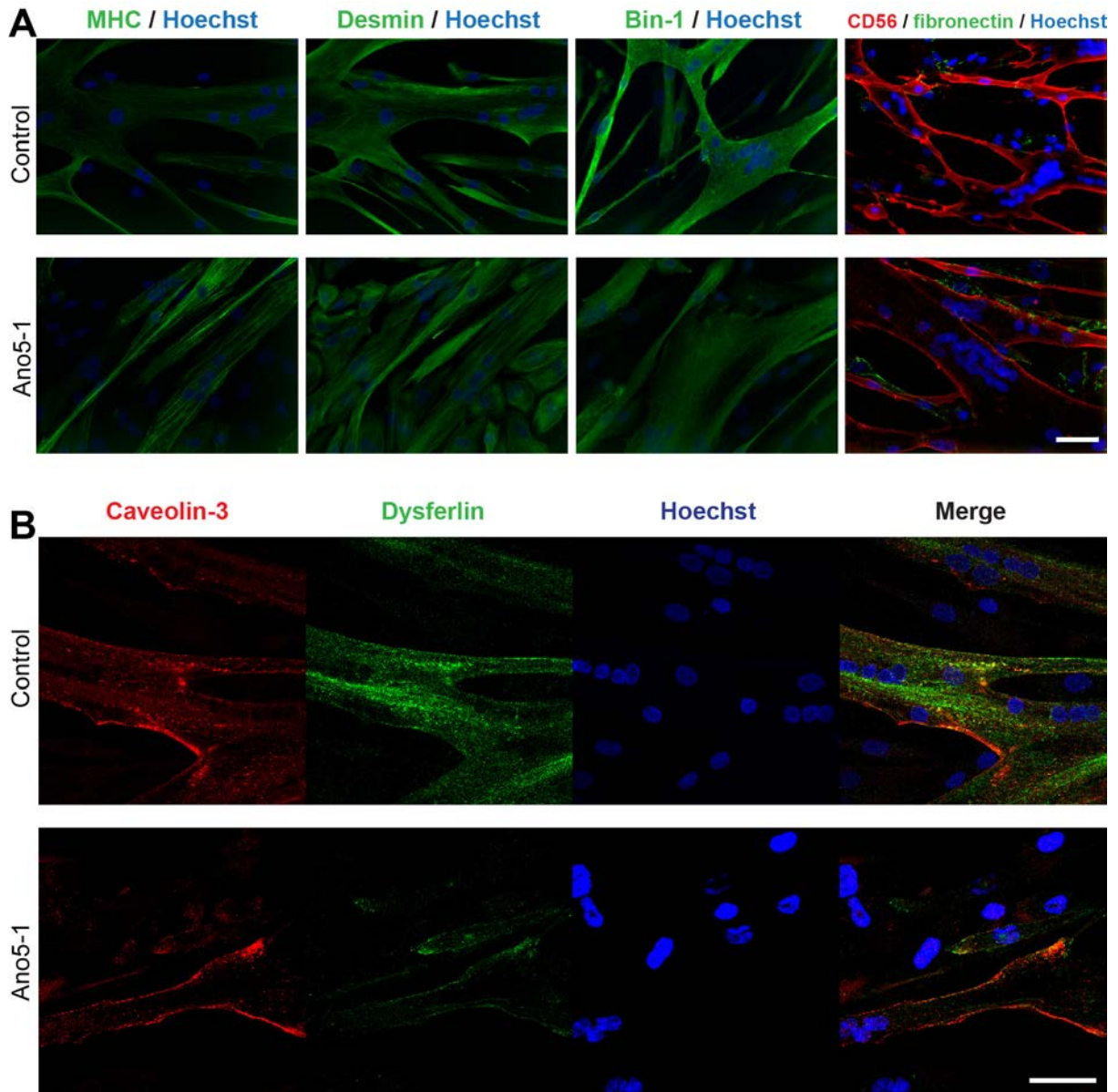
Figure 4.2 Localization of differentiation markers and proteins involved in LGMD

Labelling of the myogenic markers MHC, desmin and Bin-1, and the cell-cell adhesion proteins CD56 and fibronectin, showed no abnormal localization in myotubes derived from LGMD 2L patients in comparison to control cells (A). In Figure B the subcellular localization for dysferlin and cav-3 is shown. Original magnification has been 40x for (A) and 63x for (B). Scale bars were identical in all pictures and represent 50 μm.

4.1.3 Investigation of membrane repair in LGMD 2L myotubes

A laser-induced wounding assay was used to analyze plasma membrane resealing properties in myotubes from patients harboring mutations in *ANO5*. Primary control and LGMD 2L patient cell lines were subjected to laser wounding (see Figure 4.3). The membrane probe FM1-43 was used to track plasma membrane repair, since the dye cannot pass intact plasma membrane structures. After injury, plasma membrane resealed within 60 seconds in control myotubes with low amounts of FM1-43 dye entering the cell (see Figure 4.3 A). Membrane resealing in myotubes involves intracellular rearrangements of actin and the formation of a repair dome at the site of injury (Marg et al., 2012). In dysferlin-deficient myotubes the membrane repair process is disturbed. Thus, FM1-43 dye entry cannot be prevented or membrane resealing is extensively delayed (Philippi et al., 2012). However, wounding of Ano5-1 and Ano5-2 myotubes did show no defect in membrane resealing (see Figure 4.3 C).

Results
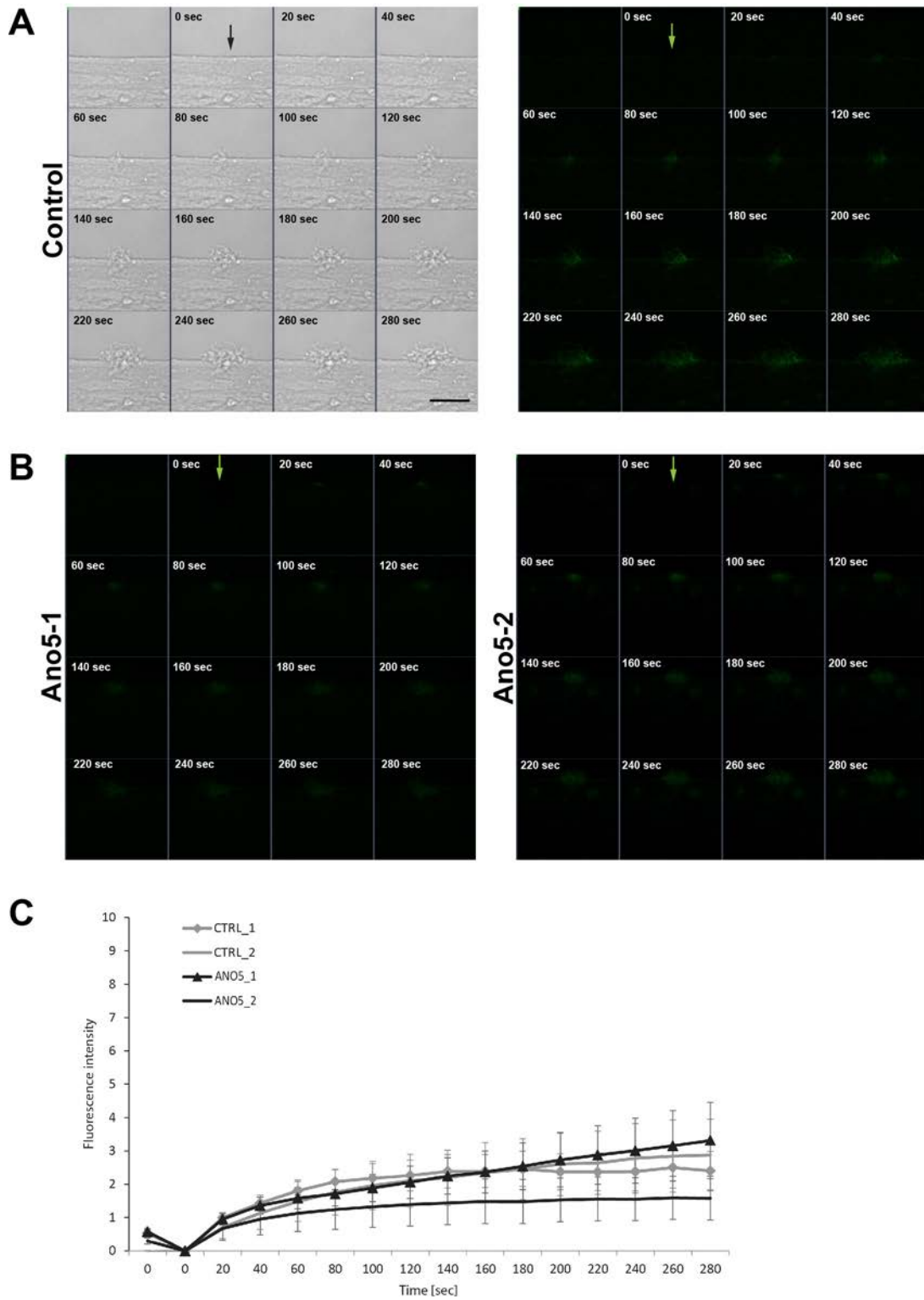
Figure 4.3 Analysis of membrane repair by laser-induced cell wounding

Myotubes derived from unaffected (A) and LGMD 2 L patient skeletal muscle (B) were wounded by laser irradiation for 38 sec (arrows). The influx of the fluorescent dye FM1-43 was observed every 20 sec for a total of 300 sec. Myotubes with *ANO5*-mutations showed no alterations of membrane resealing after wounding. (B). In (C) data for FM1-43 dye entry for all myotubes are summarized. Data represent means ± SEM (Ctrl-1: n=7; Ctrl-2: n=5; Ano5-1: n=7; Ano5-2: n=6). Scale bars were identical in all pictures and represent 10 µm.

4.2 Dysferlin and caveolin-3 localization in human myotubes

Dysferlin and cav-3 are localized at the sarcolemma in skeletal muscle (see Figure 4.4). Primary human myotubes derived from skeletal muscle biopsies have been used to investigate the localization of dysferlin and cav-3 on subcellular level. It has been shown that these two proteins are closely linked, whereas the molecular basis and the nature of the interaction still remain unclear.
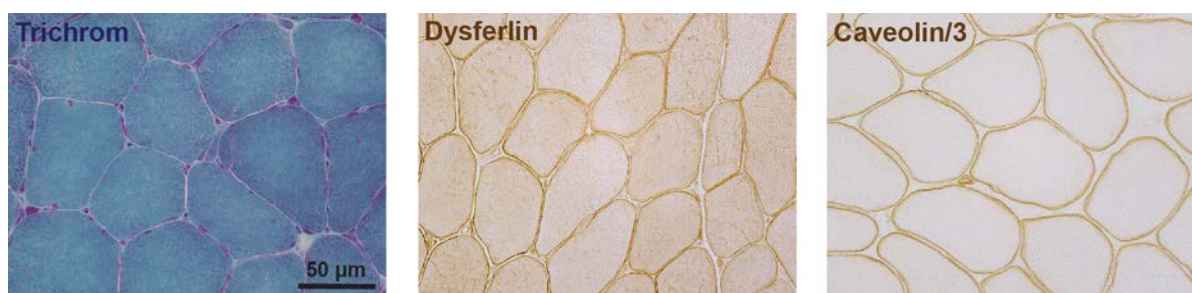
Figure 4.4 Localization of dysferlin and cav-3 at the sarcolemma in normal skeletal muscle

Trichrom staining shows typical characteristics of healthy skeletal muscle such as regular fiber diameters ranging from 80-100 µm and nuclei at the periphery of muscle fibers. Dysferlin and cav-3 localization is predominantly allocated to the sarcolemma. Scale bars were identical in all pictures.

The subcellular localization of affected proteins in LGMD (dysferlin, cav-3), a non-caveolae lipid raft (LR) marker (flotillin-1), as well as a differentiation marker (MHC) were analysed in cell lines originating from patients with LGMD 2B (dysferlinopathy) or LGMD 1C (caveolinopathy) and unaffected individuals. After 5 days of differentiation, all cell lines were able to fuse into myotubes expressing MHC (see Figure 4.5). Note that some cell lines show weak expression of myosin already in the undifferentiated myoblast state. This effect might be due to unevenly distribution of myoblasts during culture, and could result in contact-induced early differentiation. Myoblasts and myotubes showed no alterations for the plasma LR marker flotillin-1. During differentiation, levels of dysferlin and cav-3 increased (see Figure 1.1 B). The dysferlin-deficient cell lines, Dysf-1 and Dysf-4, showed no dysferlin protein. Dysf-2 and Dysf-3 muscle cells showed in both differentiation states (myoblasts and myotubes) a reduction of dysferlin levels. Cav3-1, -2, and -3 myoblasts and myotubes displayed no reduced dysferlin levels, but lower amounts of cav-3. Since LGMD 1C is an autosomal dominant muscular dystrophy, it leads to reduced but not absent amounts of cav-3 on protein level. No significant increase during differentiation was observed.
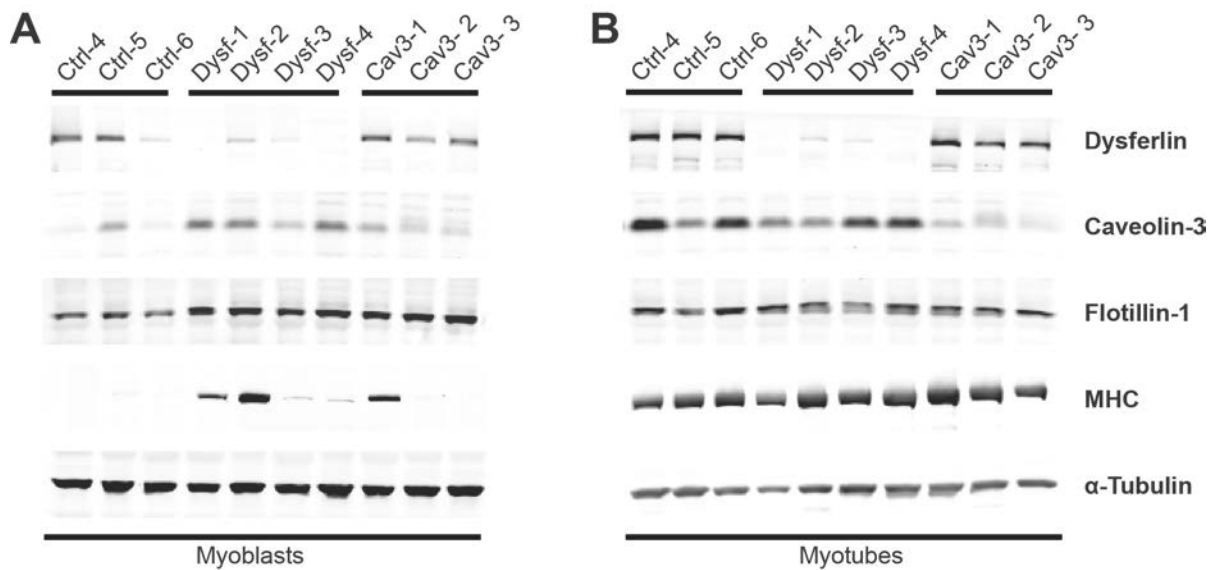
Figure 4.5 Comparison of human immortalized myoblasts and myotubes from healthy and LGMD skeletal muscle

Expression of the affected proteins dysferlin (230 kDa) and cav-3 (21 kDa), flotillin-1 (47 kDa) and the myogenic differentiation marker (MHC, 200 kDa) was analyzed by western blot. α-tubulin (50 kDa) has been used as loading control. Dysferlin-deficient cell lines, Dysf-1 and Dysf-4, showed no dysferlin protein, whereas Dysf-2 and Dysf-3 had reduced levels both in myoblasts (A) and myotubes (B). Cav3-1, -2 and -3 myoblasts and myotubes displayed no reduced dysferlin protein levels, but reduced amounts of cav-3. Myogenic differentiation and plasma LRs were not disturbed.

Subcellular localization of dysferlin was investigated in immortalized myotubes derived from healthy individuals as well as from patients with *DYSF* and *CAV3* mutations. To confirm that immortalized control cell lines show no alterations in subcellular localization of proteins of interests in comparison to primary cell lines, a primary myoblast cell line derived from unaffected skeletal muscle was included in the study (Ctrl-3). Dysferlin localization was observed predominantly at the plasma membrane but also within the cytosol. Dysf-2 and Dysf-3 myotubes showed decreased dysferlin levels at the plasma membrane und intracellular accumulation of the protein. Dysf-1 and Dysf-4 presented with total absence of dysferlin protein equivalent to western blot experiments. Cav-3 myotubes showed normally localized dysferlin, whereas in cell lines Cav3-2 and Cav3-3 dysferlin protein levels were increased. Dysferlin is known to be weakly expressed in myoblasts and shows increased levels during differentiation. This might explain the strong expression in Cav3-2 and Cav3-3 compared to Cav3-1 myotubes as they are in a later state of differentiation.
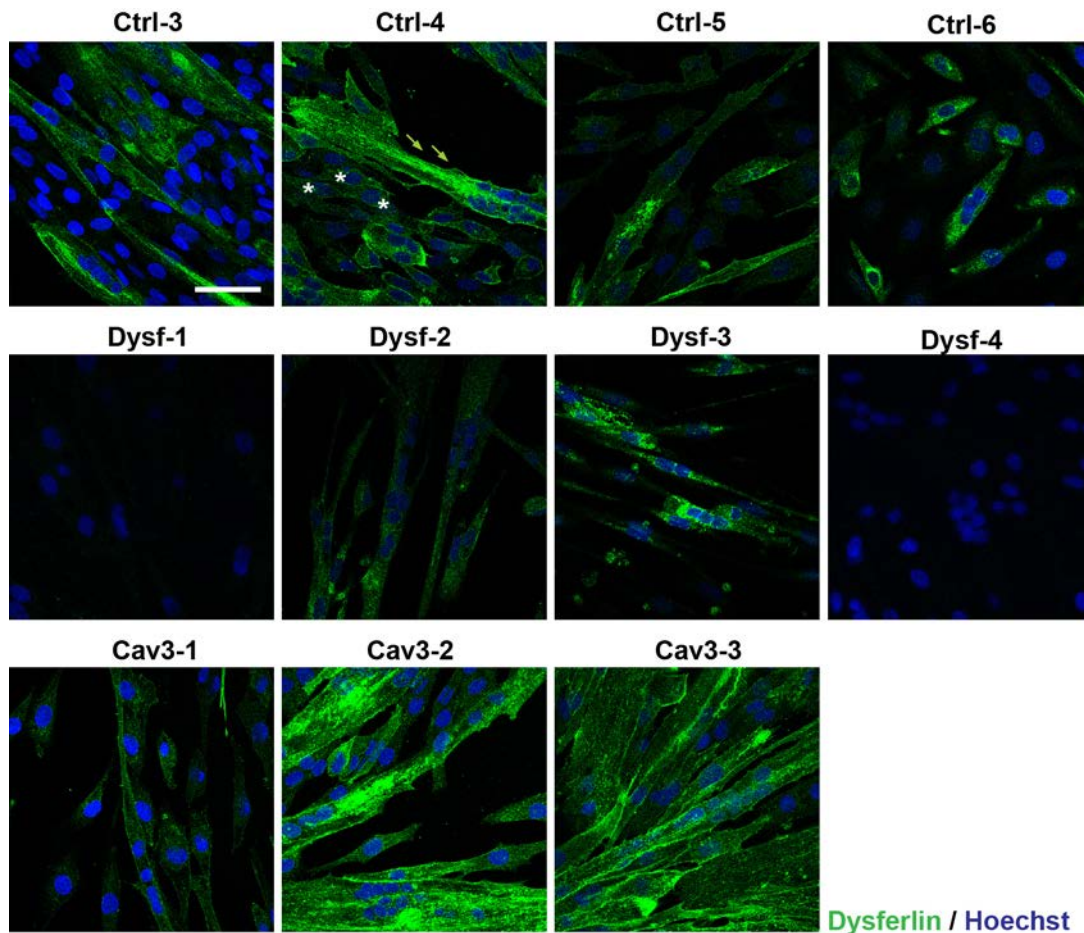
Figure 4.6 Subcellular localization of dysferlin in immortalized myotubes derived from healthy and LGMD patient skeletal muscle

Localization of dysferlin in control (Ctrl-3-6) and LGMD 1C myotubes (Cav3-1-3) was predominantly assigned to the plasma membrane (arrows). Expression of dysferlin increased during differentiation of myoblasts (asterisks) to multinucleated myotubes. Note that Dysf-2 and Dysf-3 showed decreased levels of plasma membrane dysferlin and intracellular accumulation of mutated protein, whereas in Dysf-1 and Dysf-4 dysferlin was completely absent. Original magnification was 63x. Scale bars were identical in all pictures and represent 50 µm.

The subcellular localization of cav-3 was predominantly allocated to the plasma membrane. Cav-3 expression was, as shown for dysferlin, strongly induced during differentiation. In control myotubes, localization at the plasma membrane occurred frequently in bigger structures near cell protrusions (arrows). Myotubes from patients with *DYSF* mutations showed normal cav-3 localization. In comparison to western blot analysis, Cav3-2 and Cav3-2 myotubes displayed a less prominent decrease in cav-3 protein levels. Nevertheless, accumulation of cav-3 at the plasma membrane seemed to be smaller in Cav3-2 and Cav3-3, and less abundant in Cav3-1 myotubes, which thereby correlates with decreased protein levels seen in western blot experiments.

Results
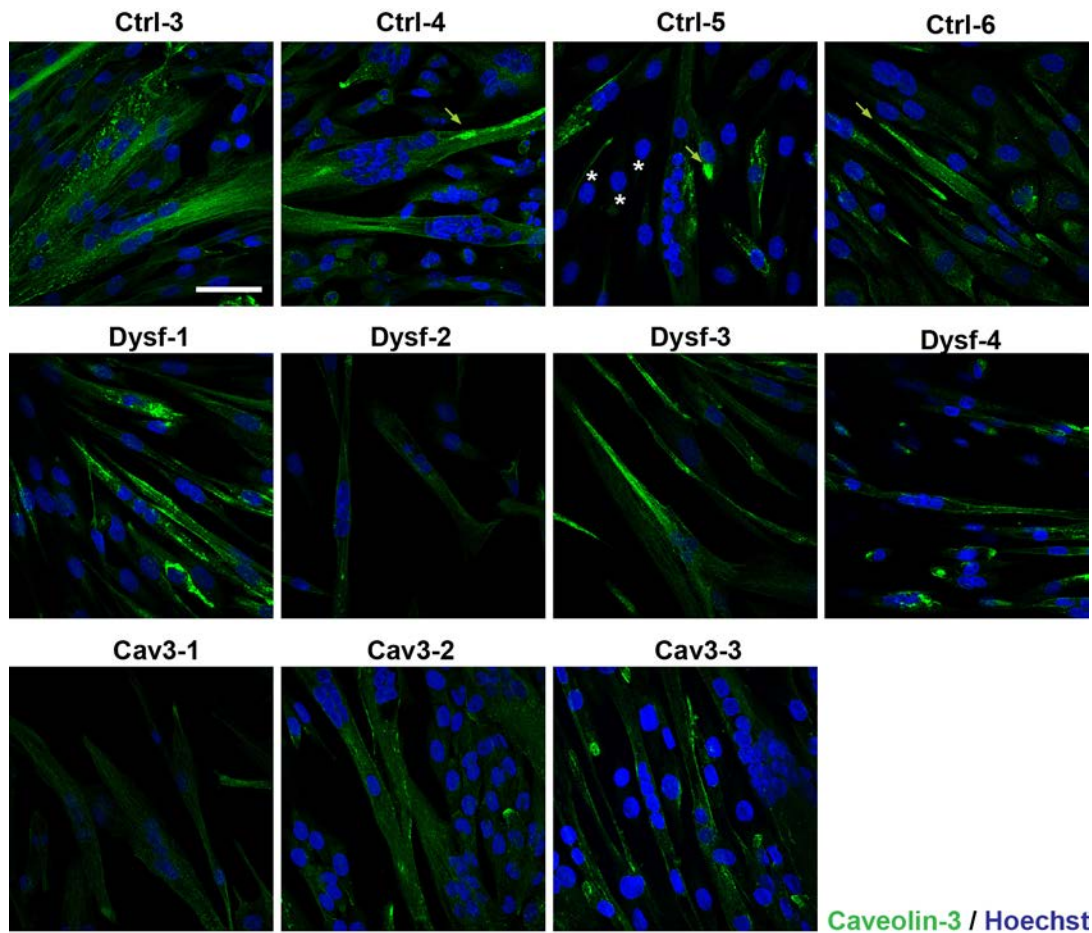
Figure 4.7 Subcellular localization of cav-3 in differentiated immortalized myotubes derived from healthy and LGMD patient skeletal muscle

Cav-3 localized predominantly at the plasma membrane forming bigger areas of accumulated protein (arrows) in control and LGMD 2B (Dysf-1-4) myotubes. Expression of cav-3 strongly increased during differentiation of myoblasts (asterisks) to multinucleated myotubes. Note that cell lines with *CAV3* mutations showed no significant decrease of plasma membrane localized cav-3 protein, although accumulations seemed to be smaller in Cav3-2 and Cav3-3, and were absent in Cav3-1 myotubes. Original magnification was 63x. Scale bars were identical in all pictures represent 50 μm.

Investigation of dysferlin and cav-3 localization in control and LGMD myotubes was done using the transmission electron microscopy (TEM)-suitable immunolabeling technique after Tokuyasu. Since no specific anti-cav-3 antibodies were available for TEM-immunolabeling, caveolae had to be labeled with an anti-PTRF (Polymerase I and transcript release factor; synonym to cavin-1) antibody. Cavins are the second important structural and functional component of caveolae beside caveolins. In Figure 4.8 the subcellular localization for dysferlin and PTRF is shown. Dysferlin was found predominantly associated to membranous structures as the plasma membrane and to intracellular vesicles. PTRF labeling was mainly found at the plasma membrane, especially on caveolar structures and plasma membrane vesicles, and to some extent within the cytosol. Localization of PTRF in control as well as in myotubes from patients with *DYSF* and *CAV3* mutations was not significantly altered.
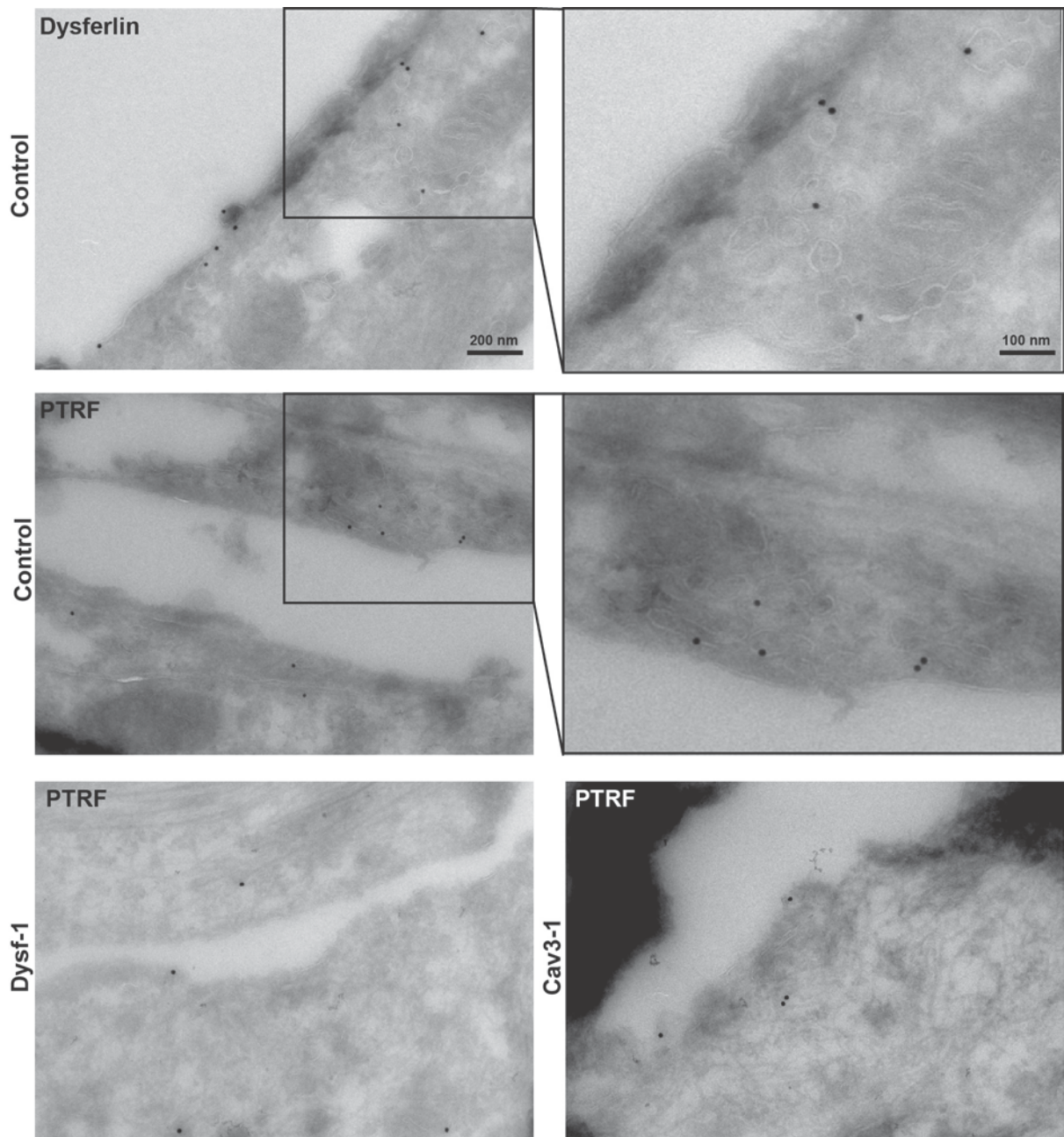
Figure 4.8 Localization of dysferlin and the caveolae protein PTRF in control and LGMD myotubes

Localization of dysferlin and PTRF could be attributed to cellular membranous structures like the plasma membrane, caveolae, subcellular, and intracellular vesicles. Antigen-binding was visualized by using of an anti-mouse bridging antibody raised in rabbit and Protein-A coupled to ø10 nm gold. Original magnification of TEM pictures was 12,500 x. Scale bar represents 200nm if not indicated differently.

4.3 Dysferlin and lipid rafts

Isolation of detergent-resistant membranes (DRMs) has been shown to be a biochemical tool to characterize the LR compartment in cell culture systems (Lingwood & Simons, 2007). After treatment with the nonionic detergent Triton X-100, DRMs can be isolated through flotation on a sucrose density gradient after equilibrium ultracentrifugation.

4.3.1 Association of dysferlin with detergent-resistant membranes (DRMs) in human myotubes

Titration of the optimal detergent concentration for the DRM flotation assay is shown for C2C12 myotubes in Figure 4.9. A balance between detergent resistance (low detergent concentrations) and mobilization of LRs from membrane compartments (high detergent concentrations) should be achieved. For efficient separation of LRs from the plasma membrane compartment, it is crucial to have an effective detergent to lipid to protein ratio. For Triton X-100, a mass ratio of 5:1 was used in this study. As shown in Figure 4.9 A the skeletal muscle specific LR marker cav-3 was enriched at the 5 %/30 % sucrose interface (fractions 4-6). Treatment with higher concentrations of detergent led to a shift from DRM fractions 4-8 to lighter fractions (3-5). Dysferlin was found in LRs as well as in heavy fractions (9-12), representing detergent-soluble proteins. An increase of detergent reduced dysferlin association to DRMs. Isolation of DRMs from murine and human differentiated myotubes was optimized for detergent concentration of 0.5 % Triton X-100 and a detergent to protein ratio of 5:1 (see Figure 4.9).

Successful isolation of DRMs from murine C2C12 as well as from human immortalized myotubes was confirmed by presence of the LR markers flotillin-1 and cav-3. As mentioned above, dysferlin associates with DRM fractions 4-6 at the 5 %/30 % sucrose interface in murine as well as in human differentiated myotubes, which is demonstrated in Figure 4.9.
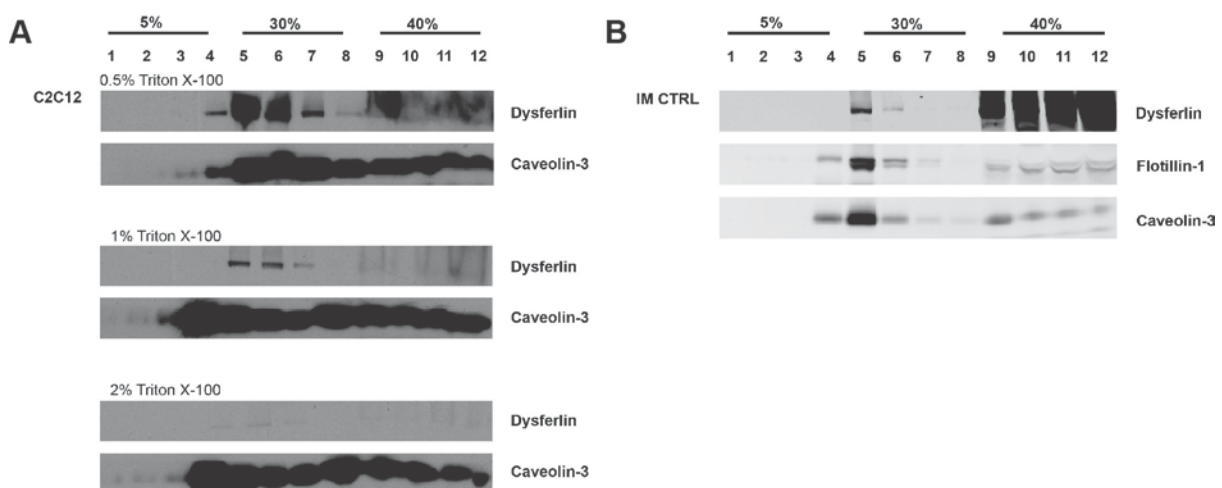
Figure 4.9 Association of dysferlin with DRMs

Titration of the optimal detergent concentration was done for C2C12 myotubes (A). Treatment with 0.5 % Triton X-100 induced typical association of the LR marker cav-3 (18 kDa) with fractions 4-8. Dysferlin (231 kDa) was found in LR fractions and in heavy fractions (9-12) representing detergent-solubilized proteins. Increase of detergent concentration led to a shift of the cav-3-distribution within the gradient to lighter fractions 3-5 and a dislocation of dysferlin from the LR compartment. Isolation of DRMs from human immortalized control myotubes derived from healthy skeletal muscle biopsies showed an association of dysferlin with DRMs

(B). The LR marker flotillin-1 (47 kDa) and cav-3 were found in LR fractions 4-6 at the 5 %/30 % sucrose interface.

4.3.2 Association of dysferlin with DRMs in human myotubes derived from LGMD 2B patients

To investigate the effect of dysferlin-deficiency on the LR compartment, preparations of DRMs from human myotubes derived from patients harboring dysferlin mutations were done. Mutations, which led to total absence of dysferlin protein in western blot and immunofluorescence experiments, showed no dysferlin in LR fractions 4-6 (see Figure 4.10 A). The distribution of LR specific markers, flotillin-1 and cav-3, within the gradient were not altered. Myotubes from patients harboring mutations, leading to a decrease in total dysferlin protein levels as well as intracellular accumulated and mislocated protein, also showed no alterations in flotillin-1 and cav-3 distribution (see Figure 4.10 B). However, the total dysferlin protein amount was decreased and dysferlin predominantly associated with heavier fractions 9-12 (40% sucrose), which represent the detergent-soluble portion of intracellular dysferlin. Distribution of LR markers was not altered.
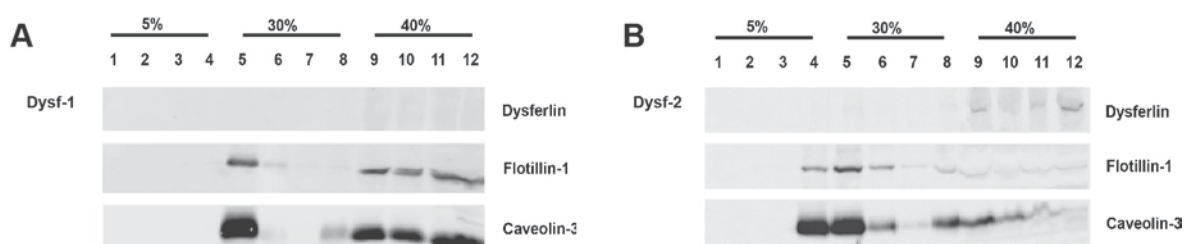
Figure 4.10 Investigations on DRMs from myotubes derived from LGMD 2B patient skeletal muscle

Patients harbored mutations, which either led to total absence of protein in western blot or immunofluorescence experiments (Dysf-1) (A) or to mislocated intracellular accumulated protein (Dysf-2) (B). Dysferlin protein (231 kDa) was absent in Dysf-1 myotubes, whereas in Dysf-2 myotubes dysferlin protein levels were decreased. Dysferlin associated only with heavy fractions 9-12, which represent detergent-soluble proteins. The distribution of the LR markers flotillin-1 (47 kDa) and cav-3 (18 kDa) was not altered in DRMs from myotubes harboring *DYSF* mutations.

4.3.3 Association of dysferlin with DRMs linked to the actin-cytoskeleton

Several protocols have been developed to investigate the association of proteins with a subtype of LRs linked to the actin-cytoskeleton (Bodin et al., 2005; Cartaud et al., 2011) (see also 3.4.3.2). DRMs were purified from murine C2C12 and human immortalized control myotubes (see Figure 4.11 A). The LR marker cav-3 was enriched in DRM fractions. In agreement with Bodin et al. (2004) most soluble actin associated with heavier fractions (40% sucrose). Actin involvement with LR is confirmed by association of actin with DRM fractions at the 5%/30% sucrose interface. Dysferlin was found in fractions 4-5

representing actin-linked DRMs, and in heavier fractions 8-12. Disruption of LRs was induced by depletion of cholesterol using methyl-β-cyclodextrin (mβCD) before DRM isolation. Depletion of cholesterol from myotubes severely impaired the association of dysferlin with DRMs linked to the actin-cytoskeleton (see Figure 4.11 B).
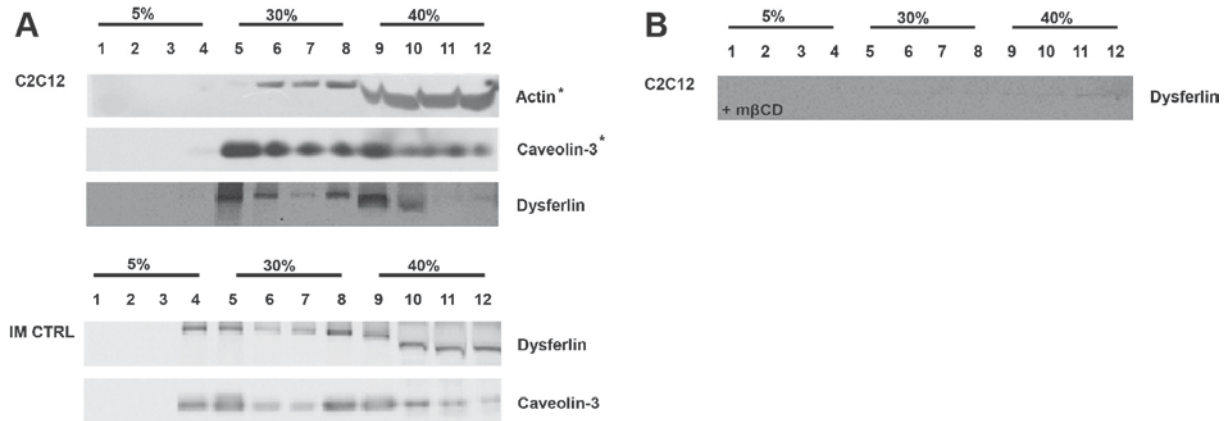
Figure 4.11 Investigations on DRMs linked to the actin-cytoskeleton from murine and human myotubes

Western blots of actin-linked DRMs from murine C2C12 and human immortalized myotubes are shown (A). Soluble actin (42 kDa) was mostly recovered in the heavier non-raft fractions 9-12, whereas cav-3 (18 kDa) was mostly detected in lighter fractions 4-8. Dysferlin (231 kDa) is enriched in fractions 4-5, representing the 5%/30% sucrose interface, and in fractions 7-9 representing detergent-soluble proteins. Depletion of cholesterol from myotubes with mβCD before isolation of actin-linked DRMs, severely impaired the association of dysferlin with LR stabilized by the actin-cytoskeleton (B). *Western blots of actin-linked DRMs have been done in cooperation with Jean Cartaud (Cell Biology of Membranes, Institut Jacques Monod, Paris, France). Membranes probed for actin and cav-3 have already been published in Biology of the Cell (Cartaud et al., 2011) and could be used in agreement with the authors (A). *Western blots of preparations of actin-linked DRMS from C2C12 myotubes (+/- mβCD) were used in agreement with Jean Cartaud (B).

4.4 Quantification of endocytic structures at the plasma membrane

Western blot analysis and biochemical purification of DRMs suggested a role of LR in LGMD 2B. As biochemical purification methods have limitations concerning illustration of membrane morphology, TEM investigations of the sarcolemma in myotubes from control and LGMD patients were done.

4.4.1 Abundance of endocytic structures at the plasma membrane in primary human myotubes

Different LGMD cell lines with mutations in genes encoding for dysferlin (Dysf-1-3), cav-3 (Cav3-1-3), and ano-5 (Ano5-1-2), as well as control cell lines (Ctrl1-5) derived from unaffected skeletal muscle, were differentiated to multinucleated myotubes and processed for epon embedding. For quantification studies only myotubes fulfilling the following criteria (illustrated in Figure 4.12) were selected; (A) the plasma membrane showed a sharp contrast and endocytic structures could be visualized, (B) total length of the plasma membrane per section per cell was accessible, (C) one transverse section exposed >20 µm of plasma membrane, and (D) cells showed no strong artefacts due to fixation such as extracted organelles, vacuoles, ruptured cell surface. As additional selection criteria, transverse sections had to display myotube features like (E) ≥2 nuclei or (F) "presarcomeric rearrangements" of the cytoskeleton. These presarcomeric structures presented as organized rearrangements of the cytoskeleton near the plasma membrane, and could only be observed in myotubes. Caveolae have been identified as flask-shaped invaginations of the plasma membrane with a characteristic size of 40-80 nm in diameter. Depending on the sectioning angle, they appeared as caveolae in open state or as vesicles close to the plasma membrane (see Figure 4.12 A). Clathrin-coated pits could easily be distinguished from caveolae, since they were bigger in size with a diameter of 100-200 nm and displayed an electron dense protein coat.

Orientation during sectioning of cells within the pellet was random. Abundance of endocytic structures at the plasma membrane was variable in myotubes, which is exemplary shown for caveolae in Figure 4.13 B. High abundance was predominantly observed at cell-cell contact sites or cell protrusions. No prevalence of plasma membrane structures for the apical versus basolateral membrane of adherent myotubes could be observed.
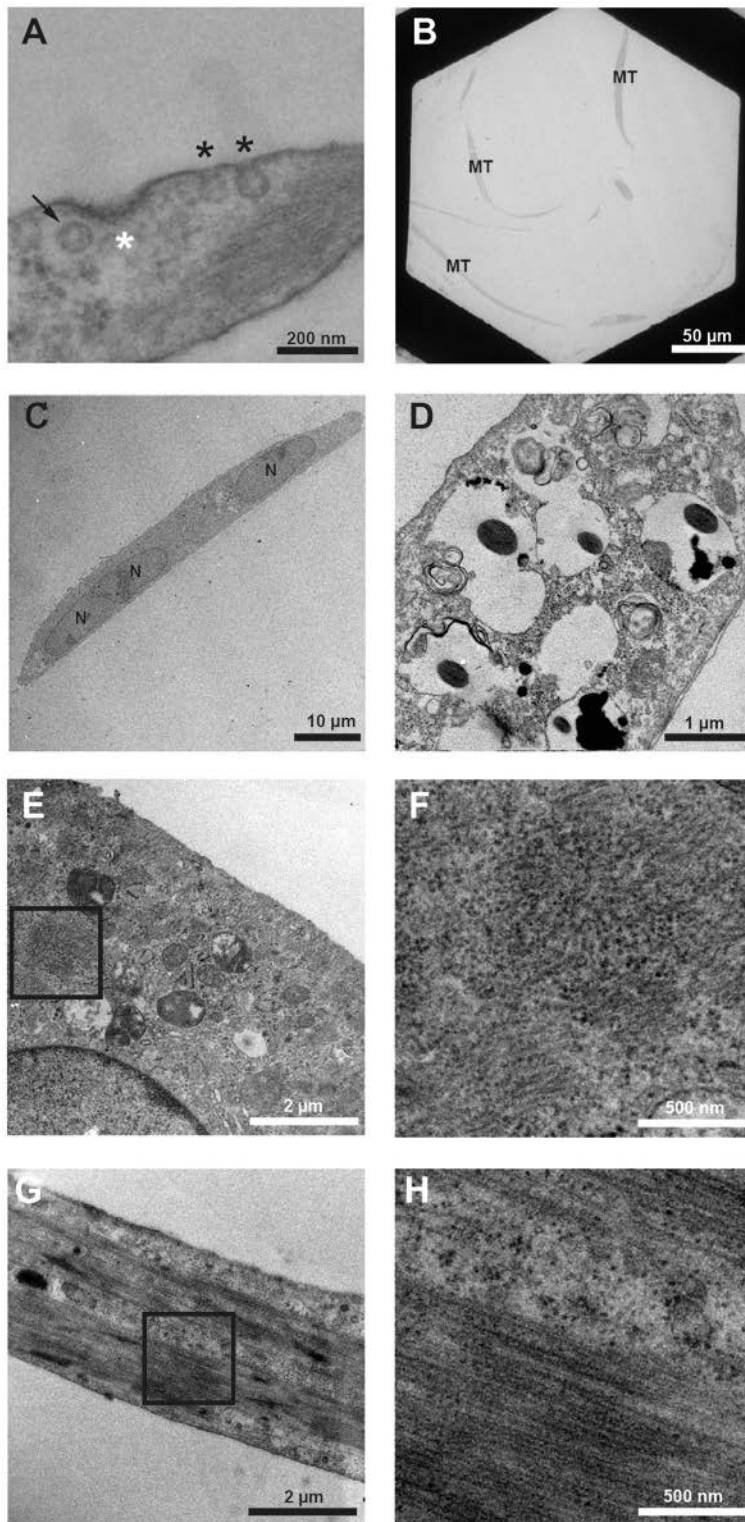
Figure 4.12 Selection criteria for quantitative studies of endocytic structures at the plasma membrane

Structures at the plasma membrane, such as caveolae in open state (black asterisks), clathrin-coated pits (white asterisk), and plasma membrane vesicles (arrows), were visualized (A). Selection criteria for myotubes were: (A) contrasted and sharp plasma membrane, (B) fully accessible transversal or longitudinal sections, (C) lack of fixation-related artefacts such as vacuoles, extracted organelles, or ruptured cells. As morphological differentiation markers, the presence of more than two nuclei (D) or presarcomeric structures (E-H) were defined for quantification. Figure (E) represents a transverse and (G) a longitudinal section of a myotube; (F) and (H) a magnified segment of each picture, respectively. MT: myotube, N: nucleus.
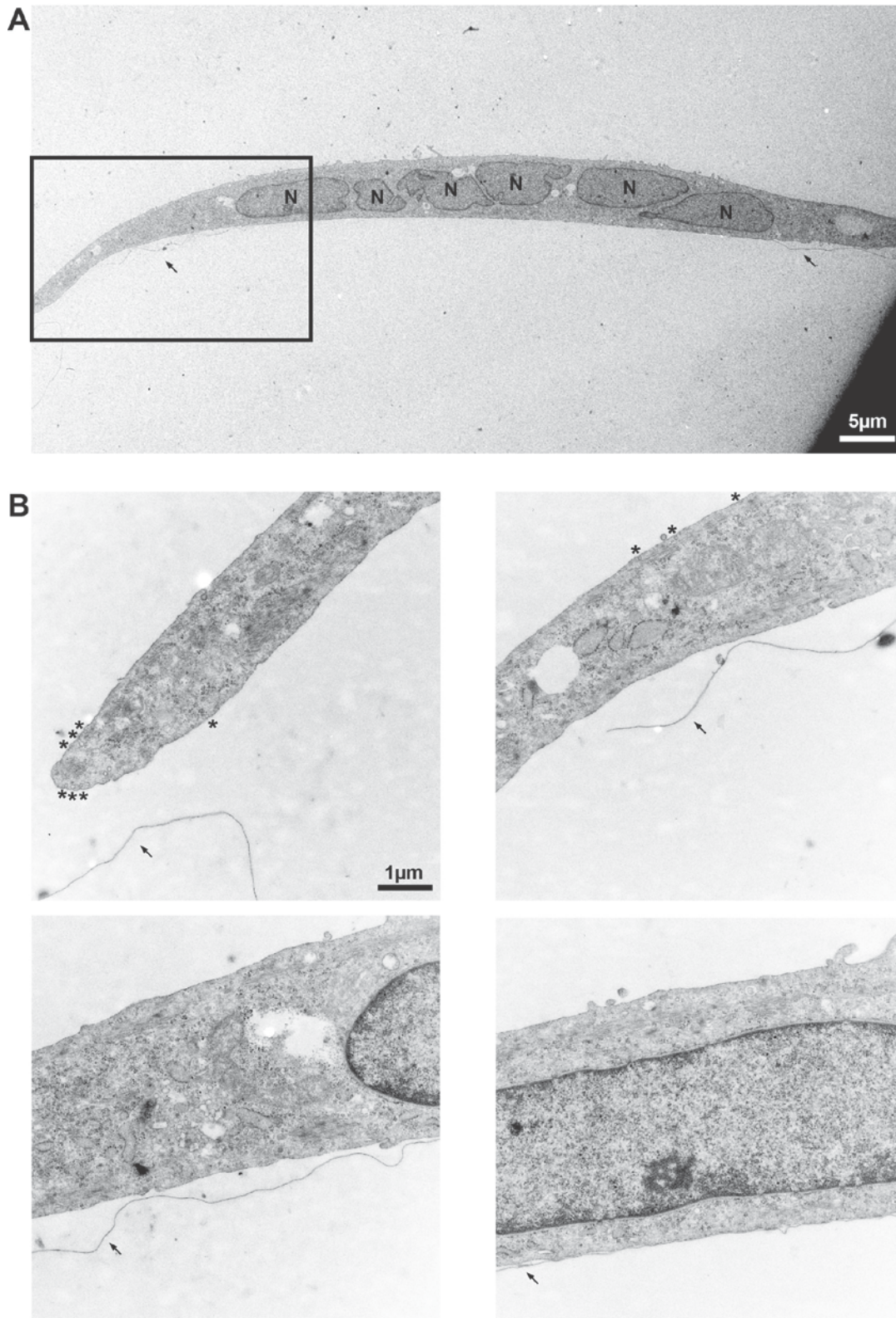
Figure 4.13 Abundance of endocytic structures at the plasma membrane in human myotubes

In figure A, a myotube fulfilling all selection criteria defined in chapter 4.4.1 is illustrated. During TEM preparation, detachment of myotubes from the cell culture dish was accomplished with release of a thin plastic layer (arrows). This had no effect on cell morphology, and therefore could be neglected during analysis. Magnified pictures of the area highlighted in B show the distribution of caveolae in open state over the plasma membrane (asterisks). (N=nucleus)

Quantification of endocytic structures at the plasma membrane covered a minimum of 600 µm per myotube. For each cell line, 10-13 myotubes were subjected to quantification. For details on total numbers of data obtained see Table 4-1.

Table 4-1   Data from quantification analysis of endocytic structures at the plasma membrane

Cell line	Amount of myotubes	Caveolea in open state	Caveolae total	Plasma membrane vesicles	Clathrin-coated pits	Plasma membrane length [µm]
Ctrl-1	10	93	200	107	29	712,03
Ctrl-2	11	146	325	179	29	1368,19
Ctrl-3	10	48	169	121	13	963,26
Ctrl-4	12	37	207	170	32	1164,20
Ctrl-5	12	104	280	176	28	1155,78
Cav3-1	13	79	257	178	62	1322,86
Cav3-2	12	93	307	214	47	2482,13
Cav3-3	11	39	92	53	18	668,81
Dysf-1	10	258	501	243	7	849,67
Dysf-2	10	86	215	129	18	1096,93
Dysf-3	11	32	195	163	38	1573,40
Ano-1	10	258	408	150	27	931,45
Ano-2	12	104	206	102	21	1032,52
PTRF-/-	10	0	37	37	31	602,18

4.4.2 Abundance of endocytic structures at the plasma membrane in primary human myotubes derived from LGMD patients

As mentioned above, selected myotubes had to fulfill various criteria. However, the length of exposed plasma membrane per cell varied because of cell size, sectioning level, and myotube differentiation status. This resulted in different total numbers of data acquired per picture and per cell. As can be seen in Figure 4.14 A approximately 15 µm plasma membrane per TEM picture (median) was quantified. Data obtained for one myotube ranged from 5 to 36 µm quantified plasma membrane length per picture (see Figure 4.14 A; *e.g.*: Ctrl myotube 3). As variations were constant for all different cell lines, data were grouped per myotube section (Figure 4.14 B). In Ctrl myotubes the length of plasma membrane measured per section had a median of 96 µm with a 25th percentile (Q_1) of 57 and a 75th percentile (Q_3) of 133. Highest variability was described for LGMD 1C myotubes (Cav3) with a median of 78 µm (Q_1:55/ Q_3:146); e. g. Cav3-1 ranging from 35 to 350 µm. In fibroblast deficient for PTRF the ratio of length of plasma membrane per section was significantly smaller in comparison to myotubes. This is due to the fact that fibroblasts are smaller than differentiated myotubes, and thereby displayed less plasma membrane per cell. However, approximately the same cell number (10-13) per cell line was subjected to quantification analysis.
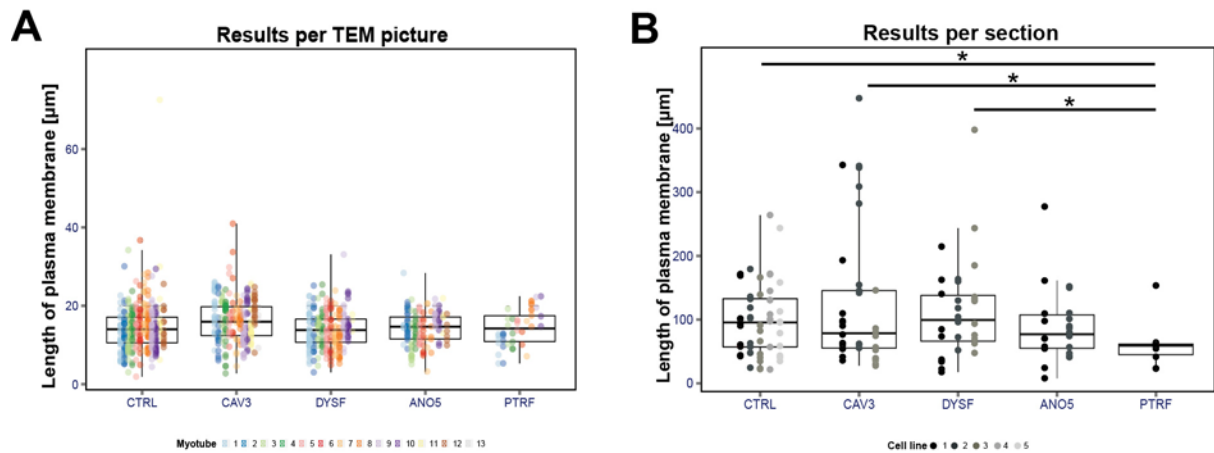
Figure 4.14 Data acquisition for quantification of endocytic events at the plasma membrane

To cover the full plasma membrane length of one myotube, multiple TEM pictures had to be taken. Data are displayed for each TEM picture (A) and grouped for each myotube section (B). Cell lines are named Ctrl (n=5), Cav3 (n=3), Dysf (n=3) and Ano5 (n=2) derived from unaffected, LGMD 1C, LGMD 2B and LGMD 2L skeletal muscle, respectively. As negative control PTRF-deficient fibroblasts have been used. Pictures were taken at a magnification of 5000 x. *P*-values were displayed for <0.05 (*) and <0.005 (**).

4.4.2.1   <u>Caveolae in open state</u>

Caveolae were defined as flask-shaped invaginations of the plasma membrane with a diameter ranging from 40-80 nm. In Ctrl myotubes the abundance of caveolae in open state over the plasma membrane displayed variances of 0.01-0.5 with a median of 0.05. Dysf and Ano-5 myotubes showed greater variances up to 0.8 caveolae per μm plasma membrane. Depending on the cell line, the abundance of caveolae varied for different myotubes of the same cell line. Ctrl-1 myotubes revealed caveolae abundance within the range of 0.01-0.1, whereas in Ctrl-5 myotubes the caveolae abundance ranged from 0 to 0.55 caveolae per μm plasma membrane. Ano5-1 showed the greatest variances of caveolae abundance ranging from 0-0.8. Figure 4.15 B illustrates that Cav3 myotubes have a similar absolute frequency of caveolae abundance in comparison to Ctrl myotubes. Myotubes derived from Dysf and Ano-5 patient muscle show greater variability in caveolae abundance and higher numbers of caveolae. Myotubes derived from LGMD 1C patients (Cav3) had significantly less caveolae in open state than myotubes with mutations in *DYSF* or *ANO5*. However, in comparison to Ctrl myotubes they showed no significant decrease.

Figure 4.15 Quantification of caveolae in open state at the plasma membrane of control and LGMD myotubes

In A the amount of caveolae in open state per μm plasma membrane is displayed (*P*-value for results per: 0.11). Dysf myotubes showed an increase of caveolae in comparison to Cav3 myotubes (*P*-value=0.046). PTRF-deficient fibroblasts showed no caveolae at the plasma membrane. Absolute frequencies of caveolae abundance showed similar profiles for Ctrl and LGMD myotubes (B). Note that Dysf and Ano-5 myotubes had more plasma membrane areas with higher caveolae abundance in comparison to Ctrl. *P*-values were displayed for <0.05 (*) and <0.005 (**).

PTRF-deficient fibroblasts from patients with congenital generalized lipodystrophy associated with muscle rippling disease have no caveolae (Rajab et al., 2010). These cells, therefore, were used as negative control during quantification studies. Absence of caveolae at the plasma membrane was confirmed on ultrastructural level by TEM (see Figure 4.16). Differentiated myotubes derived from patients with mutations in *CAV3* (Cav3-1-3), however, showed morphologically intact caveolae at the plasma membrane (see Figure 4.16) with an abundance similar to control myotubes from skeletal muscle of healthy individuals (see Figure 4.15).
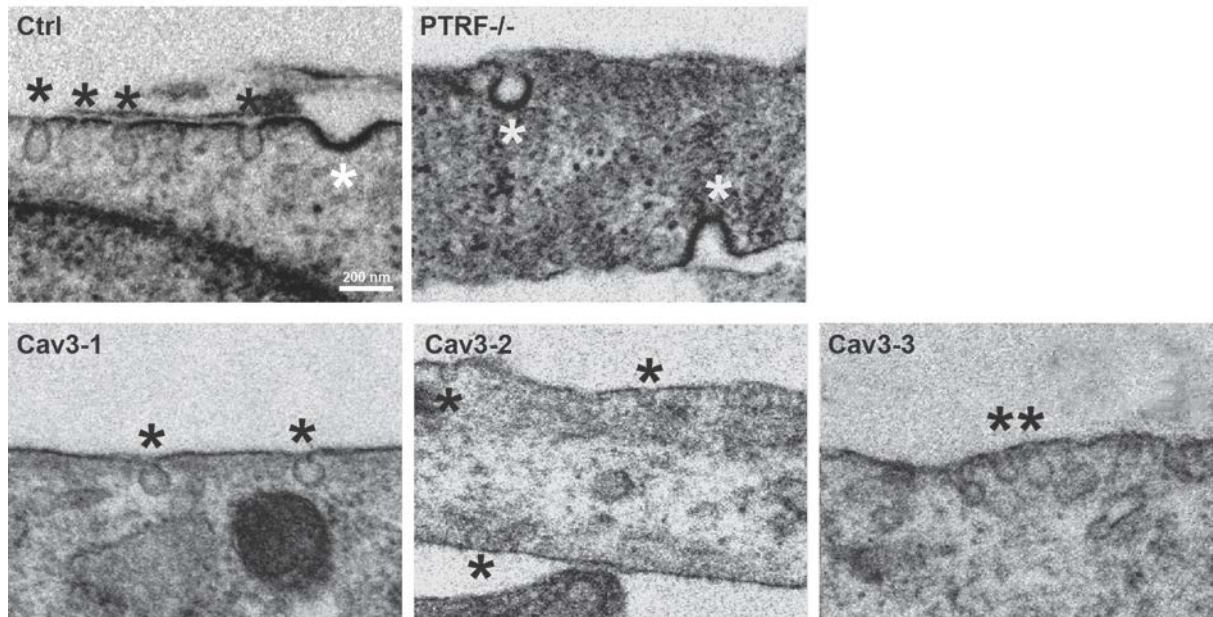
Figure 4.16 Endocytic structures at the plasma membrane of PTRF-deficient fibroblasts and myotubes derived from patients with mutations in *CAV3*

TEM pictures of myotubes derived from normal (Ctrl) and LGMD 1C patient skeletal muscle (Cav3-1-3) revealed endocytic invaginations at the plasma membrane. PTRF-/- fibroblasts were deficient for caveolae (black asterisks), but not for clathrin-coated pits (white asterisks). Original magnification was 5,000 x. Scale bars are identical in all pictures.

Dysf myotubes displayed a significant variability between different cell lines (see Figure 4.15). Dysf-1 myotubes, with mutations resulting in total absence of dysferlin, showed the greatest variances and the highest amount of caveolae. In contrast, Dysf-2 and Dysf-3 myotubes, having reduced levels or mislocated dysferlin, seemed to harbor less caveolae. Abundance of caveolae in open state from different LGMD 2B cell lines (Dysf-1-3) significantly varied within the group (see Table 4-2).

Table 4-2 Variations of caveolae abundance of different LGMD 2B cell lines

Cell line	Median	Quartile range	vs Dysf-1	vs Dysf -2
Dysf -1	0.32	0.21-0.45	-	-
Dysf -2	0.07	0.045-0.086	0.001*	-
Dysf -3	0.02	0.015-0.039	0.001*	0.002*

Abundance of caveolae at the plasma membrane from different LGMD 2B cell lines (Dysf-1-3) was compared within the group. *P-values were calculated post hoc by unpaired t-testing using R software.

4.4.2.2 Plasma membrane vesicles

Accumulation of subsarcolemmal vesicles have been described for human skeletal muscle biopsies from dysferlinopathy patients (Selcen, Stilling, & Engel, 2001). To investigate if human control and LGMD myotubes reflect this phenotype *in vitro*, we addressed this question by quantification of vesicles in less than 200 nm proximity to the cell surface.

Results

Abundance of plasma membrane vesicles showed a median of 1.2 structures per μm plasma membrane with an interquartile range of 0.08 to 0.19. Dysf and Ano-5 myotubes showed no significant alteration in comparison to Ctrl myotubes, although they exposed greater variability within one cell line (e.g. Dysf-1 and Ano5-2). As seen for caveolae in open state, different *DYSF* mutations resulted in different numbers of caveolae at the plasma membrane; ranging from 0.08-0.9 vesicles per μm plasma membrane for Dysf-1 to 0.03-0.17 for Dysf-3, respectively. For myotubes from LGMD 1C patients, a significant decrease in plasma membrane vesicles in comparison to Ctrl and Dysf myotubes was observed.
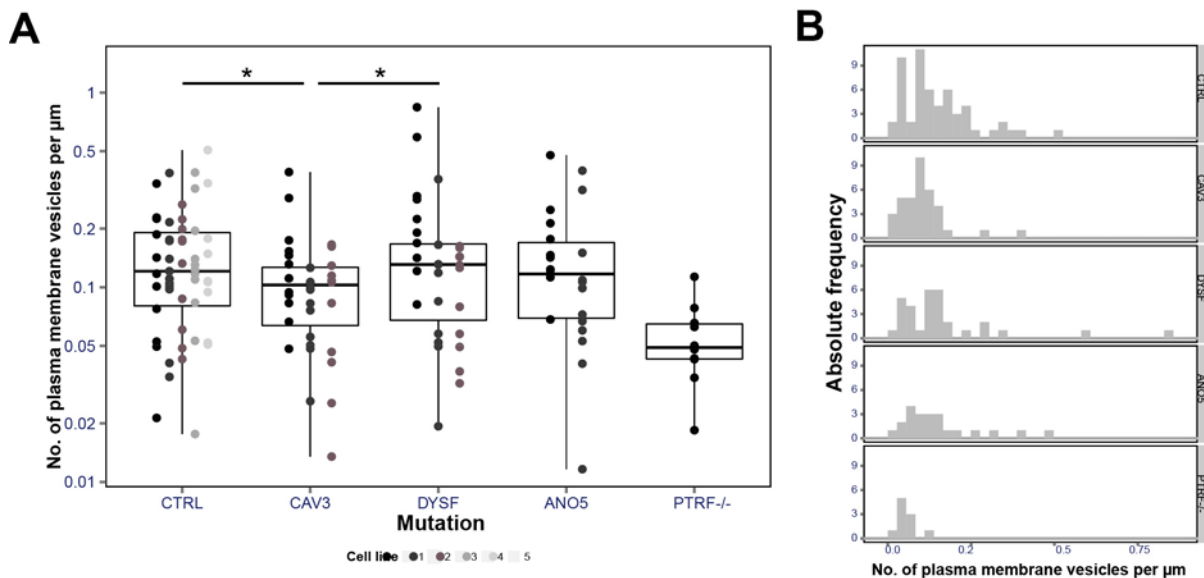
Figure 4.17 Quantification of plasma membrane vesicles at the plasma membrane of control and LGMD myotubes

In A the amount of caveolae in open state per μm plasma membrane is displayed. *P*-value for results per section was 0.007. Cav-3 myotubes showed an increase of plasma membrane vesicles at the plasma membrane in comparison to Ctrl and Dysf myotubes (*P*-value=0.038 for Cav-3 vs Ctrl / 0.047 for DYSF vs Ctrl). Absolute frequency of vesicle abundance in myotubes showed similar profiles for Ctrl and LGMD myotubes (B). Note that PTRF-deficient fibroblasts showed significantly less plasma membrane vesicles at the plasma membrane than Ctrl and LGMD myotubes (*P*-values <0.002). *P*-values were displayed for <0.05 (*) and <0.005 (**).

4.4.2.3 Percentage of caveolae in open state

Sectioning level has an impact on visualization of caveolae. In chapter 4.4.2.1 only invaginations with a visible connection to the plasma membrane have been referred to as caveolae in open state. However, not only invaginations with the typical flask shape should be addressed during quantification analysis. Therefore, in addition to caveolae in open state, also vesicles in less than 200 nm proximity to the cell surface have been quantified and are referred to as plasma membrane vesicles (see 4.4.2.2). In this chapter, data from both populations are pooled and declared as total caveolae.

In Ctrl myotubes the amount of total caveolae showed a median of 0.19 with an interquartile range from 0.12 to 0.27 caveolae per µm plasma membrane. Cav-3 myotubes had significantly less caveolae than Ctrl, Dysf, and Ano-5 myotubes. Highest scattering was observed for Ano-5 myotubes, as well as for cell line Dysf-1. Dysf-2 and Dysf-3 showed variances from 0.03-0.6, in comparison to 0.18-1.4 caveolae per µm plasma membrane for Dysf-1. PTRF-deficient fibroblasts had significantly less caveolae per µm membrane (median of 0.05). As confirmed by TEM investigations, these cells displayed no caveolae in open state with a connection to the plasma membrane. Low numbers of total caveolae in this data set are due to background from quantified plasma membrane vesicles equivalent to endo-or exocytic vesicles non-related to caveolae (see also Table 4-1).
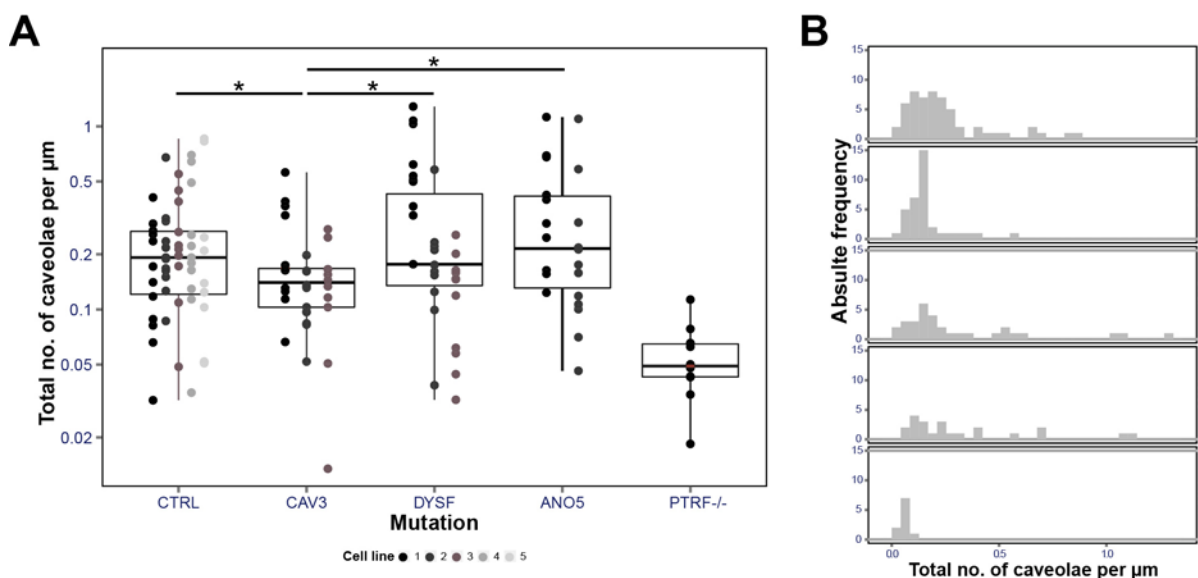
Figure 4.18 Quantification of total number of caveolae at the plasma membrane of control and LGMD myotubes

In A the total amount caveolae per µm plasma membrane is displayed. *P*-value for results per section is 0.001. Cav-3 myotubes showed an increase of caveolae at the plasma membrane in comparison to Ctrl and Dysf myotubes (*P*-value=0.043 for Cav-3 vs Ctrl / 0.018 for Cav-3 vs Dysf /0.005 for Cav-3 vs Ano-5). Distribution of absolute frequency in myotubes showed that Cav-3 myotubes had fewer areas with high caveolae frequency than Ctrl (B). Dysf and Ano-5 myotubes revealed plasma membrane areas with high (total) caveolae abundance of >10 caveolae per µm plasma membrane. Note that PTRF-deficient fibroblasts showed significantly less total caveolae than Ctrl and LGMD myotubes (p-values <0.001). *P*-values were displayed for <0.05 (*) and <0.005 (**).

Figure 4.19 displays the percentage of caveolae in open state related to the total amount of caveolae at the plasma membrane. For Ctrl myotubes around 30 % (median) of all caveolae were defined as caveolae in open state. Cav-3 myotubes showed no significant alterations in caveolae percentage compared to Ctrl myotubes. Dysf myotubes showed a slight increase to 38 %, although was not significant compared to controls. Interestingly, the different LGMD 2B cell lines clearly showed variances within the group. Cell line Dysf-

Results

1 had a higher percentage of caveolae in open state (50%) than dysf-3 (< 20%). A significant increase was shown for Ano-5 myotubes with a median of 45% (Q_1:32/Q_3:64). Distribution of absolute frequency showed a similar pattern for Ctrl, Cav-3 and Dysf myotubes. Myotubes derived from patients with *ANO5* mutations displayed a shift to higher percentages of caveolae in open.
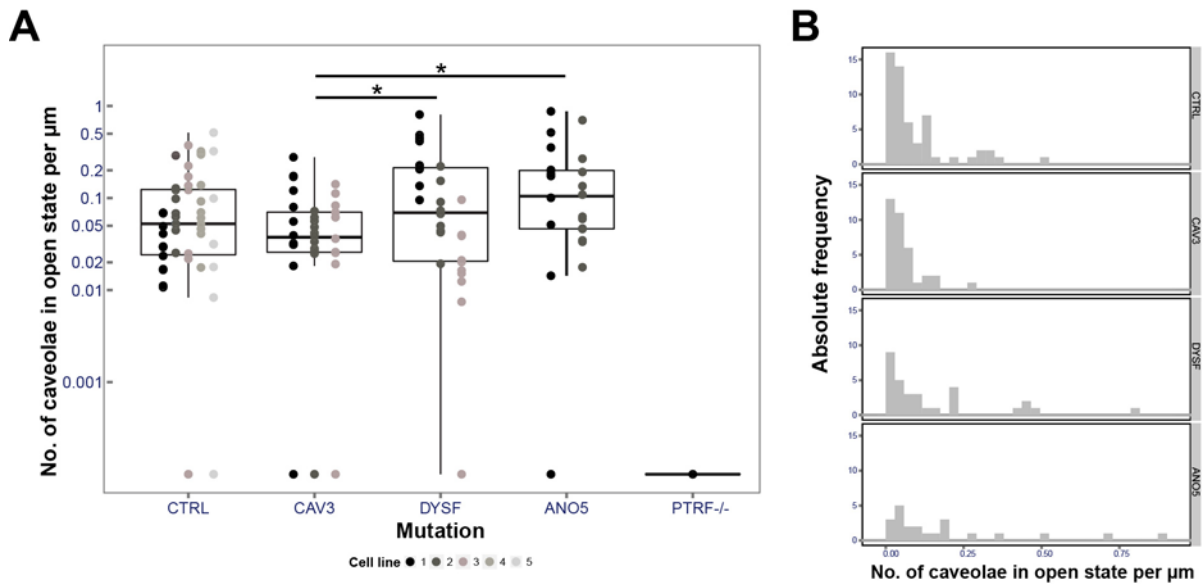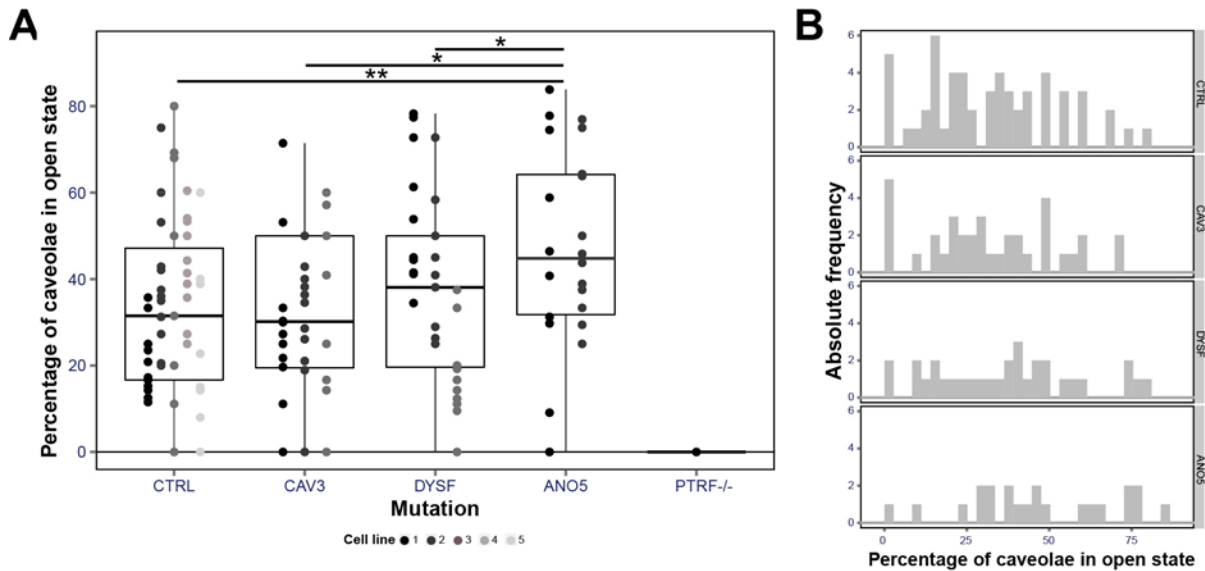

Figure 4.19 Percentage of caveolae in open state at the plasma membrane of control and LGMD myotubes

In A the percentage of caveolae in open state compared to the total amount of caveolae at the plasma membrane is shown. *P*-value for results per section is 0.031. Ano-5 myotubes showed a significant increase of open caveolae in comparison to Ctrl (*P*-value= 0.003) and LGMD myotubes (*P*-value=0.005 for Ano-5 vs Cav-3 / 0.05 for Ano-5 vs Dysf). Absolute frequency of caveolae abundance in myotubes (B) showed a similar distribution for Ctrl and Cav-3 myotubes. Dysf, but more significantly Ano-5 myotubes showed a shift to higher abundance of open caveolae at the plasma membrane. *P*-values were displayed for <0.05 (*) and <0.005 (**).

4.4.2.4 Clathrin-coated pits

Besides caveolae and plasma membrane vesicles, also the abundance of clathrin-coated pits (CCPs) has been analyzed. Quantification revealed a lower abundance of CCPs at the plasma membrane in comparison to caveolae and plasma membrane vesicles. The amount of CCPs in Ctrl myotubes had a median of 0.02 CCPs per μm plasma membrane (Q_1:0.008/Q_3:0.032), 10% compared to the total amount of caveolae. Myotubes derived from LGMD 2B patient muscle (Dysf) showed a significant increase in CCPs with a median of 0.01 (Q_1:0/Q_3:0.02). Interestingly, the different Dysf cell lines showed variances in CCP abundance correlating with the disease-causing mutation. Dysf-1 showed an abundance of only 0-0.02 in contrast to Dysf-3 with up to 0.05 CCPs per μm plasma membrane. As described before, PTRF-deficient fibroblasts did not show any caveolae in open state and significantly reduced amounts of plasma membrane vesicles. Abundance of CCPs in PTRF-deficient fibroblasts, however, was comparable to Ctrl as well as LGMD

myotubes with a median of 0.05 and an interquartile range from 0.043-0.065. Notably, the scattering ranged between 0 and 0.11 CCPs per µm plasma membrane.
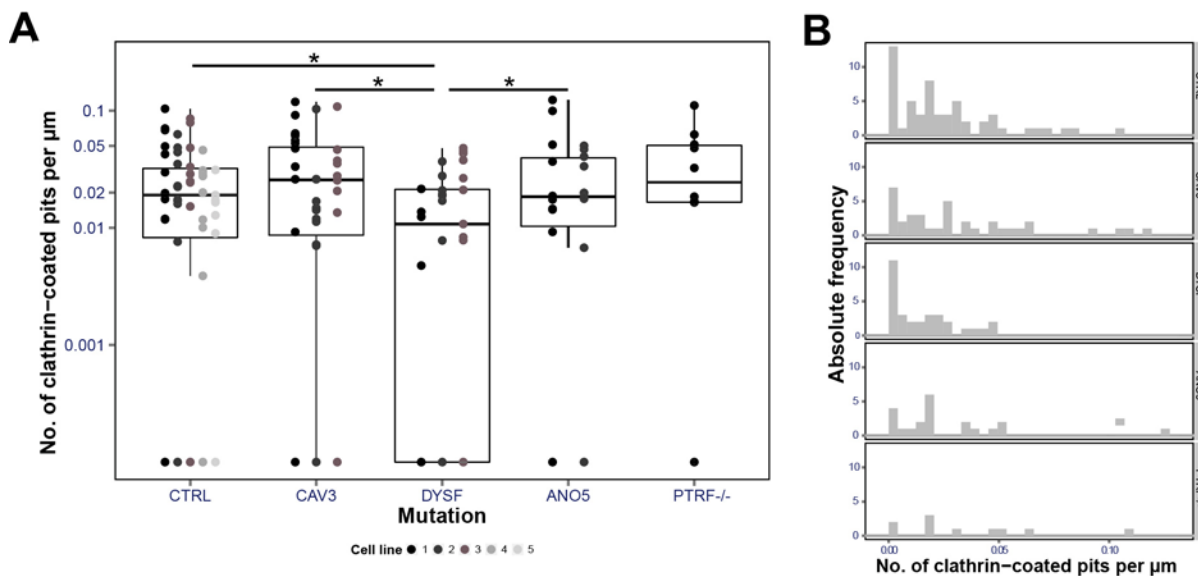
Figure 4.20 Quantification of clathrin-coated pits at the plasma membrane of control and LGMD myotubes

In A the amount of clathrin-coated pits (CCPs) per µm plasma membrane is displayed. *P*-value for results per section is 0.243. Dysf myotubes showed an increase of CCPs at the plasma membrane in comparison to Ctrl and LGMD myotubes (*P*-value=0.042 for Dysf vs Ctrl / 0.021 for Dysf vs Cav-3 / 0.041 for Dysf vs Ano-5). Absolute frequency of CCPs abundance in myotubes showed that myotubes and PTRF-/- fibroblasts had similar profiles (B). Dysf myotubes displayed an abundance of less than 0.05 CCPs per µm plasma membrane, whereas profiles from Ctrl, Cav-3, and Ano-5 myotubes ranged from 0 to 0.14. *P*-values were displayed for <0.05 (*) and <0.005 (**).

4.5 Immunopurification of dysferlin-containing morphological intact vesicles

Quantification of caveolae at the plasma membrane does not reveal caveolar protein content nor caveolae-associated proteins. Studies on the subcellular localization of dysferlin and cav-3 showed partial codistribution of both proteins at the plasma membrane. Therefore, we aimed to purify dysferlin vesicles and to analyze their protein content. Immunopurification (IP) of dysferlin-containing vesicles required subcellular fractionation beforehand to avoid contaminations with cell debris, components of the cytoskeleton, and organelles. Subcellular fractionation was achieved either through equilibrium centrifugation on a sucrose step gradient (see 4.5.1) or through differential ultracentrifugation (see 4.5.2).

4.5.1 Subcellular fractionation by equilibrium centrifugation

Ultracentrifugation to equilibrium in a 0.2-1.6 M sucrose density step gradient was used to separate different cellular compartments according to their size and buoyant density. The cell lysate was loaded on bottom of the tube and overlaid with the sucrose step gradient. Structural features of separated organelles in the different fractions were detected by TEM and their protein content was analyzed by western blot analysis.

Dysferlin containing organelles were found at densities of 0.6-1.4 M sucrose, with highest yields at 1-1.2 M sucrose. Organelles containing the LR marker cav-3 found their equilibrium around density of 0.8-1.2 M. Components of the cytoskeleton separated at highest sucrose densities (>1.2 M). TEM investigation of the dysferlin-containing fractions 5-8 revealed vesicular structures with diameters ranging from 50-500 nm. Fractions 5-8, representing a sucrose density of 0.7-1.1 M, were used as input for downstream applications to exclude bigger organelles and contamination from cytoskeleton components.
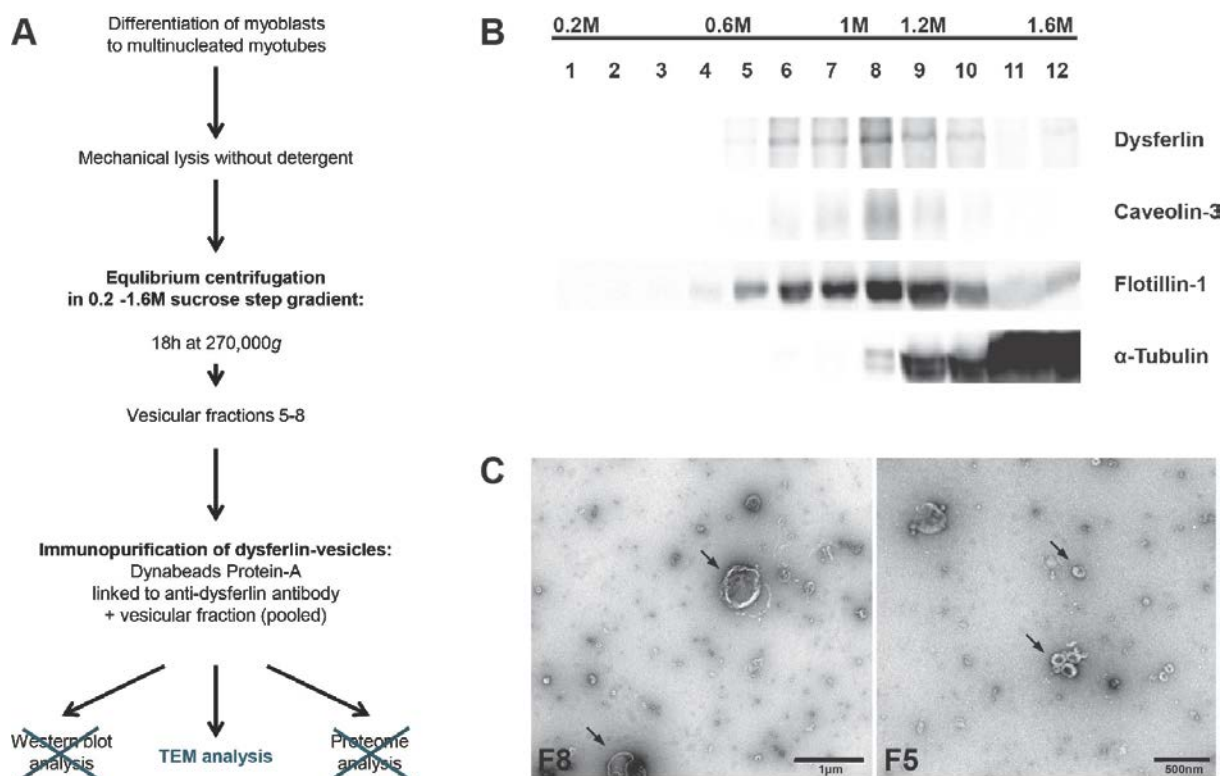
Figure 4.21 Subcellular fractionation by equilibrium sucrose density centrifugation

Protocol used for subcellular fractionation involved mechanical lysis of myotubes without membrane-disrupting detergent. Lysate was overlaid with a 0.2-1.6 M sucrose step gradient and centrifuged for 18 hours at 270,000 g until equilibrium was reached (A). Fractions of 1 ml were collected from top to bottom and analyzed for their protein content by western blot (B). Dysferlin protein could be detected in fractions representing densities of 0.6-1.4 M sucrose. Cav-3 and flotillin-1 colocalized to dysferlin-containing fractions. To avoid contamination from the cytoskeleton, fractions 5-8 were used for IP experiments. TEM analysis of these fractions revealed vesicular structures ranging from 50-500 nm in diameter (C).

An IP for dysferlin-containing structures was done as described in 3.4.6. Vesicles of 50-200 nm diameters were trapped and visualized by TEM. Furthermore, immunolabeling with a second anti-dysferlin antibody confirmed that the purified vesicle population contained dysferlin (see Figure 4.22). Unfortunately, the amount of protein after IP was not sufficient for western blot and subsequent proteomic analysis. Another limitation was that volumes of sample loaded under the density step gradient were restricted. This made it difficult to get adequate amounts of protein for downstream analysis. Despite the high accuracy of the purification with this technique, the experimental setup was switched to another subcellular fractionation method.
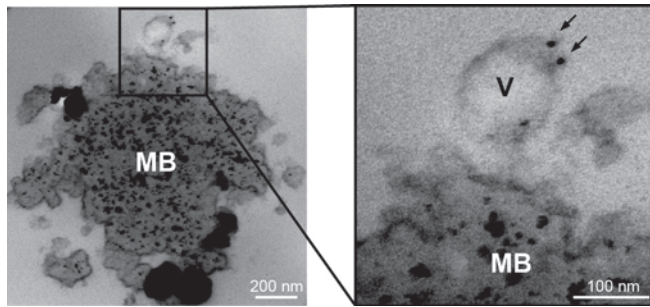
Figure 4.22: Immunolabeling of dysferlin-containing vesicles

Vesicular fractions 5-8 after subcellular fractionation were pooled and used as input for IP with magnetic beads. Magnetic beads were coated with Protein A and therefore could be linked to a monoclonal anti-dysferlin antibody raised in rabbit (rAb). Bound vesicles could be visualized by TEM. Pre-embedding immunolabeling was addressed with a second anti-dysferlin antibody raised in mouse (NCL-Hamlet). Binding of the secondary anti-mouse ø 12 nm gold antibody revealed that immunopurified vesicles contain dysferlin (arrows).

4.5.2 Subcellular fractionation through differential ultracentrifugation by velocity

Fractionation by differential ultracentrifugation has the advantage that enrichment of organelles of a particular size from large volumes of starting material is possible. This technique was used to enrich intracellular vesicles (microsomes) according to their size by serial spins at increasing *g*-force and centrifugation times. In contrast to the subcellular fractionation method, this resulted in a higher protein yield adequate for western blot and proteomic analysis. Figure 4.23 B shows purified and enriched intracellular vesicles of diameters ranging from 50-200 nm.
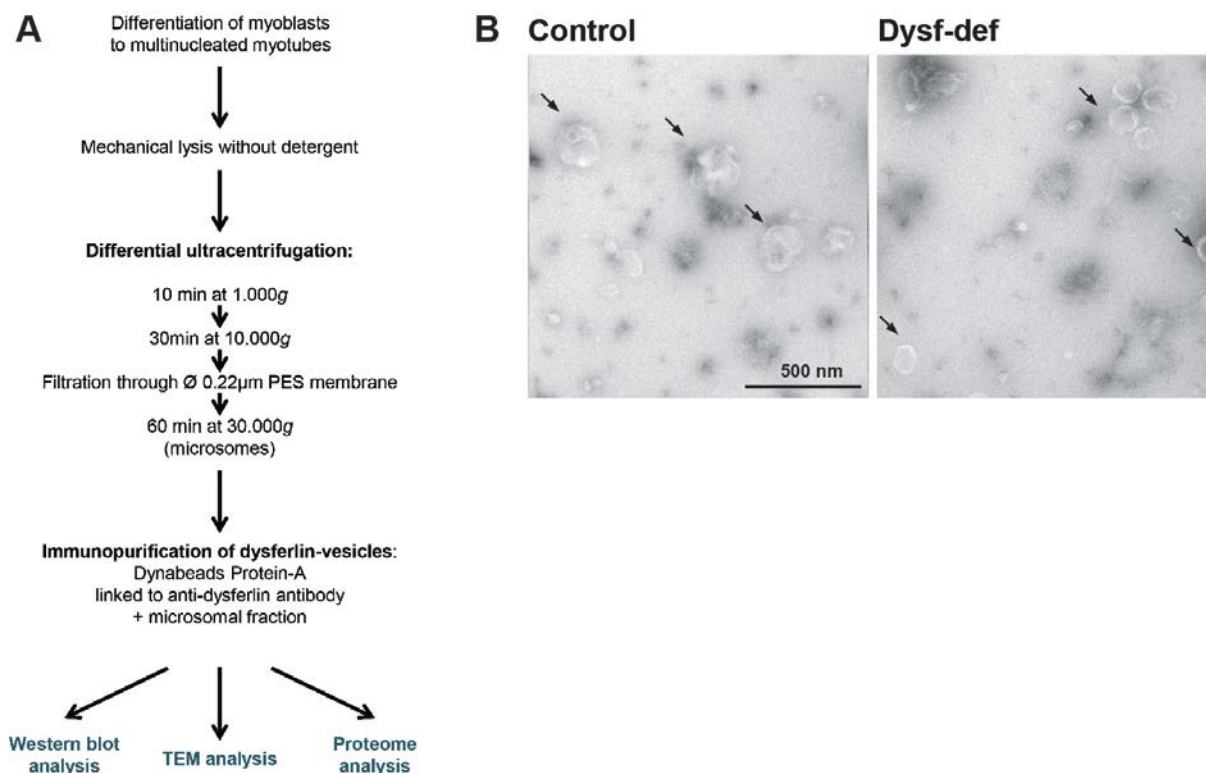
Figure 4.23: Subcellular fractionation of intracellular vesicles by differential ultracentrifugation

Protocol used for subcellular fractionation involved mechanical lysis of myotubes without membrane-disrupting detergent. Lysate was subjected to differential subsequent centrifugation steps for 10 min at 1.000 g, 30 min at 10.000 g, and 60 min at 30.000 g. (A). The pellet contained intracellular vesicles, also referred to as microsomal fraction. Investigation of morphological features was done by TEM and revealed vesicular structures ranging from 50-500 nm in diameter suitable for downstream IP applications (B).

4.5.3 Immunopurification of dysferlin-containing vesicles

Purified microsomal fractions from control and dysferlin-deficient myotubes were used as input for IP experiments as described in 3.4.6. Immunopurified vesicles were analyzed for specificity and purity, and were processed for detailed western blot and liquid chromatography–mass spectrometry LC-MS analysis (see 4.5.4). As negative control, Protein A-beads with no antibody were incubated with vesicular fractions from both cell lines. For detailed information on samples see the following table.

Results

Table 4-3   List of samples obtained from immunopurification of dysferlin-containing vesicles

Sample ID	Cell line	Anti-dysferlin antibody (Ab)
Ctrl-rAb	Control	rAb
Ctrl-VHH	Control	VHH
Dysf-rAb	Dysferlin-deficient	rAb
Dysf-VHH	Dysferlin-deficient	VHH
Ctrl-NC	Control	-
Dysf-NC	Dysferlin-deficient	-

Microsomal fractions were prepared from immortalized control (Ctrl) and dysferlin-deficient myotubes (Dysf). IP was either achieved using an anti-dysferlin llama-derived variable heavy chain antibody fragment (VHH) or using a monoclonal immunoglobulin-1 antibody raised in rabbit (rAb). The VHH, which targets a synthetic human peptide spanning over exon 1-7 (position 2-245 aa) was kindly provided by Prof. Silvére van de Maarel (Leiden University Medical Center). The anti-dysferlin rabbit-derived monoclonal targets the N-terminus of the dysferlin protein at exon 5 (position 123-142 aa).

Both antibodies were able to bind a subset of proteins during IP, which can be seen in Figure 4.24 A and C. The Coomassie Brilliant Blue staining revealed purified proteins of different sizes. Target binding was optimized for 2 hours at 4 °C, to obtain balance between optimal purification of dysferlin-containing structures and non-specific background. The variable heavy chain antibody fragment (VHH) also binds a remarkably high amount of proteins in dysferlin-deficient myotubes (Figure 4.24 C). In contrasts, bound fractions from IP with rabbit monoclonal antibody (rAb) and pure Protein A-beads (negative control) showed no remarkable protein pattern. This indicates that the IP with the rAb is more specific than the IP with the VHH.

Investigations on the protein content through western blotting revealed that the bound fraction after IP with VHH and rAb contained dysferlin. Purification amount could be estimated to 18-24 %. Interestingly, both anti-dysferlin antibodies were able to purify a fraction containing cav-3. Screening for several cell compartment markers i.e. Na^+-K^+-ATPase, calnexin, α-tubulin, and GAPDH, was found to be negative in bound versus non-bound fractions and thereby confirmed specificity of the purification assay (see Figure 4.24 B and D). Note that purification did not result in contamination from the plasma membrane, which was confirmed by western blot analysis for Na^+-K^+-ATPase. This is of interest because dysferlin is primarily localized to the plasma membrane, thus indicates that only the dysferlin-vesicle pool was addressed during purification. The antibodies used for IP were not covalently bound to Protein A-beads to prevent decrease of antigen binding properties. This led to some contamination of VHH/IgG 1 into downstream applications. After denaturation in SDS-sample buffer, VHHs dissociate to monomers, and therefore run during gel electrophoresis at 12-15 kDa and IgG 1 at 25 kDa and 50 kDa, respectively (see Figure 4.24 A and C). With careful selection of specific antibodies from other species and screening for non-specific background, the contamination by IgG-fragments could be neglected during further analysis.
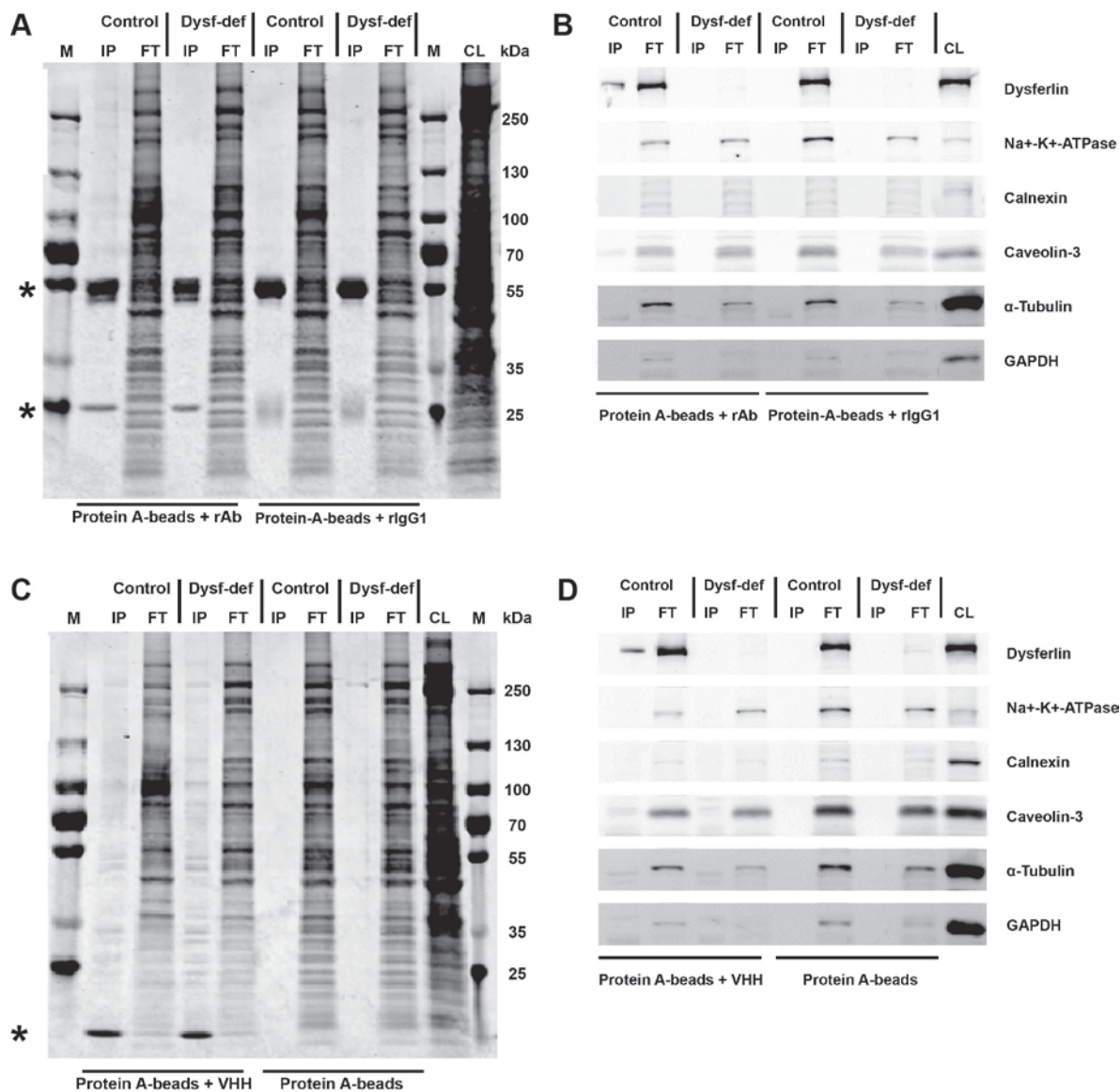
Figure 4.24 Western blot analysis of purified fractions

Immunopurified (IP) bound and flow-through (FT) fractions after immunopurification from control and dysferlin –deficient (Dysf-def) myotubes were analyzed by SDS-PAGE. A detergent-containing lysate from control myotubes (CL) was loaded as control. Coomassie staining (A, C) reveals that incubation of Protein-A-beads and control rabbit IgG1 antibody with input alone did not result in immunopurification. Immunopurification with monoclonal anti-dysferlin antibody (rAb) and variable heavy chain antibody fragment (VHH) resulted in successful purification of proteins from control cells. IgGs dissociated under denaturing conditions to their light and heavy chains (asterisks); for rAb to 25 kDa and 55 kDa and for VHH-fragment to 15 kDa, respectively. Western blotting (B, D) revealed purification of approximately 18-24 % of total dysferlin. Probing for different cell compartment markers confirmed no contamination by components of the plasma membrane (Na$^+$-K$^+$-ATPase), the endoplasmic reticulum (calnexin), cytosol (GAPDH) and the cytoskeleton (α-tubulin). Note that cav-3 was found in the bound fraction after IP with rAb (14 % of total cav-3) and VHH-fragment (8 % of total cav-3).

TEM analysis of the dysferlin-containing bound fractions was done directly after IP. Bound structures were not separated or eluted of Protein A-beads to prevent disassembly of associated organelles. Samples were fixed, dehydrated and embedded in epon for ultrathin sectioning. Figure 4.25 displays TEM pictures of the immunopurified fractions

from control as well as dysferlin-deficient myotubes. Antigen-binding to antibodies and therefore association of vesicular structures to the bead surface were detected for fractions from control myotubes. Vesicular structures of 50-200 nm diameters visualized. Incubation of the microsomal fraction with pure Protein A-beads did not result in unspecific background. IP with the VHH from dysferlin-deficient myotubes resulted in unspecific association of vesicles to the Protein A-beads (see Figure 4.25). Samples from dysferlin-IP were processed further for more detailed analysis of their protein content via LC-MS analysis.
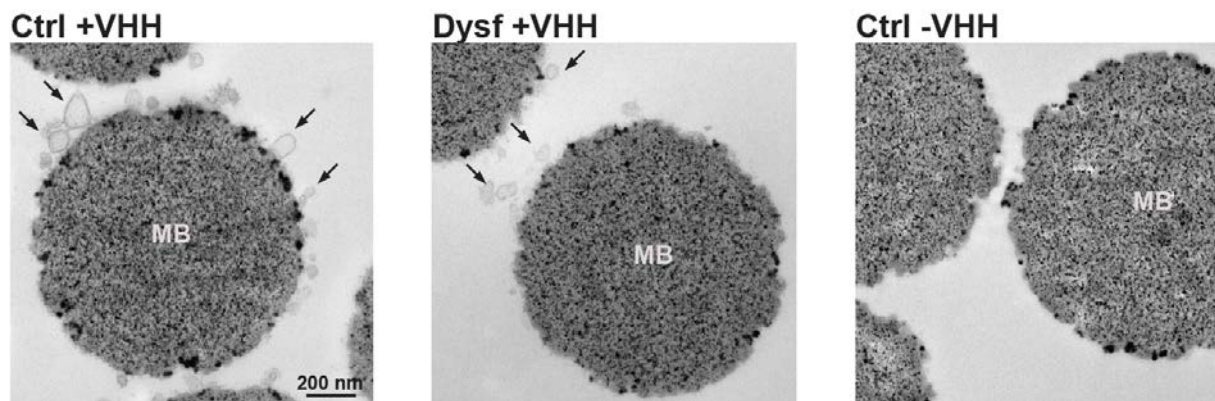
Figure 4.25 Morphological characterization of immunopurified vesicles

Immunopurified fraction was fixed in glutaraldehyde and processed for TEM. IP with the anti-dysferlin VHH from control myotubes revealed association of vesicular membranous structures (arrows) to the magnetic bead (MB) surface. IP from dysferlin-deficient myotubes (Dysf-def) resulted significant decrease of vesicles binding, but residual unspecific background binding of smaller vesicular structures was present. Incubation of beads without VHH with the microsomal fraction did not result in unspecific binding (negative control).

4.5.4 Proteome analysis of immunopurified dysferlin vesicles

Proteome analysis by LC-MS after IP revealed a total of 1194 proteins detected in all samples. Data analysis was done with the MaxQuant analysis software Perseus as described in 3.6.4.

Both anti-dysferlin antibodies were able to specifically enrich dysferlin from control myotubes (see Figure 4.26 D). Protein raw intensities for IP from control cells with the rAb were 6×10^7 and for the VHH 2×10^7, respectively. For protein values see also Table 7-1, but note that log2-transformed data are displayed. Venn diagrams in Figure 4.26 A-C display the number of common proteins purified from two fractions. Interestingly, the monoclonal rAb and the VHH purified a subset of 502 common proteins from control myotubes (see Figure 4.26 A). A list of these proteins can be found in the supplement section (page 142). Note that 94 % of all proteins purified with the rAb in control cells were also purified with the VHH. In contrast, from all proteins purified with the VHH only about 43 % were isolated by IP with the rAb. This could be due to a lower specificity of the VHH.

The second Venn diagram (Figure 4.26 B) shows that the rAb selectively purified 533 proteins from control myotubes representing 67 % of total proteins purified with the rAb. 101 proteins (16 %) were purified from control as well as dysferlin-deficient myotubes, and therefore represent unspecifically bound proteins. Remarkably, IP with the VHH resulted in purification of 1047 proteins from both cell lines (see Figure 4.26 C). Only 9 % of all proteins purified with the VHH were selective for the IP from control myotubes. Most proteins (88 %) were purified from both cell lines representing putative unspecific coimmunopurification. This shows that IP with the VHH results in 5.5 fold higher unspecific binding compared to the rAb.

The profile plot for the dysferlin protein is illustrated in Figure 4.26 D. It represents the abundance of dysferlin within the set of analyzed samples. The dysferlin profile correlates with the expected abundance of the target protein within the different samples. The top 200 proteins correlating with the dysferlin abundance profile are listed in supplement Table 7-1 (see page 133). The protein profile for cav-3 is exemplarily highlighted in Figure 4.26 D, and reveals 1.5 fold enrichment in control myotubes compared to negative control samples after IP with the rAb and of 1.4 fold after IP with the VHH, respectively. Protein raw intensities for IP from control cells with the rAb were 7×10^5, and for the VHH 6×10^5, respectively.
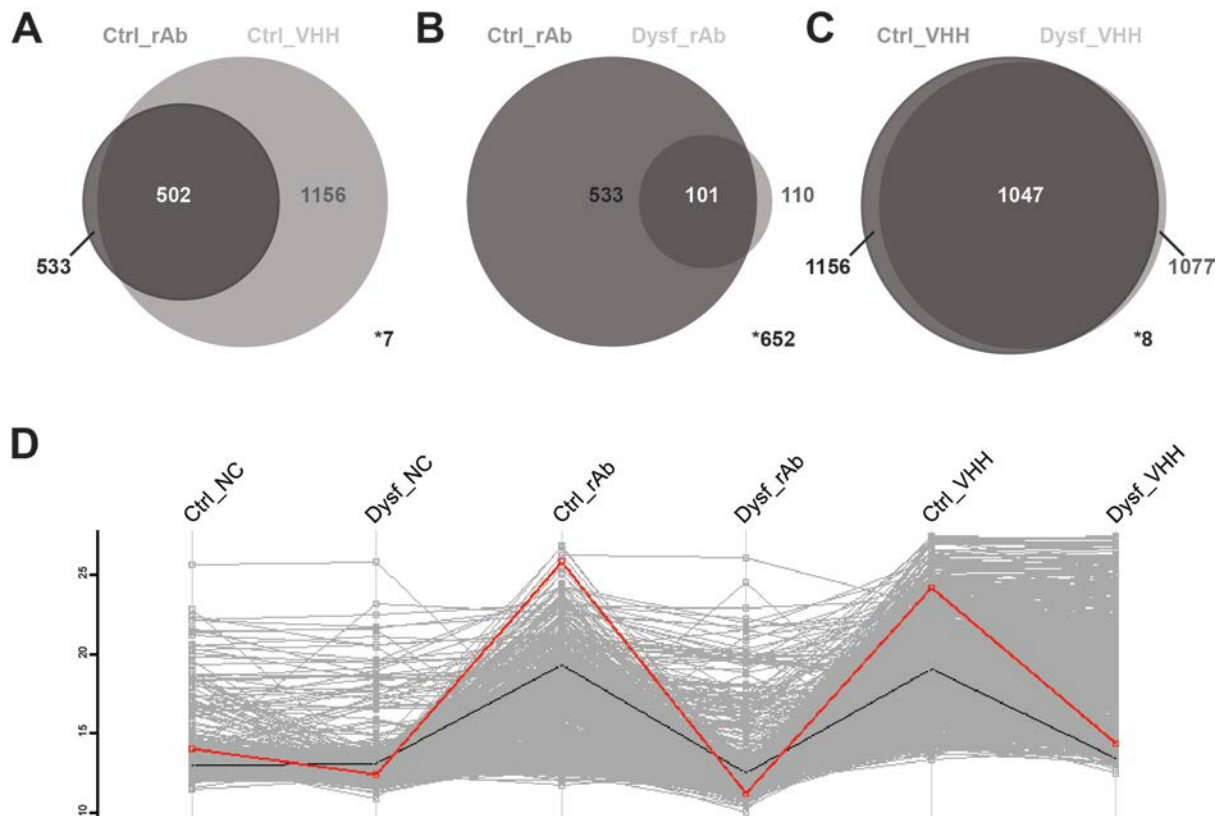
Figure 4.26 Proteome analysis of immunopurified dysferlin vesicles

The first Venn diagram (A) displays the 502 common proteins found in both anti-dysferlin IP samples from control (Ctrl) myotubes. The second Venn diagram (B) shows that the rabbit-derived monoclonal antibody (rAb) selectively purified 67 % of all proteins from control (Ctrl) in comparison to dysferlin-deficient (Dysf) myotubes. The rAb copurified 101 proteins (15 %) from Ctrl as well as Dysf myotubes. The VHH antibody fragment (VHH) only purified 9 % of all proteins from Ctrl myotubes (C). The VHH copurifies 1047 (88 %) proteins unspecifically from both cell lines. Numbers marked with asterisks represent the amount of proteins not detected in the two samples compared (from total amount of proteins identified through mass spectrometry). Note that 652 proteins (55 % of all proteins identified) were not detected by IP with the rAb. A profile plot of the target protein dysferlin (D) confirmed successful and selective purification of dysferlin from Ctrl cells. Dysferlin profile is highlighted in red. Negative control samples from both cell lines as well as IP fractions from Dysf myotubes displayed reduced levels for dysferlin in comparison to Ctrl samples. Exemplary, the profile plot for cav-3 is highlighted in black. For protein profile analysis, undetected proteins with protein raw intensities of 0 have been replaced by values estimated from a normal distribution to enable further analysis. Intensity values have been log2 transformed.

The heat map in Figure 4.27 A illustrates that samples after IP separate into two clusters; cluster 1 with the VHH IP fractions and cluster 2 with rAb and NC samples. Within the second cluster, the sample from rAb-IP from control myotubes separated from the rAb-IP from dysferlin-deficient myotubes as well as the negative controls. This emphasizes that the IP from the dysferlin-deficient and NC fractions contain similar proteins, which can be considered as nonspecifically purified background proteins. Samples from control and dysferlin-deficient myotubes after IP with the VHH cluster together, indicating that the VHH purified a similar set of putative unspecific proteins. The VHH seemed to be less specific during IP. Scatter plots in Figure 4.27 B displays the performance of the two antibodies during IP. During IP with the VHH, more proteins were purified from control

myotubes than with the rAb. Proteins purified by both antibodies have a high probability of being components or cargo of dysferlin vesicles and are listed in Table 7-2.

Unfortunately, IP with the VHH did also purify a large set of proteins from dysferlin-deficient myotubes, which might represent unspecific background (see Figure 4.27 D). This is exemplarily shown for myoferlin, which is selectively enriched in control, but not in dysferlin-deficient myotubes after IP with the rAb. Controversially, IP with the VHH resulted in enrichment of myoferlin from control but also from dysferlin-deficient myotubes. However, enrichment for dysferlin from control myotubes seems to be specific.
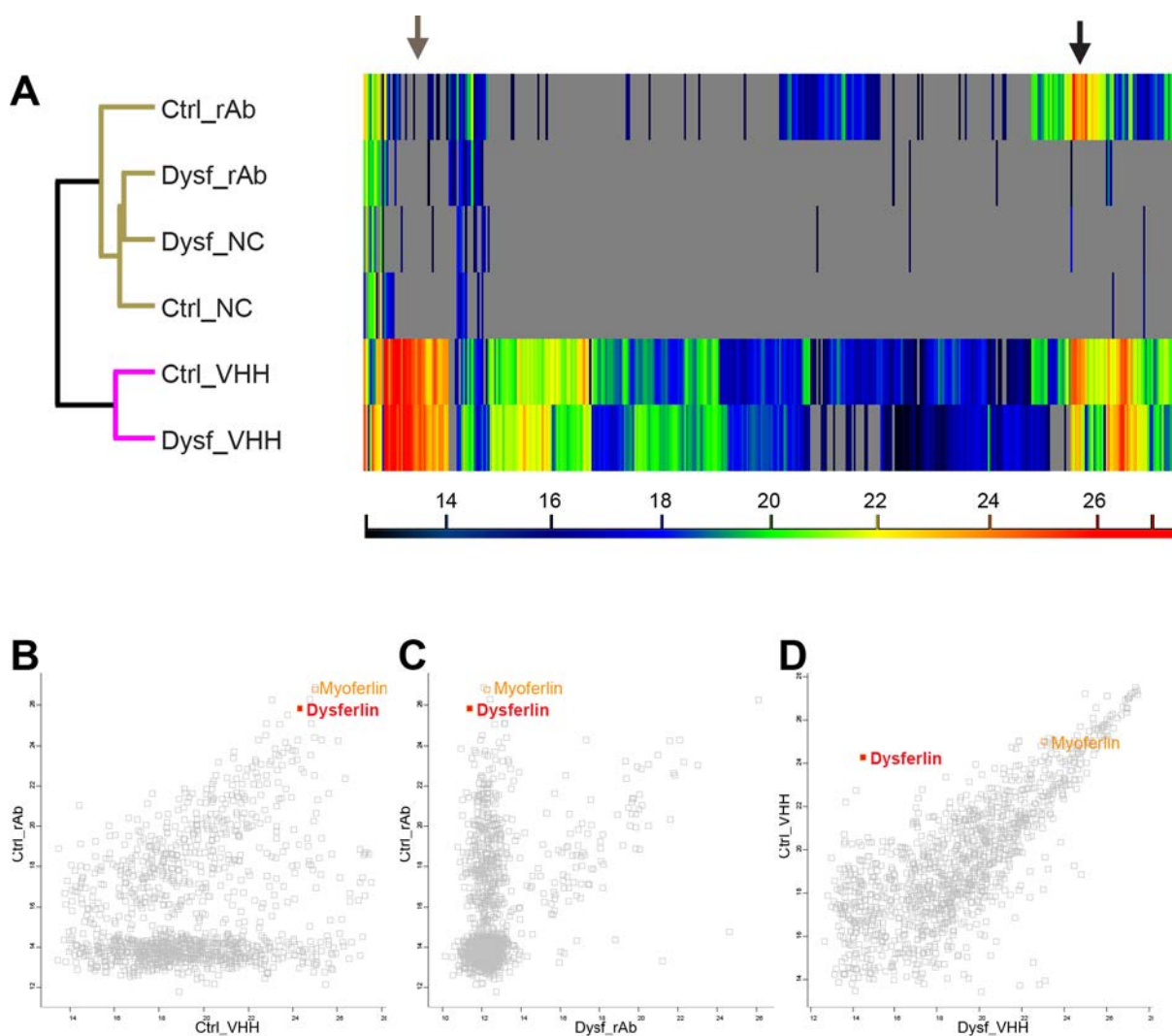
Figure 4.27 Hierarchical clustering and scatter plots of proteins detected by LC-MS from immunopurified dysferlin vesicles

The heat map displays a hierarchal clustering of all proteins detected by LC-MS (A). Note that IP with VHH antibody fragment (VHH) results in isolation of proteins from control (Ctrl) as well as from dysferlin-deficient (Dysf) myotubes (grey arrow). A subset of proteins containing dysferlin was enriched by anti-dysferlin monoclonal rabbit antibody (rAb) as well as by the VHH from Ctrl samples (black arrow). Scatter plot of IP (B-D) revealed enrichment of dysferlin in Ctrl in comparison to Dysf myotubes. B shows scatter plot for IP with rAb and VHH-fragment for Ctrl myotubes revealing a set of shared purified proteins. Note that the VHH-fragment purified a large amount of proteins from control as well as dysferlin-deficient myotubes (D), whereas the rAb was more specific during IP (C). This is exemplarily shown for myoferlin (B-D).

Results

Most proteins from purified fractions detected by LC-MS could be assigned to cellular processes such as endocytosis (cav-3), exocytosis (VAMPs), association with cytoskeleton (actin, α-tubulin), vesicular trafficking and fusion (Rab proteins), and cell adhesion (CAMs, integrins). A complete list of all proteins detected by both dysferlin antibodies can be found in the supplement section (Table 7-2). Already described dysferlin interacting partners such as myoferlin, annexin A1 and A2, ahnak, MG53 (TRIM72), α-tubulin, EHD2, PTRF, and cav-3 were found in IP fractions from control cells.

Top canonical functions, identified by IPA software analysis in association with dysferlin vesicles are shown in Table 4-4. Many of the identified pathways revealed known functions of dysferlin such in endocytosis and recently described cell adherence, but also reveal rather unexpected pathways such as germ cell-sertoli cell signaling and agrin interactions at the neuromuscular junction (NMJ).

Table 4-4 Canonical pathways identified by Ingenuity Pathway Analysis

Canonical pathways	*P* value	Ratio
Virus Entry via Endocytic Pathways	1.28E-14	24/81
Clathrin-mediated Endocytosis Signaling	5.16E-13	31/159
Caveolar-mediated Endocytosis Signaling	1.32E-12	20/66
Epithelial Adherens Junction Signaling	8.98E-12	27/135
Germ Cell-Sertoli Cell Junction Signaling	7.13E-11	27/147
Agrin Interactions at Neuromuscular Junction	4.97E-10	17/32
Molecular and cellular functions	***P* value**	**Number of proteins**
Molecular transport	1.72E-14 - 7.15E-3	112
Cellular function and maintenance	9.91E-14 – 5.11E-3	96
Cellular assembly and organization	2.93E-10 – 5.84E-3	100
Cell-to-cell signaling and interaction	1.09E-8 – 7.15E-3	62

The *P* value was calculated by the IPA software using a right-tailed Fisher Exact Test and it represents the likelihood that the association between the set of analyzed proteins and a given pathway is due to random chance. The ratio describes the fraction of proteins fitting a certain pathway within the analyzed data set compared to the total amount of proteins resumed to be associated with that pathway in the IPA data base.

Proteins detected in samples of rAb-IP from control myotubes were ranked according to protein raw intensities and the first 10 proteins are listed in Table 4-5. The ferlin proteins, dysferlin and myoferlin, and endocytic proteins such as clathrin and Rab-family interacting proteins were found. Involvement of dysferlin on cell-adhesion was represented by presence of the neural cell adhesion molecule 1. Rather unexpected proteins with high protein raw intensities were the prolow-density lipoprotein receptor-related protein 1 with protein raw intensities of 1×10^8 (rAb) and 3×10^7 (VHH) and mannose-receptor with values of 5×10^7 (rAb) and 1×10^7 (VHH) (see also Table 7-1).

Table 4-5   List of proteins immunopurified with both anti-dysferlin antibodies from human skeletal muscle cells

Protein name	Gene name	GO Biological Processes	GO Cellular Compartments	KEGG pathway
Prolow-density lipoprotein receptor-related protein 1	LRP1	Cellular lipid metabolic process; cellular membrane	Cytoplasmic vesicle membrane	Alzheimer's disease; Malaria
Myoferlin	MYOF	Cellular membrane organization	Caveola; cytoplasmic vesicle	-
Transferrin receptor protein 1	TFRC	Cellular iron ion homeostasis; cation transport	Cytoplasmic vesicle	Endocytosis
Dysferlin	DYSF	Cellular component organization	Cytoplasmic vesicle membrane; plasma membrane; T-tubule	-
Cation-independent mannose-6-phosphate receptor	IGF2R	Membrane invagination; receptor-mediated endocytosis; vesicle-	Clathrin-coated vesicle; cytoplasmic vesicle; endocytic vesicle	Lysosome
DnaJ homolog subfamily C member 13	DNAJC13	-	Lysosomal membrane; extracellular vesicular exosomes	-
C-type mannose receptor 2	MRC2	Endocytosis; membrane invagination; membrane organization; vesicle-	Integral to membrane	-
Rab11 family-interacting protein 5	RAB11FIP5	Protein transport	Endosome membrane; intracellular organelle part	Endocytosis
Clathrin heavy chain 1	CLTC	Antigen processing and presentation	Clathrin-coated vesicle membrane	Endocytosis
Neural cell adhesion molecule 1	NCAM1	Cell-cell adhesion	Anchored to membrane, cytoplasmic part	Cell adhesion molecules

List here represents an extract (top 10) from list S2 which can be found in the supplement section (page 133). This list contains the 200 proteins found to correlate with dysferlin profile within analyzed samples. The list was ranked for protein raw intensities of IP fraction purified by rAb from control myotubes. Gene Ontology (GO) terms for biological function and cellular compartment, and Kyoto Encyclopedia of Genes and Genomes (KEGG) terms associated to vesicles are displayed.

Results

5 Discussion

Limb-girdle muscular dystrophies (LGMDs) are a heterogeneous group of progressive muscular dystrophies with common features such as elevated serum creatine kinase (CK) values and skeletal muscle weakness caused by mutations of proteins involved in different cellular functions. Mutations in the dysferlin gene cause LGMD 2B. Skeletal muscle of patients was shown to display accumulation of subsarcolemmal vesicles (Cenacchi, Fanin, De Giorgi, & Angelini, 2005). Dysferlin is a transmembrane protein and its subcellular localization is predominantly allocated to the plasma membrane but also to developing T-tubules and intracellular vesicles. Dysferlin was shown to be crucial for membrane repair at the plasma membrane of muscle cells (Bansal, Miyake et al. 2003), although it has been proposed to be involved in many other cellular mechanisms. Another type of LGMD, LGMD 1C, is caused by mutations in the caveolin-3 (cav-3) gene (Minetti, Sotgia et al. 1998). Cav-3 is the muscle-specific isoform of the caveolins which, along with the cavin protein family, are the major structural and functional components of caveolae. Caveolae represent a specialized type of membrane microdomains referred to as lipid rafts (LRs). These dynamic membrane domains are characterized by their distinct protein and lipid composition, which differentiates them from the surrounding membrane environment. They have multiple roles in cellular signaling, endocytosis, lipid and cholesterol metabolism as well as mechanosensing (reviewed by Bastiani and Parton, 2010). Interestingly, cav-3 regulates dysferlins localization and rate of endocytosis at the plasma membrane (Hernandez-Deviez, Howes et al. 2008), which indicates that both proteins might be linked functionally. Recently, recessive mutations in the anoctamin-5 (ano-5) gene could also be related to LGMDs (Bolduc, Marlow et al. 2010). As seen for dysferlinopathies, *ANO5* mutations can lead to a LGMD or MM clinical phenotype. Ano-5 is a member of the anoctamin protein family which share protein domain similarities and thereby are thought to function as calcium-activated chloride channels (reviewed in Kunzelmann, Tian et al. (2011). Interestingly, the clinical picture of anoctaminopathies displays various similarities compared to dysferlinopathies.

In order to reveal the molecular mechanisms underlying LGMD and to investigate the putative interactions of dysferlin, cav-3, and ano5, experiments on primary skeletal muscle cell lines with disease-related mutations in *DYSF*, *CAV3,* and *ANO5* have been analyzed in this study.

Discussion

5.1   Characterization of the LGMD 2L phenotype

5.1.1 Comparison of histopathological features in LGMD 2B and LGMD 2L

LGMD 2L is a muscular dystrophy caused by *ANO5* mutations, which has been described quite recently and many characteristics of the disease still remain unclear. During my PhD, skeletal muscle biopsies from two diagnosed LGMD 2L patients were available for investigations on tissue as well as on cellular level (see Table 5-1). Patient Ano5-1 harbors the common founder mutation c.191dupA in a homozygous state, which results in a shift of the reading frame and introduces a premature stop codon in exon 5 (Bolduc et al., 2010). Patient Ano5-2 presented with the c.191dupA mutation in a compound heterozygous state and with a second mutation in intron 8. The second mutation is thought to introduce a putative splice site. Both mutations are located within the N-terminus of the protein before the first transmembrane domain. As mentioned above the c.191dupA mutation introduces a stop codon. Thus it is highly probable that the protein is not functional and loses its membrane binding capacity. However, heterozygous carriers seem not to be affected which makes a dominant effect of the mutation unlikely (Hicks et al., 2011). Clinical presentation was similar for both patients in this study. They presented with clinical symptoms similar to LGMD 2B such as slowly progressive weakness of limb-girdle muscles and disease onset in adulthood. Interestingly, patients were good sportsmen in early adulthood and remain ambulant at that time.

Histopathological findings show strong similarities to dysferlinopathies. Skeletal muscle biopsies revealed typical dystrophic features like increase of centralized nuclei, connective tissue split, and whirled fibers. Surprisingly, dysferlin labeling did not seem to be absent or mislocalized in skeletal muscle tissue from LGMD 2L patients, though dysferlin pattern seems to be slightly irregular (see Figure 4.1). LGMD 2B was the first muscular dystrophy described to associate with amyloidosis (Spuler et al., 2008). Amyloid deposits were found in blood vessels as well as at the sarcolemma of muscle fibers and contained a putatively cleaved form of dysferlin. Due to the prominent clinical similarity between LGMD 2B and LGMD 2L, we hypothesized that patients with *ANO5* mutations might also be associated with amyloidosis. We could show the presence of amyloid deposits in LGMD 2L skeletal muscle localized in the perivascular space but also around muscle fibers. Several recent studies during my PhD also reported amyloid deposits in skeletal muscle from anoctaminopathy patients, though predominantly around blood vessels (Liewluck et al., 2013; Wahbi et al., 2013). In one publication, the protein composition of amyloid plaques from anoctaminopathy and dysferlinopathy patient muscle was analyzed by laser caption

microdissection and mass spectrometry (Liewluck et al., 2013). In vascular amyloid deposits neither dysferlin nor ano-5 could be detected. This might be due to low amounts of both proteins within the deposits or due to a different amyloid forming process. It has to be mentioned that dysferlin and ano-5 could also not be detected in amyloid deposits from other dystrophic muscles used as controls (dysferlinopathy and gelsolin amyloid deposits) indicating technical limitations of this study. In contrast to the other studies, we could show that amyloid deposits were not only found at blood vessels but also around muscle fibers. Further characterization of the protein composition of the amyloid plaques remains to be done. Presence of amyloid deposits around muscle fibers indicate that ano-5 indeed has a function at the sarcolemma and that protein mutations might lead to misfolding and loss of function. It can be speculated that aggregation of cleaved forms of the ano-5 protein are responsible for the formation of amyloid plaques as has been described for *DYSF* mutations (Spuler et al., 2008). Furthermore, this study proposes that during the differential diagnosis of LGMDs amyloid deposits should not only be attributed to LGMD 2B but also to LGMD 2L.

LGMD 2B patient muscle was shown to display inflammatory changes (Cenacchi et al., 2005; Gallardo et al., 2001; Spuler & Engel, 1998). It could be shown that in LGMD 2B skeletal muscle biopsies CD4- and CD8-positive infiltrating cells were present, mainly located in the perivascular space (Choi et al., 2009). Here, immunolabeling for CD4 and CD8 in LGMD 2L patient muscles also revealed an infiltration of the perivascular space between muscle fibers with CD4- and CD8-positive cells. The presence of inflammatory changes in LGMD 2L needs to be taken into account during clinical diagnosis. Especially, misdiagnosis with other inflammatory myopathies such as polymyositis should be avoided. Taken together, various histopathological similarities between LGMD 2B and LGMD 2L could be demonstrated, further raising the question if dysferlin and ano-5 interact and how they might be linked to each other.

5.1.2 Characterization of recently recruited LGMD 2L patients

In order to reveal ano-5 function in skeletal muscle, more studies on tissue as well as on subcellular levels should be performed. Lately, four new patients with ANO5 mutations could be recruited from our outpatient clinic. Patient ANO5-3 harbors the founder mutation c.191dupA in a homozygous state equivalent to patient ANO5-1 included in this study. Myoblast culture from patient ANO5-1 was difficult because the primary cell population contained high amounts of contamination from non-muscle cells. We improved the myoblast purification procedure and could further increase the purity of myoblast isolates for this sample. The patient presented with very high CK-values (see Table 5-1), problems

during walking, and asymmetric atrophy of calve muscles (see also Figure 1.11). Within 10 years, muscle weakness of proximal muscles of the limb-girdle as well as of distal hand muscles developed. Patient ANO5-4 harbors the founder mutation in a compound heterozygous state together with a second mutation in exon 11. First symptoms were hyperCKemia, exercise-induced myalgia in hand muscles, and problems during climbing of stairs in adulthood. During the progress of the disease asymmetric hypertrophy of calves and weakness of proximal arm muscles developed. Since occurrence of first skeletal muscle symptoms, also tachycardia was prominent and a limited cardiac function manifested. Patient ANO5-5 harbors the founder mutation c.191dupA and the mutation c.877A>C in exon 9, both in a compound heterozygous state. The patient presented with first symptoms during stair climbing and uphill walking around 47 years. Disease course proceeded with impairment in ambulation, frequent occurrence of cramps in hands and feet, and myalgia in proximal limb-girdle muscles. About five years later, the patient was unable to work due to proximal and distal muscle weakness as well as low atrophy in biceps muscles. Asymmetrical involvement of distal muscles was also prominent. Histological characterization displays highly dystrophic features but no inflammatory signs. However, Congo red staining also shows amyloid accumulation around muscle fibers (data not shown). It has to be mentioned that the patient also harbors a non-clinical relevant calpain-3 mutation (c.134C>T, exon 27, homozygous). Patient ANO5-6 presented with hypertrophy of calves and sports-induced myalgia in early adulthood. The histological picture is composed of fiber size variations, presence of necrotic fibers, and increase in endomysial connective tissue. Interestingly, dysferlin and desmin labeling showed an irregular pattern. The patient has a homozygous mutation in exon 21, which has been described in homozygous as well as in heterozygous state together with the founder mutation in few patients from the United States (Liewluck et al., 2013; Witting et al., 2013). Interestingly, this patient also presented first symptoms such as hyperCKemia and exercise-induced myalgia in early adulthood. For this patient also a mild cardiomyopathy has been described. Another patient who harbors this mutation in a homozygous state was symptomatic indicating that this mutation is pathogenic (www.dmd.nl). Exon 21 is predicted to be localized in an extracellular loop before the eighth transmembrane domain at the C-terminus of the protein. The pathogenicity of this mutation indicates that this protein domain might be important for protein function. Whether it is crucial for oligomerization of anoctamins or for interaction with other proteins remains to be elucidated.

Table 5-1 Details on LGMD 2L patient recruited from our outpatient clinic

Patient number	Mutation on cDNA level	State	Mutation on protein level	CK level [U/l]	Biopsy [age]	Gender
ANO-5_1*	c.191dupA (exon 5)	Homozygous	p.Asn64LysfsX15	N.A.	Vastus lateralis [38]	M
ANO-5_2*	c.191dupA / c.2521-1delG	Compound heterozygous	p.Asn64LysfsX15 Putative splice site	>3,000	Vastus lateralis [43]	M
ANO-5_3	c.191dupA (exon 5)	Homozygous	p.Asn64LysfsX15	>10,000	-	M
ANO-5_4	c.191dupA / c.1119+1G>T (exon 11)	Compound heterozygous	p.Asn64LysfsX15 -	>3,000	-	F
ANO-5_5	c.191dupA / c.877A>C (exon 9)	Compound heterozygous	p.Asn64LysfsX15 p.Lys293Gln	>3,000	Vastus lateralis [64]	F
ANO-5_6	c.2498T>A (exon 21)	Homozygous	p.Met833Lys	>3,000	Vastus lateralis [28]	F

*Patients have already been included in this study.

Abundance of the founder mutation c.191dupA in the cohort of anoctaminopathy patients from our outpatient clinic is coherent with the known prevalence for the founder mutation in Northern Europe (Hicks et al., 2011). Further investigations on tissue as well as cellular level *in vitro* will help to dissect ano-5 function and explain the multiple common features of LGMD 2B and LGMD 2L. It is needless to say that the generation of a capable anti-ano-5 antibody would ameliorate research conditions enormously, particularly because studies on overexpressed non-endogenous protein already led to much confusion in the field.

5.1.3 Characterization of human primary myotubes derived from LGMD 2L patient muscle

Results from histological investigations on tissue level propose a functional link between ano-5 and dysferlin. We aimed to get a closer look on the putative interaction of these two proteins on cellular level. Primary myoblasts were purified from LGMD 2L skeletal muscle biopsies and, hence, represent a great tool to investigate the subcellular localization of proteins that might be involved with ano-5 function. Differentiation of LGMD 2L myoblasts to myotubes was shown not to be impaired which was confirmed by the presence of several myogenic differentiation markers (see Figure 4.2 A). This indicates that ano-5 is not involved in membrane fusion during myotube formation *in vitro*. Concerning dysferlin, functions during membrane fusion and cell-adhesion have been proposed lately (de Morree et al., 2013). However, the cell-cell adhesion marker CD56 together with the extracellular matrix glycoprotein fibronectin showed a normal distribution, which further supports the conclusion that ano-5 might not be involved in the cell adhesion process. Investigation of dysferlin and cav-3 subcellular localization showed no alterations especially not at the plasma membrane. Quantification of morphologically defined

caveolae at the plasma membrane have been done for several LGMD skeletal muscle cell lines, including cells from patients with mutations in *ANO5*. Interestingly, the percentage of caveolae with a visible connection to the plasma membrane confirmed by transmission electron microscopy (TEM) was significantly increased in cell lines with *ANO5* mutations compared to control and cell lines with mutations in *DYSF* and *CAV3*.

Ano-5 is a member of the anoctamin protein family. They are thought to be membranous proteins and might function as CaCCs. So far, *in vitro* studies give contradictory results on the functionality of ano-5. Only anoctamin-1 and anoctamin-2 were found to create currents similar to endogenous CaCC currents at the plasma membrane (Schreiber et al., 2010), whereas for ano-5 strong evidence is missing. Additionally, the subcellular localization of ano-5 is still unknown. The first description of ano-5 postulated a colocalization with calreticulin at the endoplasmic reticulum (Tsutsumi et al., 2004), which could not be confirmed in later studies. Localization at the plasma membrane was demonstrated for overexpressed protein, but functionality at this site remains controversial. Several points indicate that some anoctamins might not function at the plasma membrane at all but rather in intracellular membrane compartments. Endogenous levels of ano-5 seem to be low. Controversial results on subcellular localization might arise from artefacts caused by protein overexpression. Indeed, the major issue up to this date is non-availability of a suitable antibody to target endogenous protein. Therefore, we attempted to create a polyclonal peptide-derived anti-ano-5 antibody raised in rabbit. Three different peptides targeting the human ano-5 protein sequence were designed and three animals per peptide were immunized. As mentioned above, proteins of the anoctamin family are thought to harbor eight transmembrane domains, which made it difficult to find a suitable target sequence for antigen binding. Several studies indicate that anoctamins might oligomerize at the membrane to form a transmembrane pore (Kunzelmann et al., 2011) which further complicates predicting putative antigen-binding peptides. Three different peptides were designed whereas two were targeting the N-terminus and one peptide targeting the C-terminus. Unfortunately, none of the affinity-purified antibodies did result in specific detection of endogenous ano-5. Specificity was evaluated by immunofluorescence on frozen sections of human skeletal muscle tissue, on acetone or formaldehyde fixed primary human muscle cells, and finally by western blot analysis of the denatured protein from whole cell lysates (data not shown).

5.1.4 Anoctamin-5 and membrane repair in skeletal muscle cells

Similarities between LGMD 2B and LGMD 2L patients were observed from clinical presentation as well as by histopathological findings. Since dysferlin is thought to be

involved in plasma membrane repair, we hypothesized that ano-5 might have a similar skeletal muscle related function. Defects during membrane repair *in vitro* could be described for non-dysferlinopathy MM fibroblasts (Jaiswal et al., 2007). To explore the role of ano-5 in dysferlin-mediated membrane repair, we used a well-established assay from our group (Marg et al., 2012). Myotubes have been injured by laser-irradiation in presence of a membrane impermeable fluorescent dye. In normal myotubes, the membrane rapture can be resealed shortly after injury and the fluorescent dye is prevented to further enter the cell. In this study, membrane resealing capacity for differentiated myotubes derived from LGMD 2 L patient muscles appeared to be normal. These results show that ano-5 might not be involved in membrane repair but rather in other processes at the sarcolemma or might function in intracellular membrane compartments.

It is of interest to know whether ano-5 is localized to the sarcolemmal in healthy skeletal muscle, particularly to understand how dysferlin, cav-3, and ano-5 might be linked to each other. The interaction of dysferlin and cav-3 alone already seems to be complex. On the one hand, dysferlin localization and rate of endocytosis at the plasma membrane is dependent on cav-3. On the other hand, involvement of caveolae during dysferlin-mediated membrane repair might be relevant. In order to reveal this complex association between dysferlin and cav-3, studies on subcellular localization have been done.

5.2   Dysferlin and caveolae

5.2.1 Subcellular localization of dysferlin and caveolin-3 in human myotubes

Immunohistochemistry experiments showed that dysferlin and cav-3 are predominantly localized at the sarcolemma in healthy skeletal muscle (see also Figure 4.4). However, after antigen-retrieval dysferlin labeling can also be found inside of glycolytic type 2 fibers (see Figure 1.6). The association of both proteins with the sarcolemma is known but if these proteins interact directly remains to be elucidated.

Subcellular localization of dysferlin and cav-3 was analyzed by immunofluorescence and revealed a partial colocalization of both proteins in control myotubes. Dysferlin and cav-3 colocalize in distinct areas at the plasma membrane, although most of the labeling is assigned to different cellular compartments. Dysferlin is predominantly localized in a more diffuse pattern at the plasma membrane and inside the cytosol. This supports the hypothesis that dysferlin might be involved in many intracellular processes such as vesicular transport and glycolysis (Schoewel, Keller et al. 2014; submitted manuscript). In

contrast, cav-3 shows a more prominent localization to the plasma membrane compartment compared with dysferlin, as well as an accumulation within distinct areas. Interestingly, sites of colocalization with dysferlin appear to be in regions of accumulated cav-3 possibly reflecting clustering of caveolae/LR. As caveolae cannot be visualized by conventional light microscopy techniques due to the resolution limit, more detailed investigation were done by TEM.

TEM analyses reveal information on ultrastructural level but are limited regarding the detection of immunolabeling. The immunolabeling technique developed by Tokuyasu makes it possible to obtain a convenient preservation of ultrastructure and accessibility of antigens due to rather light fixation compared to conventional TEM sample preparation. Nevertheless, this technique is highly dependent on capable antibodies as background labeling can easily lead to misinterpretation of data. Antibodies for the muscle-specific cav-3 were not suitable for immunolabeling and gave no specific results. Therefore, we decided to use PTRF as marker for caveolae. We could show that PTRF localizes in vesicular structures at the plasma membrane in normal skeletal muscle cells. Labeling was also found inside the cytosol probably reflecting soluble protein. Mutations in *DYSF* and *CAV3* did not alter PTRF localization at the plasma membrane. However, the Tokuyasu technique only reveals antigens at the surface of ultrathin sections, which makes it difficult to detect low abundant proteins. In the last years, many good tools for visualization of such complex endocytic events developed in the last years. Particularly, a variety of correlative light and electron microscopy (CLEM) approaches emerged. Such techniques would be suitable tools to further investigate the complex interplay of dysferlin and cav-3 in context to LR dynamics. So far, these approaches require complex technical setups and correlation software, but have not been available during my doctoral thesis. Nevertheless, first hints on an association of dysferlin with the LR compartment can be obtained by experiments on membrane resistance to detergents, which is described in the next chapter.

5.2.2 Dysferlin and lipid rafts

LR are dynamic and distinct platforms within cellular membranes that are involved in membrane trafficking, cell polarization, and signal transduction (Rajendran & Simons, 2005). They are enriched in cholesterol, sphingolipids, and membrane-associated proteins such as GPI-anchored, transmembrane, or acylated proteins. The distinct lipid and protein environment differentiates them as liquid-ordered membrane platform from the surrounding more liquid-disordered phase (Simons & Ikonen, 1997). This feature makes it possible to biochemically purify LR as so-called detergent-resistant membranes (DRMs)

by treatment with a nonionic detergent and flotation to a characteristic density following an equilibrium density gradient centrifugation. DRM purification has for many years been the gold standard for investigations on LR, although it has to be kept in mind that DRMs do not reflect the membrane organization at steady state in cellular membranes. Biochemical purification of DRMs does have intrinsic limitations and cannot be directly equated with LR *in vitro* or *in vivo*. Nevertheless, it is a simple and powerful tool for investigations on proteins that might be localized to these distinct membrane compartments (Lingwood & Simons, 2007).

Results from our group showed that dysferlin-deficiency leads to down-regulation of the complement inhibitor, decay-accelerating factor/CD55, a GPI-anchored protein, in murine and human skeletal muscle (Wenzel et al., 2006). Therefore, it was hypothesized that dysferlin might be associated with LR and that LR-formation might be disrupted in dysferlinopathy. It has been reported that dysferlin associates with DRMs from human endothelial cells (Karsan et al., 2005; A. Sharma et al., 2010) and human neutrophil azurophil granules (Feuk-Lagerstedt, Movitz, Pellme, Dahlgren, & Karlsson, 2007). More recently, it could be shown that dysferlin is aggregated in LR macrodomains after Fas-ligand stimulation in bovine coronary arterial endothelial cells (CAECs) (W. Q. Han et al., 2012). In this study, however, we showed that dysferlin associates with LR in murine and human skeletal muscle cells. Cav-3, a marker for caveolae, which represents a subclass of LR, was found in the same DRM fractions as dysferlin. It has to be mentioned that most dysferlin is localized to soluble fractions representing cytosolic proteins and detergent non-resistant membranes. Localization studies on subcellular level showed that dysferlin is indeed localized in intracellular vesicular membrane compartments (see chapter 4.2). Thus, these results indicate that plasma membrane dysferlin is associated with the membrane raft compartment. We also investigated if DRM isolation might be impaired in dysferlinopathy. Therefore, we isolated DRM from human differentiated muscle cells derived from LGMD 2B patient skeletal muscle. In these patients, mutations in *DYSF* either led to dysferlin deficiency, or reduced levels of dysferlin with absent localization at the plasma membrane and intracellular accumulated protein (Philippi et al., 2012). DRM formation was not impaired in dysferlinopathy, regardless if dysferlin is totally absent or only reduced. In the latter case, immunofluorescence labeling showed that dysferlin, indeed, was not localized at its major site of function at the plasma membrane but was retained within the cell (see also chapter 4.2). DRM preparation from this cell line showed that dysferlin protein levels were significantly reduced and residual dysferlin was only found in heavy gradient fractions representing detergent-soluble and cytosolic proteins (see Figure 4.10). Dysferlin showed no association with DRMs, reflecting that plasma membrane dysferlin is absent in these cells. A recent publication from our group showed

that treatment with cell-penetrating TAT-peptides can reallocate mutant dysferlin back to the plasma membrane and restores its functional ability for membrane repair. Laser-induced membrane injuries could be resealed with values close to control cells from unaffected skeletal muscle (Schoewel et al., 2012). It would be interesting to investigate, if the reallocation of mutant dysferlin to the plasma membrane also leads to a "re-association" with the raft compartment. This would emphasize that plasma membrane dysferlin is associated with LRs. Enrichment of dysferlin in DRMs after TAT-treatment would also indicate that dysferlin function in membrane repair might be mediated by formation of LR macrodomains. Aggregation of LR nanoclusters to macrodomains at the plasma membrane are thought to be mediated by rearrangements of the cytoskeleton, namely by actin-filaments. In order to reveal if dysferlin might be involved in actin-mediated LR formation we conducted further experiments on DRMs linked to the actin-cytoskeleton.

5.2.3 Dysferlin and actin-related cellular functions

As mentioned above, an association of dysferlin with DRMs could be demonstrated for murine and human differentiated skeletal muscle cells. Several studies propose a role for dysferlin as membrane fusion and vesicle transport protein. Vesicle transport within the cell is closely linked to components of the cytoskeleton such as microtubules and actin-filaments. The actin-cytoskeleton is a highly dynamic structure, which can be regulated by extracellular signals. In many cell types the actin-cytoskeleton plays an important role in the formation and dynamics of LRs. Especially, aggregation of raft nanoclusters to macrodomains is thought to be mediated by signals that induce actin polymerization/nucleation to cellular membranes (Rajendran & Simons, 2005). In chapter 4.3.3 we showed that dysferlin associates with a subgroup of DRMs linked to the actin-cytoskeleton in human myotubes. Depletion of cholesterol by treatment with methyl-β-cyclodextrin completely abolished the association of dysferlin with the actin-cytoskeleton. This indicates that the presence of dysferlin in DRMs reflects its presence in actin-linked LR at the plasma membrane.

Studies from our group showed that actin is involved in the formation of a membrane repair dome in laser-injured muscle cells (Marg et al., 2012). This repair dome occurred shortly after membrane rapture but built up for several minutes beyond membrane rupture resealing. Proteins found to localize to the dome were dysferlin, annexin A1, F-actin, EHD2, but not cav-3. EHD2 is a member of the EH domain-containing protein family and could be related to membrane repair for the first time. Furthermore, other studies showed that EHD2 can link clathrin-mediated endocytosis to actin dynamics (Guilherme et al.,

2004). During membrane repair actin-rearrangement are crucial for recruitment of intracellular vesicles to site of injury, formation of a resealing patch as well as for endocytosis of ruptured membrane. Dysferlin and cav-3 were found to be closely related during intracellular trafficking (Cai, Weisleder, et al., 2009; Hernandez-Deviez et al., 2008; Matsuda et al., 2001). Conversely, they do not seem to interact directly with each other at the plasma membrane, thus, a possible link during membrane repair could be EHD2. In a recent publication, EHD2 was found to be localized to caveolae and seems to be crucial for caveolae stability and dynamics (Moren et al., 2012).

A recent publication by McDade et al. (2014) investigated the membrane repair mechanism in relation to actin dynamics at the plasma membrane. They proposed an alternative model where sarcolemmal-derived dysferlin is recruited to the site of injury. Thus, plasma membrane wounding is resealed by "pulling in" of sarcolemmal dysferlin where it forms a stable dysferlin rich structure. Additionally, they observed increased endocytosis at the site of membrane rupture followed by formation of large dysferlin-containing vesicles. Interference with the actin-cytoskeleton impaired the membrane resealing through blocking the recruitment of plasma membrane dysferlin to the site of injury. However, endocytosis and formation of dysferlin vesicles seem to be actin-independent. This model is contradictory to the popular model of membrane repair where dysferlin-mediated intracellular derived vesicles are recruited to the site of injury and subsequently form a resealing patch. The recruitment of dysferlin to the plasma membrane is thereby dependent on cav-3 (Hernandez-Deviez et al., 2006). In the same study, they postulated that dysferlin is only localized to the sarcolemma and T-tubules, but could not be found in intracellular vesicles. In this study, however, we could clearly show that dysferlin was localized at the plasma membrane as well as in intracellular vesicles in differentiated skeletal muscle cells (see chapter 4.2). As dysferlin was proposed to have multiple cellular functions and the number of reported putative interacting partners is increasing, it is highly unlikely that dysferlin is not localized to an intracellular vesicular compartment.

Studies by our group showed that membrane resealing indeed is mediated by extensive actin-rearrangements at the site of membrane disruption in differentiated muscle cells. After laser-induced injury, the surrounding plasma membrane reacts by a "contraction" of the myotube visible under the microscope and subsequently the repair dome is formed. If these massive actin-rearrangements are mediated by aggregation of LR to macrodomains, thereby recruiting proteins of the repair machinery remains to be elucidated. Attempts to induce membrane injury on high numbers of adherent cells by glass bead wounding did not result in satisfactory levels detectable by DRM purification.

Discussion

Minor compartment switches of membrane proteins after membrane wounding might be too delicate to monitor and should be confirmed with more suitable techniques. Pharmacological manipulation of actin polymerization would have been a great tool to investigate the role of actin-linked LRs in dysferlin-mediated membrane repair. Interestingly, proteome analysis of dysferlin-containing vesicles revealed the presence of the LR marker cav-3 as well as actin. This shows that results obtained by DRM purification indeed reflect an association of dysferlin with LR linked to the actin-cytoskeleton.

To bring these observations together, it can be speculated that shortly after membrane rupture plasma membrane dysferlin is recruited to the site of injury through lateral lipid and protein movements. This could be done through clustering of dysferlin-containing LR mediated by actin rearrangements. The association of dysferlin with DRMs linked to the actin-cytoskeleton supports this model. Raft clustering at the site of injury is thought to be an early response to membrane injury, as actin-rearrangements were described to be present during the first seconds after injury (Marg et al., 2012). Together with other proteins such as MG53 and annexins, dysferlin might also mediate recruitment of intracellular vesicles for resealing. These membrane fusion events require further intracellular reorganization of the cytoskeleton to make recruitment of intracellular vesicles and patch formation possible. Rearrangements at the plasma membrane due to the resealing processes might be indirectly linked to caveolae. It has to be kept in mind that the plasma membrane has a delicate lipid-protein environment with distinct forces which have to be in equilibrium. Caveolae were shown to be able to buffer tension and act a membrane reservoir at the plasma membrane (Sinha et al., 2011). This study underlines how crucial it is to maintain membrane integrity in the surrounding membrane environment during the resealing process.

As mentioned above, an association of dysferlin to LRs should be confirmed by other techniques besides biochemical purification of DRMs. Some years ago, visualization of these dynamic membrane platforms was difficult and led to the uncertainty if LRs exists *in vivo*. Nowadays, several techniques with high temporal and spatial resolution such as total internal reflection fluorescence (TIRF) microscopy make it possible to extensively study LR dynamics at the plasma membrane. Moreover, super-resolution optical microscopy such as stimulated emission depletion (STED) microscopy have been used to track lipids and GPI-anchored proteins to cholesterol enriched complexes (Eggeling et al., 2009). To learn more about the impact of lipid and protein composition on the formation of membrane rafts, artificial systems like giant unilamellar vesicles (GUVs) or supported bilayers can be used (Kahya & Schwille, 2006). Minor shifts of proteins from the non-raft

liquid-disordered to the liquid-ordered phases can thereby be monitored. Some of these techniques could used to characterize the putative association of dysferlin with LRs linked to the actin-cytoskeleton further. This association might be relevant to fully resolve the processes underlying membrane repair.

Summarized, biochemical purification of DRMs revealed that dysferlin might be involved in actin-mediated LR rearrangements at the sarcolemma during membrane repair. To further investigate the role of caveolae in the context of LGMD, we aimed to characterize their ultrastructure by TEM.

5.2.4 Abundance of caveolae in human skeletal muscle cells

Caveolae have been shown to be relatively stable and immobile structures at the plasma membrane (Hommelgaard et al., 2005), although budding can be induced under specific conditions such as viral infection or treatment with cholera toxin. In this study, we circumvented the induction of budding events, because we wanted to monitor the endogenous pool of caveolae under non-stimulated conditions. A relatively high abundance of caveolae has been described especially for adipocytes, endothelial cells, and smooth muscle (reviewed in Parton and Simons (2007)). Our results revealed that the abundance of caveolae in skeletal muscle cells is less frequent with values around 0.05 caveolae per µm plasma membrane. As mentioned above, this might be due to missing triggering of endocytosis by extracellular signals. In many studies the unspecific marker ruthenium red is used to enhance plasma membrane contrast and to label endocytic structures. This plasma membrane marker has the advantage to mark structures which are connected to the cell surface or have been endocytosed during the fixation process. Nevertheless, the labeling remains unspecific for all endocytic events and it cannot be excluded that treatment with ruthenium red might induce artefacts at the plasma membrane. Decreased amounts of caveolae in comparison to the literature might be due to lack of additional plasma membrane contrast or due to fewer numbers of caveolae in myotubes *per se*. In this thesis, different approaches for caveolae quantification have been used to address this question. First, caveolae in open state with direct connection to the plasma membrane were counted. Second, structures which might have been missed due to a wrong sectioning angle (vesicles in vicinity of 200 nm to the plasma membrane) were included during quantification (see also Figure 4.12 A). This population was defined as plasma membrane vesicles. The amount of total caveolae resulted from addition of caveolae in open state and plasma membrane vesicles. As negative control PTRF-deficient fibroblasts lacking caveolae were used (Rajab et al., 2010). Our results show that the endogenous pool of caveolae can be visualized at the plasma membrane of skeletal

muscle cells without using ruthenium red as cell surface label or inducing caveolae-mediated endocytosis. Quantification of these structures was able to reveal differences in caveolae frequency between different muscle cell lines derived from LGMD patients.

As demonstrated, deficiency in PTRF, a major structural protein of caveolae, results in lack of caveolae at the cell surface. Surprisingly, muscle cells derived from patients with mutations in *CAV3*, a gene coding for the second major structural protein of caveolae in muscle cells, do show morphological intact caveolae at the plasma membrane. Furthermore, quantification of caveolae in open state revealed an abundance of caveolae at the plasma membrane equal to control cells derived from normal skeletal muscle. In this context, the caveolae structure protein PTRF seems to be crucial for formation and stability of caveolae, whereas cav-3 seem to be less relevant. Nonetheless, it has to be kept in mind that LGMD 1C is an autosomal dominant MD and mutations in *CAV3* thereby do not lead to a total absence of cav-3. These results highlight that even though cav-3 protein levels are reduced, residual protein seems to be sufficient for caveolae formation. It is astonishing that patient derived myotubes show no alterations in caveolae abundance at the plasma membrane, because the dystrophic phenotype in patients and mouse models would indicate an alteration of the sarcolemmal structure. The amount of plasma membrane vesicles is significantly reduced in LGMD 1C myotubes compared to control and LGMD 2B myotubes indicating defects in endo- or exocytosis. Accumulation of subsarcolemmal vesicles as seen in LGMD 2B has not been reported so far in skeletal muscle from LGMD 1C patients. As already mentioned, cav-3 was reported to regulate dysferlin localization to the plasma membrane and rate of endocytosis (Hernandez-Deviez et al., 2008). Decrease of plasma membrane vesicles in LGMD 1C myotubes might be due to disturbed dysferlin endocytosis caused by non-functional cav-3.

Several publications described an accumulation of subsarcolemmal vesicles in dysferlinopathy (Cenacchi et al., 2005; Selcen et al., 2001) which nicely correlates with dysferlins role during patch-mediated membrane resealing. Here, we wanted to explore if variations in vesicle amounts are also present on subcellular level. TEM analysis were conducted on three different cell lines from LGMD 2B patients with different *DYSF* mutations leading to reduced or total absence of dysferlin protein. Surprisingly, significant variances in caveolae abundance at the plasma membrane could not be shown for LGMD 2B myotubes when compared to controls. A closer look on the data for the different LGMD 2B cell lines revealed variances in caveolae numbers probably due to different *DYSF* mutations. Mutations resulting in total protein absence led to significant increase in caveolae and membrane vesicles. The two LGMD 2B cell lines with mutations only leading to reduced protein levels showed values similar to control myotubes for both

endocytic structures. Interestingly, the number of clathrin-coated pits seemed to be inversely correlated to the number of caveolae. We speculate that the decrease of caveolae numbers is buffered by increase of the clathrin-mediated endocytic pathway. As subsarcolemmal accumulation of vesicles has been reported in human skeletal muscle (Selcen et al., 2001), it would be interesting to investigate whether *DYSF* mutation-correlated effects are also detectable in mature skeletal muscle. These results further support an impact of dysferlin on caveolae structure, dynamics, and function at the sarcolemma. The molecular mechanism underlying the correlation of dysferlin protein amounts with abundance of caveolae at the plasma membrane remains to be elucidated.

5.2.5 Investigations on caveolar dynamics

Investigations on caveolae dynamics and trafficking remain difficult as few specific cargo proteins are known for simple marker uptake experiments. Also caveolae budding was described to be infrequent and less dynamic in comparison to clathrin-mediated endocytosis (Hommelgaard et al., 2005; Thomsen, Roepstorff, Stahlhut, & van Deurs, 2002). Caveolins, the major structural components of caveolae are membrane-scaffolding proteins with the N-and C-terminus facing the cytosol. Caveolins can oligomerize, which results in approximately 140 copies per caveolae (Pelkmans & Zerial, 2005). Due to its protein structure and oligomerization capacity, external epitopes are not accessible for uptake experiments. However, to better understand caveolae function during endocytosis, monitoring of cholera toxin B (CTB) uptake was shown to be a powerful tool (Kirkham et al., 2005). Many studies use standard or even more advanced light microscopy (LM) techniques such as TIRF and STED/STORM for studies on endo and exocytosis (Willig, Rizzoli, Westphal, Jahn, & Hell, 2006). Unfortunately, LM does not reveal structural information behind the fluorescently labeled proteins. This limitation was overcome by applying correlative techniques such as correlative light and electron microscopy (CLEM). Another correlative approach is to visualize caveolae with confocal laser scanning fluorescence microscopy combined with atomic force microscopy (AFM). Recently, it was shown in our group that clathrin-coated pits as well as caveolae can be monitored and aligned by correlative LM-AFM (Timmel, Schuelke, & Spuler, 2014). Fibroblasts from patients deficient for *PTRF* (synonym to cavin-1) (Rajab et al., 2010) have been used in this approach as well as in this study. We analyzed these cells by conventional TEM and did not detect any caveolae in open state with direct connection to the plasma membrane (see also Figure 4.15). Quantification of so-called total caveolae resulted in significantly decreased amounts compared to control cells (see Figure 4.15). As mentioned above, data from caveolae in open state as well as vesicles in 200 nm proximity to the cell surface were grouped for the quantification of total caveolae. The low numbers of "total caveolae"

Discussion

in PTRF-deficient cells can therefore be explained by the fact that vesicles non-related to caveolae could not be distinguished from "real" caveolae in this assay. However, in further studies we could show that transfection of human primary fibroblasts with EGFP-tagged PTRF restored morphological intact caveolae at the plasma membrane, which also was confirmed by TEM (data not shown) (Timmel, Kunz et al. 2014; submitted manuscript). Furthermore, correlative LM-AFM revealed colocalization of PTRF with caveolin-1 at cell membrane depressions. Additionally, we were interested in investigating the impact of caveolae on CTB uptake. In our studies, fluorescence microscopy experiments showed that in control fibroblasts caveolin-1 colocalized with fluorescently-labeled CTB. This colocalization was absent in PTRF-deficient fibroblasts confirming the absence of caveolae at the plasma membrane (data not shown). In a second step, we used fluorescence-activated cell sorting (FACS) as a high throughput assay for monitoring CTB uptake. This assay was established as alternative to LM studies which can be susceptible to user bias and are limited for detailed statistical analysis. It has been reported that entry of CTB is not affected by presence or absence of caveolae (Kirkham & Parton, 2005). Interestingly, FACS sorting revealed that CTB uptake is decreased in PTRF-deficient fibroblasts compared to controls, which showed that caveolae indeed are involved in CTB uptake (data not shown). We could exclude bias by uptake through other endocytic pathways by colocalization with endogenous caveolin-1. As mentioned above, LM and TEM analysis showed that rescue through *PTRF*-transfection restored caveolae at the plasma membrane. We then hypothesized that rescue of caveolae structure at the cell surface would thereby also result in changes in CTB uptake. Unfortunately, FACS-analysis did not confirm our results from microscopy (data not shown) (Timmel, Kunz et al. 2014; submitted manuscript). Further experiments have to be done to reveal why morphologically intact caveolae at the plasma membrane do not seem to be functional.

Recently, a crucial role for caveolae in the context of membrane repair has been proposed (reviewed in Andrews, Almeida, and Corrotte (2014)). It has been hypothesized that membrane resealing is achieved by wound removal via endocytosis rather than by "patching" of the injury site. It is not known whether these mechanisms function independently or if they might be linked somehow. It remains to be elucidated if they are dependent on the cell type and tissue, thus are triggered by different injury-sensing factors.

5.3 Intracellular dysferlin vesicles

5.3.1 Establishment of an immunopurification assay for dysferlin-containing vesicles

The role of dysferlin during membrane repair in muscle cells has been extensively studied. Nonetheless, many aspects are still unclear and the underlying molecular pathways remain to be resolved. Many dysferlin functions might be linked to its localization in intracellular compartments, because many proposed interacting partners for dysferlin were not found to colocalize at the sarcolemma. To address this question, we aimed to purify the cytosolic dysferlin vesicle pool. Exploring the protein content of these vesicles could help to understand dysferlin function in membrane repair non-related processes. Additionally, we might learn more about rather indirect interactions through dysferlin vesicle cargo proteins. So far, analyses on dysferlin protein function were based on immunoprecipitation and localization studies of putative candidates (Huang et al., 2007; Matsuda et al., 2001; A. Sharma et al., 2010). Another more global approach was realized by immunoprecipitation of the dysferlin protein complex with subsequent liquid chromatography-mass spectrometry (LC-MS) analysis. Recently, several papers using this approach have been published proposing a wide range of putative new dysferlin interacting partners (de Morree et al., 2010; Flix et al., 2013).

The goal of this work was to establish a vesicle immunopurification (IP) assay for morphological intact dysferlin-containing vesicles. IP was performed with Protein A-beads linked to an anti-dysferlin antibody targeting the N-terminus of the protein. So far, structural information on the dysferlin protein are limited (Sula, Cole, Yeats, Orengo, & Keep, 2014; Xu et al., 2011), but it can be hypothesized from these studies that the N-terminus is available for antigen targeting. Due to protein domain similarities to other ferlin proteins, it has been proposed that the mayor part of the protein remains intracellular. The short C-terminal part of the protein following the transmembrane domain remains extracellular or inside vesicles, respectively. To this day, no clear evidence for the position of the protein within membranes has been shown. Here, we can demonstrate that intracellular vesicles can be trapped by antibodies targeting the N-terminal part of the protein (see Figure 4.22). This supports the hypothesis that dysferlin is associated with vesicular membranes and that the main (N-terminal) part of the protein remains inside the cytosol.

Discussion

5.3.1.1 Purity of the vesicle preparation

We could confirm enrichment of dysferlin in purified fractions and specificity of the assay for both tested anti-dysferlin antibodies by western blot analysis. Crude contamination by non-vesicular cellular components was ruled out by marker proteins for the endoplasmic reticulum, the plasma membrane, the nucleus, and the cytoskeleton. TEM analysis revealed that immunopurified structures were morphologically intact vesicles. These results showed that subcellular fractionation prior to IP was substantial to diminish contamination. The microsomal fraction used as IP input was shown to contain vesicles with diameters ranging from 50 to 200 nm. TEM analysis further confirmed that this prepurification step was successful to exclude cytoskeleton components. Most important, labeling of immunopurified vesicles bound to the bead surface confirmed that trapped vesicles were containing dysferlin (see Figure 4.22). These results along with analysis on dysferlin subcellular localization showed that dysferlin indeed is localized in intracellular vesicles. Accumulation of subsarcolemmal vesicle in dysferlinopathy patients and animal models also indicate a crucial involvement of dysferlin in intracellular vesicle trafficking in skeletal muscle. Immunolabeling of vesicular dysferlin in mature skeletal muscle should be confirmed on ultrastructural level in future experiments.

5.3.1.2 Specificity of different anti-dysferlin antibodies

Several anti-dysferlin antibodies targeting different protein domains are commercially available. Many immunoprecipitation studies were done using the NCL-Hamlet antibody (Novocastra) which targets the C-terminal part of the protein at position 1999-2016 aa in exon 53. However, first experiments did not give satisfactory results and we decided to exclude this antibody from IP experiments. As we aimed to purify intact vesicular dysferlin, we decided to use anti-dysferlin antibodies which target the N-terminus of the protein. For this application we used an antibody, which is commercially available and routinely used in our laboratory (see also 3.4.6). Heavy chain antibody fragments developed in the laboratory of Silvère van de Maarel were demonstrated to be a powerful tool for dysferlin detection (Huang et al., 2005). They were obtained from a nonimmune llama-derived phage-display library and were shown to be suitable for immunoprecipitation experiments (de Morree et al., 2010; Flix et al., 2013; Huang et al., 2005). For our studies, we selected the VHH antibody fragment (VHH) Dysf-F4 targeting exons 1-7 at the N-terminus of the protein.

Results from western blot as well as from LC-MS analysis showed that both antibodies were able to enrich dysferlin from control myotubes during purification with protein raw intensities of 6×10^7 for the rAb and 2×10^7 for the VHH. Surprisingly, the monoclonal

rabbit-derived antibody (rAb) did perform with a higher specificity compared to the VHH (see chapter 4.5.3). Proteome analysis of the vesicle fraction after IP with the rAb showed that this antibody is highly capable of purifying dysferlin-containing vesicles selectively from control cells (see Figure 4.26). It has to be mentioned that around 16 % of all proteins detected with the rAb were also purified from dysferlin-deficient myotubes. These proteins might represent cellular components attached to the trapped vesicles. Despite the fact that the microsomal fraction has been well resuspended, it cannot be excluded that cellular organelles might stick to each other. During subcellular fractionation the microsomal fraction is concentrated to obtain enough material for IP. Vesicles were carefully resuspended in EDTA-containing buffer to avoid sticking of vesicles to each other. Although TEM analysis revealed non-accumulated vesicular structures of various sizes, aggregation of vesicles could not be excluded and had to be considered as background in IP experiments. Note that only 1.7 % of all proteins detected with the rAb were exclusively isolated from dysferlin-deficient myotubes, which shows that the antibody did marginally copurify unspecific proteins due to sequence homologies to other proteins. In comparison, the VHH purified over 85 % of all detected proteins from both cell lines. Only around 9 % of all proteins purified with the VHH were selective for control myotubes. This high percentage of unspecific binding was also confirmed by TEM analysis. Incubation with microsomes from dysferlin-deficient myotubes resulted in binding of vesicular structures to the bead surface (see Figure 4.25). Unspecific binding to the Protein A-bead surface was excluded, thus no aggregation of vesicles was observed. It can be speculated that unspecific binding might be due to recognition of antigen sites in other proteins, for example myoferlin. It was found to be enriched after IP with the rAb from control myotubes with protein raw intensities of 1×10^8. Purification with the VHH resulted in values of 3×10^7 for control and 1×10^7 for dysferlin-deficient myotubes, respectively. Myoferlin shares a sequence identity around 70 % with dysferlin and has been described to be involved in dysferlin function (Davis et al., 2000). Overexpression of myoferlin in dysferlin-deficient mice restores dysferlin membrane resealing function *in vitro* although skeletal muscles still display a dystrophic phenotype (Lostal et al., 2012). In the key publication by de Morrée et al. (2013), results from immunoprecipitation experiments of the dysferlin protein complex using the same VHH also revealed high levels of myoferlin. They claimed that the VHH was specific for dysferlin and could not bind myoferlin directly. These conclusions were drawn from negative IP for myoferlin in U2OS cells, which do not express dysferlin. It has to be mentioned that, when expressing recombinant dysferlin in these cells, small amounts of myoferlin were co-immunoprecipitated with dysferlin which was not the case in non-transfected cells. They also claimed that immunoprecipitation of myoferlin with VHH fragment antibodies was not

successful in dysferlin negative myoblasts and myoblasts as judged from coomassie and western blot analysis, but not proteome analysis (data not shown). In comparison to our results, it is highly likely that the VHH Dysf-F4 did recognize another antigen, reflected by the high amounts of proteins detected in purified fractions from dysferlin-deficient myotubes. Whether the antigen detected was myoferlin or not remains to be elucidated with further experiments, although high raw intensities of myoferlin protein in VHH-IP fractions from dysferlin-deficient cells support this hypothesis (see Figure 4.27 D).

5.3.2 Identification of protein content of dysferlin vesicles by mass spectrometry

Immunopurification of dysferlin-containing vesicles was performed with two anti-dysferlin antibodies on control and dysferlin-deficient differentiated myotubes. Antibodies can be covalently bound to magnetic beads using chemical crosslinkers to prevent "leakage" of immunoglobulins in downstream applications. Here, we omitted this step because crosslinking might impair antigen-binding capacities of the antibodies. Proteins from bound fractions were separated through SDS-PAGE and analyzed by LC-MS. Protein A-beads alone were incubated with microsomal fractions from both cell lines and represented the negative control. With this approach nearly 1200 proteins were detected from all samples. 502 proteins were purified from control myotubes with both anti-dysferlin antibodies (see page 142). Data revealed that dysferlin vesicles contain already described interaction partners such as myoferlin, cav-3, annexin A1 and A2, ahnak, MG53 (TRIM72), α-tubulin, EHD2, and PTRF. Interestingly, also cav-1 and cav-2, and annexin A5 and A6 were also present in dysferlin vesicles, whereas calpain-3 was missing. Calpain-3 was shown to be a major component of the dysferlin protein complex purified by conventional immunoprecipitation assays. Calpain-3 is known to bind annexins A1 and A2 and to be involved in membrane repair (Lennon et al., 2003). The absence of calpain-3 in dysferlin vesicles confirms that the IP was selective for intact intracellular dysferlin vesicles and not for the dysferlin protein complex at the plasma membrane. Known dysferlin interacting partners not detected in IP fractions besides calpain-3, were the dihydropyridine receptor (DHPR) and affixin. Absence of these proteins in immunopurified dysferlin vesicles might reflect that the interaction with dysferlin is not mediated by vesicular but rather by plasma membrane-localized dysferlin.

5.3.2.1 <u>Classification of immunopurified dysferlin vesicle proteins</u>

As mentioned above, dysferlin was enriched in IP samples from control but not from dysferlin-deficient and negative control samples. Using the MaxQuant bioinformatics tool

Perseus, a dysferlin profile of the analyzed samples was created (see Figure 4.26). Correlating to this profile 200 proteins were grouped and are listed in Table 7-1. Exemplarily, the first 10 proteins are listed in Table 4-5. Proteins with highest raw intensities were prolow-density lipoprotein receptor-related protein 1 (LRP1), myoferlin (MYOF), transferrin receptor protein 1, and dysferlin. LRP1 belongs to the LDLR protein family and is thought to be involved in endocytic events at the plasma membrane. The high abundance of dysferlin and myoferlin confirmed that successful targeting of dysferlin-containing vesicles as dysferlin is known to interact with myoferlin. The role of the transferrin receptor in context to dysferlin function is unclear and will be discussed in chapter 5.3.2.2.

Analysis of gene ontology (GO)-terms by the GOrilla software (http://cbl-gorilla.cs.technion.ac.il/) revealed that immunopurified proteins can be attributed to the following cellular components: endo- and exocytotic vesicles, cytosolic vesicles, lysosomes, plasma membrane, clathrin-coated pits, and caveolae (see supplement Figure 7.1 GO classification of proteins for cellular compartments). These results correlate with already known dysferlin functions like membrane repair, cellular signaling, and vesicular transport, and additionally further strengths our hypothesis that dysferlin is closely associated with caveolae. Comparison analysis using the Ingenuity Pathway Analysis (IPA) software tool revealed the top canonical pathways possibly associated with dysferlin vesicles (see Table 4-4). Many of the identified pathways revealed known features of dysferlin function such as endocytic signaling, whereas some top-ranked pathways were rather unexpected. Germ cell-sertoli cell signaling and agrin interactions at the neuromuscular junction (NMJ) have not been described in context with dysferlin function. The clear meaning of these pathways in context to dysferlin function and LGMD remains to be established. At this point, we cannot exclude if results are representing a "real" biological process in dysferlin vesicles or if it is an issue related to *in silico* analysis. In future analysis, biological as well as technical replicates should be increased. Mass spectrometry is a powerful tool for proteome analysis but resulting data have to be interpreted with care and should be secured by statistical significant sample numbers and elaborate study design. Significance of the obtained data in this study for biological processes has also to be confirmed by colocalization studies and functional assays. The underlying molecular mechanism and their impact on muscular disease remain to be resolved in further experiments. However, these results indicate that dysferlin might be involved in many cellular processes which have not been described yet.

Discussion

5.3.2.2 <u>Putative novel dysferlin-associated proteins</u>

In this study, we found that agrin was enriched in immunopurified fractions from control myotubes with raw intensities around 2-5 x 10^7 for IP with both anti-dysferlin antibodies (see also Table 7-2). These results propose that agrin could be a dysferlin interacting partner or cargo of dysferlin vesicles. Recessive mutations in *AGRIN* can lead to congenital myasthenic syndromes (Maselli et al., 2012). Recently, a cohort of patients with a mixed phenotype of congenital myasthenic syndromes and distal myopathy were found to harbor mutations in *AGRIN* (Nicole et al., 2014). Congenital myasthenic syndromes are a clinically and genetically heterogeneous group of rare diseases affecting limb-girdle muscles resulting from impaired neuromuscular transmission. Distal myopathies are a form of primary muscle disorders, where weakness and atrophy are restricted to distal muscles. This is interesting in context to our finding that dysferlin vesicles contain agrin as well as the muscle-specific tyrosine-protein kinase receptor (MuSK). Recruitment of agrin to the MuSK signaling complex induces phosphorylation and activation of MuSK. In myotubes, MuSK activation mediates the formation of NMJs, through the regulation of different processes such as NMJ gene expression, the reorganization of the actin-cytoskeleton, and acetylcholine receptors (AChR) clustering in the postsynaptic membrane. Besides the neural isoform of agrin, which plays a crucial role at the NMJ, a muscle-specific isoform is known.

Interestingly, transferrin receptor protein 1 (TFRC1) and serotransferrin were enriched in IP fractions from control myotubes. For the TFRC1, protein raw intensities for IP from control cells with the rAb were 8 x 10^7 and for the VHH 3 x 10^7; and for serotransferrin 1 x 10^7, (rAb) and 3 x 10^6 (VHH), respectively. Transferrins are iron binding transport proteins, which are responsible for transport of iron ions from site of absorption to those of storage and utilization. Cellular uptake of iron occurs via receptor-mediated endocytosis of ligand-occupied transferrin receptor into specialized endosomes. So far, dysferlin-endocytosis was reported to be caveolin-dependent, possibly CTB-associated but transferrin-independent (Evesson et al., 2010; Hernandez-Deviez et al., 2006). However, Demonbreun et al. (2011) showed that transferrin and transferrin receptor recycling is impaired in dysferlin-deficient myoblasts. They showed that the rate of endocytic receptor-recycling is decreased and internalized transferrin remains accumulated near the nucleus. This fits with our data, because the presence of transferrin and TFRC1 in dysferlin-containing vesicles supports the hypothesis that dysferlin mediates receptor-recycling back to the plasma membrane. The mechanisms underlying this process and the role of dysferlin in endosomal iron-transport remain to be elucidated in further experiments.

5.4 Outlook and impact of the study

In this study, we showed that dysferlin and cav-3 function is closely connected, although a direct colocalization is not present. Cav-3, however, but not ano-5, was detected in dysferlin-containing vesicles by LC-MS analysis. We propose that caveolae play a crucial role in dysferlin-mediated membrane repair at the sarcolemma. Our data show that dysferlin is associated with actin-linked lipid rafts. Aggregation of lipid rafts to macrodomains might represent the underlying mechanism mediating dysferlin function during membrane repair or other processes at the plasma membrane. Ultrastructural investigations on plasma membrane morphology of skeletal muscle cells from patients with *DYSF*, *CAV3*, and *ANO5* mutations indicate that caveolae abundance is correlated with the phenotype of disease-causing mutations, especially for LGMD 2B.

Furthermore, we were able to successfully establish an IP assay for morphological intact dysferlin-containing vesicles. We also confirmed on ultrastructural level that dysferlin is associated with cytoplasmic vesicles in differentiated myotubes. Data validate already described dysferlin roles in endocytosis and vesicular trafficking, but also suggest novel functions like transferrin and transferrin receptor recycling, and MuSK-mediated AChR clustering. In further experiments, this assay could represent a specific and easy tool to monitor changes within the cytosolic dysferlin vesicle pool upon treatment with cellular signals. Recent work of our group showed that glycolysis seems to be disturbed in dysferlinopathy (Schoewel, Keller et al. 2014; submitted manuscript). Data suggest a direct involvement of dysferlin, although the impact of dysferlin function on metabolic cellular processes still remains to be elucidated. This assay might represent an appropriate tool to detect major players in metabolic processes mediated by dysferlin.

Discussion

6 Bibliography

Aartsma-Rus, A., Singh, K. H., Fokkema, I. F., Ginjaar, I. B., van Ommen, G. J., den Dunnen, J. T., & van der Maarel, S. M. (2010). Therapeutic exon skipping for dysferlinopathies? *Eur J Hum Genet, 18*(8), 889-894.

Achanzar, W. E., & Ward, S. (1997). A nematode gene required for sperm vesicle fusion. *J Cell Sci, 110 (Pt 9)*, 1073-1081.

Almaca, J., Tian, Y., Aldehni, F., Ousingsawat, J., Kongsuphol, P., Rock, J. R., . . . Kunzelmann, K. (2009). TMEM16 proteins produce volume-regulated chloride currents that are reduced in mice lacking TMEM16A. *J Biol Chem, 284*(42), 28571-28578.

Ampong, B. N., Imamura, M., Matsumiya, T., Yoshida, M., & Takeda, S. (2005). Intracellular localization of dysferlin and its association with the dihydropyridine receptor. *Acta Myol, 24*(2), 134-144.

Anderson, L. V., Davison, K., Moss, J. A., Young, C., Cullen, M. J., Walsh, J., . . . Bushby, K. M. (1999). Dysferlin is a plasma membrane protein and is expressed early in human development. *Hum Mol Genet, 8*(5), 855-861.

Andrews, N. W., Almeida, P. E., & Corrotte, M. (2014). Damage control: cellular mechanisms of plasma membrane repair. *Trends Cell Biol*.

Aoki, M., Liu, J., Richard, I., Bashir, R., Britton, S., Keers, S. M., . . . Brown, R. H., Jr. (2001). Genomic organization of the dysferlin gene and novel mutations in Miyoshi myopathy. *Neurology, 57*(2), 271-278.

Azakir, B. A., Di Fulvio, S., Salomon, S., Brockhoff, M., Therrien, C., & Sinnreich, M. (2012). Modular dispensability of dysferlin C2 domains reveals rational design for mini-dysferlin molecules. *J Biol Chem, 287*(33), 27629-27636.

Azakir, B. A., Di Fulvio, S., Therrien, C., & Sinnreich, M. (2010). Dysferlin interacts with tubulin and microtubules in mouse skeletal muscle. *PLoS One, 5*(4), e10122.

Bansal, D., Miyake, K., Vogel, S. S., Groh, S., Chen, C. C., Williamson, R., . . . Campbell, K. P. (2003). Defective membrane repair in dysferlin-deficient muscular dystrophy. *Nature, 423*(6936), 168-172.

Barnes, J. A., & Gomes, A. V. (2002). Proteolytic signals in the primary structure of annexins. *Mol Cell Biochem, 231*(1-2), 1-7.

Bashir, R., Britton, S., Strachan, T., Keers, S., Vafiadaki, E., Lako, M., . . . Bushby, K. (1998). A gene related to Caenorhabditis elegans spermatogenesis factor fer-1 is mutated in limb-girdle muscular dystrophy type 2B. *Nat Genet, 20*(1), 37-42.

Bastiani, M., Liu, L., Hill, M. M., Jedrychowski, M. P., Nixon, S. J., Lo, H. P., . . . Parton, R. G. (2009). MURC/Cavin-4 and cavin family members form tissue-specific caveolar complexes. *J Cell Biol, 185*(7), 1259-1273.

Bastiani, M., & Parton, R. G. (2010). Caveolae at a glance. *J Cell Sci, 123*(Pt 22), 3831-3836.

Bauer, P. M., Yu, J., Chen, Y., Hickey, R., Bernatchez, P. N., Looft-Wilson, R., . . . Sessa, W. C. (2005). Endothelial-specific expression of caveolin-1 impairs microvascular permeability and angiogenesis. *Proc Natl Acad Sci U S A, 102*(1), 204-209.

Blandin, G., Marchand, S., Charton, K., Daniele, N., Gicquel, E., Boucheteil, J. B., . . . Richard, I. (2013). A human skeletal muscle interactome centered on proteins involved in muscular dystrophies: LGMD interactome. *Skelet Muscle, 3*(1), 3.

Bodin, S., Soulet, C., Tronchere, H., Sie, P., Gachet, C., Plantavid, M., & Payrastre, B. (2005). Integrin-dependent interaction of lipid rafts with the actin cytoskeleton in activated human platelets. *J Cell Sci, 118*(Pt 4), 759-769.

Bolduc, V., Marlow, G., Boycott, K. M., Saleki, K., Inoue, H., Kroon, J., . . . Brais, B. (2010). Recessive mutations in the putative calcium-activated chloride channel Anoctamin 5 cause proximal LGMD2L and distal MMD3 muscular dystrophies. *Am J Hum Genet, 86*(2), 213-221.

Bonne, G., Di Barletta, M. R., Varnous, S., Becane, H. M., Hammouda, E. H., Merlini, L., . . . Schwartz, K. (1999). Mutations in the gene encoding lamin A/C cause autosomal dominant Emery-Dreifuss muscular dystrophy. *Nat Genet, 21*(3), 285-288.

Bouter, A., Gounou, C., Berat, R., Tan, S., Gallois, B., Granier, T., . . . Brisson, A. R. (2011). Annexin-A5 assembled into two-dimensional arrays promotes cell membrane repair. *Nat Commun, 2*, 270.

Bucci, M., Gratton, J. P., Rudic, R. D., Acevedo, L., Roviezzo, F., Cirino, G., & Sessa, W. C. (2000). In vivo delivery of the caveolin-1 scaffolding domain inhibits nitric oxide synthesis and reduces inflammation. *Nat Med, 6*(12), 1362-1367.

Buckingham, M. (2007). Skeletal muscle progenitor cells and the role of Pax genes. *C R Biol, 330*(6-7), 530-533.

Bushby, K. (2009). Diagnosis and management of the limb girdle muscular dystrophies. *Pract Neurol, 9*(6), 314-323.

Bushby, K. M. (1999). Making sense of the limb-girdle muscular dystrophies. *Brain, 122 (Pt 8)*, 1403-1420.

Cai, C., Masumiya, H., Weisleder, N., Matsuda, N., Nishi, M., Hwang, M., . . . Ma, J. (2009). MG53 nucleates assembly of cell membrane repair machinery. *Nat Cell Biol, 11*(1), 56-64.

Cai, C., Weisleder, N., Ko, J. K., Komazaki, S., Sunada, Y., Nishi, M., . . . Ma, J. (2009). Membrane repair defects in muscular dystrophy are linked to altered interaction between MG53, caveolin-3, and dysferlin. *J Biol Chem, 284*(23), 15894-15902.

Bibliography

Cao, H., Alston, L., Ruschman, J., & Hegele, R. A. (2008). Heterozygous CAV1 frameshift mutations (MIM 601047) in patients with atypical partial lipodystrophy and hypertriglyceridemia. *Lipids Health Dis, 7*, 3.

Capozza, F., Combs, T. P., Cohen, A. W., Cho, Y. R., Park, S. Y., Schubert, W., . . . Lisanti, M. P. (2005). Caveolin-3 knockout mice show increased adiposity and whole body insulin resistance, with ligand-induced insulin receptor instability in skeletal muscle. *Am J Physiol Cell Physiol, 288*(6), C1317-1331.

Carl, M., Rocken, C., & Spuler, S. (2009). [Amyloidosis in muscular dystrophy]. *Pathologe, 30*(3), 235-239.

Cartaud, A., Stetzkowski-Marden, F., Maoui, A., & Cartaud, J. (2011). Agrin triggers the clustering of raft-associated acetylcholine receptors through actin cytoskeleton reorganization. *Biol Cell, 103*(6), 287-301.

Cenacchi, G., Fanin, M., De Giorgi, L. B., & Angelini, C. (2005). Ultrastructural changes in dysferlinopathy support defective membrane repair mechanism. *J Clin Pathol, 58*(2), 190-195.

Charge, S. B., & Rudnicki, M. A. (2004). Cellular and molecular regulation of muscle regeneration. *Physiol Rev, 84*(1), 209-238.

Cheng, Z. J., Singh, R. D., Marks, D. L., & Pagano, R. E. (2006). Membrane microdomains, caveolae, and caveolar endocytosis of sphingolipids. *Mol Membr Biol, 23*(1), 101-110.

Choi, J. H., Park, Y. E., Kim, S. I., Kim, J. I., Lee, C. H., Park, K. H., & Kim, D. S. (2009). Differential immunohistological features of inflammatory myopathies and dysferlinopathy. *J Korean Med Sci, 24*(6), 1015-1023.

Collins, B. M., Davis, M. J., Hancock, J. F., & Parton, R. G. (2012). Structure-based reassessment of the caveolin signaling model: do caveolae regulate signaling through caveolin-protein interactions? *Dev Cell, 23*(1), 11-20.

Collins, C. A., Olsen, I., Zammit, P. S., Heslop, L., Petrie, A., Partridge, T. A., & Morgan, J. E. (2005). Stem cell function, self-renewal, and behavioral heterogeneity of cells from the adult muscle satellite cell niche. *Cell, 122*(2), 289-301.

Corrotte, M., Almeida, P. E., Tam, C., Castro-Gomes, T., Fernandes, M. C., Millis, B. A., . . . Andrews, N. W. (2013). Caveolae internalization repairs wounded cells and muscle fibers. *Elife (Cambridge), 2*, e00926.

Crosbie, R. H., Yamada, H., Venzke, D. P., Lisanti, M. P., & Campbell, K. P. (1998). Caveolin-3 is not an integral component of the dystrophin glycoprotein complex. *FEBS Lett, 427*(2), 279-282.

Damm, E. M., Pelkmans, L., Kartenbeck, J., Mezzacasa, A., Kurzchalia, T., & Helenius, A. (2005). Clathrin- and caveolin-1-independent endocytosis: entry of simian virus 40 into cells devoid of caveolae. *J Cell Biol, 168*(3), 477-488.

Darras, B. T., Koenig, M., Kunkel, L. M., & Francke, U. (1988). Direct method for prenatal diagnosis and carrier detection in Duchenne/Becker muscular dystrophy using the entire dystrophin cDNA. *Am J Med Genet, 29*(3), 713-726.

Davis, D. B., Delmonte, A. J., Ly, C. T., & McNally, E. M. (2000). Myoferlin, a candidate gene and potential modifier of muscular dystrophy. *Hum Mol Genet, 9*(2), 217-226.

Davis, D. B., Doherty, K. R., Delmonte, A. J., & McNally, E. M. (2002). Calcium-sensitive phospholipid binding properties of normal and mutant ferlin C2 domains. *J Biol Chem, 277*(25), 22883-22888.

de Morree, A., Flix, B., Bagaric, I., Wang, J., van den Boogaard, M., Grand Moursel, L., . . . van der Maarel, S. M. (2013). Dysferlin regulates cell adhesion in human monocytes. *J Biol Chem, 288*(20), 14147-14157.

de Morree, A., Hensbergen, P. J., van Haagen, H. H., Dragan, I., Deelder, A. M., t Hoen, P. A., . . . van der Maarel, S. M. (2010). Proteomic analysis of the dysferlin protein complex unveils its importance for sarcolemmal maintenance and integrity. *PLoS One, 5*(11), e13854.

Demonbreun, A. R., Fahrenbach, J. P., Deveaux, K., Earley, J. U., Pytel, P., & McNally, E. M. (2011). Impaired muscle growth and response to insulin-like growth factor 1 in dysferlin-mediated muscular dystrophy. *Hum Mol Genet, 20*(4), 779-789.

Doherty, K. R., Cave, A., Davis, D. B., Delmonte, A. J., Posey, A., Earley, J. U., . . . McNally, E. M. (2005). Normal myoblast fusion requires myoferlin. *Development, 132*(24), 5565-5575.

Duran, C., Qu, Z., Osunkoya, A. O., Cui, Y., & Hartzell, H. C. (2012). ANOs 3-7 in the anoctamin/Tmem16 Cl-channel family are intracellular proteins. *Am J Physiol Cell Physiol, 302*(3), C482-493.

Dutta, A. K., Khimji, A. K., Kresge, C., Bugde, A., Dougherty, M., Esser, V., . . . Feranchak, A. P. (2011). Identification and functional characterization of TMEM16A, a Ca2+-activated Cl- channel activated by extracellular nucleotides, in biliary epithelium. *J Biol Chem, 286*(1), 766-776.

Eden, E., Navon, R., Steinfeld, I., Lipson, D., & Yakhini, Z. (2009). GOrilla: a tool for discovery and visualization of enriched GO terms in ranked gene lists. *BMC Bioinformatics, 10*, 48.

Eggeling, C., Ringemann, C., Medda, R., Schwarzmann, G., Sandhoff, K., Polyakova, S., . . . Hell, S. W. (2009). Direct observation of the nanoscale dynamics of membrane lipids in a living cell. *Nature, 457*(7233), 1159-1162.

Eggermont, J. (2004). Calcium-activated chloride channels: (un)known, (un)loved? *Proc Am Thorac Soc, 1*(1), 22-27.

Ehmsen, J., Poon, E., & Davies, K. (2002). The dystrophin-associated protein complex. *J Cell Sci, 115*(Pt 14), 2801-2803.

Engel, W. K., & Cunningham, G. G. (1963). Rapid Examination of Muscle Tissue. An Improved Trichrome Method for Fresh-Frozen Biopsy Sections. *Neurology, 13*, 919-923.

Epand, R. M., Sayer, B. G., & Epand, R. F. (2005). Caveolin scaffolding region and cholesterol-rich domains in membranes. *J Mol Biol, 345*(2), 339-350.

Eriksson, M., Brown, W. T., Gordon, L. B., Glynn, M. W., Singer, J., Scott, L., . . . Collins, F. S. (2003). Recurrent de novo point mutations in lamin A cause Hutchinson-Gilford progeria syndrome. *Nature, 423*(6937), 293-298.

Evesson, F. J., Peat, R. A., Lek, A., Brilot, F., Lo, H. P., Dale, R. C., . . . Cooper, S. T. (2010). Reduced plasma membrane expression of dysferlin mutants is attributed to accelerated endocytosis via a syntaxin-4-associated pathway. *J Biol Chem, 285*(37), 28529-28539.

Fallah, G., Romer, T., Detro-Dassen, S., Braam, U., Markwardt, F., & Schmalzing, G. (2011). TMEM16A(a)/anoctamin-1 shares a homodimeric architecture with CLC chloride channels. *Mol Cell Proteomics, 10*(2), M110 004697.

Fanin, M., & Angelini, C. (2002). Muscle pathology in dysferlin deficiency. *Neuropathol Appl Neurobiol, 28*(6), 461-470.

Fee, D. B., So, Y. T., Barraza, C., Figueroa, K. P., & Pulst, S. M. (2004). Phenotypic variability associated with Arg26Gln mutation in caveolin3. *Muscle Nerve, 30*(3), 375-378.

Fernandez-Rojo, M. A., Gongora, M., Fitzsimmons, R. L., Martel, N., Martin, S. D., Nixon, S. J., . . . Parton, R. G. (2013). Caveolin-1 is necessary for hepatic oxidative lipid metabolism: evidence for crosstalk between caveolin-1 and bile acid signaling. *Cell Rep, 4*(2), 238-247.

Fernandez, M. A., Albor, C., Ingelmo-Torres, M., Nixon, S. J., Ferguson, C., Kurzchalia, T., . . . Pol, A. (2006). Caveolin-1 is essential for liver regeneration. *Science, 313*(5793), 1628-1632.

Feuk-Lagerstedt, E., Movitz, C., Pellme, S., Dahlgren, C., & Karlsson, A. (2007). Lipid raft proteome of the human neutrophil azurophil granule. *Proteomics, 7*(2), 194-205.

Fielding, C. J., & Fielding, P. E. (2001). Caveolae and intracellular trafficking of cholesterol. *Adv Drug Deliv Rev, 49*(3), 251-264.

Flix, B., de la Torre, C., Castillo, J., Casal, C., Illa, I., & Gallardo, E. (2013). Dysferlin interacts with calsequestrin-1, myomesin-2 and dynein in human skeletal muscle. *Int J Biochem Cell Biol, 45*(8), 1927-1938.

Fra, A. M., Williamson, E., Simons, K., & Parton, R. G. (1995). De novo formation of caveolae in lymphocytes by expression of VIP21-caveolin. *Proc Natl Acad Sci U S A, 92*(19), 8655-8659.

Fujita, E., Kouroku, Y., Isoai, A., Kumagai, H., Misutani, A., Matsuda, C., . . . Momoi, T. (2007). Two endoplasmic reticulum-associated degradation (ERAD) systems for the novel variant of the mutant dysferlin: ubiquitin/proteasome ERAD(I) and autophagy/lysosome ERAD(II). *Hum Mol Genet, 16*(6), 618-629.

Galbiati, F., Engelman, J. A., Volonte, D., Zhang, X. L., Minetti, C., Li, M., . . . Lisanti, M. P. (2001). Caveolin-3 null mice show a loss of caveolae, changes in the microdomain distribution of the dystrophin-glycoprotein complex, and t-tubule abnormalities. *J Biol Chem, 276*(24), 21425-21433.

Galbiati, F., Volonte, D., Chu, J. B., Li, M., Fine, S. W., Fu, M., . . . Lisanti, M. P. (2000). Transgenic overexpression of caveolin-3 in skeletal muscle fibers induces a Duchenne-like muscular dystrophy phenotype. *Proc Natl Acad Sci U S A, 97*(17), 9689-9694.

Gallardo, E., Rojas-Garcia, R., de Luna, N., Pou, A., Brown, R. H., Jr., & Illa, I. (2001). Inflammation in dysferlin myopathy: immunohistochemical characterization of 13 patients. *Neurology, 57*(11), 2136-2138.

Garcia-Cardena, G., Martasek, P., Masters, B. S., Skidd, P. M., Couet, J., Li, S., . . . Sessa, W. C. (1997). Dissecting the interaction between nitric oxide synthase (NOS) and caveolin. Functional significance of the nos caveolin binding domain in vivo. *J Biol Chem, 272*(41), 25437-25440.

Gazzerro, E., Sotgia, F., Bruno, C., Lisanti, M. P., & Minetti, C. (2010). Caveolinopathies: from the biology of caveolin-3 to human diseases. *Eur J Hum Genet, 18*(2), 137-145.

Gentil, B. J., Delphin, C., Benaud, C., & Baudier, J. (2003). Expression of the Giant Protein AHNAK (Desmoyokin) in Muscle and Lining Epithelial Cells. *Journal of Histochemistry & Cytochemistry, 51*(3), 339-348.

Gilbert, S. F. (2000). Developmental Biology: Sinauer Associates.

Grounds, M. D., Terrill, J. R., Radley-Crabb, H. G., Robertson, T., Papadimitriou, J., Spuler, S., & Shavlakadze, T. (2014). Lipid accumulation in dysferlin-deficient muscles. *Am J Pathol, 184*(6), 1668-1676.

Guilherme, A., Soriano, N. A., Bose, S., Holik, J., Bose, A., Pomerleau, D. P., . . . Czech, M. P. (2004). EHD2 and the novel EH domain binding protein EHBP1 couple endocytosis to the actin cytoskeleton. *J Biol Chem, 279*(11), 10593-10605.

Hackman, P., Vihola, A., Haravuori, H., Marchand, S., Sarparanta, J., De Seze, J., . . . Udd, B. (2002). Tibial muscular dystrophy is a titinopathy caused by mutations in TTN, the gene encoding the giant skeletal-muscle protein titin. *Am J Hum Genet, 71*(3), 492-500.

Han, R. (2011). Muscle membrane repair and inflammatory attack in dysferlinopathy. *Skelet Muscle, 1*(1), 10.

Han, W. Q., Xia, M., Xu, M., Boini, K. M., Ritter, J. K., Li, N. J., & Li, P. L. (2012). Lysosome fusion to the cell membrane is mediated by the dysferlin C2A domain in coronary arterial endothelial cells. *J Cell Sci, 125*(Pt 5), 1225-1234.

Hansen, C. G., Howard, G., & Nichols, B. J. (2011). Pacsin 2 is recruited to caveolae and functions in caveolar biogenesis. *J Cell Sci, 124*(Pt 16), 2777-2785.

Hattori, H., Nagata, E., Oya, Y., Takahashi, T., Aoki, M., Ito, D., & Suzuki, N. (2007). A novel compound heterozygous dysferlin mutation in Miyoshi myopathy siblings responding to dantrolene. *Eur J Neurol, 14*(11), 1288-1291.

Bibliography

Hayashi, T., Arimura, T., Ueda, K., Shibata, H., Hohda, S., Takahashi, M., . . . Kimura, A. (2004). Identification and functional analysis of a caveolin-3 mutation associated with familial hypertrophic cardiomyopathy. *Biochem Biophys Res Commun, 313*(1), 178-184.

Henley, J. R., Krueger, E. W., Oswald, B. J., & McNiven, M. A. (1998). Dynamin-mediated internalization of caveolae. *J Cell Biol, 141*(1), 85-99.

Hernandez-Deviez, D. J., Howes, M. T., Laval, S. H., Bushby, K., Hancock, J. F., & Parton, R. G. (2008). Caveolin regulates endocytosis of the muscle repair protein, dysferlin. *J Biol Chem, 283*(10), 6476-6488.

Hernandez-Deviez, D. J., Martin, S., Laval, S. H., Lo, H. P., Cooper, S. T., North, K. N., . . . Parton, R. G. (2006). Aberrant dysferlin trafficking in cells lacking caveolin or expressing dystrophy mutants of caveolin-3. *Hum Mol Genet, 15*(1), 129-142.

Hettmer, S., & Wagers, A. J. (2010). Muscling in: Uncovering the origins of rhabdomyosarcoma. *Nat Med, 16*(2), 171-173.

Hicks, D., Sarkozy, A., Muelas, N., Koehler, K., Huebner, A., Hudson, G., . . . Bushby, K. (2011). A founder mutation in Anoctamin 5 is a major cause of limb-girdle muscular dystrophy. *Brain, 134*(Pt 1), 171-182.

Hoffman, E. P., Brown, R. H., Jr., & Kunkel, L. M. (1987). Dystrophin: the protein product of the Duchenne muscular dystrophy locus. *Cell, 51*(6), 919-928.

Hommelgaard, A. M., Roepstorff, K., Vilhardt, F., Torgersen, M. L., Sandvig, K., & van Deurs, B. (2005). Caveolae: stable membrane domains with a potential for internalization. *Traffic, 6*(9), 720-724.

Hornsey, M. A., Laval, S. H., Barresi, R., Lochmuller, H., & Bushby, K. (2013). Muscular dystrophy in dysferlin-deficient mouse models. *Neuromuscul Disord, 23*(5), 377-387.

Huang, Y., Laval, S. H., van Remoortere, A., Baudier, J., Benaud, C., Anderson, L. V., . . . van der Maarel, S. M. (2007). AHNAK, a novel component of the dysferlin protein complex, redistributes to the cytoplasm with dysferlin during skeletal muscle regeneration. *FASEB J, 21*(3), 732-742.

Huang, Y., Verheesen, P., Roussis, A., Frankhuizen, W., Ginjaar, I., Haldane, F., . . . van der Maarel, S. M. (2005). Protein studies in dysferlinopathy patients using llama-derived antibody fragments selected by phage display. *Eur J Hum Genet, 13*(6), 721-730.

Jaiswal, J. K., Marlow, G., Summerill, G., Mahjneh, I., Mueller, S., Hill, M., . . . Bashir, R. (2007). Patients with a non-dysferlin Miyoshi myopathy have a novel membrane repair defect. *Traffic, 8*(1), 77-88.

Jansa, P., Mason, S. W., Hoffmann-Rohrer, U., & Grummt, I. (1998). Cloning and functional characterization of PTRF, a novel protein which induces dissociation of paused ternary transcription complexes. *EMBO J, 17*(10), 2855-2864.

Kahya, N., & Schwille, P. (2006). Fluorescence correlation studies of lipid domains in model membranes. *Mol Membr Biol, 23*(1), 29-39.

Kaplan, J.-C., & Hamroun, D. (2013). The 2014 version of the gene table of monogenic neuromuscular disorders (nuclear genome). *Neuromuscular Disorders, 23*(12), 1081-1111.

Karsan, A., Blonder, J., Law, J., Yaquian, E., Lucas, D. A., Conrads, T. P., & Veenstra, T. (2005). Proteomic analysis of lipid microdomains from lipopolysaccharide-activated human endothelial cells. *J Proteome Res, 4*(2), 349-357.

Kim, C. A., Delepine, M., Boutet, E., El Mourabit, H., Le Lay, S., Meier, M., . . . Magre, J. (2008). Association of a homozygous nonsense caveolin-1 mutation with Berardinelli-Seip congenital lipodystrophy. *J Clin Endocrinol Metab, 93*(4), 1129-1134.

Kirkham, M., Fujita, A., Chadda, R., Nixon, S. J., Kurzchalia, T. V., Sharma, D. K., . . . Parton, R. G. (2005). Ultrastructural identification of uncoated caveolin-independent early endocytic vehicles. *J Cell Biol, 168*(3), 465-476.

Kirkham, M., & Parton, R. G. (2005). Clathrin-independent endocytosis: new insights into caveolae and non-caveolar lipid raft carriers. *Biochim Biophys Acta, 1746*(3), 349-363.

Klinge, L., Aboumousa, A., Eagle, M., Hudson, J., Sarkozy, A., Vita, G., . . . Bushby, K. (2010). New aspects on patients affected by dysferlin deficient muscular dystrophy. *J Neurol Neurosurg Psychiatry, 81*(9), 946-953.

Klinge, L., Dean, A. F., Kress, W., Dixon, P., Charlton, R., Muller, J. S., . . . Bushby, K. (2008). Late onset in dysferlinopathy widens the clinical spectrum. *Neuromuscul Disord, 18*(4), 288-290.

Klinge, L., Harris, J., Sewry, C., Charlton, R., Anderson, L., Laval, S., . . . Bushby, K. (2010). Dysferlin associates with the developing T-tubule system in rodent and human skeletal muscle. *Muscle Nerve, 41*(2), 166-173.

Klinge, L., Laval, S., Keers, S., Haldane, F., Straub, V., Barresi, R., & Bushby, K. (2007). From T-tubule to sarcolemma: damage-induced dysferlin translocation in early myogenesis. *FASEB J, 21*(8), 1768-1776.

Knudsen, K. A. (1990). Cell adhesion molecules in myogenesis. *Curr Opin Cell Biol, 2*(5), 902-906.

Kobayashi, K., Izawa, T., Kuwamura, M., & Yamate, J. (2010). The distribution and characterization of skeletal muscle lesions in dysferlin-deficient SJL and A/J mice. *Exp Toxicol Pathol, 62*(5), 509-517.

Kobayashi, K., Izawa, T., Kuwamura, M., & Yamate, J. (2012). Dysferlin and animal models for dysferlinopathy. *J Toxicol Pathol, 25*(2), 135-147.

Krahn, M., Wein, N., Bartoli, M., Lostal, W., Courrier, S., Bourg-Alibert, N., . . . Levy, N. (2010). A naturally occurring human minidysferlin protein repairs sarcolemmal lesions in a mouse model of dysferlinopathy. *Sci Transl Med, 2*(50), 50ra69.

Kramerova, I., Kudryashova, E., Wu, B., Ottenheijm, C., Granzier, H., & Spencer, M. J. (2008). Novel role of calpain-3 in the triad-associated protein complex regulating calcium release in skeletal muscle. *Hum Mol Genet, 17*(21), 3271-3280.

Kunzelmann, K., Tian, Y., Martins, J. R., Faria, D., Kongsuphol, P., Ousingsawat, J., . . . Schreiber, R. (2011). Anoctamins. *Pflugers Arch, 462*(2), 195-208.

Kurzchalia, T. V., Dupree, P., Parton, R. G., Kellner, R., Virta, H., Lehnert, M., & Simons, K. (1992). VIP21, a 21-kD membrane protein is an integral component of trans-Golgi-network-derived transport vesicles. *J Cell Biol, 118*(5), 1003-1014.

Le Lay, S., Hajduch, E., Lindsay, M. R., Le Liepvre, X., Thiele, C., Ferre, P., . . . Dugail, I. (2006). Cholesterol-induced caveolin targeting to lipid droplets in adipocytes: a role for caveolar endocytosis. *Traffic, 7*(5), 549-561.

Le Lay, S., & Kurzchalia, T. V. (2005). Getting rid of caveolins: phenotypes of caveolin-deficient animals. *Biochim Biophys Acta, 1746*(3), 322-333.

Lek, A., Evesson, F. J., Lemckert, F. A., Redpath, G. M., Lueders, A. K., Turnbull, L., . . . Cooper, S. T. (2013). Calpains, cleaved mini-dysferlinC72, and L-type channels underpin calcium-dependent muscle membrane repair. *J Neurosci, 33*(12), 5085-5094.

Lennon, N. J., Kho, A., Bacskai, B. J., Perlmutter, S. L., Hyman, B. T., & Brown, R. H., Jr. (2003). Dysferlin interacts with annexins A1 and A2 and mediates sarcolemmal wound-healing. *J Biol Chem, 278*(50), 50466-50473.

Lerario, A., Cogiamanian, F., Marchesi, C., Belicchi, M., Bresolin, N., Porretti, L., & Torrente, Y. (2010). Effects of rituximab in two patients with dysferlin-deficient muscular dystrophy. *BMC Musculoskelet Disord, 11*, 157.

Levy, J. R., Campbell, K. P., & Glass, D. J. (2013). MG53's new identity. *Skelet Muscle, 3*(1), 25.

Li, S., Couet, J., & Lisanti, M. P. (1996). Src tyrosine kinases, Galpha subunits, and H-Ras share a common membrane-anchored scaffolding protein, caveolin. Caveolin binding negatively regulates the auto-activation of Src tyrosine kinases. *J Biol Chem, 271*(46), 29182-29190.

Liewluck, T., Winder, T. L., Dimberg, E. L., Crum, B. A., Heppelmann, C. J., Wang, Y., . . . Milone, M. (2013). ANO5-muscular dystrophy: clinical, pathological and molecular findings. *Eur J Neurol, 20*(10), 1383-1389.

Lingwood, D., & Simons, K. (2007). Detergent resistance as a tool in membrane research. *Nat Protoc, 2*(9), 2159-2165.

Liu, J., Aoki, M., Illa, I., Wu, C., Fardeau, M., Angelini, C., . . . Brown, R. H., Jr. (1998). Dysferlin, a novel skeletal muscle gene, is mutated in Miyoshi myopathy and limb girdle muscular dystrophy. *Nat Genet, 20*(1), 31-36.

Lostal, W., Bartoli, M., Roudaut, C., Bourg, N., Krahn, M., Pryadkina, M., . . . Richard, I. (2012). Lack of correlation between outcomes of membrane repair assay and correction of dystrophic changes in experimental therapeutic strategy in dysferlinopathy. *PLoS One, 7*(5), e38036.

Ludwig, A., Howard, G., Mendoza-Topaz, C., Deerinck, T., Mackey, M., Sandin, S., . . . Nichols, B. J. (2013). Molecular composition and ultrastructure of the caveolar coat complex. *PLoS Biol, 11*(8), e1001640.

Mahjneh, I., Bushby, K., Pizzi, A., Bashir, R., & Marconi, G. (1996). Limb-girdle muscular dystrophy: a follow-up study of 79 patients. *Acta Neurol Scand, 94*(3), 177-189.

Marg, A., Schoewel, V., Timmel, T., Schulze, A., Shah, C., Daumke, O., & Spuler, S. (2012). Sarcolemmal repair is a slow process and includes EHD2. *Traffic, 13*(9), 1286-1294.

Martins, J. R., Faria, D., Kongsuphol, P., Reisch, B., Schreiber, R., & Kunzelmann, K. (2011). Anoctamin 6 is an essential component of the outwardly rectifying chloride channel. *Proc Natl Acad Sci U S A, 108*(44), 18168-18172.

Maselli, R. A., Fernandez, J. M., Arredondo, J., Navarro, C., Ngo, M., Beeson, D., . . . Ferns, M. J. (2012). LG2 agrin mutation causing severe congenital myasthenic syndrome mimics functional characteristics of non-neural (z-) agrin. *Hum Genet, 131*(7), 1123-1135.

Matsuda, C., Hayashi, Y. K., Ogawa, M., Aoki, M., Murayama, K., Nishino, I., . . . Brown, R. H., Jr. (2001). The sarcolemmal proteins dysferlin and caveolin-3 interact in skeletal muscle. *Hum Mol Genet, 10*(17), 1761-1766.

Matsuda, C., Kameyama, K., Tagawa, K., Ogawa, M., Suzuki, A., Yamaji, S., . . . Hayashi, Y. K. (2005). Dysferlin interacts with affixin (beta-parvin) at the sarcolemma. *J Neuropathol Exp Neurol, 64*(4), 334-340.

Mauro, A. (1961). Satellite cell of skeletal muscle fibers. *J Biophys Biochem Cytol, 9*, 493-495.

Mayor, S., & Pagano, R. E. (2007). Pathways of clathrin-independent endocytosis. *Nat Rev Mol Cell Biol, 8*(8), 603-612.

McDade, J. R., & Michele, D. E. (2014). Membrane damage-induced vesicle-vesicle fusion of dysferlin-containing vesicles in muscle cells requires microtubules and kinesin. *Hum Mol Genet, 23*(7), 1677-1686.

McNeil, P. (2009). Membrane repair redux: redox of MG53. *Nat Cell Biol, 11*(1), 7-9.

Menke, M., Gerke, V., & Steinem, C. (2005). Phosphatidylserine membrane domain clustering induced by annexin A2/S100A10 heterotetramer. *Biochemistry, 44*(46), 15296-15303.

Menko, A. S., & Boettiger, D. (1987). Occupation of the extracellular matrix receptor, integrin, is a control point for myogenic differentiation. *Cell, 51*(1), 51-57.

Mercuri, E., & Muntoni, F. (2013). Muscular dystrophy: new challenges and review of the current clinical trials. *Curr Opin Pediatr, 25*(6), 701-707.

Bibliography

Milenkovic, V. M., Brockmann, M., Stohr, H., Weber, B. H., & Strauss, O. (2010). Evolution and functional divergence of the anoctamin family of membrane proteins. *BMC Evol Biol, 10*, 319.

Milone, M., Liewluck, T., Winder, T. L., & Pianosi, P. T. (2012). Amyloidosis and exercise intolerance in ANO5 muscular dystrophy. *Neuromuscul Disord, 22*(1), 13-15.

Minetti, C., Bado, M., Broda, P., Sotgia, F., Bruno, C., Galbiati, F., . . . Cordone, G. (2002). Impairment of caveolae formation and T-system disorganization in human muscular dystrophy with caveolin-3 deficiency. *Am J Pathol, 160*(1), 265-270.

Minetti, C., Sotgia, F., Bruno, C., Scartezzini, P., Broda, P., Bado, M., . . . Zara, F. (1998). Mutations in the caveolin-3 gene cause autosomal dominant limb-girdle muscular dystrophy. *Nat Genet, 18*(4), 365-368.

Mizuta, K., Tsutsumi, S., Inoue, H., Sakamoto, Y., Miyatake, K., Miyawaki, K., . . . Itakura, M. (2007). Molecular characterization of GDD1/TMEM16E, the gene product responsible for autosomal dominant gnathodiaphyseal dysplasia. *Biochem Biophys Res Commun, 357*(1), 126-132.

Moore, S. A., Shilling, C. J., Westra, S., Wall, C., Wicklund, M. P., Stolle, C., . . . Mendell, J. R. (2006). Limb-girdle muscular dystrophy in the United States. *J Neuropathol Exp Neurol, 65*(10), 995-1003.

Moren, B., Shah, C., Howes, M. T., Schieber, N. L., McMahon, H. T., Parton, R. G., . . . Lundmark, R. (2012). EHD2 regulates caveolar dynamics via ATP-driven targeting and oligomerization. *Mol Biol Cell, 23*(7), 1316-1329.

Muller, J. S., Piko, H., Schoser, B. G., Schlotter-Weigel, B., Reilich, P., Gurster, S., . . . Walter, M. C. (2006). Novel splice site mutation in the caveolin-3 gene leading to autosomal recessive limb girdle muscular dystrophy. *Neuromuscul Disord, 16*(7), 432-436.

Nalini, A., & Gayathri, N. (2008). Dysferlinopathy: a clinical and histopathological study of 28 patients from India. *Neurol India, 56*(3), 379-385; discussion 386-377.

Nicole, S., Chaouch, A., Torbergsen, T., Bauche, S., de Bruyckere, E., Fontenille, M. J., . . . Lochmuller, H. (2014). Agrin mutations lead to a congenital myasthenic syndrome with distal muscle weakness and atrophy. *Brain, 137*(Pt 9), 2429-2443.

Nigro, V. (2003). Molecular bases of autosomal recessive limb-girdle muscular dystrophies. *Acta Myol, 22*(2), 35-42.

Nigro, V., & Piluso, G. (2012). Next generation sequencing (NGS) strategies for the genetic testing of myopathies. *Acta Myol, 31*(3), 196-200.

Nigro, V., & Savarese, M. (2014). Genetic basis of limb-girdle muscular dystrophies: the 2014 update. *Acta Myol, 33*(1), 1-12.

Palade, G. E. (1953). Fine structure of blood capilaries. *Journal of Applied Physics, 24*(1424).

Parton, R. G. (1996). Caveolae and caveolins. *Curr Opin Cell Biol, 8*(4), 542-548.

Parton, R. G., & Simons, K. (2007). The multiple faces of caveolae. *Nat Rev Mol Cell Biol, 8*(3), 185-194.

Parton, R. G., Way, M., Zorzi, N., & Stang, E. (1997). Caveolin-3 associates with developing T-tubules during muscle differentiation. *J Cell Biol, 136*(1), 137-154.

Patel, H. H., Murray, F., & Insel, P. A. (2008). G-protein-coupled receptor-signaling components in membrane raft and caveolae microdomains. *Handb Exp Pharmacol*(186), 167-184.

Pelkmans, L., Kartenbeck, J., & Helenius, A. (2001). Caveolar endocytosis of simian virus 40 reveals a new two-step vesicular-transport pathway to the ER. *Nat Cell Biol, 3*(5), 473-483.

Pelkmans, L., & Zerial, M. (2005). Kinase-regulated quantal assemblies and kiss-and-run recycling of caveolae. *Nature, 436*(7047), 128-133.

Penttila, S., Palmio, J., Suominen, T., Raheem, O., Evila, A., Muelas Gomez, N., . . . Udd, B. (2012). Eight new mutations and the expanding phenotype variability in muscular dystrophy caused by ANO5. *Neurology, 78*(12), 897-903.

Philippi, S., Bigot, A., Marg, A., Mouly, V., Spuler, S., & Zacharias, U. (2012). Dysferlin-deficient immortalized human myoblasts and myotubes as a useful tool to study dysferlinopathy. *PLoS Curr, 4*, RRN1298.

Pietuch, A., Bruckner, B. R., & Janshoff, A. (2013). Membrane tension homeostasis of epithelial cells through surface area regulation in response to osmotic stress. *Biochim Biophys Acta, 1833*(3), 712-722.

Rahimov, F., & Kunkel, L. M. (2013). The cell biology of disease: cellular and molecular mechanisms underlying muscular dystrophy. *J Cell Biol, 201*(4), 499-510.

Rajab, A., Straub, V., McCann, L. J., Seelow, D., Varon, R., Barresi, R., . . . Schuelke, M. (2010). Fatal cardiac arrhythmia and long-QT syndrome in a new form of congenital generalized lipodystrophy with muscle rippling (CGL4) due to PTRF-CAVIN mutations. *PLoS Genet, 6*(3), e1000874.

Rajendran, L., & Simons, K. (2005). Lipid rafts and membrane dynamics. *J Cell Sci, 118*(Pt 6), 1099-1102.

Rasche, S., Toetter, B., Adler, J., Tschapek, A., Doerner, J. F., Kurtenbach, S., . . . Neuhaus, E. M. (2010). Tmem16b is specifically expressed in the cilia of olfactory sensory neurons. *Chem Senses, 35*(3), 239-245.

Rayavarapu, S., Van der Meulen, J. H., Gordish-Dressman, H., Hoffman, E. P., Nagaraju, K., & Knoblach, S. M. (2010). Characterization of dysferlin deficient SJL/J mice to assess preclinical drug efficacy: fasudil exacerbates muscle disease phenotype. *PLoS One, 5*(9), e12981.

Razani, B., Wang, X. B., Engelman, J. A., Battista, M., Lagaud, G., Zhang, X. L., . . . Lisanti, M. P. (2002). Caveolin-2-deficient mice show evidence of severe pulmonary dysfunction without disruption of caveolae. *Mol Cell Biol, 22*(7), 2329-2344.

Richter, T., Floetenmeyer, M., Ferguson, C., Galea, J., Goh, J., Lindsay, M. R., . . . Parton, R. G. (2008). High-resolution 3D quantitative analysis of caveolar ultrastructure and caveola-cytoskeleton interactions. *Traffic, 9*(6), 893-909.

Roostalu, U., & Strahle, U. (2012). In vivo imaging of molecular interactions at damaged sarcolemma. *Dev Cell, 22*(3), 515-529.

Rothberg, K. G., Heuser, J. E., Donzell, W. C., Ying, Y. S., Glenney, J. R., & Anderson, R. G. (1992). Caveolin, a protein component of caveolae membrane coats. *Cell, 68*(4), 673-682.

Roux, I., Safieddine, S., Nouvian, R., Grati, M., Simmler, M. C., Bahloul, A., . . . Petit, C. (2006). Otoferlin, defective in a human deafness form, is essential for exocytosis at the auditory ribbon synapse. *Cell, 127*(2), 277-289.

Scherer, P. E., Okamoto, T., Chun, M., Nishimoto, I., Lodish, H. F., & Lisanti, M. P. (1996). Identification, sequence, and expression of caveolin-2 defines a caveolin gene family. *Proc Natl Acad Sci U S A, 93*(1), 131-135.

Schlormann, W., Steiniger, F., Richter, W., Kaufmann, R., Hause, G., Lemke, C., & Westermann, M. (2010). The shape of caveolae is omega-like after glutaraldehyde fixation and cup-like after cryofixation. *Histochem Cell Biol, 133*(2), 223-228.

Schoewel, V., Marg, A., Kunz, S., Overkamp, T., Carrazedo, R. S., Zacharias, U., . . . Spuler, S. (2012). Dysferlin-peptides reallocate mutated dysferlin thereby restoring function. *PLoS One, 7*(11), e49603.

Schreiber, R., Uliyakina, I., Kongsuphol, P., Warth, R., Mirza, M., Martins, J. R., & Kunzelmann, K. (2010). Expression and function of epithelial anoctamins. *J Biol Chem, 285*(10), 7838-7845.

Schroeder, B. C., Cheng, T., Jan, Y. N., & Jan, L. Y. (2008). Expression cloning of TMEM16A as a calcium-activated chloride channel subunit. *Cell, 134*(6), 1019-1029.

Selcen, D., Stilling, G., & Engel, A. G. (2001). The earliest pathologic alterations in dysferlinopathy. *Neurology, 56*(11), 1472-1481.

Sharma, A., Yu, C., Leung, C., Trane, A., Lau, M., Utokaparch, S., . . . Bernatchez, P. (2010). A new role for the muscle repair protein dysferlin in endothelial cell adhesion and angiogenesis. *Arterioscler Thromb Vasc Biol, 30*(11), 2196-2204.

Sharma, D. K., Brown, J. C., Cheng, Z., Holicky, E. L., Marks, D. L., & Pagano, R. E. (2005). The glycosphingolipid, lactosylceramide, regulates beta1-integrin clustering and endocytosis. *Cancer Res, 65*(18), 8233-8241.

Shvets, E., Ludwig, A., & Nichols, B. J. (2014). News from the caves: update on the structure and function of caveolae. *Curr Opin Cell Biol, 29C*, 99-106.

Simons, K., & Ikonen, E. (1997). Functional rafts in cell membranes. *Nature, 387*(6633), 569-572.

Sinha, B., Koster, D., Ruez, R., Gonnord, P., Bastiani, M., Abankwa, D., . . . Nassoy, P. (2011). Cells respond to mechanical stress by rapid disassembly of caveolae. *Cell, 144*(3), 402-413.

Song, R., Peng, W., Zhang, Y., Lv, F., Wu, H. K., Guo, J., . . . Xiao, R. P. (2013). Central role of E3 ubiquitin ligase MG53 in insulin resistance and metabolic disorders. *Nature, 494*(7437), 375-379.

Sotgia, F., Lee, J. K., Das, K., Bedford, M., Petrucci, T. C., Macioce, P., . . . Lisanti, M. P. (2000). Caveolin-3 directly interacts with the C-terminal tail of beta -dystroglycan. Identification of a central WW-like domain within caveolin family members. *J Biol Chem, 275*(48), 38048-38058.

Spuler, S., Carl, M., Zabojszcza, J., Straub, V., Bushby, K., Moore, S. A., . . . Rocken, C. (2008). Dysferlin-deficient muscular dystrophy features amyloidosis. *Ann Neurol, 63*(3), 323-328.

Spuler, S., & Engel, A. G. (1998). Unexpected sarcolemmal complement membrane attack complex deposits on nonnecrotic muscle fibers in muscular dystrophies. *Neurology, 50*(1), 41-46.

Stephan, A. B., Shum, E. Y., Hirsh, S., Cygnar, K. D., Reisert, J., & Zhao, H. (2009). ANO2 is the cilial calcium-activated chloride channel that may mediate olfactory amplification. *Proc Natl Acad Sci U S A, 106*(28), 11776-11781.

Stohr, H., Heisig, J. B., Benz, P. M., Schoberl, S., Milenkovic, V. M., Strauss, O., . . . Schulz, H. L. (2009). TMEM16B, a novel protein with calcium-dependent chloride channel activity, associates with a presynaptic protein complex in photoreceptor terminals. *J Neurosci, 29*(21), 6809-6818.

Sula, A., Cole, A. R., Yeats, C., Orengo, C., & Keep, N. H. (2014). Crystal structures of the human Dysferlin inner DysF domain. *BMC Struct Biol, 14*, 3.

Suzuki, J., Fujii, T., Imao, T., Ishihara, K., Kuba, H., & Nagata, S. (2013). Calcium-dependent phospholipid scramblase activity of TMEM16 protein family members. *J Biol Chem, 288*(19), 13305-13316.

Tahir, S. A., Yang, G., Goltsov, A., Song, K. D., Ren, C., Wang, J., . . . Thompson, T. C. (2013). Caveolin-1-LRP6 signaling module stimulates aerobic glycolysis in prostate cancer. *Cancer Res, 73*(6), 1900-1911.

Thomsen, P., Roepstorff, K., Stahlhut, M., & van Deurs, B. (2002). Caveolae are highly immobile plasma membrane microdomains, which are not involved in constitutive endocytic trafficking. *Mol Biol Cell, 13*(1), 238-250.

Tian, Y., Schreiber, R., & Kunzelmann, K. (2012). Anoctamins are a family of Ca2+-activated Cl- channels. *J Cell Sci, 125*(Pt 21), 4991-4998.

Timmel, T., Schuelke, M., & Spuler, S. (2014). Identifying dynamic membrane structures with atomic-force microscopy and confocal imaging. *Microsc Microanal, 20*(2), 514-520.

Tsutsumi, S., Kamata, N., Vokes, T. J., Maruoka, Y., Nakakuki, K., Enomoto, S., . . . Itakura, M. (2004). The novel gene encoding a putative transmembrane protein is mutated in gnathodiaphyseal dysplasia (GDD). *Am J Hum Genet, 74*(6), 1255-1261.

Urtizberea, J. A., Bassez, G., Leturcq, F., Nguyen, K., Krahn, M., & Levy, N. (2008). Dysferlinopathies. *Neurol India, 56*(3), 289-297.

Vafiadaki, E., Reis, A., Keers, S., Harrison, R., Anderson, L. V., Raffelsberger, T., . . . Bashir, R. (2001). Cloning of the mouse dysferlin gene and genomic characterization of the SJL-Dysf mutation. *Neuroreport, 12*(3), 625-629.

Bibliography

van der Kooi, A. J., Frankhuizen, W. S., Barth, P. G., Howeler, C. J., Padberg, G. W., Spaans, F., . . . Ginjaar, H. B. (2007). Limb-girdle muscular dystrophy in the Netherlands: gene defect identified in half the families. *Neurology, 68*(24), 2125-2128.

Vinten, J., Voldstedlund, M., Clausen, H., Christiansen, K., Carlsen, J., & Tranum-Jensen, J. (2001). A 60-kDa protein abundant in adipocyte caveolae. *Cell Tissue Res, 305*(1), 99-106.

Waddell, L. B., Lemckert, F. A., Zheng, X. F., Tran, J., Evesson, F. J., Hawkes, J. M., . . . Cooper, S. T. (2011). Dysferlin, annexin A1, and mitsugumin 53 are upregulated in muscular dystrophy and localize to longitudinal tubules of the T-system with stretch. *J Neuropathol Exp Neurol, 70*(4), 302-313.

Wahbi, K., Behin, A., Becane, H. M., Leturcq, F., Cossee, M., Laforet, P., . . . Duboc, D. (2013). Dilated cardiomyopathy in patients with mutations in anoctamin 5. *Int J Cardiol, 168*(1), 76-79.

Wang, X., Xie, W., Zhang, Y., Lin, P., Han, L., Han, P., . . . Cheng, H. (2010). Cardioprotection of ischemia/reperfusion injury by cholesterol-dependent MG53-mediated membrane repair. *Circ Res, 107*(1), 76-83.

Way, M., & Parton, R. G. (1996). M-caveolin, a muscle-specific caveolin-related protein. *FEBS Lett, 378*(1), 108-112.

Wein, N., Avril, A., Bartoli, M., Beley, C., Chaouch, S., Laforet, P., . . . Levy, N. (2010). Efficient bypass of mutations in dysferlin deficient patient cells by antisense-induced exon skipping. *Hum Mutat, 31*(2), 136-142.

Weisleder, N., Takeshima, H., & Ma, J. (2008). Immuno-proteomic approach to excitation--contraction coupling in skeletal and cardiac muscle: molecular insights revealed by the mitsugumins. *Cell Calcium, 43*(1), 1-8.

Wenzel, K., Carl, M., Perrot, A., Zabojszcza, J., Assadi, M., Ebeling, M., . . . Spuler, S. (2006). Novel sequence variants in dysferlin-deficient muscular dystrophy leading to mRNA decay and possible C2-domain misfolding. *Hum Mutat, 27*(6), 599-600.

Wenzel, K., Zabojszcza, J., Carl, M., Taubert, S., Lass, A., Harris, C. L., . . . Spuler, S. (2005). Increased susceptibility to complement attack due to down-regulation of decay-accelerating factor/CD55 in dysferlin-deficient muscular dystrophy. *J Immunol, 175*(9), 6219-6225.

Williams, T. M., & Lisanti, M. P. (2004). The Caveolin genes: from cell biology to medicine. *Ann Med, 36*(8), 584-595.

Willig, K. I., Rizzoli, S. O., Westphal, V., Jahn, R., & Hell, S. W. (2006). STED microscopy reveals that synaptotagmin remains clustered after synaptic vesicle exocytosis. *Nature, 440*(7086), 935-939.

Witting, N., Duno, M., Petri, H., Krag, T., Bundgaard, H., Kober, L., & Vissing, J. (2013). Anoctamin 5 muscular dystrophy in Denmark: prevalence, genotypes, phenotypes, cardiac findings, and muscle protein expression. *J Neurol, 260*(8), 2084-2093.

Woodman, S. E., Sotgia, F., Galbiati, F., Minetti, C., & Lisanti, M. P. (2004). Caveolinopathies: mutations in caveolin-3 cause four distinct autosomal dominant muscle diseases. *Neurology, 62*(4), 538-543.

Xu, L., Pallikkuth, S., Hou, Z., Mignery, G. A., Robia, S. L., & Han, R. (2011). Dysferlin forms a dimer mediated by the C2 domains and the transmembrane domain in vitro and in living cells. *PLoS One, 6*(11), e27884.

Yamada, E. (1955). The fine structure of the renal glomerulus of the mouse. *J Histochem Cytochem, 3*(4), 309.

Yamamoto, H., Sakane, H., Michiue, T., & Kikuchi, A. (2008). Wnt3a and Dkk1 regulate distinct internalization pathways of LRP6 to tune the activation of beta-catenin signaling. *Dev Cell, 15*(1), 37-48.

Yang, Y. D., Cho, H., Koo, J. Y., Tak, M. H., Cho, Y., Shim, W. S., . . . Oh, U. (2008). TMEM16A confers receptor-activated calcium-dependent chloride conductance. *Nature, 455*(7217), 1210-1215.

Yasunaga, S., Grati, M., Cohen-Salmon, M., El-Amraoui, A., Mustapha, M., Salem, N., . . . Petit, C. (1999). A mutation in OTOF, encoding otoferlin, a FER-1-like protein, causes DFNB9, a nonsyndromic form of deafness. *Nat Genet, 21*(4), 363-369.

Zacharias, U., Purfurst, B., Schowel, V., Morano, I., Spuler, S., & Haase, H. (2011). Ahnak1 abnormally localizes in muscular dystrophies and contributes to muscle vesicle release. *J Muscle Res Cell Motil, 32*(4-5), 271-280.

Zhu, H., Lin, P., De, G., Choi, K. H., Takeshima, H., Weisleder, N., & Ma, J. (2011). Polymerase transcriptase release factor (PTRF) anchors MG53 protein to cell injury site for initiation of membrane repair. *J Biol Chem, 286*(15), 12820-12824.

7 Supplement

Table 7-1 List of top 200 proteins correlating with the dysferlin profile within the analyzed data set

CTRL_ NC	DYSF_ NC	CTRL_ rAb	DYSF_ rAb	CTRL_ VHH	DYSF_ VHH	Protein name	Protein IDs	Gene name
13,39	12,88	26,90	12,08	25,00	21,86	Prolow-density lipoprotein receptor-related protein 1	Q07954	LRP1
13,55	14,13	26,78	12,24	25,01	23,02	Myoferlin	Q9NZM1-6	MYOF
14,21	12,78	26,31	12,42	24,77	21,52	Transferrin receptor protein 1	P02786	TFRC
14,13	12,51	25,86	11,38	24,29	14,47	Dysferlin	O75923-8	DYSF
14,04	12,86	25,56	12,01	23,75	22,08	Cation-independent mannose-6-phosphate receptor	P11717	IGF2R
13,19	12,56	25,10	13,18	22,78	17,27	DnaJ homolog subfamily C member 13	O75165	DNAJC13
13,99	12,64	25,06	12,65	23,38	18,41	C-type mannose receptor 2	Q9UBG0	MRC2
12,81	13,50	24,53	12,00	22,77	14,12	Rab11 family-interacting protein 5	Q9BXF6	RAB11FIP5
13,21	13,01	24,30	17,29	22,43	19,10	Clathrin heavy chain 1	Q00610-2	CLTC
13,12	13,50	24,20	12,85	23,63	21,42	Neural cell adhesion molecule 1	P13591	NCAM1
13,90	12,33	23,93	12,99	23,77	21,16	Secretory carrier-associated membrane protein 2	O15127	SCAMP2
13,40	12,45	23,85	10,93	23,16	19,50	Basal cell adhesion molecule	P50895	BCAM
12,70	12,98	23,70	12,65	21,36	18,07	Leucyl-cystinyl aminopeptidase	Q9UIQ6	LNPEP
13,12	13,20	23,67	11,69	23,54	21,11	Sodium/potassium-transporting ATPase subunit alpha-1	P05023-3	ATP1A1
13,10	13,78	23,39	11,49	21,32	16,99	Serotransferrin	TRFE_HUMAN	TF
13,41	13,81	23,33	12,70	22,28	19,08	Solute carrier family 12 member 4	Q9UP95-2	SLC12A4
13,16	13,38	23,24	13,04	23,96	19,80	Basement membrane-specific heparan sulfate proteoglycan core prot.	P98160	HSPG2
13,05	12,93	23,19	13,37	22,32	20,34	Vesicle-associated membrane protein 3	Q15836	VAMP3
13,65	13,73	23,11	11,59	22,53	19,35	Secretory carrier-associated membrane protein 1	O15126	SCAMP1
13,54	13,15	22,87	13,45	21,95	16,98	Syntaxin-12	Q86Y82	STX12
22,24	21,76	22,54	21,83	22,77	22,03	Dermcidin	P81605	DCD

						Protein	ID	Gene
13,64	12,97	22,53	11,95	20,53	18,47	Sortilin	Q99523	SORT1
13,40	13,43	22,51	13,02	21,88	19,72	Secretory carrier-associated membrane protein 3	O14828	SCAMP3
12,97	13,18	22,46	12,05	22,40	17,10	Solute carrier family 12 member 2	P55011	SLC12A2
12,19	12,96	22,41	11,91	21,02	18,81	Solute carrier family 2, facilitated glucose transporter member 1	P11166	SLC2A1
13,85	12,99	22,37	12,56	21,45	19,36	Synaptogyrin-2	O43760	SYNGR2
12,77	12,57	22,26	13,60	20,43	15,83	V-type proton ATPase 116 kDa subunit a isoform 1	Q93050-1	ATP6V0A1
13,07	12,56	22,13	12,28	21,71	19,74	Synaptophysin-like protein 1	Q16563-2	SYPL1
13,10	12,88	22,13	12,10	22,21	18,60	Thrombospondin-1	P07996	THBS1
13,42	13,11	22,13	12,24	20,35	14,89	H(+)/Cl(-) exchange transporter 5	P51795	CLCN5
12,84	13,73	22,07	12,38	21,28	18,85	Syntaxin-7	O15400-2	STX7
13,51	12,84	22,07	12,09	22,46	20,29	Catenin alpha-1	P35221	CTNNA1
14,24	13,54	21,90	11,91	19,11	14,07	Autophagy-related protein 9A	Q7Z3C6	ATG9A
13,02	13,64	21,88	13,49	20,36	14,27	Voltage-dependent calcium channel subunit alpha-2/delta-1	P54289-4	CACNA2D1
13,76	12,58	21,87	12,04	20,11	16,37	Cation-dependent mannose-6-phosphate receptor	P20645	M6PR
13,06	13,18	21,69	12,37	19,15	16,91	Low-density lipoprotein receptor	P01130-3	LDLR
13,58	12,34	21,67	12,04	19,49	14,41	Two pore calcium channel protein 1	Q9ULQ1-3	TPCN1
13,34	12,48	21,65	12,68	21,69	18,93	Cadherin-15	P55291	CDH15
14,39	13,04	21,65	12,27	17,69	14,52	Rho GTPase-activating protein 10	A1A4S6	ARHGAP10
12,96	13,82	21,64	12,23	21,70	18,41	Plasma membrane calcium-transporting ATPase 1	P20020-6	ATP2B1
13,64	12,84	21,59	11,82	21,25	19,84	Catenin beta-1	P35222	CTNNB1
13,05	13,05	21,53	11,84	20,30	13,55	Podocalyxin	O00592-2	PODXL
14,21	13,44	21,48	12,72	21,80	19,83	Integrin alpha-6	P23229-4	ITGA6
13,50	13,64	21,48	11,93	21,52	19,91	Gelsolin	P06396-2	GSN
13,37	12,83	21,45	11,32	19,33	14,95	Vacuolar protein sorting-associated protein 45	Q9NRW7	VPS45
13,76	13,08	21,40	11,72	20,42	17,93	Carboxypeptidase D	O75976	CPD

						Protein	Accession	Gene
13,44	12,75	21,39	12,06	20,83	19,10	Cadherin-13	P55290	CDH13
13,71	12,82	21,32	12,15	20,39	13,62	SPARC	P09486	SPARC
13,80	12,62	21,31	11,82	22,19	13,66	Gamma-glutamyltransferase 5	P36269-2	GGT5
13,00	13,46	21,30	12,57	21,30	16,86	Dystroglycan	Q14118	DAG1
13,05	13,97	21,21	12,10	19,82	15,80	Lysosome-associated membrane glycoprotein 2	P13473-2	LAMP2
13,33	12,70	21,20	11,76	20,35	15,75	Metalloreductase STEAP3	Q658P3-3	STEAP3
14,74	12,60	21,19	12,06	20,09	17,32	Nicastrin	Q92542-2	NCSTN
14,08	11,96	21,13	12,23	17,48	13,28	Galectin-1	P09382	LGALS1
12,78	12,57	20,84	12,10	18,84	15,99	Voltage-dependent L-type calcium channel subunit alpha-1S	Q13698	CACNA1S
13,71	13,96	20,66	15,27	19,66	17,53	Cathepsin D	P07339	CTSD
13,08	13,51	20,56	10,99	17,95	14,87	AP-1 complex subunit mu-1	Q9BXS5	AP1M1
13,04	13,47	20,45	12,72	16,63	14,52	Chloride transport protein 6	P51797-6	CLCN6
13,62	13,05	20,43	12,61	20,06	16,58	Junctional adhesion molecule C	Q9BX67	JAM3
13,78	12,27	20,38	11,75	19,69	16,81	V-type proton ATPase catalytic subunit A	P38606	ATP6V1A
13,49	12,46	20,32	12,57	20,13	16,26	V-type proton ATPase subunit d 1	P61421	ATP6V0D1
13,71	12,61	20,27	11,91	20,56	17,64	Alkaline phosphatase, tissue-nonspecific isozyme	P05186-2	ALPL
12,99	13,19	20,19	13,01	18,37	14,48	Rab11 family-interacting protein 2	Q7L804	RAB11FIP2
12,98	13,36	20,14	11,29	19,64	12,97	Pigment epithelium-derived factor	P36955	SERPINF1
13,04	13,04	20,13	11,61	19,42	18,55	Serine incorporator 1	Q9NRX5	SERINC1
13,10	13,02	20,12	12,78	19,90	16,67	Plexin-A1	Q9UIW2	PLXNA1
14,03	13,44	20,11	12,66	21,18	16,85	Vesicle-associated membrane protein 5	O95183	VAMP5
13,31	12,31	20,10	11,66	21,47	18,80	Laminin subunit gamma-1	P11047	LAMC1
13,16	13,32	20,07	12,63	17,41	13,57	AP-1 complex subunit gamma-1	O43747	AP1G1
13,14	12,72	20,06	11,75	19,69	14,75	V-type proton ATPase subunit B, brain isoform	P21281	ATP6V1B2
13,50	13,24	20,06	12,38	21,92	19,13	Laminin subunit alpha-5	O15230	LAMA5

12,50	12,77	20,02	11,91	18,71	14,24	Treacle protein	Q13428-2	TCOF1
12,73	13,29	20,01	12,15	20,36	14,75	Catenin delta-1	O60716-13	CTNND1
13,11	11,99	19,90	12,86	20,88	18,23	Integrin beta-6	P18564	ITGB6
13,47	12,67	19,88	12,12	20,15	15,61	Integrin alpha-V	P06756-3	ITGAV
13,87	13,29	19,86	12,77	19,26	14,61	Tyrosine-protein kinase Yes	P07947	YES1
14,40	13,67	19,82	12,70	17,06	15,23	V-type proton ATPase 116 kDa subunit a isoform 2	Q9Y487	ATP6V0A2
13,26	12,90	19,76	11,85	19,71	14,67	Vesicle-associated membrane protein 2	P63027	VAMP2
13,85	14,25	19,75	12,08	18,37	13,78	Syntaxin-16	O14662-6	STX16
13,57	13,26	19,73	12,20	17,14	14,29	Low-density lipoprotein receptor-related protein 4	O75096	LRP4
12,73	12,56	19,69	14,17	19,54	14,26	Apolipoprotein E	P02649	APOE
13,10	13,02	19,62	12,29	19,51	14,35	Anthrax toxin receptor 1	Q9H6X2-5	ANTXR1
12,64	13,15	19,56	12,91	16,01	15,05	Platelet receptor Gi24	Q9H7M9	C10orf54
12,98	13,87	19,55	12,47	15,76	12,64	Signal peptide peptidase-like 2A	Q8TCT8	SPPL2A
13,24	13,35	19,53	13,77	16,63	14,01	WD repeat and FYVE domain-containing protein 1	Q8IWB7	WDFY1
13,50	13,33	19,52	11,65	21,52	17,75	Laminin subunit beta-2	P55268	LAMB2
13,58	13,45	19,52	11,66	17,63	13,09	Serine/threonine-protein kinase LMTK2	Q8IWU2	LMTK2
14,08	13,00	19,43	12,45	20,58	14,70	Integral membrane protein 2C	Q9NQX7-2	ITM2C
13,25	12,74	19,39	12,34	17,28	13,58	Transmembrane protein 9B	Q9NQ34	TMEM9B
13,63	13,20	19,39	12,24	18,01	14,22	AP-1 complex subunit beta-1	Q10567-3	AP1B1
13,42	13,02	19,38	12,27	19,09	15,87	Guanine nucleotide-binding protein G(I)/G(S)/G(T) subunit	P62879	GNB2
13,14	13,19	19,37	12,66	19,11	13,59	Caveolin-3	P56539	CAV3
14,11	13,30	19,35	12,92	17,81	15,42	CD97 antigen	P48960-2	CD97
13,14	13,31	19,28	12,32	19,34	16,85	Aminopeptidase N	P15144	ANPEP
14,10	12,81	19,27	11,31	18,14	17,60	Amyloid beta A4 protein	P05067-7	APP
13,29	13,13	19,24	11,86	18,88	16,78	Dipeptidyl peptidase 4	P27487	DPP4

13,05	12,63	19,10	11,66	16,44	14,59	CD276 antigen	Q5ZPR3-3	CD276
13,34	13,69	19,09	12,97	19,65	16,49	Catenin alpha-2	P26232-2	CTNNA2
13,53	13,44	19,07	12,48	18,73	15,01	Neprilysin	P08473	MME
13,61	12,61	19,06	12,87	20,20	14,37	Guanine nucleotide-binding protein subunit alpha-11	P29992	GNA11
13,15	12,50	19,03	11,52	17,59	14,04	Muscle, skeletal receptor tyrosine-protein kinase	O15146	MUSK
13,29	13,48	19,01	11,81	17,88	12,80	Sodium/hydrogen exchanger 9	Q8IVB4	SLC9A9
13,31	13,53	19,00	13,25	19,16	13,79	Equilibrative nucleoside transporter 1	Q99808	SLC29A1
13,16	13,14	18,95	12,33	18,53	14,30	CD109 antigen	Q6YHK3-2	CD109
13,54	12,61	18,85	15,89	20,39	15,38	Cytoplasmic dynein 1 heavy chain 1	Q14204	DYNC1H1
13,79	12,61	18,75	11,94	17,84	15,10	Syntaxin-10	O60499	STX10
13,07	12,55	18,73	12,20	19,37	16,86	Integrin beta-5	P18084	ITGB5
13,75	12,69	18,73	12,85	19,57	16,36	Ras-related protein Rab-4A	P20338	RAB4A
13,53	13,58	18,70	11,43	19,78	17,30	Guanine nucleotide-binding protein G(q) subunit alpha	P50148	GNAQ
12,63	13,76	18,70	13,21	18,30	13,68	Protein Smaug homolog 1	Q9UPU9-2	SAMD4A
13,67	12,69	18,67	13,00	15,79	15,00	Thioredoxin-interacting protein	Q9H3M7	TXNIP
13,73	13,46	18,66	12,57	18,24	14,11	V-type proton ATPase subunit E 1	P36543-3	ATP6V1E1
14,52	13,15	18,63	12,23	17,67	14,59	Syntaxin-6	O43752	STX6
13,65	12,90	18,59	13,30	18,60	15,81	Transmembrane protein 50A	O95807	TMEM50A
14,06	13,47	18,55	12,54	18,18	14,39	Ras-related protein Rap-2b	P61225	RAP2B
12,98	13,83	18,54	11,46	17,39	13,59	Phosphatidylinositol 4-kinase type 2-alpha	Q9BTU6	PI4K2A
13,99	12,85	18,48	11,95	20,70	13,55	Elastin	P15502-5	ELN
13,53	13,03	18,47	12,75	19,02	14,34	Poliovirus receptor	P15151-3	PVR
14,15	13,85	18,45	12,20	16,75	13,92	Guanine nucleotide-binding protein subunit alpha-13	Q14344	GNA13
13,63	12,73	18,43	12,85	18,57	13,12	Prostaglandin F2 receptor negative regulator	Q9P2B2	PTGFRN
12,98	13,64	18,43	12,36	15,62	13,83	Rab11 family-interacting protein 1	Q6WKZ4	RAB11FIP1

14,01	12,66	18,40	12,04	15,74	13,76	Transmembrane protein 63B	Q5T3F8-2	TMEM63B
13,76	13,58	18,36	12,47	17,62	17,18	Sodium-dependent phosphate transporter 2	Q08357	SLC20A2
13,49	13,59	18,36	12,40	18,65	13,98	Choline transporter-like protein 1	Q8WWI5-3	SLC44A1
12,97	13,30	18,29	12,21	17,66	15,78	Major prion protein	P04156-2	PRNP
13,06	13,01	18,29	12,01	17,27	16,48	Trans-Golgi network integral membrane protein 2	O43493-4	TGOLN2
13,81	12,39	18,28	11,95	16,67	14,05	Kinase D-interacting substrate of 220 kDa	Q9ULH0-2	KIDINS220
13,35	13,12	18,26	10,87	18,15	14,27	Teneurin-3	Q9P273	TENM3
13,97	12,30	18,20	11,95	19,26	13,77	Protein unc-45 homolog B	Q8IWX7-2	UNC45B
13,52	12,22	18,17	12,84	17,56	14,08	UPF0606 protein KIAA1549	Q9HCM3-2	KIAA1549
12,36	12,65	18,16	12,71	18,83	13,87	Aldehyde dehydrogenase family 3 member B1	P43353	ALDH3B1
13,82	13,52	18,12	11,73	16,76	14,08	Proactivator polypeptide	P07602	PSAP
13,04	13,44	18,07	12,17	18,05	14,06	T-complex protein 1 subunit theta	P50990	CCT8
12,90	13,31	18,07	12,27	14,49	13,20	Transmembrane protein 2	Q9UHN6-2	TMEM2
13,24	12,53	17,90	11,15	16,49	14,85	Voltage-dependent L-type calcium channel subunit beta-1	Q02641-3	CACNB1
13,34	12,37	17,86	12,81	18,89	15,96	Plexin-B2	O15031	PLXNB2
13,25	14,10	17,84	11,98	18,85	13,64	Cyclin-Y	Q8ND76-3	CCNY
13,22	13,53	17,84	12,07	15,37	14,68	Calcium-transporting ATPase type 2C member 1	P98194-2	ATP2C1
13,54	12,16	17,84	12,56	14,23	13,12	Intersectin-2	Q9NZM3-2	ITSN2
13,20	12,83	17,83	11,84	17,37	12,96	Matrix metalloproteinase-14	P50281	MMP14
13,22	12,48	17,82	11,62	16,27	13,47	Lysosomal protective protein	P10619	CTSA
13,36	13,24	17,77	13,12	18,12	16,96	Collagen alpha-2(I) chain	P08123	COL1A2
13,31	12,70	17,74	11,27	16,62	14,08	Sodium/potassium-transporting ATPase subunit beta-1	P05026-2	ATP1B1
13,02	13,29	17,71	11,66	19,12	16,99	Agrin	O00468-2	AGRN
13,93	12,20	17,70	12,18	16,61	15,15	Protein YIPF6	Q96EC8	YIPF6
13,85	13,45	17,70	12,19	15,11	14,07	Calsyntenin-2	Q9H4D0	CLSTN2

						Protein	UniProt	Gene
14,17	13,46	17,70	11,46	17,57	13,68	Vesicle transport through interaction with t-SNAREs homolog 1B	Q9UEU0	VTI1B
12,46	13,54	17,66	11,81	17,79	15,17	Cell surface glycoprotein MUC18	P43121	MCAM
13,67	12,64	17,62	12,06	17,09	13,50	KN motif and ankyrin repeat domain-containing protein 2	Q63ZY3-3	KANK2
14,13	13,09	17,61	11,18	16,29	14,80	N-acetylglucosamine-6-sulfatase	P15586	GNS
14,06	13,43	17,60	11,78	18,13	13,39	Matrix-remodeling-associated protein 8	Q9BRK3	MXRA8
13,35	13,20	17,53	11,65	16,80	13,87	Transmembrane protein 9	Q9P0T7	TMEM9
14,08	12,92	17,53	12,70	17,57	15,05	Rho guanine nucleotide exchange factor 6	Q15052-2	ARHGEF6
13,48	12,40	17,51	12,14	17,38	14,38	Clathrin interactor 1	Q14677	CLINT1
13,13	12,11	17,50	11,01	14,58	13,75	Probable phospholipid-transporting ATPase IIB	O43861-2	ATP9B
13,86	13,13	17,49	12,90	18,62	14,05	Phospholipase D3	Q8IV08	PLD3
13,36	13,27	17,48	12,15	16,46	13,33	Copper-transporting ATPase 1	Q04656-5	ATP7A
13,08	12,70	17,47	11,90	17,23	15,14	Caveolin-1	Q03135-2	CAV1
13,95	12,60	17,38	12,16	17,27	15,84	Monocarboxylate transporter 8	P36021	SLC16A2
13,89	13,51	17,37	11,78	18,65	15,83	Synaptosomal-associated protein 23	O00161-2	SNAP23
15,88	12,86	17,34	12,68	18,57	14,36	Protein MB21D2	Q8IYB1	MB21D2
13,27	12,82	17,32	12,57	19,12	13,40	Casein kinase II subunit alpha 3	Q8NEV1	CSNK2A3
13,41	13,06	17,30	12,27	14,50	13,97	Receptor-type tyrosine-protein phosphatase kappa	Q15262-2	PTPRK
14,30	12,73	17,25	12,65	17,28	13,18	RING finger protein 11	Q9Y3C5	RNF11
14,09	13,50	17,22	12,87	16,51	15,00	Kinesin-1 heavy chain	P33176	KIF5B
13,99	13,30	17,16	12,54	19,76	16,43	Vesicle-associated membrane protein 7	P51809-3	VAMP7
12,65	13,25	17,16	12,63	19,36	15,07	Peroxidasin homolog	Q92626	PXDN
14,64	12,99	16,97	12,30	17,31	14,05	G-protein coupled receptor family C group 5 member B	Q9NZH0	GPRC5B
12,82	12,96	16,90	11,78	16,85	14,95	Protocadherin gamma-C3	Q9UN70	PCDHGC3
13,82	13,43	16,81	13,47	17,79	14,38	Secretory carrier-associated membrane protein 4	Q969E2-2	SCAMP4
13,31	13,35	16,74	11,62	16,72	14,41	Disheveled-associated activator of morphogenesis 2	Q86T65-4	DAAM2

						Protein	Accession	Gene
14,32	12,98	16,62	12,21	16,19	14,11	Protein FAM171A2	A8MVW0	FAM171A2
13,86	13,76	16,57	12,05	18,25	13,38	Neuropilin-1	O14786	NRP1
13,19	12,44	16,57	12,63	16,40	14,14	Sarcospan	Q14714-2	SSPN
13,38	11,84	16,55	12,38	20,26	13,95	Unconventional myosin-Ib	O43795-2	MYO1B
13,64	13,16	16,54	11,65	16,86	13,80	Vesicle transport protein SFT2B	O95562	SFT2D2
12,60	13,22	16,54	12,27	16,26	14,42	Phosphatidylinositol-binding clathrin assembly protein	Q13492-4	PICALM
13,72	12,67	16,51	12,55	17,37	14,81	Neutral alpha-glucosidase AB	Q14697	GANAB
13,86	13,91	16,51	11,42	15,00	13,59	Prothymosin alpha	P06454-2	PTMA
14,71	12,81	16,42	11,65	17,16	14,62	Casein kinase II subunit alpha	P19784	CSNK2A2
12,80	11,84	16,33	12,17	17,00	13,52	Voltage-dependent calcium channel gamma-1 subunit	Q06432	CACNG1
12,86	12,98	16,31	12,31	16,48	14,16	Deoxyribonuclease-1-like 1	P49184	DNASE1L1
12,82	11,76	16,30	11,43	14,10	14,02	Transmembrane protein 108	Q6UXF1	TMEM108
14,25	13,69	16,28	11,81	17,33	13,37	Casein kinase II subunit beta	P67870	CSNK2B
13,10	12,28	16,23	13,13	16,96	14,94	Syntaxin-binding protein 3	O00186	STXBP3
14,55	12,46	16,16	12,73	18,16	13,22	Receptor tyrosine-protein kinase erbB-2	P04626-4	ERBB2
13,98	14,21	16,13	12,99	18,45	14,42	Monocarboxylate transporter 4	O15427	SLC16A3
12,34	12,83	16,09	12,80	17,15	14,52	Syndecan-4	P31431-2	SDC4
13,13	12,75	16,08	12,53	15,60	13,93	General vesicular transport factor p115	O60763	USO1
13,41	13,32	16,05	12,42	18,95	13,86	PTB domain-containing engulfment adapter protein 1	Q9UBP9-2	GULP1
13,82	13,71	15,95	12,66	14,83	13,48	Receptor tyrosine-protein kinase erbB-3	P21860-4	ERBB3
13,07	13,25	15,94	11,96	15,40	14,87	Huntingtin-interacting protein 1	O00291-3	HIP1
13,49	13,12	15,92	12,38	14,78	14,04	Transmembrane protein 132A	Q24JP5-4	TMEM132A
13,95	13,07	15,66	12,78	16,75	14,22	Cullin-associated NEDD8-dissociated protein 1	Q86VP6-2	CAND1
12,92	12,42	15,62	12,44	15,33	14,55	RuvB-like 2	Q9Y230	RUVBL2
13,39	13,33	15,51	12,57	18,39	13,60	Collagen alpha-1(III) chain	P02461	COL3A1

13,13	13,74	15,50	12,63	16,59	14,33	Syntaxin-4	Q12846	STX4
13,41	13,30	15,33	12,45	15,99	14,03	Protein sprouty homolog 4	Q9C004-2	SPRY4
13,37	13,00	15,22	12,43	16,02	14,72	Serine/threonine-protein phosphatase 2A 65 kDa regulatory subunit A α	P30153	PPP2R1A
13,61	12,54	14,15	12,49	14,25	13,58	Chloride intracellular channel protein 1	O00299	CLIC1

Immunopurification was done with an anti-dysferlin monoclonal antibody from rabbit (rAb) or a llama-derived VHH-antibody fragment (VHH). Logarithmized protein intensities (log2) of immunopurified samples from control (CTRL) and dysferlin-deficient (DYSF) myotubes are shown. Note that values from non-detected proteins after LC-MS analysis have been imputed by values estimated from a normal distribution of the data set (Perseus software, version 1.4.1.3). Negative control samples are listed as NC. UniProt-protein IDs, protein, and gene names are displayed. Proteins were sorted for protein intensities of CTRL-rAb samples.

Supplement

Table 7-2 List of common proteins detected in IP-samples from rAb and VHH

Protein name	Protein ID	Gene name
Extended synaptotagmin-2	A0FGR8-2	ESYT2
Rho GTPase-activating protein 10	A1A4S6	ARHGAP10
Protein FAM171A2	A8MVW0	FAM171A2
Actin, cytoplasmic 1	P60709	ACTB
Collagen alpha-1(III) chain	P02461	COL3A1
Annexin A5	ANXA5_HUMAN	ANXA5
Beta-2-microglobulin	P61769	B2M
Filaggrin-2	Q5D862	FLG2
Catalase	CATA_HUMAN	CAT
Cathepsin D	P07339	CTSD
Gelsolin	P06396-2	GSN
Serum albumin	P02768	ALB
Thrombospondin-1	P07996	THBS1
Tropomyosin beta chain	P07951	TPM2
Tubulin alpha-1B chain	P68363	TUBA1B
Lysozyme C	P61626	LYZ
Unconventional myosin-Ic	O00159-3	MYO1C
Synaptosomal-associated protein 23	O00161-2	SNAP23
Syntaxin-binding protein 3	O00186	STXBP3
Huntingtin-interacting protein 1	O00291-3	HIP1
Golgi integral membrane protein 4	O00461	GOLIM4
Agrin	O00468-2	AGRN
Podocalyxin	O00592-2	PODXL
Syntaxin-16	O14662-6	STX16
Disintegrin and metalloproteinase domain-containing protein 10	O14672	ADAM10
Neuropilin-1	O14786	NRP1
Secretory carrier-associated membrane protein 3	O14828	SCAMP3
Calsequestrin-2	O14958	CASQ2
Sarcoplasmic/endoplasmic reticulum calcium ATPase 1	O14983	ATP2A1
Plexin-B2	O15031	PLXNB2
Secretory carrier-associated membrane protein 1	O15126	SCAMP1
Secretory carrier-associated membrane protein 2	O15127	SCAMP2
Muscle, skeletal receptor tyrosine-protein kinase	O15146	MUSK
Laminin subunit alpha-5	O15230	LAMA5
Leptin receptor gene-related protein	O15243	LEPROT
Surfeit locus protein 4	O15260-2	SURF4
Syntaxin-7	O15400-2	STX7
Monocarboxylate transporter 4	O15427	SLC16A3
Centromere/kinetochore protein zw10 homolog	O43264	ZW10
Trans-Golgi network integral membrane protein 2	O43493-4	TGOLN2
AP-1 complex subunit gamma-1	O43747	AP1G1
Syntaxin-6	O43752	STX6
Synaptogyrin-2	O43760	SYNGR2
Unconventional myosin-Ib	O43795-2	MYO1B
Probable phospholipid-transporting ATPase IIB	O43861-2	ATP9B

Syntaxin-10	O60499	STX10
Catenin delta-1	O60716-13	CTNND1
General vesicular transport factor p115	O60763	USO1
Low-density lipoprotein receptor-related protein 4	O75096	LRP4
DnaJ homolog subfamily C member 13	O75165	DNAJC13
Vesicle-trafficking protein SEC22b	O75396	SEC22B
Renin receptor	O75787	ATP6AP2
PRA1 family protein 3	O75915	ARL6IP5
Dysferlin	O75923-8	DYSF
Triple functional domain protein	O75962-5	TRIO
Carboxypeptidase D	O75976	CPD
Signal recognition particle subunit SRP72	O76094	SRP72
E3 UFM1-protein ligase 1	O94874	UFL1
Endonuclease domain-containing 1 protein	O94919	ENDOD1
AP-2 complex subunit alpha-2	O94973	AP2A2
Vesicle-associated membrane protein 5	O95183	VAMP5
Myotubularin-related protein 5	O95248	SBF1
Vesicle-associated membrane protein-associated protein B/C	O95292	VAPB
Vesicle transport protein SFT2B	O95562	SFT2D2
Long-chain-fatty-acid--CoA ligase 3	O95573	ACSL3
E3 ubiquitin-protein ligase HERC2	O95714	HERC2
AP-2 complex subunit alpha-1	O95782-2	AP2A1
Transmembrane protein 50A	O95807	TMEM50A
Serum deprivation-response protein	O95810	SDPR
BAG family molecular chaperone regulator 2	O95816	BAG2
L-lactate dehydrogenase A chain	P00338	LDHA
NADH-cytochrome b5 reductase 3	P00387-2	CYB5R3
Phosphoglycerate kinase 1	P00558	PGK1
Cystatin-A	P01040	CSTA
Low-density lipoprotein receptor	P01130-3	LDLR
Collagen alpha-1(I) chain	P02452	COL1A1
Apolipoprotein E	P02649	APOE
Fibronectin	P02751-5	FN1
Transferrin receptor protein 1	P02786	TFRC
Fructose-bisphosphate aldolase A	P04075	ALDOA
Annexin A1	P04083	ANXA1
Major prion protein	P04156-2	PRNP
Thy-1 membrane glycoprotein	P04216	THY1
Glyceraldehyde-3-phosphate dehydrogenase	P04406-2	GAPDH
Receptor tyrosine-protein kinase erbB-2	P04626-4	ERBB2
Heat shock protein beta-1	P04792	HSPB1
Dolichyl-diphosphooligosaccharide--protein glycosyltransferase subunit 1	P04843	RPN1
Dolichyl-diphosphooligosaccharide--protein glycosyltransferase subunit 2	P04844	RPN2
Guanine nucleotide-binding protein G(i) subunit alpha-2	P04899	GNAI2
Histone H2A type 1-C	Q93077	HIST1H2AC
Sodium/potassium-transporting ATPase subunit alpha-1	P05023-3	ATP1A1

Sodium/potassium-transporting ATPase subunit beta-1	P05026-2	ATP1B1
Amyloid beta A4 protein	P05067-7	APP
Arginase-1	P05089	ARG1
Protein S100-A8	P05109	S100A8
ADP/ATP translocase 2	P05141	SLC25A5
Alkaline phosphatase, tissue-nonspecific isozyme	P05186-2	ALPL
60S acidic ribosomal protein P2	P05387	RPLP2
60S acidic ribosomal protein P0	P05388	RPLP0
Integrin beta-1	P05556	ITGB1
Protein S100-A9	P06702	S100A9
Alpha-enolase	P06733	ENO1
Integrin alpha-V	P06756-3	ITGAV
L-lactate dehydrogenase B chain	P07195	LDHB
Annexin A2	P07355	ANXA2
Tubulin beta chain	P07437	TUBB
Proactivator polypeptide	P07602	PSAP
Heat shock protein HSP 90-alpha	P07900	HSP90AA1
Tyrosine-protein kinase Yes	P07947	YES1
Heat shock 70 kDa protein 1A/1B	P08107	HSPA1A
Collagen alpha-2(I) chain	P08123	COL1A2
Annexin A6	P08133-2	ANXA6
4F2 cell-surface antigen heavy chain	P08195-2	SLC3A2
Heat shock protein HSP 90-beta	P08238	HSP90AB1
Neprilysin	P08473	MME
Integrin alpha-5	P08648	ITGA5
CD63 antigen	P08962-3	CD63
Galectin-1	P09382	LGALS1
SPARC	P09486	SPARC
Ubiquitin-60S ribosomal protein L40	P62987	UBA52
Lysosomal protective protein	P10619	CTSA
78 kDa glucose-regulated protein	P11021	HSPA5
Laminin subunit gamma-1	P11047	LAMC1
Myosin-3	P11055	MYH3
Heat shock cognate 71 kDa protein	P11142	HSPA8
Solute carrier family 2, facilitated glucose transporter member 1	P11166	SLC2A1
Lysosome-associated membrane glycoprotein 1	P11279	LAMP1
Dystrophin	P11532-4	DMD
Cation-independent mannose-6-phosphate receptor	P11717	IGF2R
Polyadenylate-binding protein 1	P11940-2	PABPC1
Collagen alpha-1(XI) chain	P12107-3	COL11A1
Prolactin-inducible protein	P12273	PIP
Creatine kinase B-type	P12277	CKB
Myosin-7	P12883	MYH7
Lysosome-associated membrane glycoprotein 2	P13473-2	LAMP2
Myosin-8	P13535	MYH8
Neural cell adhesion molecule 1	P13591	NCAM1
Elongation factor 2	P13639	EEF2

Glycogen [starch] synthase, muscle	P13807-2	GYS1
CD59 glycoprotein	P13987	CD59
CD99 antigen	P14209-3	CD99
Pyruvate kinase isozymes M1/M2	P14618	PKM
Endoplasmin	P14625	HSP90B1
Junction plakoglobin	P14923	JUP
Aminopeptidase N	P15144	ANPEP
Poliovirus receptor	P15151-3	PVR
Elastin	P15502-5	ELN
N-acetylglucosamine-6-sulfatase	P15586	GNS
Desmoplakin	P15924	DSP
CD44 antigen	P16070-18	CD44
Histone H1.5	P16401	HIST1H1B
Histone H1.2	P16403	HIST1H1C
NADPH--cytochrome P450 reductase	P16435	POR
Sarcoplasmic/endoplasmic reticulum calcium ATPase 2	P16615-2	ATP2A2
Heat shock 70 kDa protein 6	P17066	HSPA6
HLA class I histocompatibility antigen, alpha chain G	P17693	HLA-G
T-complex protein 1 subunit alpha	P17987	TCP1
Integrin beta-5	P18084	ITGB5
60S ribosomal protein L7	P18124	RPL7
Integrin beta-6	P18564	ITGB6
Casein kinase II subunit alpha	P19784	CSNK2A2
Plasma membrane calcium-transporting ATPase 1	P20020-6	ATP2B1
Ras-related protein Rab-4A	P20338	RAB4A
Ras-related protein Rab-6A	P20340	RAB6A
Ras-related protein Rab-6A	P20340-2	RAB6A
Cation-dependent mannose-6-phosphate receptor	P20645	M6PR
V-type proton ATPase subunit B, brain isoform	P21281	ATP6V1B2
5-nucleotidase	P21589-2	NT5E
Voltage-dependent anion-selective channel protein 1	P21796	VDAC1
Ryanodine receptor 1	P21817-2	RYR1
Receptor tyrosine-protein kinase erbB-3	P21860-4	ERBB3
Integrin alpha-6	P23229-4	ITGA6
40S ribosomal protein S3	P23396	RPS3
Cofilin-1	P23528	CFL1
Zinc-alpha-2-glycoprotein	P25311	AZGP1
ATP synthase subunit alpha, mitochondrial	P25705	ATP5A1
Integrin alpha-3	P26006	ITGA3
Catenin alpha-2	P26232-2	CTNNA2
60S ribosomal protein L13	P26373	RPL13
Erythrocyte band 7 integral membrane protein	P27105	STOM
14-3-3 protein theta	P27348	YWHAQ
Dipeptidyl peptidase 4	P27487	DPP4
Microtubule-associated protein 4	P27816	MAP4
Microtubule-associated protein 4	P27816-4	MAP4
Calnexin	P27824	CANX

Guanine nucleotide-binding protein subunit alpha-11	P29992	GNA11
Thioredoxin-dependent peroxide reductase, mitochondrial	P30048-2	PRDX3
60S ribosomal protein L12	P30050	RPL12
Serine/threonine-protein phosphatase 2A 65 kDa regulatory subunit A alpha isoform	P30153	PPP2R1A
HLA class I histocompatibility antigen, A-34 alpha chain	P30453	HLA-A
HLA class I histocompatibility antigen, B-41 alpha chain	P30479	HLA-B
HLA class I histocompatibility antigen, B-42 alpha chain	P30480	HLA-B
Syndecan-4	P31431-2	SDC4
Caspase-14	P31944	CASP14
14-3-3 protein sigma	P31947-2	SFN
Kinesin-1 heavy chain	P33176	KIF5B
Glypican-1	P35052	GPC1
Catenin alpha-1	P35221	CTNNA1
Catenin beta-1	P35222	CTNNB1
60S ribosomal protein L22	P35268	RPL22
Myosin-9	P35579	MYH9
Coatomer subunit beta	P35606	COPB2
Basigin	P35613-2	BSG
Monocarboxylate transporter 8	P36021	SLC16A2
Gamma-glutamyltransferase 5	P36269-2	GGT5
V-type proton ATPase subunit E 1	P36543-3	ATP6V1E1
60S ribosomal protein L4	P36578	RPL4
Pigment epithelium-derived factor	P36955	SERPINF1
V-type proton ATPase catalytic subunit A	P38606	ATP6V1A
60S ribosomal protein L3	P39023	RPL3
Dolichyl-diphosphooligosaccharide--protein glycosyltransferase 48 kDa subunit	P39656	DDOST
T-complex protein 1 subunit zeta	P40227-2	CCT6A
Isoleucine--tRNA ligase, cytoplasmic	P41252	IARS
60S ribosomal protein L35	P42766	RPL35
Cell surface glycoprotein MUC18	P43121	MCAM
Aldehyde dehydrogenase family 3 member B1	P43353	ALDH3B1
Vesicle-fusing ATPase	P46459	NSF
40S ribosomal protein S5	P46782	RPS5
Ras GTPase-activating-like protein IQGAP1	P46940	IQGAP1
CD151 antigen	P48509	CD151
CD97 antigen	P48960-2	CD97
Deoxyribonuclease-1-like 1	P49184	DNASE1L1
Protein ERGIC-53	P49257	LMAN1
Fatty acid synthase	P49327	FASN
T-complex protein 1 subunit gamma	P49368-2	CCT3
Transmembrane emp24 domain-containing protein 10	P49755	TMED10
Guanine nucleotide-binding protein G(q) subunit alpha	P50148	GNAQ
Matrix metalloproteinase-14	P50281	MMP14
Emerin	P50402	EMD
Serpin H1	P50454	SERPINH1
Basal cell adhesion molecule	P50895	BCAM

60S ribosomal protein L14	P50914	RPL14
T-complex protein 1 subunit theta	P50990	CCT8
T-complex protein 1 subunit delta	P50991-2	CCT4
Fragile X mental retardation syndrome-related protein 1	P51114	FXR1
Ras-related protein Rab-5C	P51148	RAB5C
Ras-related protein Rab-7a	P51149	RAB7A
B-cell receptor-associated protein 31	P51572	BCAP31
Caveolin-2	P51636-2	CAV2
H(+)/Cl(-) exchange transporter 5	P51795	CLCN5
Chloride transport protein 6	P51797-6	CLCN6
Vesicle-associated membrane protein 7	P51809-3	VAMP7
Heterogeneous nuclear ribonucleoprotein M	P52272-2	HNRNPM
AP-2 complex subunit sigma	P53680	AP2S1
Voltage-dependent calcium channel subunit alpha-2/delta-1	P54289-4	CACNA2D1
Sodium/potassium-transporting ATPase subunit beta-3	P54709	ATP1B3
Alpha-soluble NSF attachment protein	P54920	NAPA
Solute carrier family 12 member 2	P55011	SLC12A2
Laminin subunit beta-2	P55268	LAMB2
Cadherin-13	P55290	CDH13
Cadherin-15	P55291	CDH15
Caveolin-3	P56539	CAV3
Transmembrane protein 33	P57088	TMEM33
CD81 antigen	P60033	CD81
Triosephosphate isomerase	P60174-4	TPI1
Eukaryotic initiation factor 4A-I	P60842	EIF4A1
Cell division control protein 42 homolog	P60953	CDC42
Ras-related protein Rab-2A	P61019	RAB2A
Ras-related protein Rab-10	P61026	RAB10
Ras-related protein Rab-14	P61106	RAB14
ADP-ribosylation factor 1	P84077	ARF1
Ras-related protein Rap-1A	P61224-2	RAP1A
Ras-related protein Rap-2b	P61225	RAP2B
V-type proton ATPase subunit d 1	P61421	ATP6V0D1
Transforming protein RhoA	P61586	RHOA
Heterogeneous nuclear ribonucleoprotein K	P61978-3	HNRNPK
14-3-3 protein gamma	P61981	YWHAG
Ras-related protein R-Ras2	P62070	RRAS2
14-3-3 protein epsilon	P62258-2	YWHAE
60S ribosomal protein L7a	P62424	RPL7A
Histone H4	P62805	HIST1H4A
Ras-related protein Rab-1A	P62820	RAB1A
GTP-binding nuclear protein Ran	P62826	RAN
Guanine nucleotide-binding protein G(I)/G(S)/G(T) subunit beta-1	P62873	GNB1
Guanine nucleotide-binding protein G(I)/G(S)/G(T) subunit beta-2	P62879	GNB2
60S ribosomal protein L30	P62888	RPL30
60S ribosomal protein L11	P62913	RPL11
60S ribosomal protein L8	P62917	RPL8

Peptidyl-prolyl cis-trans isomerase A	PPIA_HUMAN	PPIA
Ras-related C3 botulinum toxin substrate 1	P63000	RAC1
AP-2 complex subunit beta	P63010	AP2B1
Vesicle-associated membrane protein 2	P63027	VAMP2
Actin, cytoplasmic 2	P63261	ACTG1
Casein kinase II subunit beta	P67870	CSNK2B
Actin, alpha cardiac muscle 1	P68032	ACTC1
Putative elongation factor 1-alpha-like 3	Q5VTE0	EEF1A1P5
Tubulin beta-4B chain	P68371	TUBB4B
Casein kinase II subunit alpha 3	Q8NEV1	CSNK2A3
T-complex protein 1 subunit beta	P78371	CCT2
DNA-dependent protein kinase catalytic subunit	P78527	PRKDC
Dermcidin	P81605	DCD
Basement membrane-specific heparan sulfate proteoglycan core protein	P98160	HSPG2
Calcium-transporting ATPase type 2C member 1	P98194-2	ATP2C1
Peroxiredoxin-1	Q06830	PRDX1
Clathrin heavy chain 1	Q00610-2	CLTC
Fatty acid-binding protein, epidermal	Q01469	FABP5
Interferon-induced transmembrane protein 3	Q01628	IFITM3
Large neutral amino acids transporter small subunit 1	Q01650	SLC7A5
Desmoglein-1	Q02413	DSG1
60S ribosomal protein L18a	Q02543	RPL18A
Voltage-dependent L-type calcium channel subunit beta-1	Q02641-3	CACNB1
60S ribosomal protein L6	Q02878	RPL6
Caveolin-1	Q03135	CAV1
Copper-transporting ATPase 1	Q04656-5	ATP7A
Proteolipid protein 2	Q04941	PLP2
Voltage-dependent calcium channel gamma-1 subunit	Q06432	CACNG1
60S ribosomal protein L18	Q07020	RPL18
Cytoskeleton-associated protein 4	Q07065	CKAP4
Prolow-density lipoprotein receptor-related protein 1	Q07954	LRP1
Protein-glutamine gamma-glutamyltransferase E	Q08188	TGM3
ATP-dependent RNA helicase A	Q08211	DHX9
Sodium-dependent phosphate transporter 2	Q08357	SLC20A2
Lactadherin	Q08431-2	MFGE8
Desmocollin-1	Q08554-2	DSC1
Neuroblast differentiation-associated protein AHNAK	Q09666	AHNAK
AP-1 complex subunit beta-1	Q10567-3	AP1B1
Syntaxin-4	Q12846	STX4
Vesicular integral-membrane protein VIP36	Q12907	LMAN2
26S proteasome non-ATPase regulatory subunit 2	Q13200	PSMD2
Transcription intermediary factor 1-beta	Q13263-2	TRIM28
Gamma-sarcoglycan	Q13326	SGCG
Treacle protein	Q13428-2	TCOF1
Phosphatidylinositol-binding clathrin assembly protein	Q13492-4	PICALM
Ras-related protein Rab-32	Q13637	RAB32
Integrin alpha-7	Q13683-7	ITGA7

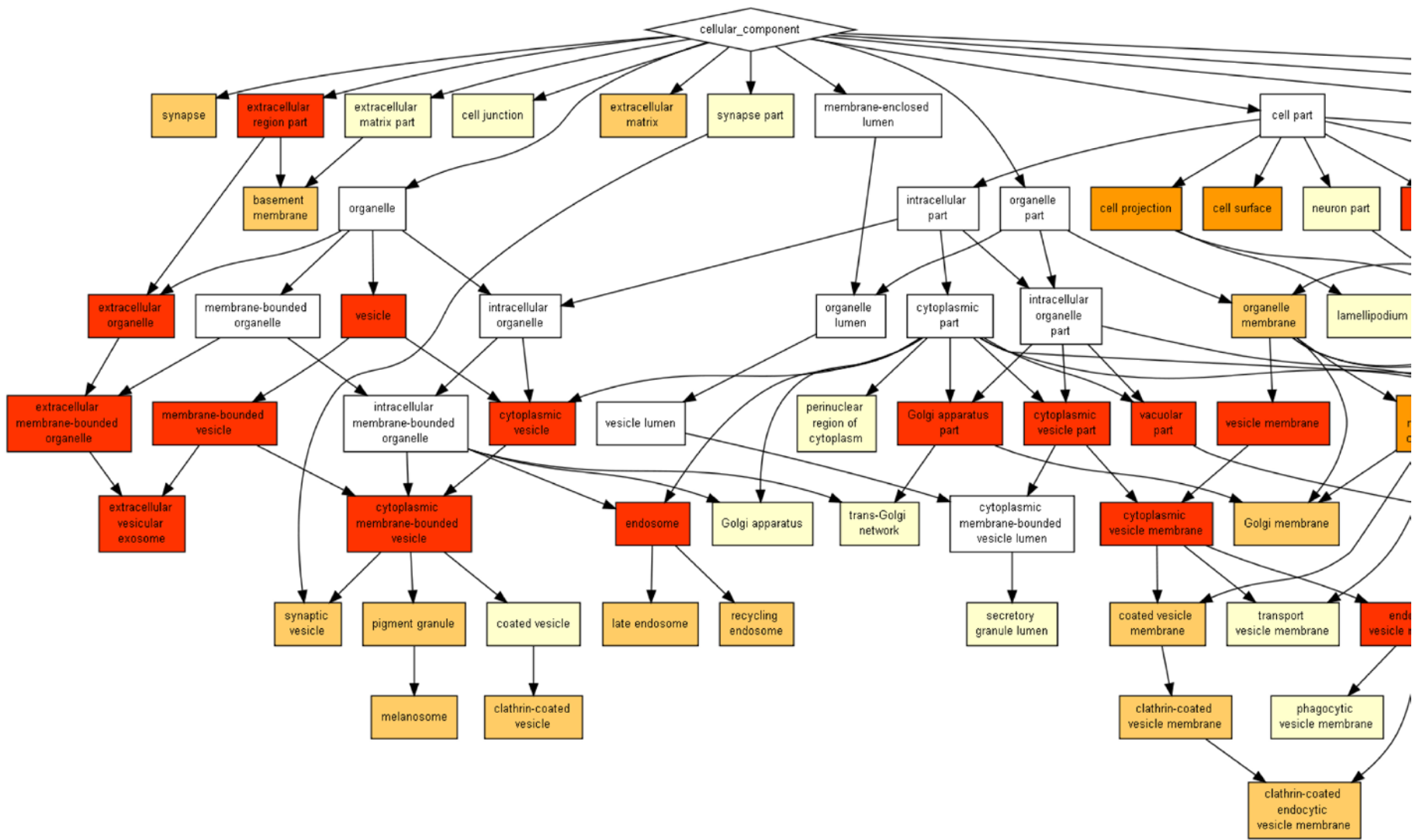|		
Voltage-dependent L-type calcium channel subunit alpha-1S	Q13698	CACNA1S
Bleomycin hydrolase	Q13867	BLMH
Lysosome membrane protein 2	Q14108-2	SCARB2
Dystroglycan	Q14118	DAG1
ARF GTPase-activating protein GIT2	Q14161-8	GIT2
Cytoplasmic dynein 1 heavy chain 1	Q14204	DYNC1H1
Filamin-C	Q14315-2	FLNC
Guanine nucleotide-binding protein subunit alpha-13	Q14344	GNA13
Clathrin interactor 1	Q14677	CLINT1
Neutral alpha-glucosidase AB	Q14697	GANAB
Raftlin	Q14699	RFTN1
Sarcospan	Q14714-2	SSPN
Major vault protein	Q14764	MVP
Importin subunit beta-1	Q14974	KPNB1
Signal peptidase complex subunit 2	Q15005	SPCS2
Rho guanine nucleotide exchange factor 6	Q15052-2	ARHGEF6
Plectin	Q15149	PLEC
Pericentriolar material 1 protein	Q15154-2	PCM1
Receptor-type tyrosine-protein phosphatase kappa	Q15262-2	PTPRK
Poly(rC)-binding protein 1	Q15365	PCBP1
Poly(rC)-binding protein 2	Q15366-7	PCBP2
Splicing factor 3B subunit 3	Q15393	SF3B3
Synaptonemal complex protein 1	Q15431	SYCP1
Neutral amino acid transporter B(0)	Q15758	SLC1A5
Vesicle-associated membrane protein 3	Q15836	VAMP3
V-type proton ATPase subunit S1	Q15904	ATP6AP1
Ras-related protein Rab-11B	Q15907	RAB11B
Synaptophysin-like protein 1	Q16563-2	SYPL1
Alpha-sarcoglycan	Q16586-2	SGCA
Transmembrane protein 132A	Q24JP5-4	TMEM132A
Estradiol 17-beta-dehydrogenase 12	Q53GQ0	HSD17B12
Cytochrome b reductase 1	Q53TN4-3	CYBRD1
Protein YIF1B	Q5BJH7-3	YIF1B
Transmembrane protein 63B	Q5T3F8-2	TMEM63B
Keratinocyte proline-rich protein	Q5T749	KPRP
CD276 antigen	Q5ZPR3-3	CD276
KN motif and ankyrin repeat domain-containing protein 2	Q63ZY3-3	KANK2
Metalloreductase STEAP3	Q658P3-3	STEAP3
Olfactomedin-like protein 2A	Q68BL7	OLFML2A
Ras-related protein Rab-12	Q6IQ22	RAB12
Polymerase I and transcript release factor	Q6NZI2	PTRF
Neutral cholesterol ester hydrolase 1	Q6PIU2	NCEH1
Chondroitin sulfate proteoglycan 4	Q6UVK1	CSPG4
Transmembrane protein 108	Q6UXF1	TMEM108
Rab11 family-interacting protein 1	Q6WKZ4	RAB11FIP1
CD109 antigen	Q6YHK3-2	CD109
Tripartite motif-containing protein 72	Q6ZMU5	TRIM72

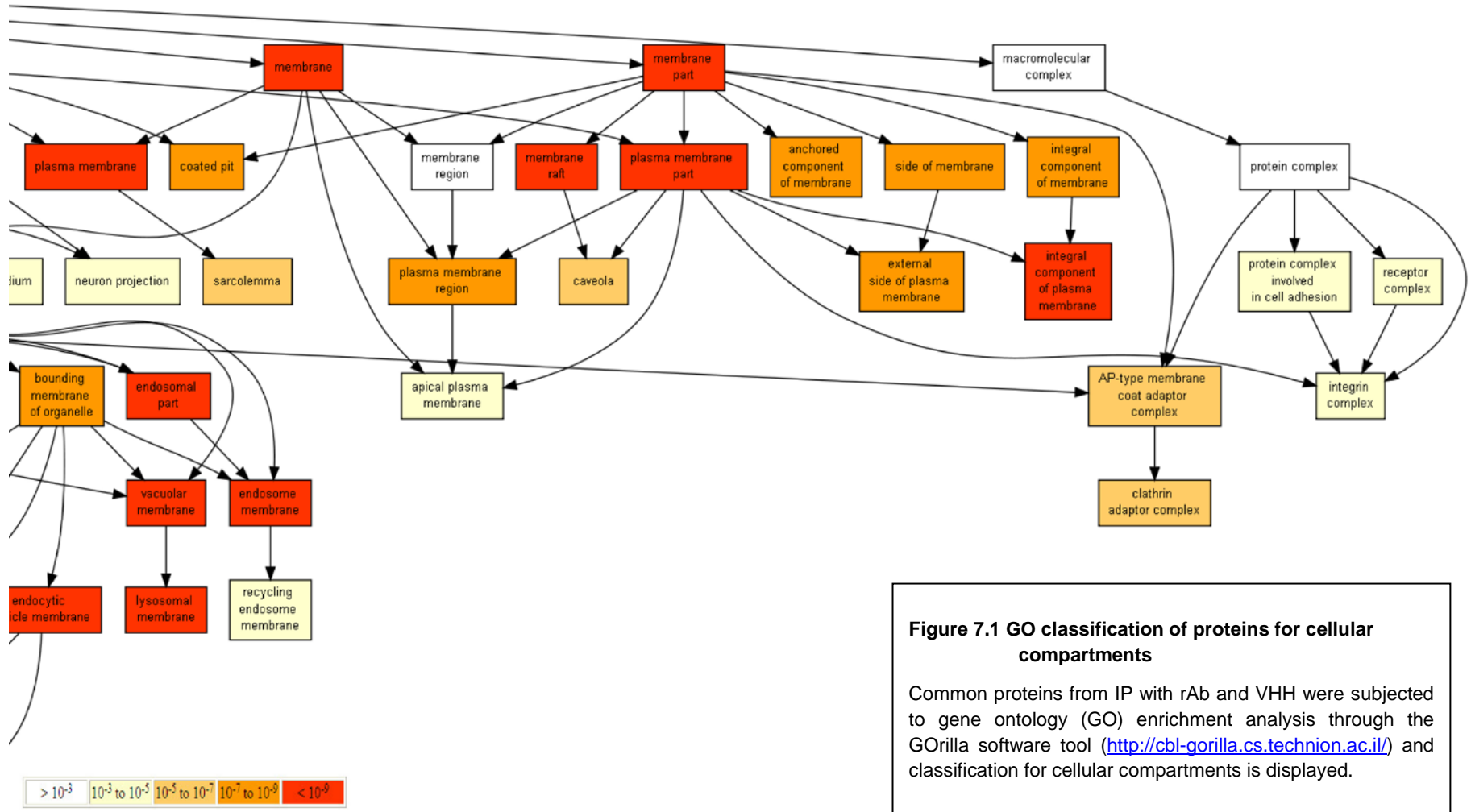|		
Major facilitator superfamily domain-containing protein 6	Q6ZSS7	MFSD6
Tubulin alpha-1A chain	Q71U36-2	TUBA1A
Rab11 family-interacting protein 2	Q7L804	RAB11FIP2
Autophagy-related protein 9A	Q7Z3C6	ATG9A
Myosin-14	Q7Z406	MYH14
Disheveled-associated activator of morphogenesis 2	Q86T65-4	DAAM2
Protein LYRIC	Q86UE4	MTDH
Kinectin	Q86UP2	KTN1
Cullin-associated NEDD8-dissociated protein 1	Q86VP6-2	CAND1
Extracellular matrix protein FRAS1	Q86XX4	FRAS1
Syntaxin-12	Q86Y82	STX12
Phospholipase D3	Q8IV08	PLD3
Sodium/hydrogen exchanger 9	Q8IVB4	SLC9A9
Choline transporter-like protein 2	Q8IWA5-3	SLC44A2
WD repeat and FYVE domain-containing protein 1	Q8IWB7	WDFY1
Serine/threonine-protein kinase LMTK2	Q8IWU2	LMTK2
Protein unc-45 homolog B	Q8IWX7-2	UNC45B
Protein MB21D2	Q8IYB1	MB21D2
ELMO domain-containing protein 2	Q8IZ81	ELMOD2
EH domain-binding protein 1-like protein 1	Q8N3D4	EHBP1L1
Transmembrane protein 87A	Q8NBN3-3	TMEM87A
Saccharopine dehydrogenase-like oxidoreductase	Q8NBX0	SCCPDH
Cyclin-Y	Q8ND76-3	CCNY
Signal peptide peptidase-like 2A	Q8TCT8	SPPL2A
Protein prune homolog 2	Q8WUY3-4	PRUNE2
Dephospho-CoA kinase domain-containing protein	Q8WVC6	DCAKD
Sec1 family domain-containing protein 1	Q8WVM8	SCFD1
Fatty acyl-CoA reductase 1	Q8WVX9	FAR1
Choline transporter-like protein 1	Q8WWI5-3	SLC44A1
ATP-dependent RNA helicase DDX1	Q92499	DDX1
Nicastrin	Q92542-2	NCSTN
Sodium/hydrogen exchanger 6	Q92581-2	SLC9A6
Pre-mRNA-splicing factor ATP-dependent RNA helicase PRP16	Q92620	DHX38
Peroxidasin homolog	Q92626	PXDN
Delta-sarcoglycan	Q92629-3	SGCD
Ryanodine receptor 2	Q92736	RYR2
Serine protease HTRA1	Q92743	HTRA1
Probable ATP-dependent RNA helicase DDX17	Q92841-1	DDX17
Golgi apparatus protein 1	Q92896	GLG1
Rho guanine nucleotide exchange factor 2	Q92974-3	ARHGEF2
V-type proton ATPase 116 kDa subunit a isoform 1	Q93050-1	ATP6V0A1
Secretory carrier-associated membrane protein 4	Q969E2-2	SCAMP4
Endoplasmic reticulum-Golgi intermediate compartment protein 1	Q969X5-2	ERGIC1
Leucine-rich repeat-containing protein 59	Q96AG4	LRRC59
Pre-B-cell leukemia transcription factor-interacting protein 1	Q96AQ6	PBXIP1
AP-2 complex subunit mu	Q96CW1-2	AP2M1
Protein YIPF6	Q96EC8	YIPF6

Protein disulfide-isomerase TMX3	Q96JJ7	TMX3
Serpin B12	Q96P63	SERPINB12
Membrane-spanning 4-domains subfamily A member 10	Q96PG2	MS4A10
Gasdermin-A	Q96QA5	GSDMA
Myeloid-associated differentiation marker	Q96S97	MYADM
Sortilin	Q99523	SORT1
Prohibitin-2	Q99623	PHB2
Heterogeneous nuclear ribonucleoprotein A/B	Q99729-3	HNRNPAB
Equilibrative nucleoside transporter 1	Q99808	SLC29A1
Junctophilin-2	Q9BR39	JPH2
Matrix-remodeling-associated protein 8	Q9BRK3	MXRA8
Endoplasmic reticulum resident protein 44	Q9BS26	ERP44
Extended synaptotagmin-1	Q9BSJ8	ESYT1
Phosphatidylinositol 4-kinase type 2-alpha	Q9BTU6	PI4K2A
Transmembrane protein 43	Q9BTV4	TMEM43
Tubulin beta-6 chain	Q9BUF5	TUBB6
Tubulin beta-2B chain	Q9BVA1	TUBB2B
Transmembrane protein 109	Q9BVC6	TMEM109
Transmembrane emp24 domain-containing protein 9	Q9BVK6	TMED9
Junctional adhesion molecule C	Q9BX67	JAM3
Rab11 family-interacting protein 5	Q9BXF6	RAB11FIP5
AP-1 complex subunit mu-1	Q9BXS5	AP1M1
Oxysterol-binding protein-related protein 8	Q9BZF1-3	OSBPL8
Protein sprouty homolog 4	Q9C004-2	SPRY4
Ras-related protein Rab-1B	Q9H0U4	RAB1B
Thioredoxin-interacting protein	Q9H3M7	TXNIP
Thioredoxin-related transmembrane protein 1	Q9H3N1	TMX1
Calsyntenin-2	Q9H4D0	CLSTN2
Golgi-associated plant pathogenesis-related protein 1	Q9H4G4	GLIPR2
Anthrax toxin receptor 1	Q9H6X2-5	ANTXR1
Platelet receptor Gi24	Q9H7M9	C10orf54
UPF0606 protein KIAA1549	Q9HCM3-2	KIAA1549
Probable cation-transporting ATPase 13A1	Q9HD20	ATP13A1
Transmembrane 9 superfamily member 3	Q9HD45	TM9SF3
Adipocyte plasma membrane-associated protein	Q9HDC9	APMAP
Ras-related protein Rab-18	Q9NP72	RAB18
Transmembrane protein 9B	Q9NQ34	TMEM9B
Reticulon-4	Q9NQC3	RTN4
Kinesin-like protein KIF13B	Q9NQT8	KIF13B
Integral membrane protein 2C	Q9NQX7-2	ITM2C
Vacuolar protein sorting-associated protein 45	Q9NRW7	VPS45
Serine incorporator 1	Q9NRX5	SERINC1
Protein SDA1 homolog	Q9NVU7	SDAD1
Inositol monophosphatase 3	Q9NX62	IMPAD1
G-protein coupled receptor family C group 5 member B	Q9NZH0	GPRC5B
Myoferlin	Q9NZM1-6	MYOF
Intersectin-2	Q9NZM3-2	ITSN2

EH domain-containing protein 2	Q9NZN4	EHD2
Calmodulin-like protein 5	Q9NZT1	CALML5
Very-long-chain (3R)-3-hydroxyacyl-[acyl-carrier protein] dehydratase 3	Q9P035	PTPLAD1
Vesicle-associated membrane protein-associated protein A	Q9P0L0	VAPA
Transmembrane protein 9	Q9P0T7	TMEM9
Teneurin-3	Q9P273	TENM3
Prostaglandin F2 receptor negative regulator	Q9P2B2	PTGFRN
Leucine--tRNA ligase, cytoplasmic	Q9P2J5	LARS
Coatomer subunit gamma-2	Q9UBF2	COPG2
C-type mannose receptor 2	Q9UBG0	MRC2
Guanine nucleotide-binding protein G(I)/G(S)/G(O) subunit gamma-12	Q9UBI6	GNG12
PTB domain-containing engulfment adapter protein 1	Q9UBP9-2	GULP1
Vesicle transport through interaction with t-SNAREs homolog 1B	Q9UEU0	VTI1B
Transmembrane protein 2	Q9UHN6-2	TMEM2
NADH-cytochrome b5 reductase 1	Q9UHQ9	CYB5R1
Leucyl-cystinyl aminopeptidase	Q9UIQ6	LNPEP
Plexin-A1	Q9UIW2	PLXNA1
Ras-related protein Rab-21	Q9UL25	RAB21
Kinase D-interacting substrate of 220 kDa	Q9ULH0-2	KIDINS220
Protein HEG homolog 1	Q9ULI3	HEG1
Two pore calcium channel protein 1	Q9ULQ1-3	TPCN1
Protocadherin gamma-C3	Q9UN70	PCDHGC3
Solute carrier family 12 member 4	Q9UP95-2	SLC12A4
Microtubule-actin cross-linking factor 1, isoforms 1/2/3/5	Q9UPN3	MACF1
Arf-GAP with GTPase, ANK repeat and PH domain-containing protein 1	Q9UPQ3-3	AGAP1
Protein Smaug homolog 1	Q9UPU9-2	SAMD4A
RuvB-like 2	Q9Y230	RUVBL2
RING finger protein 11	Q9Y3C5	RNF11
Vesicle transport protein GOT1B	Q9Y3E0	GOLT1B
V-type proton ATPase 116 kDa subunit a isoform 2	Q9Y487	ATP6V0A2
Talin-1	Q9Y490	TLN1
Neuroplastin	Q9Y639-3	NPTN
Numb-like protein	Q9Y6R0	NUMBL
Serotransferrin	TRFE_HUMAN	TF

Immunopurification was done with a monoclonal antibody from rabbit (rAb) or a llama-derived VHH-antibody fragment (VHH) from control myotubes. A total of 502 common proteins were detected by LC-MS in both samples. UniProt-protein IDs, protein, and gene names are listed.

Figure 7.1 GO classification of proteins for cellular compartments

Common proteins from IP with rAb and VHH were subjected to gene ontology (GO) enrichment analysis through the GOrilla software tool (http://cbl-gorilla.cs.technion.ac.il/) and classification for cellular compartments is displayed.

8 Publications

PUBLISHED

Dysferlin-peptides reallocate mutated dysferlin thereby restoring function

Schoewel V, Marg A, <u>Kunz S</u>, Overkamp T, Carrazedo RS, Zacharias U, Daniel PT, Spuler S.

PLoS One. 2012;7(11):e49603. doi:10.1371/journal.pone.0049603. Epub 2012 Nov 20.

Contribution: I conducted cell culture handling, immunofluorescence labeling, and data acquisition by confocal microscopy.

IN SUBMISSION

Caveolar function does not follow caveolar morphology

<u>Kunz S</u>*,Timmel T*, Schülke M, Spuler S

*Co-first author

Contribution: I planned and conducted sample preparation for TEM, as well as data acquisition, and analysis with TEM imaging software. I also contributed to interpretation of data and writing of the manuscript.

Hexokinase II function depends on dysferlin

Schoewel V*, Keller S*, <u>Kunz S</u>, Birkenfeld AL, Zhou Z, Mastrobuoni G, Pietzke, Opialla T, Zacharias U, Herrmann C, Dokas J, Weis J, Boschmann M, Al-Hasani H, Kempa S, Spuler S

Journal: Cell Metabolism

*Co-first author

Contribution: I conducted immunofluorescence labeling and data acquisition by confocal microscopy, and was involved in interpretation and quantification of data.

Publications

9 Acknowledgements